TO CONSERVE, OR NOT TO CONSERVE . . . Large eddy simulation of wind farms with energy-conserving schemes

Dhruv Mehta

TO CONSERVE, OR NOT TO CONSERVE . . .

Large eddy simulation of wind farms with energy-conserving schemes

Proefschrift

ter verkrijging van de graad van doctor aan de Technische Universiteit Delft, op gezag van de Rector Magnificus prof. ir. K.C.A.M. Luyben; voorzitter van het College voor Promoties, in het openbaar te verdedigen op woensdag 2 november 2016 om 15:00 uur

door

Dhruv MEHTA

Master of Science in Aerospace Dynamics, Cranfield University, UK, geboren te Pune, India Dit proefschrift is goedgekeurd door de

promotor: Prof. dr. ir. drs. H. Bijl copromotor: Dr. ir. A. H. van Zuijlen

Samenstelling promotiecommissie:

Rector Magnificus, voorzitter

Prof. dr. ir. drs. H. Bijl, Technische Universiteit Delft Dr. ir. A. H. van Zuijlen, Technische Universiteit Delft

Onafhankelijke leden:

Prof. dr. ir. G. A. M. van Kuik, Technische Universiteit Delft Prof. dr. ir. R. W. C. P. Verstappen, Rijksuniversiteit Groningen

Prof. dr. ir. J. Meyers, KU Leuven

Prof. dr. S. Hickel, Technische Universiteit Delft

Dr. P. J. Eecen, ECN

Het promotieonderzoek met betrekking tot dit proefschrift werd uitgevoerd bij de faculteit Luchtvaart -en Ruimtevaarttechniek van de Technische Universiteit Delft. Het werk werd ondersteund door Energieonderzoek Centrum Nederland door middel van de Europese Commissie subsidie 309395. Het onderzoek maakte deel uit van het project MARE-WINT (new MAterials and REliability in offshore WINd Turbines technology) van het Marie Skłodowska-Curie actions (MSCA).







Drukpers: Ipskamp Printing, Enschede (NL)

Omslag: Kleurpotlood, Shru-Dhru

ISBN: 978-94-6186-731-5

NUR: 910

E-versie: http://repository.tudelft.nl (gratis)

Dedicated to the loving memory of Spyke; 20/12/2005-27/01/2015 for the 3 a.m.-ers till the JEE.

Strange! An impulse stemming from a source so puzzling, Look! In the wee hours him his water guzzling, Hark! Ample wit yet struggling, Bark! Is Pinacol-Pinacolone nay so puzzling?

ACKNOWLEDGEMENT

I believe this is the most important chapter in this book. It refers to the people, events and places that have influenced and supported my doctoral work. I wish to thank,

• For the doctoral research ...

- Mr. Michiel Houkema, Prof. Hester Bijl and Dr. Alexander van Zuijlen for offering me a chance to pursue doctoral research at ECN and TU Delft; and for trusting me to complete the task on time.
 - Michiel, thank you for permitting me to work from Delft, where the environment outside of work was highly conducive to progress at work.
 - · Hester, thank you for all the freedom, motivation, positivity and valuable suggestions that you offered as a promotor.
 - Sander, thank you for seeing me through my doctoral research. Your constant and careful supervision, analysis of my work, the feedback and suggestions, and the freedom you offered are invaluable.

Colleagues at ECN

- Dr. Jessica Holierhoek for being a friendly and thoughtful supervisor, and for her constant support during my time at ECN.
- · Mr. Gerard Kist for providing me all the books and articles that I needed during my review of existing literature.
- · Ms. Ineke Wouts for her assistance with the administrative matters concerning my doctoral work at ECN.
- · Dr. Gerard Schepers for his supervision during the initial months of my work.
- · Dr. Jan-Willem Wagenaar for providing me with experimental data whenever I needed it, and Mr. Edwin Bot for performing simulations to support my work.
- · Mr. Arne van Garrel and Dr. Huseyin Ozdemir for their support with the code's amendments.
- · Mr. Ingmar Alting for all the nice conversations and my first boerenkool stamppot.
- · Dr. Peter Eecen for his contribution to reviewing this thesis and being a part of the defence committee.

- · Dr. Marc Langelaar for constantly reviewing my progress during my work at ECN.
- The secretarial team for helping me organise my frequent trips and sorting out matters beyond my understanding. Thank you very much!

- Colleagues at TU Delft

- Dr. Lorenzo Lignarolo for giving me the chance to work together on a project that contributed greatly to the final chapters of this thesis. Thank you for your trust and friendship!
- Ye Zhang for making chapter 5 possible through his selfless assistance. I hope to have the article ready soon! Thanks for letting me grab snacks off your table!
- · Evangelos Ploumakis and Hans van Heemst for being the finest master's degrees students that a doctoral researcher could ever have. It is equally incumbent on me to thank the other students in the **student room** where I would chime in to have some fun. Thank you all!
- · René Bos for offering me his code. A major part of this work would have been back breaking without his help.
- · Dr. Axelle Viré for helping me understand the simulation of the decay of turbulence, a concept that is central to this thesis.
- · Gael de Oliveira Andrade, for the codes he provided.
- · Prof. Gerard van Bussel and Dr. Carlos Simão-Ferreira, for offering a chance to explore the field of teaching after my doctoral research.
- · Ms. Colette Russo and Ms. Sylvia Willems, for their timely help with administrative matters.
- The doctoral students at Wind Energy and Aerodynamics for their friendship, presence, suggestions and interesting conversations.
- Dr. Richard Stevens for helping me understand the basics of large eddy simulation during the initial months of my research. You cleared doubts that would otherwise have lingered for a long time.
- Prof. Gijs van Kuik, Prof. Roel Verstappen, Prof. Johan Meyers and Prof. Stefan Hickel for reviewing my thesis and being a part of the defence committee.
- Outside the university ... where the things I did made the time I spent at the university more productive
 - The Fellowship of the Wint, for the crazy times we spent all over the continent during our regular meetings. It was a pleasure working ..., sorry partying with you all!

- All the friends I made during my stay in the Netherlands, right from Den Helder to Eindhoven, for all the crazy moments. I truly value the time we spent cycling, climbing, you cooking and me eating, or you tolerating my constant chattering (I noticed I do talk a lot, don't I?) and teasing (I think I am getting good at it, I should stop!). I hope we continue being this way, or you continue letting me be this way. Thank you very much, each and everyone! It would be hard, nay, impossible, to complete a PhD without you as a distraction.
- The Netherlands, for being a home away from home, and for the amazing, sporadic showers (not rain) that render the cycle paths empty enough for me to ride on the right side of the road.
- The constant supply of hot water, I think that is a real luxury!

• Back home ... there is nothing like it!

- The Indian Institute of Technology Kanpur, for being a university so beautiful and unique, and for providing me with memories so cherished! Thanks to your facilities, I never had to cook, clean, study etc., and only swim my way to the podium.
- D-TOP the the original and the extended for being the best friends that one could ever have! I am puzzled how we all ended up in one place and have stuck together these years. Thank you for shaping me into an adult (I know the process will continue till I am 75!) and never making me feel alone. Watching you struggle towards the goals that most have now achieved, was a pleasure and constant source of inspiration. Not a single day goes by when I don't think about the times we spent together; the best however, are yet to come!
- Cousins, uncles, aunts and grandparents for providing me with holiday homes, unique food, entertainment and a lot of fun!
- Mrs. Niranjana Mehta and Colonel Sudeepkumar Mehta for loving me to bits, being great and liberal parents and tolerating a good-for-nothing brat like me; the latter being a stellar achievement on their part. Further, I hold a deep reservoir of gratitude and pride for Dad having served the Olive Green and India, and for the Indian Army having selflessly provided me with a very special childhood, spent at times in the most exotic locations. Finally, thank you mom for being my first teacher (Your words not mine!).
- Kunaal Mehta for being the mature, responsible and apparently taller younger brother, while the elder never demonstrated these fine qualities. It seems that years of discord have brought out eerie similarities, or am I just being too optimistic?
- Spyke Mehta, for never leaving my side though I sadly left his.
 You will always be missed.

- Shruti Agrawal for *Shru-Dhru* and a life full of troubles. Words fail me when I try to express my fear of all the **belts** you have earned or strive to earn in East Asian martial arts. Please don't *Ippon*-me in my sleep.
- India, for all the excitement, splendour, diversity and noise that I haven't found elsewhere.

Finally, I would like to acknowledge Marie Skłodowska-Curie actions for funding my doctoral work.

It is hard to grow up, isn't it? I think it is far easier to remain youthful!

Dhruv Mehta Vrouwjuttenland, Delft

September 2016

CONTENTS

Acknowledgement					
i	REVIEW				
1	INTRODUCTION				
	1.1	Setting	4		
	1.2	Stimulus	4		
2	LAR	GE EDDY SIMULATION AND WIND FARM AERODYNAMICS	6		
	2.1	Wind farm aerodynamics	6		
		2.1.1 Wind turbine wakes	6		
		2.1.2 Far wake methods	8		
	2.2	Large Eddy Simulation	10		
		2.2.1 A statistical approach	10		
		2.2.2 Fundamentals of LES	12		
		2.2.3 SGS models in wind farm aerodynamics	18		
		2.2.4 Other models	23		
		2.2.5 Summary	23		
	2.3	Turbine modelling	24		
	2.4	A range of LES codes	25		
	2.5	Applications of LES to wind farm aerodynamics	27		
		2.5.1 Design of wind farms	27		
		2.5.2 Wind turbine array boundary layer	28		
		2.5.3 Wind turbine parametrisation for LES	29		
		2.5.4 LES or synthetic ABL	29		
		2.5.5 Horns Rev comparison	32		
		2.5.6 Reduced order models and coupling	33		
		2.5.7 Numerics	34		
	2.6	Conclusions	36		
	2.7	Motivation and open questions	38		
	2.8	The challenge	40		
	2.9	Contents	41		
ii	SCR	UTINY	43		
3	THE	ENERGY-CONSERVING NAVIER-STOKES CODE	44		
	3.1	Conservation of kinetic energy	44		
	3.2	Kinetic energy of the large scales	47		
	3.3	Kinetic energy equation for the resolved field	49		
	3.4	ECNS	52		
		3.4.1 The Harlow-Welch scheme	52		
		3.4.2 Time integration schemes	55		
4	TIM	E INTEGRATION	57		
	4.1	Introduction	57		

	4.2	.2 Dissipation expressed mathematically				
	4.3	Methodology	59			
		4.3.1 Grid-generated turbulence	60			
		4.3.2 Tests	61			
	4.4	Effect of time step and time integration schemes	63			
	4.5	Conclusion	70			
5	SPA	TIAL DISCRETISATION	71			
	5.1	Introduction	72			
	5.2	Spatial discretisation and numerical dissipation	72			
	5.3	The schemes within OpenFOAM	74			
	5.4	Convection of an inviscid vortex	75			
		5.4.1 Set-up: inviscid vortex	75			
		5.4.2 Observations	76			
		5.4.3 Non-Uniform Grids	79			
	5.5	Grid generated turbulence	81			
		5.5.1 Decaying turbulence: CBC	81			
		5.5.2 Preliminary Analysis	82			
		5.5.3 An Alternative Analysis	83			
	5.6	Conclusion	88			
	<i>J</i> .0	Concentration				
iii	TH	E TEST	90			
6	A C	OMPARATIVE STUDY OF LES CODES	91			
	6.1	The experimental set-up	91			
	6.2	Analogy	92			
	6.3	Tests	96			
	6.4 Grid convergence		97			
	6.5	Observations	100			
		6.5.1 With a laminar inflow	100			
		6.5.2 With a turbulent inflow	100			
	6.6	Conclusions	101			
7		D FARM AERODYNAMICS	107			
/	7.1	Start-up	108			
	7.1	7.1.1 Velocity profile	108			
		7.1.2 Wall stress	100			
		7.1.3 Modulation of the Smagorinsky constant	110			
	7 2	Atmospheric simulations				
	7.2	Simulation of a simple wind farm				
	7.3	Simulation of the EWTW	114			
	7.4		116			
	7.5	Conclusion	118			
CC	NCL	USIONS	123			
	RECOMMENDATIONS					
SUMMARY						
	SAMENVATTING					
r. ľ	LLUG	(U.E.	122			

iv	APPENDICES		134	
A SIMPLE NUMERICAL TESTS WITH THE ECNS		PLE NUMERICAL TESTS WITH THE ECNS	135	
	A.1	Shear layer in 2-D	136	
	A.2	Taylor-Green vortex in 3-D	138	
B HIGHER ORDER REQUIREMENT		HER ORDER REQUIREMENT	141	
	B.1	The fourth order formulation	141	
	B.2	Convection of an inviscid vortex	142	
C	VALIDATION OF A FAR WAKE ENGINEERING MODEL 144			
D EFFECT OF THE SMAGORINSKY CONSTANT ON ACTUATOR				
	PRE	DICTIONS	147	
	D.1	Sensitivity to the Smagorinsky constant	147	
		Sensitivity to grid resolution	148	
	D.3	Inference	148	
BI	BIBLIOGRAPHY			
CURRICULUM VITAE				

Part I

REVIEW

This part introduces the reader to the basics of wind farm aerodynamics, the current practices and the related computational fluid dynamics. It reviews the contributions of large eddy simulation to subject and the challenges that must be tackled to promote its use within the industry. Finally, it lists the questions that this thesis addresses.

INTRODUCTION

Assume that one is given a large number of wind turbines, say 80, which one could place wherever one prefers over a specified piece of land (or at sea)¹. All one must ensure is that the power these turbines produce as a wind farm, over a year, should be the maximum that they can deliver under the constraints of area and atmospheric conditions. What information does one require to determine the optimal placement?

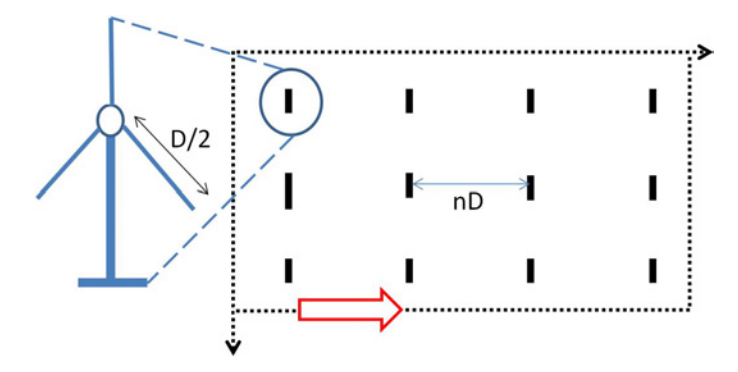


Figure 1.1: A simple aligned placement of wind turbines. D is the rotor diameter.

To help one get under way, figure 1.1 depicts a simple configuration that one may choose². With this configuration, the problem seems simpler as one must only move the turbines apart or nearer, along the axis indicated by the red arrow, as long as all the turbines are placed within the area enclosed by the dotted lines.

Therefore, the problem is now simplified to that of finding the optimal distance. But this simplification is rather specious! When a turbine extracts energy from the wind, it produces a wake that is slower than the incoming flow and bears a higher level of turbulence. Thus, a turbine downstream of another is likely to interact with the wake of the latter and in doing so, deliver lesser power due to reduced wind speed, while also suffering a greater load (force on the blades) due to the increased turbulence, which in the long run, reduces the turbine's longevity (Thomsen and Sørensen, 1999).

The reduction in power while a turbine operates in the wake of another has been established not only through measurements from wind farms (Taylor, 1990; Barthelmie et al., 2007) and wind tunnel experiments (Chamorro

¹ On land, one must also consider the influence of topology (trees) and man-made structures, if present in proximity.

² Distances to points downstream of a turbine would henceforth be mentioned as nD, where n is a positive real number and D is the turbine's rotor's diameter.

and Porté-Agel, 2011) but also through computational fluid dynamics (CFD) (Barthelmie et al., 2009; Stevens et al., 2013a). Hence, placing the turbines close enough to minimise the area they require is certainly not viable, which brings one back to the old problem of optimal placement.

However, studies also indicate that if the wake from the first turbine is allowed to travel over land or water for a suitable distance, the combined effect of the wake's and the atmosphere's turbulence will ensure that the wake is re-energised by increasing its velocity. The distance over which the wake can achieve this recovery and its variation with atmospheric conditions, must obviously be determined beforehand.

Determining this distance is quite difficult because the atmospheric boundary layer (ABL) can veer the wakes away from the turbine's centreline, which may not lead to interaction with another downstream turbine at all! Although this is much beneficial, it cannot always be known in advance. Further, we have only considered a single wind direction while 'simplifying' this problem. The wind direction varies (if not significantly) and influences the development of the wakes, which must be taken into account. These changes in wind directions can also be local, which are generally hard to predict and analyse.

Under these circumstances, it would be impractical to use a trial-and-error experiment to determine the optimal placement. Nonetheless, the combined knowledge from previous experiments and wind tunnel tests, could be used for the development of mathematical methods capable of predicting the behaviour of wind turbine wakes. The mathematical modelling of turbines, wakes and the ABL has been pursued over the last few decades with promising results. But despite the success, most of the comprehensive models are yet to be adapted for industrial applications and remain purely for academic research.

Combining mathematical models of wind turbines and turbulence into a numerical method capable of simulating wake-ABL interaction is challenged by major trade-off; the desired accuracy and comprehensiveness of the method versus the computational requirements. As regards to wake-ABL interaction, a major drawback that results from computational demands is that of using under resolved or coarse grids for discretisation.

Although, certain models for turbines, ABL and turbulence are capable of working with slightly coarse grids, not all numerical schemes used to mathematically resolve the flow, deliver good accuracy and stability on coarse grids. Nonetheless, a smart combination of numerical schemes that work well with coarse grids and mathematical models that are accurate enough for representing phenomena that govern the generation of power on a wind farm; could prove useful in the study of industrial wind farm aerodynamics.

This thesis aims to use the mathematical models of turbines, ABL and turbulence that are prevalent in academia and numerical schemes that retain their accuracy on coarse grids, to devise a method that could enable the industry to predict quickly and accurately, the features of wake-ABL interaction that are most relevant to gauging the power produced by a wind farm.

In this chapter, we describe the motivation behind this thesis and the contents of the chapters that follow. The aim is to assist a reader obtain an overview of this thesis.

1.1 SETTING

MARE-WINT or new MAterials and REliability in offshore WINd Turbines technology, is a project funded by the European Commission towards reducing the cost of wind energy. The intention is to improve the quality of resource assessment, operation and maintenance of offshore wind farms, which at the moment, is a costly affair.

A part of MARE-WINT deals with the analysis of wind turbine wakes, their impact on power generation and the longevity of turbines. This thesis intends to contribute to MARE-WINT by proposing a method that is reliable and comprehensive with regards to its purpose, i.e. simulating large wind farms within an ABL.

The Energy research Centre of the Netherlands (ECN) initiated the work in this thesis by developing the framework of a computer code called the Energy-Conserving Navier-Stokes (ECNS) code. The ECNS combines special spatial discretisation and time integration methods, known as *energy-conserving schemes* to guarantee stability with numerical simulations, theoretically, at any grid resolution and time step used for discretising space and time (Verstappen and Veldman, 2003). Additionally, these schemes guarantee the absence of *numerical dissipation* that reduces the accuracy of the schemes, especially on coarse grids.

Following the verification and validation of the ECNS for inviscid and laminar flows (Sanderse, 2013), the code has to be upgraded to simulate high Reynolds number turbulent flows. A thorough review of literature prior to this project and the favourable features of the energy-conserving (EC) scheme, made Large Eddy Simulation (LES) a logical choice for modelling the turbulent nature of the ABL. This marked the beginning of the work described in this thesis.

1.2 STIMULUS

Although it is clear that the schemes in the ECNS have a theoretical advantage over non-EC schemes, the same has yet to be evaluated in a practical setting. This advantage is the complete absence of numerical dissipation (Verstappen and Veldman, 2003). *Numerical dissipation* is known to add artificial viscosity to flow leading to the spurious withdrawal of kinetic energy (KE). On a wind farm or even within an ABL, this effect could alter the de-

velopment of wakes, lead to the decay of turbulence kinetic energy (TKE) and ultimately, faulty predictions of the power generated by the turbines.

At the same time, the LES approach that is used to model turbulence, also adds a large amount of dissipation to a simulation; the dissipation that is missing because LES only simulates the large energy-containing scales of a turbulent flow, as its name suggests. The remaining scales are mathematically modelled with a subgrid scale (SGS) model.

The large scales contain and transport a major part of the energy of a flow, which is concomitantly withdrawn by the *smaller scales* of the flow. This withdrawal of energy is quite large in magnitude for high Reynolds number flows. Further, as the Reynolds number increases, one is practically able to simulate fewer scales (but always the ones with the highest energy) for a given amount of computational resources. Hence, with increasing Reynolds number, the SGS model increasingly accounts for more and more scales, which are responsible for the dissipation of energy. A good SGS model tries to account for this *physical dissipation* as accurately as possible.

A question that arises is how beneficial is the absence of numerical or artificial dissipation, as regards to affecting the performance of an LES model by spuriously contributing to the withdrawal of energy?

This question arose during a perusal of previous studies on wind farm aerodynamics with LES. Certain studies used codes that could introduce numerical dissipation (theoretically as compared to EC schemes), in fact, certain LES approaches (not used in wind farm aerodynamics so far), rely on the artificial dissipation to model the physical dissipation, called *implicit LES* methods (Sagaut, 2006). Thus, different LES approaches each leading to favourable results, led to the question about the combined role of the LES model and schemes, which ultimately brings us to the question whether using an EC scheme for practical applications like wind farm aerodynamics is beneficial or not?

Our choices were driven by our aim to propose a framework that uses a reliable, versatile but not overly detailed LES approach to wind farm aero-dynamics, to strike a balance between accuracy and computational requirements. ECN's aim was to use such an approach to gain understanding of how models that are simpler and faster than LES, could be modified or tuned to deliver a comparable performance.

We begin with a review of numerical methods used to study wind farm aerodynamics, with emphasis on LES and its contributions to the subject. This review is used to support our choice of the LES model (the Smagorinsky model, Smagorinsky (1963)), the investigations that we performed on EC schemes, the numerical tests involved and the verification of the ECNS-LES code.

LARGE EDDY SIMULATION AND WIND FARM AERODYNAMICS

This chapter is a *literature review* and paraphrases findings reported in scientific literature to provide the reader with an overview of wind farm aerodynamics and large eddy simulation (LES).

2.1 WIND FARM AERODYNAMICS

Wind farm aerodynamics deals with the production and development of wind turbine wakes on a wind farm as they interact with the ABL, turbines and with each other. A complete aerodynamic analysis estimates not only the power produced by a wind farm but can help one understand complex situations like the effects of gusts and atmospheric stratification, the meandering of wakes and the influence a large wind farm can have on local weather.

Aerodynamic analyses require information on the velocity of air, its variation with time and other statistical derivatives. One can collect such data by deploying meteorological masts on wind farms with equipment that record the variation in wind velocity at points and even across a limited area. Nonetheless, this data is scarce to provide a clear picture of the flow of air and on a large wind farm, even more so. Further, such experiments are done on established wind farms, which rules out the possibility of a pre-deployment analysis.

Adapted from Mehta et al. (2014b)

The question that now arises, is how can one know about wind farm aerodynamics without relying completely on an established wind farm? Simulations could be an alternative! But before one can simulate a wind farm, one must know enough about modelling its components namely, the turbines and the ABL and about boundary conditions to mimic the ground and suitable for the small computational domain (with respect to the lower atmosphere) with turbines within it.

2.1.1 Wind turbine wakes

A wind turbine's wake can be divided into two regions, the *near wake* and the *far wake*. The former, lies immediately behind the turbine and is primarily a remnant of the turbine's design and operation. The loss of energy resulting from driving the wind turbine, is manifested as an expansion of the wake and a steep reduction in its velocity. The near wake generally ends between 2D and 4D (Crespo et al., 1999b), as the wake gains turbulence to transition into the far wake (Sørensen, 2011).

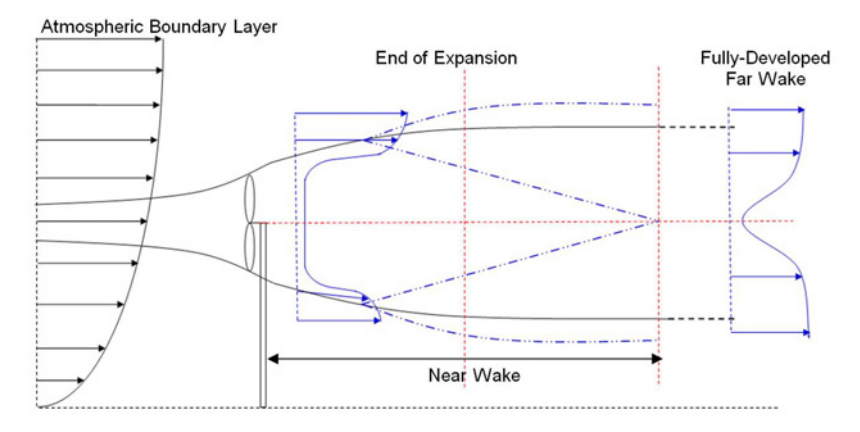


Figure 2.1: A simple illustration of the near and the far wake of a turbine operating within the atmospheric boundary layer.

An omnipresent source of turbulence is the atmosphere itself. Apart from that, the mechanical turbulence created by the turbine and that generated in the shear layer formed between the faster freestream air and the slower wake, contribute to an increased level of turbulence in the wake. In the far wake, it is this turbulence that promotes the mixing of the wake with the freestream leading to the subsequent recovery of the velocity deficit and reduction of turbulence intensity (Sanderse et al., 2011).

This thesis deals with far wake methods that do not require very detailed modelling of wind turbines because for far wake analyses, the turbine's presence need only be modelled as the correct deficit in wake velocity (velocity deficit) and an increased amount of turbulence (turbulence intensity) (PortéAgel et al., 2011). Therefore, a model of the turbine (such as actuator disk with rotation) that is capable for producing acceptable far wake velocity and turbulence statistics, is simple and accurate for wind farm simulations.

Nonetheless, the accurate modelling of turbines becomes essential for near wake analyses or obtaining details on a turbine's operation, which is a topic as complicated as far wake aerodynamics but requires a different approach. Therefore, this review encompasses only far wake and wind farm aerodynamics and the pertinent models and numerical methods. For details on near wake and rotor aerodynamics, readers may refer to reviews by Crespo et al. (1999b), Snel (1998, 2003), Vermeer et al. (2003), and a more recent one by Sanderse et al. (2011).

We begin with a short description of simple far wake models that have been used so far. By studying the benefits and limitations of simple models, we hope to develop an understanding of the features an industrial model must encompass for effective analyses of wind farm aerodynamics.

2.1.2 Far wake methods

For the sake of simplicity, early far wake methods assumed that the vertical profiles of velocity deficit and turbulence intensity in a turbine's wake, are roughly *Gaussian*, self-similar and even axisymmetric. In addition, the turbulence was treated as isotropic and homogeneous (Ainslie, 1985; Crespo et al., 1985, 1999b). Combined with approximations for modelling the turbines and the ABL, these methods could be used for wind farm simulations.

The use of such models was discontinued following evidence that did not support the assumptions of isotropy, symmetry of the wake and self-similarity of the profiles of velocity deficit and turbulence intensity (Elliot, 1991; Schelz et al., 2001; Gómez-Elvira et al., 2005). Nonetheless, the early models influenced the development of the more advanced *far wake engineering models*, which being affordable, speedy and accurate in terms of predicting the mean power generation, are now widely employed by the industry. Although it is known that engineering models may perform inaccurately for a single inflow direction, their predictions are reasonably accurate when averaged over a range of inflow angles (Barthelmie et al., 2009).

A brief account of these methods will help understand the importance of LES, which is the theme of this thesis. A complete description of traditional far wake models can be found in (Crespo et al., 1999b; Vermeer et al., 2003), which will not be quoted again for succinctness.

2.1.2.1 Individual wakes

Individual wakes were first analysed with quick *kinematic models* as self-similar profiles of velocity deduced from studies on jets (Abramovich, 1963; Lissaman, 1979). The input was in the form of a velocity profile prescribed where the wake stops expanding, which was obtained by relating the velocity deficit to the turbine's thrust coefficient. Despite various attempts to make kinematic models comprehensive, their dependence on the proper specifications of model parameters, inability to model wake meandering and the hypothesis of self-similarity that is violated by the presence of the ground, remained major drawbacks.

On the other hand, *field models* solved the parabolic *Navier-Stokes* (NS) equations by ignoring the turbulent diffusion and the gradient of pressure along the main flow direction (Sforza et al., 1981; Ainslie, 1985). This not only helped simplify the model but also reduced the computational time significantly (Cabezón et al., 2011). Field models were validated successfully against wind tunnel tests and could also account for large scale effects like wake meandering, albeit with necessary modifications.

Boundary layer wake models were a major improvement over their predecessors in terms of treating the wake as non-axisymmetric and introducing three-dimensionality, along with more detailed modelling of the ABL using Monin-Obukhov's approach (Moeng, 1984). The turbulent wake was modelled with the $\kappa - \varepsilon$ Reynolds-averaged Navier-Stokes (RANS) model, although

in a parabolic sense. An elliptic formulation that incorporated the gradient of pressure and turbulent diffusion along the main flow direction (in essence, the RANS equations), was also proposed (Cabezón et al., 2011). However, the improvements were disproportionate to the increased computational needs. Despite treating the turbulence as anisotropic, the overall performance was still dependent on the accurate specification of RANS model parameters and the initial wake deficit.

2.1.2.2 Multiple wakes and wind farms

Surface roughness models were amongst the first and simpler wind farm models. They used a logarithmic profile for the ABL and modelled the turbines as elements of extra roughness. Frandsen (1992) used two profiles, one for the flow between the ground and the turbines' hubs and another above the turbines' hubs to model the turbines' action as a drag force. Despite its simplicity, Frandsen's model proved useful in the study of the effect of large offshore wind farms on local weather (Crespo et al., 1999a) and was also improved later with the application of LES. Another model based on wake expansion is that of Frandsen et al. (2006), which is adapted to regimes that include infinite wind farms, multiple wake flows and changes in surface roughness, while considering the presence of the ground that causes asymmetric wake expansion.

A proper treatment of wakes was first done with *superposition* models that superimposed velocity perturbations caused by multiple turbines to model their combined effect. Semi-empirical modifications were made to account for the fact that downstream wakes recover more rapidly due to enhanced turbulence intensity. This was replicated by superposition models as regards to predicting power generation, which dropped significantly for the first two rows of turbines with no measurable decrease for more downstream rows. The downside of these models was the lack of physical justification for the algorithms used for superimposing the wakes.

Wind farm codes witnessed a major improvement with the advent of parabolic formulations of single wake models. Initially, all turbines were modelled as profiles of velocity deficit and added turbulence intensity allocated at the end of the wake's expansion region, which would then be transported downstream. This was later replaced with the method of assigning perturbations of flow variables at the turbine's location and finally by actuator methods (see Sanderse et al. (2011)).

Elliptic equivalents that accounted for axial pressure gradient and turbulent diffusion in the NS equations were also proposed. These modifications to the simpler parabolic form of the NS equations however, incur increased computational requirements. Although elliptic models resolve the turbulence accurately in the far wake, they over predict turbulent diffusion in the near wake and under predict the velocity deficit, unless the model's coefficients in the RANS equations are tuned appropriately. By neglecting stream wise diffusion, the parabolic form of the NS equations, predicts the

velocity deficit correctly in the near wake but underestimate it in the far wake, while overestimating the turbulence intensity. Amongst RANS models, the *Reynolds stress model* that permits the anisotropic resolution of the fluid, provides the most reliable results in both the near and the far wake. However, in the near wake it still under predicts the velocity deficit by a small amount, which could be tackled by careful tuning.

Elliptic formulations are suitable for far wake analyses that are relevant to wind farms as they predict both the turbulence intensity and velocity deficit correctly in the far wake, which ultimately may interact with a downstream turbine and is more relevant to predicting power generation. Results can generally be improved with advanced models of turbulence, like the Reynolds stress model, or with more careful specification of model parameters. On the other hand, parabolic formulations are good only for the near wake. A detailed comparison of elliptic and parabolic formulations of the NS equations can be found in Cabezón et al. (2011).

2.1.2.3 Summary

To summarise, far wake models must be able to correctly predict the turbulence intensity and velocity deficit at distances greater than 4D, which in most cases is the minimum distance between turbines on modern wind farms. The inability to generate proper results may stem from the combination of inaccurate turbulence and ABL modelling, tuning with limited field data and the inability to resolve the flow in case of multiple turbine-wake or wake-wake interactions. It is fair to mention that accurate turbine modelling is important for the proper function of *engineering models* and the simple allocation of velocity profile at the end of the near wake, to mimic the turbine, is certainly not the most accurate model.

2.2 LARGE EDDY SIMULATION

As mentioned previously, the model constants of RANS models must be predetermined using aerodynamic data from wind farms. But the scarcity of field data prevents comprehensive tuning and renders engineering models suitable only for industrial applications and not for gaining insight into the fundamental physics of wind farm aerodynamics, which demands first principle physics-based models like LES and Direct Numerical Simulation (DNS).

The aim of this section is to familiarise the reader with the fundamentals of LES.

2.2.1 A statistical approach

One can study wind farm aerodynamics with the incompressible form of the NS equations and parametrising a wind turbine as an external body force (Vermeer et al., 2003). Whilst the tip speed of large turbines might approach

the limit of incompressibility (~Mach 0.3 at sea level), the flow in the wake remains incompressible (van der Pijl, 2007).

Let us begin with NS equations in Einstein's indicial notation in which, the subscript 'o', denotes the reference value of the density and temperature,

$$\frac{\partial u_i}{\partial x_i} = 0 , \qquad (2.1)$$

$$\begin{split} \frac{\partial(\rho_{o}u_{i})}{\partial t} + \frac{\partial(\rho_{o}u_{i}u_{j})}{\partial x_{j}} &= -\frac{\partial p}{\partial x_{i}} + \frac{\partial}{\partial x_{j}} \left(\mu \left(\frac{\partial u_{i}}{\partial x_{j}} + \frac{\partial u_{j}}{\partial x_{i}} \right) \right) \\ &+ \rho_{o}f_{i} + \delta_{i3}\rho_{o}g \frac{(\theta - \langle \theta \rangle)}{\theta_{0}} \\ &+ f_{c}\varepsilon_{ij3}u_{j} \; , \end{split} \tag{2.2}$$

where

p pressure

μ molecular viscosity

ui component of velocity along the ith direction

 x_i component of the position vector along the i^{th} direction

f_i component of acceleration due to a body force along the ith direction

t time

f_c Coriolis parameter, a function of the latitude and the Earth's angular velocity

ρ density

g acceleration due to gravity

 θ potential temperature.

The *Coriolis force*¹ is pertinent only while analysing wind farms spread over a large area when its influence is mathematically comparable to other components of the NS equations (Porté-Agel et al., 2010). The term $\frac{\rho_0 \, g \, (\theta - \langle \theta \rangle)}{\theta_0}$, is *Boussinesq's approximation* of the buoyant force on a volume of fluid arising from minor variations in density brought about by changes in temperature (Boussinesq, 1877). The angled brackets stand for an averaged value, for example, over horizontal planes parallel to the ground in the case of an ABL simulation. Such thermally generated turbulence can be resolved using an additional scalar transport equation for the potential temperature,

$$\frac{\partial \theta}{\partial t} + \frac{\partial (\theta u_j)}{\partial x_j} - \alpha \frac{\partial^2 \theta}{\partial x_j^2} = q_v , \qquad (2.3)$$

where

α thermal diffusivity of the medium

 q_v heat flow from a source or to a sink.

¹ δ_{ij} is Kronecker's delta and ϵ_{ijk} is the Levi-Civita symbol for three dimensions.

If the ABL is neutral and there is no exchange of heat with the surface, both equation 2.3 and the term $\frac{\rho_0 g(\theta - \langle \theta \rangle)}{\theta_0}$ in equation 2.2 can be ignored (Panofsky and Dutton, 1984). For an incompressible flow, $\frac{\partial u_i}{\partial x_i} = 0$ and in the absence of heat sources or sinks, the above equation simplifies to,

$$\frac{\partial \theta}{\partial t} + u_j \frac{\partial \theta}{\partial x_j} - \alpha \frac{\partial^2 \theta}{\partial x_j^2} = 0.$$
 (2.4)

Turbulent flows comprise regions of swirling fluid known as *eddies*, which vary in size (formally known as length-scale) throughout the flow. Resolving eddies with the above equations is challenged by the non-linearity of the convective term, $\frac{\partial (\rho_0 u_i u_j)}{\partial x_j}$ that continually gives rise to smaller eddies through *vortex stretching* (Perić and Ferziger, 2002). As the Reynolds number of a flow increases, the smaller eddies further reduce in size, creating a greater range of eddy length scales, thus precluding an exact numerical analysis of such flows with the above equations (Davidson, 2004).

Thus, a practical approach to investigating turbulence involves a statistical analysis of the flow in the form of averages, as a trade-off between insight and computational requirements (or the resolution of experimental apparatus). The *averaging* leads to the removal of certain length (and time) scales, rendering the system more *solvable*. But such an approach is hindered by the *closure problem* of turbulence, in which, the unknowns that represent the flow's variables, exceed the equations in number (for details, please see Perić and Ferziger (2002)). To bypass this, we must resort to mathematical models that relate the unknowns to the physical nature of the flow as consistently as possible (Tennekes and Lumley, 1972). LES is one such statistical approach.

2.2.2 Fundamentals of LES

On a wind farm, the turbulent eddies range in size from the thickness of a turbine's blade's boundary layer (a few millimetres) to the distance between successive turbines (up to a kilometre), as a consequence of the high Reynolds number of the flow. This unfortunately makes DNS unworkable with today's computational means.

As an alternative, LES resolves certain eddies of a flow using a modified form of the NS equations, while mathematically modelling the remaining eddies following their removal from the flow field. In keeping with its name, the resolved eddies are the large energy-containing eddies of the flow that govern large scale phenomena like power production, wake meandering, response to gusts etc., and are comparable with or larger than the turbine's diameter.

Before getting to how these eddies can be selected and later resolved, one must first understand the mathematical basis of LES.

2.2.2.1 Eddies and the energy spectrum

Leonard (1974) defines LES as "using a more tractable form of the NS equations, to *approximate while retaining*, the most energetic features of the undisturbed problem". The eddies of a turbulent flow can be divided into three regimes,

- the large integral scales that are unaffected by molecular viscosity and bear a large portion of the flow's energy,
- the intermediate inertial scales that are unaffected by viscosity, boundary conditions and the large scales and
- the small Kolmogorov scales that are dissipated easily by molecular viscosity, which ultimately leads to the extraction of energy from the large scales.

All these scales are best represented by the energy spectrum, which relates the energy content of these scales to their length. For a turbulent flow at a high Reynolds number, the energy spectrum is similar to that shown in figure 2.2. κ is the wavenumber corresponding to an eddy's length scale (Meneveau and Katz, 2000),

$$\kappa = \frac{1}{0} \,, \tag{2.5}$$

where

0 size or the length scale of the eddy.

To the left lie the integral scales that are the most energetic and are responsible for feeding the smaller scales with their energy. Once the energy flows out of the large scales, it enters the regime of intertial scales that are quite universal in nature. Their purpose is to solely transfer the energy to the smallest scales or the Kolmogorov scales, where molecular viscosity can dissipate the energy (Pope, 2000). Figure 2.2 represents the universal nature of the inertial range through the constant slope of the spectra. The slope, as we shall mention later, is constant for homogeneous isotropic turbulent fields.

LES resolves all scales except for those comparable in size to the *Kolmogorov* scales (and the smaller scales of the inertial range, to be more precise) at which dissipation is dominant. The smallest scales that could be resolved with LES or should be resolved for an accurate LES, depend on the flow's Reynolds number that determines how wide is the range of length scales, the computational resources that set the limit on resolution and the type of data that is desired from an LES, mean flow quantities or detailed local information about the flow (see Liu et al. (1994) for such an analysis).

Once the NS equations are discretised in space on a computational grid, scales that are smaller than the grid's cells, or the subgrid scales, are automatically removed from the system. Hence, the terms *small scales* and *subgrid scales* are interchangeable in LES parlance. Instead of being resolved, these

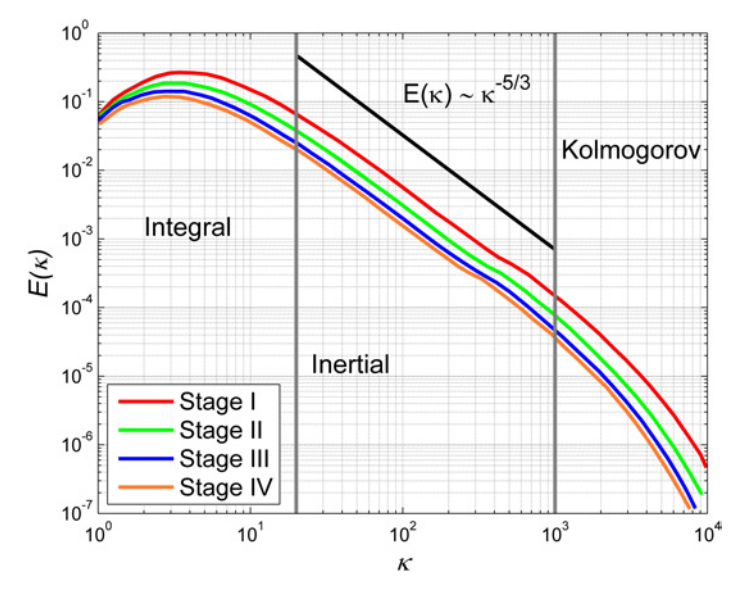


Figure 2.2: The energy spectrum of an isotropic homogeneous turbulent field. In this example, the turbulence decays under the action of molecular viscosity from Stage I to Stage IV but the distribution of energy complies with the fundamentals of turbulence (adapted from Kang et al. (2003)).

small scales must be mathematically modelled (for closure, see section 2.2.1) with what is consequently known as a *Subgrid Scale* (SGS) model.

An SGS model must encompass the fundamental properties of a turbulent flow for good results with LES. Ideally, it should dissipate the energy that the large scales would feed subgrid scales with and therefore, should be able to relate the resolved turbulent field to the dissipation. Although it sounds daunting, two very basic properties of turbulence enabled the creation of SGS models. These as paraphrased from Frisch (1995) are,

- the Kolmogorov scale is universally invariant regardless of the flow's nature, i.e. small scale turbulent motions are statistically identical for high Reynolds number turbulent fields. Further, at this scale the flow loses its directionality and becomes statistically isotropic (Pope, 2000).
- *Scale Invariance* is an integral property of the inertial range, i.e. turbulent motions occur simultaneously at different scales at nearly the same location (Meneveau and Katz, 2000) (also see Lesieur and Metais (1996)).

Kolmogorov expressed the second point in a mathematical sense by relating the energy of an eddy to its size. A dimensional analysis hinted at the scale invariance of the rate of dissipation of large scale turbulence kinetic energy (TKE) due to molecular viscosity or ε as,

$$E(k) = c_K e^{2/3} k^{-5/3}$$
, (2.6)

where

- c_K the Kolmogorov constant
- ϵ turbulence dissipation rate $(\frac{J}{kgs})$.

The quantity $\gamma^{5/3} E(\gamma k)$ is invariant in the inertial range under scale transformation i.e. $k \to \gamma k$ (γ is a real number). It is this symmetry that helps link the dynamics of the large and small scales in the modelling of turbulence.

2.2.2.2 Filtered Navier-Stokes equations

Subgrid scale modelling can be done in various ways, as long as the model encompasses the correct dissipative nature of the subgrid scales. Generally, LES is classified as being *Implicit* or *Explicit*.

Implicit LES treats SGS modelling as purely dissipative. One employs an upwind scheme to discretise the convective term or uses an artificial dissipative term to introduce dissipation, which in general, is very close to that introduced by a physical model. In practice, the numerical dissipation is second or fourth order accurate. Various methods of implicit LES are mentioned in Sagaut (2006), for a detailed description the readers are referred to Grindstein et al. (2007).

Explicit LES, which we shall use for this thesis, uses a model to represent the coupling between the resolved and the subgrid scales. One of simplest explicit LES models, the Smagorinsky model, formulates the coupling based on the equilibrium between the flow of kinetic energy (KE) from the resolved scales and its dissipation by the subgrid scales. This approach is known as functional modelling. On the other hand is structural modelling, which seeks to reproduce the statistical correlations between the large scale structures at different scales (Sagaut, 2006). Bardina's scale-similarity model falls under this category (Bardina et al., 1983). A detailed explanation of the assumptions, principles and limitations of implicit and explicit LES can be found in literature cited in this section. Nonetheless, the explicit models used for this thesis are described in this chapter.

To begin with, one must modify the NS equations to govern the dynamics of only the resolved scales because the rest are not directly a part of the mathematics that follows. This modification is best explained in terms of a *filter*.

A filter is an operator that is *high-pass* in scale size (low-pass in wavenumber and frequency) and removes eddies that are smaller than the filter's *cut-off width* (or length). The cut-off width must be large in comparison to the Kolmogorov scale, ideally somewhere in the inertial range. Mathematically, filtering a turbulent vector variable results in a filtered and a residual quantity. Therefore, *x*, with a filtering operator \mathcal{G} , decomposes *x* into a filtered and a residual quantity,

$$\mathfrak{G} * x = \widetilde{x} + x' , \qquad (2.7)$$

where

- 9 filtering operator
- x turbulent field variable
- \tilde{x} filtered value of the variable
- x' residual value of the variable.

The application of \mathcal{G} can be thought of as something similar to an ensemble average used in RANS. In LES, the filter width is generally related to or in some cases, equal to the grid size. Hence, the values x and x' would pertain to the large scales being resolved on the computational grid and the subgrid scales, respectively. Sagaut (2006) provides a good description of filtering and its mathematical operations.

Upon filtering, the incompressible NS equations (equations 2.1 and 2.2) read,

$$\frac{\partial \widetilde{u_i}}{\partial x_i} = 0 , \qquad (2.8)$$

$$\begin{split} \frac{\partial(\rho_{o}\widetilde{u_{i}})}{\partial t} + \frac{\partial(\rho_{o}\widetilde{u_{i}u_{j}})}{\partial x_{j}} &= -\frac{\partial\widetilde{p}}{\partial x_{i}} + \frac{\partial}{\partial x_{j}} \left(\mu\left(\frac{\partial\widetilde{u_{i}}}{\partial x_{j}} + \frac{\partial\widetilde{u_{j}}}{\partial x_{i}}\right)\right) + \\ &+ \rho_{o}\widetilde{f_{i}} + \delta_{i3}\rho_{o}g\frac{(\widetilde{\theta} - \langle\widetilde{\theta}\rangle)}{\theta_{0}} \\ &+ f_{c}\epsilon_{ij3}\widetilde{u_{j}} \;. \end{split} \tag{2.9}$$

In practice, the above equations *do not imply* explicit filtering. The *tilde* merely indicates that the variables pertain to the resolved scales alone, which in fact comprise the velocity field assigned to an LES grid. Scales that cannot be resolved on a grid are either smaller than the grid's size² or larger than the computational domain, which by virtue of the grid and the domain alone, are removed from the field, hence called the *filtered field*. Nonetheless, explicit filtering is used with some SGS models (see Porté-Agel et al. (2000) for a detailed description).

Decomposing the filtered convective term $\widetilde{u_iu_j}$ is not straightforward and incurs the *closure problem* for explicit-LES. Leonard (1974) addressed this issue by decomposing the term as,

$$\tau_{ij} = \widetilde{u_i u_j} - \widetilde{u}_i \widetilde{u}_j , \qquad (2.10)$$

where

 τ_{ij} subgrid-scale stress tensor or the subgrid tensor.

² subgrid or residual scales

SGS models replace τ_{ij} to close the system of equations. Using equation 2.10, the momentum equation for the LES of an incompressible flow reads,

$$\begin{split} \frac{\partial(\rho_{o}\widetilde{u_{i}})}{\partial t} + \frac{\partial(\rho_{o}\widetilde{u}_{i}\widetilde{u}_{j})}{\partial x_{j}} &= -\frac{\partial\widetilde{p}}{\partial x_{i}} + \frac{\partial}{\partial x_{j}} \left(\mu\left(\frac{\partial\widetilde{u_{i}}}{\partial x_{j}} + \frac{\partial\widetilde{u_{j}}}{\partial x_{i}}\right)\right) + \\ &+ \rho_{o}\widetilde{f_{i}} + \delta_{i3}\rho_{o}g\frac{(\widetilde{\theta} - \langle\widetilde{\theta}\rangle)}{\theta_{0}} \\ &+ f_{c}\varepsilon_{ij3}\widetilde{u_{j}} - \rho_{o}\frac{\partial\tau_{ij}}{\partial x_{j}} \,. \end{split} \tag{2.11}$$

Similarly, the filtered equivalent of equation 2.3 reads,

$$\frac{\partial\widetilde{\theta}}{\partial t} + \widetilde{u}_j \frac{\partial\widetilde{\theta}}{\partial x_j} - \alpha \frac{\partial^2\widetilde{\theta}}{\partial x_j^2} = -\frac{\partial q_j}{\partial x_j} \; , \tag{2.12} \label{eq:2.12}$$

where

- q_i SGS heat flux
- $\widetilde{\theta}$ filtered potential temperature.

Akin to τ_{ij} , q_j in the above equations is expressed as,

$$q_{i} = \widetilde{u_{i}\theta} - \widetilde{u}_{i}\widetilde{\theta}$$
 (2.13)

Details on the parametrisation of the SGS heat flux with an *eddy-diffusivity model* can be found in Porté-Agel (2004) and Porté-Agel et al. (2011). Once again, the transport equation for temperature need only be solved for a non-neutral ABL, examples of which can be found in Porté-Agel et al. (2014). This thesis covers only neutral ABLs, while also neglecting the *Coriolis* effect. In closing, the following equations form the backbone of this text,

$$\frac{\partial \widetilde{u_i}}{\partial x_i} = 0 , \qquad (2.14)$$

$$\begin{split} \frac{\partial \widetilde{u_i}}{\partial t} + \frac{\partial (\widetilde{u}_i \widetilde{u}_j)}{\partial x_j} &= -\frac{\partial \widetilde{p^*}}{\partial x_i} + \frac{\partial}{\partial x_j} \left(\nu \left(\frac{\partial \widetilde{u_i}}{\partial x_j} + \frac{\partial \widetilde{u_j}}{\partial x_i} \right) \right) + \\ &+ \widetilde{f_i} - \frac{\partial \tau_{ij}}{\partial x_j} \;. \end{split} \tag{2.15}$$

where

p* pressure normalised by reference density

ν kinematic viscosity.

2.2.3 SGS models in wind farm aerodynamics

Most LES codes for wind farm aerodynamics use *eddy-viscosity* models for the subgrid scales, which relate the dissipation through the subgrid scales with the resolved velocity field by defining a local value of *eddy-viscosity*.

2.2.3.1 The Smagorinsky model

Smagorinsky (1963) parametrised the SGS tensor by expressing its *deviatoric* component as,

$$\tau_{ij} - \frac{1}{3} \delta_{ij} \tau_{kk} = -2 \nu_T \widetilde{S}_{ij} \; , \tag{2.16} \label{eq:equation:2.16}$$

where

 ν_T eddy-viscosity

 \widetilde{S}_{ij} resolved strain-rate tensor.

 \widetilde{S}_{ij} represents strain-rate of the resolved velocity field,

$$\widetilde{S}_{ij} = \frac{1}{2} \left(\frac{\partial \widetilde{u_i}}{\partial x_j} + \frac{\partial \widetilde{u_j}}{\partial x_i} \right) . \tag{2.17}$$

 v_T is calculated locally using the strain-rate as,

$$v_{\rm T} = (C_{\rm S}\widetilde{\Delta})^2 (2|\widetilde{S}_{ij}|^2)^{\frac{1}{2}},$$
 (2.18)

where

C_S the Smagorinsky constant

 $\widetilde{\Delta}$ filter-width

 $|\widetilde{S}_{ij}|$ magnitude of the tensor \widetilde{S}_{ij} .

 $|\widetilde{S}_{ij}|$ is best explained in terms of the *Frobenius* product,

$$|\widetilde{S}_{ij}| = (\widetilde{S}_{ij} : \widetilde{S}_{ij})^{\frac{1}{2}} = \sqrt{\text{trace}(\widetilde{S}_{ij}^{\mathsf{T}} \widetilde{S}_{ij})} \ . \tag{2.19}$$

The *tilde* over Δ , represents the spatial cut-off scale associated with the filtering operator $\mathfrak{G}*x=\widetilde{x}+x'$. One mostly sets $\widetilde{\Delta}$ equal to the overall grid size, Δ_q that is expressed as,

$$\Delta_g = \sqrt[3]{\prod_{i=1}^3 \Delta_i} , \qquad (2.20)$$

where

 $\Delta_{\mathfrak{i}}$ grid size along the \mathfrak{i}^{th} direction.

One is free to set $\widetilde{\Delta}$ to a value greater that Δ_g but then one must refer to the scales smaller than $\widetilde{\Delta}$ as the *subfilter scales*. This would also be the case when the grid size differs with direction, resulting in some scales being larger than the grid size but smaller than the filters (see Sagaut (2006)).

Equation 2.16 indicates that the subgrid scale stress calculated with the Smagorinsky model, will depend on the value of $C_{\rm S}$. The values reported for $C_{\rm S}$ range from 0.1 to 0.23, of which most have been deduced through either theoretical exercise or from experimental or DNS data (see Meyers and Sagaut (2006)). In practice, LES codes report different values of $C_{\rm S}$ purely based on the study of decaying turbulence alone. Lilly (1967) proposed a value of 0.17. Bechmann (2006) obtained a value of 0.144 with the EllipSys3D LES code (Sørensen, 1995; Michelsen, 1992), whereas Viré and Knaepen (2009) use 0.15. We will report a different value of $C_{\rm S}$ with the code that we use.

These differences stem from discretisation schemes and their errors, which are always present unless the grid is very fine and the time step small and always affect how the Smagorinsky model must be tuned, as the aim is to obtain the correct overall dissipation (Canuto and Cheng, 1997; Ghosal, 1996), even for a flow as simple as an isotropic and homogeneous one.

Tests revealed that a constant value of C_S might lead to excessive dissipation near walls for wall-bounded flows (Bou-Zeid et al., 2005; Porté-Agel et al., 2000; Horiuti, 1993)³. Mason (1989) adapted the Smagorinsky model to the presence of a wall by using an *ad hoc* damping function to reduce the value of C_S closer to the walls, in connection with increased anisotropy. This method has successfully found its way into the LES of wind farms (Norris, 2000; Norris et al., 2012).

By construction, the Smagorinsky model is purely dissipative and does not permit the backscatter of energy from the dissipative scales to the large scales, as confirmed experimentally (Liu et al., 1994). Backscatter pertains to a local negative dissipation or addition of energy to the resolved scales. Additionally, equation 2.16 reflects a perfect alignment of the principal axes of τ_{ij} with those of S_{ij} , a conjecture not supported by DNS (Zang et al., 1993; Bardina et al., 1983). It is believed that assumed alignment may produce noise during simulations leading to flawed predictions of local flow statistics despite accurately gauging mean flow statistics(Lund, 1991).

Most of these shortcomings were later tackled with dynamic (Germano, 1992) and scale-dependent dynamic (Porté-Agel et al., 2000) formulations of the Smagorinsky model. These account for the variation of C_S , and by extension, the local dissipation, with anisotropy and the scale of the eddies involved. Nonetheless, the Smagorinsky model has been used successfully for the simulation of turbulent flows and even for industrial applications.

³ Please see section 2.7 for a details

2.2.3.2 Standard dynamic model

Germano (1992) proposed the *standard dynamic model* (SDM) based on what is now known as the *Germano identity*. The SDM uses a second filter⁴ called the *test filter* to relate the turbulent stresses at different scales to obtain a locally isotropic value of C_S for inhomogeneous turbulence (Germano et al., 1991; Sagaut, 2006). The test filter's cut-off width $\overline{\Delta}$, is generally set to $2\widetilde{\Delta}$ or twice the grid size.

The subgrid tensor at the test filter's scale, T_{ij} is,

$$\mathfrak{I}_{ij} = \overline{\widetilde{u_i u_j}} - \overline{\widetilde{u}_i} \ \overline{\widetilde{u}_j} \ , \tag{2.21}$$

where

 \overline{x} value of the variable filtered at $\overline{\Delta}$.

One tries to express the above in terms of the resolved velocity field by adding and subtracting $\overline{\widetilde{u}_i}\widetilde{u}_i$ on the left-hand side,

$$\mathfrak{I}_{ij} = \underbrace{\overline{\widetilde{u}_{i}\widetilde{u}_{j}} - \overline{\widetilde{u}_{i}}}_{\mathfrak{O}_{ij}} + \underbrace{\overline{\widetilde{u}_{i}\widetilde{u}_{j}} - \overline{\widetilde{u}_{i}\widetilde{u}_{j}}}_{\overline{\tau_{ij}}}, \qquad (2.22)$$

where

O_{ij} resolved stress tensor

 $\overline{\tau_{ii}}$ primary strain-rate tensor filtered at the test-filter's scale.

 \mathfrak{O}_{ij} can be evaluated using the resolved or the filtered velocity field. Using the equations of the Smagorinsky model, one is able to express the deviatoric component of \mathfrak{T}_{ij} as,

$$\mathfrak{I}_{ij} - \frac{1}{3}\delta_{ij}\mathfrak{I}_{kk} = -2(C_{S_{\overline{\Delta}}}\overline{\Delta})^2(2|\overline{\widetilde{S}_{ij}}|^2)^{\frac{1}{2}}\overline{\widetilde{S}}_{ij} \ . \tag{2.23}$$

where

 $C_{S_{\overline{\Delta}}}$ Smagorinsky constant at scale $\overline{\Delta}$

 $\overline{\Delta}$ test-filter's width or $2\widetilde{\Delta}$.

 $\bar{\tau}_{ij}$ can be obtained from equation 2.16. Upon substituting $\bar{\tau}_{ij}$ and equation 2.23 in equation 2.22, one obtains,

$$\mathcal{O}_{ij} - \frac{1}{3} \delta_{ij} \mathcal{O}_{kk} = C_S^2 \mathcal{Q}_{ij} , \qquad (2.24)$$

where

⁴ In LES, this is the *first* clear-cut filter because the grid itself is the primary filter and represents the filtered or resolved velocity field

C_S scale-invariant Smagorinsky constant,

i.e. $C_{S_{\overline{\Lambda}}}=C_{S_{\widetilde{\Lambda}}}=C_{S}.$ Also, $\mathfrak{Q}_{\mathfrak{i}\mathfrak{j}}$ is related to the strain-rate tensors through,

$$Q_{ij} = 2\widetilde{\Delta}^2 (\overline{\sqrt{2|\widetilde{S}|^2}} \widetilde{\widetilde{S}}_{ij} - 4\sqrt{2|\overline{\widetilde{S}}_{ij}^2} | \overline{\widetilde{S}}_{ij}), \qquad (2.25)$$

under the assumption that

$$C_{S\overline{\Lambda}} = C_{S\widetilde{\Lambda}} = C_{S}. \tag{2.26}$$

Lilly (1992) used the method of *least-squares* to solve this over determined system (6 equations, 1 unknown i.e. C_S) by minimising,

$$e_{ij} = \left(\mathcal{O}_{ij} - \frac{1}{3}\delta_{ij}\mathcal{O}_{kk}\right) - C_S^2\mathcal{Q}_{ij} , \qquad (2.27)$$

where

eij error due to using Smagorinsky model with the Germano identity,

obtaining C_S as,

$$C_S^2 = \frac{\mathcal{O}_{ij}\mathcal{Q}_{ij}}{\mathcal{Q}_{ij}\mathcal{Q}_{ij}} \,. \tag{2.28}$$

Apart from the scale invariance of C_S , the SDM assumes that C_S does not show significant spatial variation below the test filter's scale. This incurs some numerical instability while using the *least-squares* approach, which must be eliminated through suitable averaging of the numerator and the denominator in above equation (Ghosal, 1999).

Averaging could be done over planes within the flow, like those parallel to the wall for wall-bounded flows or a direction in which the flow is statistically homogeneous. This approach is known as *planar averaging* (Germano, 1986; Lilly, 1992; Porté-Agel et al., 2000) and is common in ABL simulations. But once wind turbines are introduced into the computational domain, the flow is no longer homogeneous along the planes parallel to the ground. Thus, alternative strategies like averaging over neighbouring points or *local averaging* (Zang et al., 1993; Basu and Porté-Agel, 2006) and *Lagrangian averaging* over pathlines in time, (Bou-Zeid et al., 2005; Stoll and Porté-Agel, 2006) are more appropriate.

Although the SDM could account for backscatter, one noticed no improvement in velocity predictions near walls. As a consequence of under dissipation, the SDM under predicts the streamwise velocity and mean shear (PortéAgel et al., 2000).

2.2.3.3 Scale-dependent dynamic model

Porté-Agel et al. (2000) extended the SDM by using the Germano identity to relate the stresses at the *primary test filter's* scale to that at a new and larger,

secondary test filter's scale, for calculating C_S locally and more important, while considering its variation with scale. The model is commonly known as the *scale-dependent dynamic model* (SDDM) and it replaces the assumption of scale invariance (see equation 2.24) with a weaker power law,

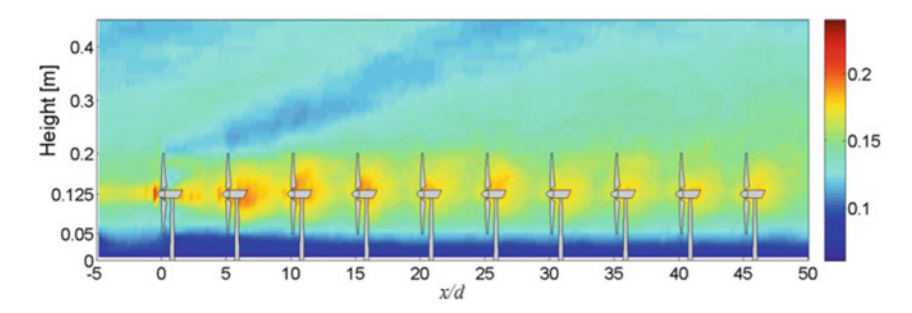


Figure 2.3: A distribution of C_S determined using the SDDM with Lagrangian averaging (reproduced from Wu and Porté-Agel (2013)).

A mathematical description of the SDDM is not provided here for the sake of succinctness. In short, an approach similar to that of SDM but relating the stresses at three filter scales is used to obtain the value of C_S . Post-simulation analyses uncovered that not only is the value of C_S spatially variant, it is also scale-dependent with marked reductions near walls, which is consistent with increased anisotropy (see figure 2.3). This observation alludes to the assumption of scale-invariance by the SDM.

In terms of *computational time with pseudo-spectral codes*, the SDM and SDDM models require only 4% and 8% more computational time than Smagorinsky model for simulating a neutral-ABL, which is acceptable considering a marked improvement in accounting for anisotropy and scale dependence. However, the increase is only marginal because of the spectral cut-off filtering used in the code with pseudo-spectral schemes, which makes filtering an inexpensive process.

As mentioned earlier, eddy-viscosity models are purely dissipative by construction. However, simulations of a neutral-ABL suggest that the SDDM correctly predicts the SGS dissipation, even in regions of increased anisotropy near walls, for a wall-bounded flow. This helps obtain the correct velocity profile and streamwise mean shear, even on relatively coarser grids (Porté-Agel et al., 2000). Stoll and Porté-Agel (2008) compared all the averaging schemes using the SDDM. It was noticed that the computational requirements for Lagrangian and local averaging are 22% and 8% higher than planar averaging, respectively. Additionally as an advantage, the results produced by the SDDM with Lagrangian averaging are nearly insensitive to the grid's resolution in the surface layer, where most wind turbines are placed (Porté-Agel et al., 2011).

2.2.4 Other models

As opposed to the purely dissipative Smagorinsky model, the *Bardina scale-similarity model* that was proposed by *Bardina et al.* (1983), is based on the principles of *structural modelling*. It is supported by experimental evidence (see Liu et al. (1994)) suggesting that the smallest eddies of the resolved scales and the largest ones of the subgrid scales are similar in structure, a relationship expressed mathematically as,

$$\tau_{ij} = C_B \left(\overline{\widetilde{u}_i \widetilde{u}_j} - \overline{\widetilde{u}}_i \overline{\widetilde{u}}_j \right) , \qquad (2.29)$$

where

C_B similarity constant,

and the *overline* stands for filtering at a scale equal to or greater than that of the filter represented by *tilde*. As opposed to the Smagorinsky model, the Bardina model requires explicit filtering. The latter delivers improved local statistics by removing the local noise arising from the presumed alignment of the two tensors in the Smagorinsky model (Zang et al., 1993). Additionally, it accounts for backscatter of energy from the dissipative scales to the inertial scales. However, this backscatter renders the model less dissipative in certain cases, which must be corrected by combining it with the purely dissipative Smagorinsky model (Mixed Model, details in Meneveau and Katz (2000)).

Another alternative to Smagorinsky model was recently introduced by Lu and Porté-Agel (2010) as the *modulated-gradient model*. It is based on the *Taylor expansion* of the SGS stresses and the evaluation of SGS kinetic energy through the assumption of local equilibrium. LES studies have revealed that the model is capable of reproducing the *log-law* mean velocity profile of an ABL and the energy spectrum correctly.

A distinct advantage this model offers, in addition to its accuracy, is the absence of explicit filtering, which makes the model ideal and computationally efficient for finite-volume codes. Using a similar approach, Lu and Porté-Agel (2013) proposed a modulated gradient model for the scalar transport of temperature. However, the model relies on the *a priori* estimation of its coefficients, just like Smagorinsky model. A dynamic or scale-dependent dynamic formulation could reduce the dependency on *a priori* estimation, but would make the model computationally demanding for finite volume codes.

2.2.5 Summary

In closing, it is certain that an SGS model cannot encompass all the physics that it is required to. However, the lack of physicality in some manner, is generally compensated by the model's ability to deliver desired results. Due

to the erratic nature of atmospheric flows, mean flow statistics are easier to analyse, which may have led to eddy-viscosity models being the popular choice for wind farm simulations, despite inconsistencies in their design.

Based on an extensive review of literature (Mehta et al., 2014b), we deemed it wise to use the Smagorinsky model for the ECNS. Notwithstanding, it is important to emphasise that the simple Smagorinsky model is not as accurate as its more comprehensive formulations. But the Smagorinsky model has been used successfully for simple applications like gauging power production, which is relevant for an industrial LES model. We shall see in a later chapter that the simple Smagorinsky model with careful numerics, can indeed be a very versatile and efficient (readers may refer to Meyers (2011) for a detailed example).

2.3 TURBINE MODELLING

It would be wise to know how the turbines must be modelled for accurate and fast wind farm simulations. Sanderse et al. (2011) provides a very detailed summary of rotor modelling methods, from which we abstract this section.

Methods for modelling wind turbines include: *actuator methods* and *direct modelling* (for CFD). Direct modelling of rotors is computationally expensive and certainly infeasible if used in combination with LES. To reduce computational costs most LES codes use the *actuator disk* (AD) and *actuator line* (AL) techniques. These methods model turbines as local volume forces that extract momentum from the flow.

The simplest approach involves implementing the axial force (or the turbine's thrust) uniformly over a disk's surface, while neglecting any tangential forces and the wake's rotation (Burton et al., 2001; Hansen, 2008). Although the AD is computationally affordable, LES studies show that incorporating tangential forces to account for the rotation of the wake (actuator disk with rotation (ADR)) and non-uniform disk loading provides a more accurate description of the wake between 5D to 7D (Porté-Agel et al., 2011).

In the AL approach, the blades are modelled as lines with forces prescribed along them. Instead of merely averaging the forces over the disk, their temporal variation is also taken into account (Sørensen and Shen, 2002). This helps resolve tip vortices correctly, which is important for detailed near wake analyses. Both methods rely on two-dimensional aerofoil data and must be corrected for tip losses (Shen et al., 2005). However, a disadvantage of the AL approach is the time step being determined by a condition more stringent than the standard *Courant-Friedrichs-Lewy* (CFL) criterion for explicit time stepping. The time step must now be chosen such that the blade tip (the fasted part of the blade) does not traverse more than one grid cell per time step (Jha et al., 2014).

Thus as a trade-off, we restrict our studies to the simple AD approach for quick calculations. Within the ECNS, the AD is available through the

CODE	SUBGRID SCALE MODEL	SPATIAL DISCRETISATION
JHU-LES	SDDM Lagrangian averaging	Horizontal: pseudo-spectral Vertical: 2 nd order finite difference
ECNS	Smagorinsky Mason wall function	Finite volume 2 nd order EC
SP-Wind	Smagorinsky Mason wall function	Horizontal: pseudo-spectral Vertical: 4 th order EC finite difference
EllipSys3D	see Tenaud et al. (2005)	Convective: Blended 3 rd order QUICK ⁶ and 4 th order central difference Others: 2 nd order central difference
EPFL-LES	SDDM Lagrangian averaging	Horizontal: pseudo-spectral Vertical: 2 nd order central difference
SnS	Smagorinsky Mason wall function	2 nd order central difference

Table 2.1: LES codes at a glance.

immersed interface method that prescribes the required volume force to the grid cells relevant to the location of the disk, instead of prescribing the force across all the cells and being regularised with a *Gaussian* function to maintain a maximum value of the disk (Sanderse, 2013).

2.4 A RANGE OF LES CODES

LES studies of wind farm aerodynamics that will be described next, are often carried out with in-house CFD codes that are summarised in table 2.1⁵.

Apart from the numerical schemes, the codes also differ in terms of the time integration scheme they use. These are summarised in table 2.2. A good summary of the importance of time integration schemes in LES can be found in (Sanderse, 2013). The general idea is to choose a scheme that does not introduce numerical dissipation that we shall see later, does affect the

⁵ JHU - Johns Hopkins University, EPFL - École Polytechnique Fédérale de Lausanne

TIME INTECDATION

CODE	TIME INTEGRATION
JHU-LES	Adams-Bashforth 2 nd non-EC Explicit
ECNS	Runge-Kutta (RK) explicit 4 th non-EC Implicit EC 2 nd & 4 th
SP-Wind	Runge-Kutta explicit 4 th non-EC
EPFL-LES	Adams-Bashforth non-EC Explicit
EllipSys ₃ D	Iterative Predictor Corrector
SnS	Viscous: Crank-Nicolson non-EC Convective: Adams-Bashforth 2 nd non-EC Explicit

CODE

Table 2.2: LES codes at a glance.

energy spectrum and leads to the spurious decay of TKE. At the same time, the scheme must also be stable and reasonably quick.

Finally, the EllipSys₃D and SnS, use a mathematical function to synthetically generate the turbulence in the domain (see Mann (1994) for details), although the latter, allows the turbulence to evolve under the effect of LES. Explicit schemes are generally not energy-conserving (EC) as they introduce dissipation. The EC methods proposed in (Sanderse, 2013) are implicit. However, at sufficiently low time steps, one can certainly use higher order (3rd or 4th) explicit schemes as a trade-off between accuracy and computational effort, while ensuring stability by using a suitable *Courant* number.

For completeness, we wish to quote the following about the grids used by the finite volume codes:

- ECNS uses a staggered and Cartesian grid that is central to the absence of numerical dissipation.
- ElliSys3D solves the discrete NS equations for the primitive variables, i.e. pressure and velocity, in general curvilinear coordinates based on a multi-grid approach (Michelsen, 1994; Ivanell et al., 2008).

On the other hand, the pseudo-spectral codes, EPFL-LES⁷ (Porté-Agel et al., 2000), SP-Wind (Meyers and Meneveau, 2010) and JHU-LES (Calaf et al., 2010) use uniform grids with periodic boundaries in the horizontal directions. Further, the pseudo-spectral schemes do not easily permit the use of wall and outflow boundaries and thus, the codes use other finite volume or finite difference methods in the vertical direction.

⁷ In 2010, EPFL-LES was still JHU-LES

2.5 APPLICATIONS OF LES TO WIND FARM AERODYNAMICS

In this section, we summarise how the above-mentioned LES codes have contributed to our understanding of wind farm aerodynamics. At the same time, we try to shed light on how one could replicate these academic LES practices for industrial use, which is the motivation behind this thesis.

2.5.1 Design of wind farms

The advantage of LES over RANS (used often by engineering models) is its ability to capture the transient evolution of turbulent eddies that are most relevant to wake development, power production and important phenomena like wave meandering, which are pivotal in determining the optimum placement of wind turbines.

Meyers and Meneveau (2010) simulated 36 uniformly spaced (7D) wind turbines modelled as actuator disks (both AD & ADR), in staggered and aligned clusters using the Smagorinsky model with wall damping implemented in the SP-Wind code. It was noticed that using the ADR method to add tangential forces, only alters the normal and spanwise velocities in the far wake but not the streamwise velocity and the power produced, at high tip speed ratios and reasonable power coefficients.

This finding is consistent with previous results that indicate that the induced tangential velocity diminishes near 5D (Troldborg, 2009). Thus, the AD method is suitable and faster if one aims to analyse only the power produced (velocity field) and if turbines are separated by a reasonable distance.

Further, staggered clusters displayed a 5% increase in power production with both AD and ADR models of the rotor because the wake is able to recover over a greater distance (twice the turbine spacing as compared to an aligned cluster, see figure 2.4). Experiments by Markfort et al. (2012) in a thermally-controlled wind tunnel, confirmed the above observations for a neutral-ABL.

Recently, Stevens et al. (2013a) used the JHU-LES to report that completely staggering a wind farm with an originally aligned configuration, *does not* optimise the farm's efficiency (ratio of power produced to the rated power), for an inflow along the direction shown in figure 2.4. In fact, a partially staggered configuration is the most optimum one for a given aligned cluster because it minimises the number of wake-turbine interactions.

Although the difference between staggered and aligned clusters can be understood with simple engineering models, only an advanced model like LES could have helped to reach a conclusion on the optimal angle of staggering. This is simply because engineering models cannot accurately account for partial wake interactions, wake meandering and wake evolution for a single wind direction but are better for predicting averaged data. Further, on large wind farms, the wake evolution after the 3rd or 4th row of turbines is governed by the vertical exchange of momentum and energy with

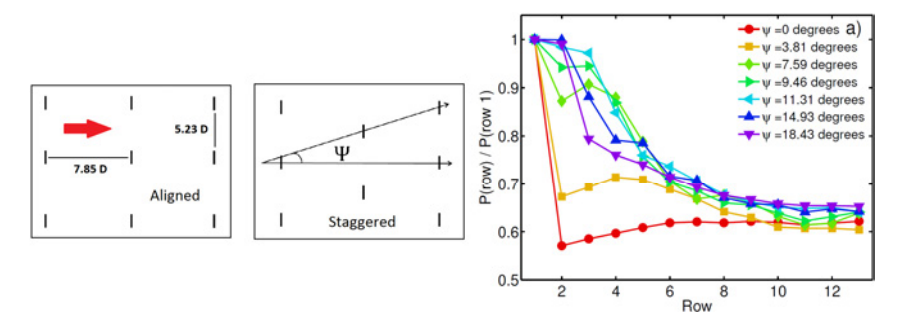


Figure 2.4: Aligned: $\psi=0^\circ$ and staggered: $\psi=18^\circ$ configurations of a wind farm (left and centre). The graph (right) displays the average output of various rows of wind turbines for different amounts of staggering, with maximum power around $\psi=11^\circ$ (reproduced from Stevens et al. (2013a)).

the ABL. Thus, engineering models with simple ABL models may not be able to model this exchange correctly.

2.5.2 Wind turbine array boundary layer

When the length of a wind farm (extent along the inflow direction, generally along the turbines) is greater than the height of the ABL, the flow through the wind farm turns into a fully-developed *wind turbine array boundary layer* (WTABL), as proposed by Calaf et al. (2010).

Within the WTABL, momentum and energy fluxes must occur vertically because the flow barely evolves spatially in the horizontal directions, instead turbulent fluxes from the faster flowing air above the farm, transfer KE into the region where the wind turbines are placed (Hamilton et al., 2012). The fluxes were observed to be equal in order of magnitude to the power extracted by the turbines, therefore hinting at a possible relation between the two.

The simpler SP-Wind code was used to collect average flow statistics, whereas the JHU-LES codes with the more advanced SDDM was used to study the ABL profiles, being more accurate in this regard (Calaf et al., 2010). The results evinced that the interaction between the wake and the ABL must be resolved precisely for simulating large wind farms, something which has been incorporated in almost all recent LES studies.

Meyers and Meneveau (2013) also used the LES data to study the fluxes of mass, momentum and KE by visualising them as *transport tubes* and discerned that the path taken while transporting these variables, depends on the turbine placement and spacing. Recent experiments on scaled wind farms suggest that turbulent structures of order the of 1D, are mainly responsible for the vertical entrainment of KE. The difference in coherence among these structures between the top and the bottom of the wake is what

drives the KE flux. Once the flow has developed along the streamwise direction, it is this flux that helps the wakes recover faster than their upstream counterparts (Hamilton et al., 2012).

Finally as an important application of LES, the codes were modified to incorporate atmospheric stability to study the effects of the WTABL on the vertical mixing of heat and moisture. Following discordance between meteorological surveys and laboratory experiments, it was finally concluded that a wind farm's presence increases the scalar fluxes from the surface in a neutral-ABL and that the change is weakly dependent on the turbines' spacing and thrust coefficients (Calaf et al., 2011).

2.5.3 Wind turbine parametrisation for LES

Porté-Agel et al. (2011) used the EPFL-LES to simulate scaled wind turbines and wind farms under neutral, stable and unstable atmospheric conditions. Instead of using data from field experiments, data from high resolution anemometry based wind tunnel experiments on scaled turbines was used for validating the code (Chamorro and Porté-Agel, 2009; Chamorro and Porté-Agel, 2011). The wind tunnel could mimic conditions that exist in the ABL under every stratification (Chamorro and Porté-Agel, 2010; Zhang et al., 2013). Notwithstanding, the Reynolds number was comparably low but enough to generate turbulence and help validate the code (Porté-Agel et al., 2010).

It was through these studies that it was observed that the AD with a uniformly loaded rotor in spite of being speedy, is not completely accurate and will lead to an under prediction in the wake's velocity deficit and the turbulence intensity at the turbine's top-tip level till 5 to 7 D (see figure 2.5). Using a non-uniformly loaded AD with both axial and tangential forces to account for the wake's rotation, or the ADR, is a wise alternative to using the computationally expensive AL technique, which is more suitable for near wake analyses (Porté-Agel et al., 2011). Grid-sensitivity tests revealed that the ADR method can be used by placing no more than 5 and 7 grid points on the disk along the spanwise and vertical directions (Wu and Porté-Agel, 2011), respectively, placing more points does not improve the results significantly (for neutral-ABL only).

However, as mentioned in section 2.5.1 and apparent in figure 2.5, the ADR approach influences the near wake to a greater extent than the far wake. Therefore, the predictions of power generation with the ADR and AD models, as long as the turbines are separated by a distance greater than 4 to 4D, are much similar.

2.5.4 LES or synthetic ABL

Most LES studies have clearly concluded that the proper modelling of the ABL is necessary for correct predictions with LES codes. With the EllipSyS₃D

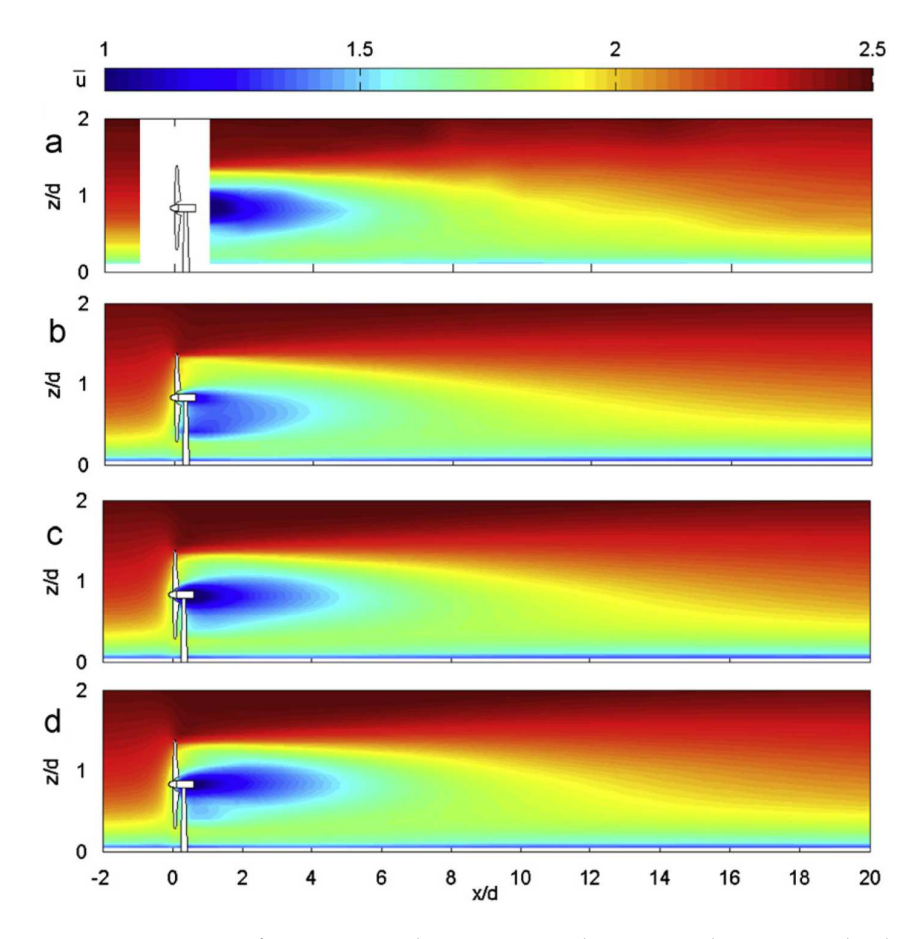


Figure 2.5: Contours of time-averaged streamwise velocity in a plane perpendicular to the turbine's plane, located at the turbine's centre line (from top to bottom: wind tunnel data, AD, ADR and AL; reproduced from Porté-Agel et al. (2011)).

code, the synthetic ABL is implemented in two steps. First, a mean shear is specified across the domain as a distribution of volume forces. Next, the turbulence intensity is set at the inflow boundary, again by means of volume forces. These forces are calculated from three-dimensional velocity fluctuation functions proposed by Mann (1994, 1998), to generate a turbulent field that is anisotropic and incompressible.

The *immersed boundary method* is used to introduce the mean shear on which the data from the turbulence field is superimposed. However, the turbulence would tend to decay till the region of interest (wind turbines), which is generally at a considerable distance from the inflow boundary. To correct this, Troldborg et al. (2013); Keck et al. (2013c) used the immersed boundary method to specify the turbulent fluctuations in a plane close to the turbines.

Comparisons with field data revealed that the turbulence characteristics in the wake of a single turbine are well resolved using this approach.

It is important to note that using a synthetic ABL inflow hinges on the assumption that the mean shear and turbulence statistics can be specified independently. This is contrary to recent conclusions by detailed LES studies that the two parameters are highly correlated (see section 2.4)⁸. Although the results obtained with this method compare well with field data from tests on single turbines, it might not be effective for a wind farm simulation that relies on the interaction between the wake and the ABL and hence its accurate modelling (see section 2.5.5).

On the other hand, the classic ABL is simulated using the Monin-Obukhov approach to define the wall stress to the first grid point above the ground, following which the boundary layer is allowed to develop in course of the simulation. Although the Monin-Obukhov formulation is meant for mean flow variables (Businger et al., 1971; Porté-Agel et al., 2000) and hence suitable for RANS, it has been used for LES due to the lack of an alternative approach (Moeng, 1984).

After introducing the SDDM (Porté-Agel et al., 2000), various studies on SGS modelling were carried out to demonstrate the importance of advanced and comprehensive SGS modelling for generating an ABL-like flow. An important conclusion was the dependence of C_S on scale, its reduction near the ground due to increased anisotropy and reduced characteristic length scales (especially in regions of large mean shear) and its increase near the wake's centre line due to reduced anisotropy (Wu and Porté-Agel, 2011; Wan and Porté-Agel, 2011). Therefore, using an SGS model that incorporates these effects is important to simulate the turbulence correctly throughout the computational domain. Additionally, using Lagrangian averaging along path lines and even local averaging produces statistics like wind speed, potential temperature, momentum and buoyancy fluxes that are less sensitive to grid resolution in the lower 10% of the ABL (surface layer), where the turbines are placed (Stoll and Porté-Agel, 2008).

As a result, for simulating an ABL of height h, over an area h^2 , a 128^3 grid would suffice and generate results similar to those produced by a 192^3 grid (Beare et al., 2006), with the SDDM-Lagrangian averaging (Stoll and Porté-Agel, 2008). A lower resolution like 64^3 would also be reasonably accurate. Local averaging on the other hand, requires high grid resolution and planar averaging is not capable of rendering the ABL correctly even at 128^3 .

Finally, the SDDM for solving the filtered transport equation for temperature was also proposed by Porté-Agel (2004). This permitted the simulation of non-neutral stratifications of the ABL (Basu and Porté-Agel, 2006) and also the investigation of their effects on wake development. For LES studies on stable and convective ABLs, the readers are referred to Lu and Porté-Agel (2011) and Porté-Agel et al. (2014), respectively. Readers may also refer to

⁸ For recent tests, see Munters et al. (2016)

Chamorro and Porté-Agel (2010) and Zhang et al. (2013) for an experimental insight into the effects of ABL stratification.

2.5.5 Horns Rev comparison

As late as 2014, there were few reports on comparisons of the LES codes mentioned in section 2.4 for a given test case. In fact, a comprehensive comparison was first proposed by Lignarolo et al. (2015), however, not for a wind farm but a single actuator disk. Thus, it has generally been hard to assess what combination of numerical schemes are best suited for the LES for wind farms, for industrial applications. However, two simulations of the Horns Rev wind farm in Denmark, provided a good place to start with.

The studies compared here are those by Ivanell (2009) and Stevens et al. (2014), with similar studies using engineering models by Barthelmie et al. (2009) (see table 2.1). Figure 2.6 illustrates the results with various codes against field data from the Horns Rev wind farm. For a detailed discussion on the engineering models, please refer to Schepers (2012).

Ivanell (2009) simulated two rows of the Horns Rev wind farm with the EllipSyS₃D code using periodic boundaries to imitate an infinitely large cluster of turbines. A distribution of volume forces was used to generate a synthetic ABL inflow and the turbines were represented by actuator disks. The code under predicted the power produced by a downstream turbine in case of a full wake interaction. A partial wake interaction on the other hand, led to over prediction. After averaging the power predictions over inflow angles in a range of 30°, engineering models were noticed to yield not better but less deviant results, as one would expect.

Stevens et al. (2014) used the JHU-LES code to simulate the entire wind farm. Instead of a synthetic ABL, a precursor method was used to generate the ABL and concomitantly feed the developing flow as an inflow condition for the wind farm simulation. A better correlation with field data averaged over 30° was obtained, which was attributed to improved ABL modelling. It was noticed that most engineering models performed well with aligned or nearly aligned wind farm configurations leading to full wake interactions. Staggering of turbines by more than 5° leads to a decline in correlation because of increased partial wake interactions.

At the same time, for a perfectly aligned configuration the engineering models were not able to predict the power production after the fourth row as accurately as JHU-LES (more on the performance of engineering models in Barthelmie et al. (2009)). A possible explanation is that following multiple full-wake interactions, the wind farm behaves nearly as a fully developed WTABL and power production is then dominated by vertical exchange of KE with the faster atmospheric freestream. In such a situation, it is imperative to model the interaction between the ABL and the wakes correctly, something which engineering models despite tuning, might not be able to achieve.

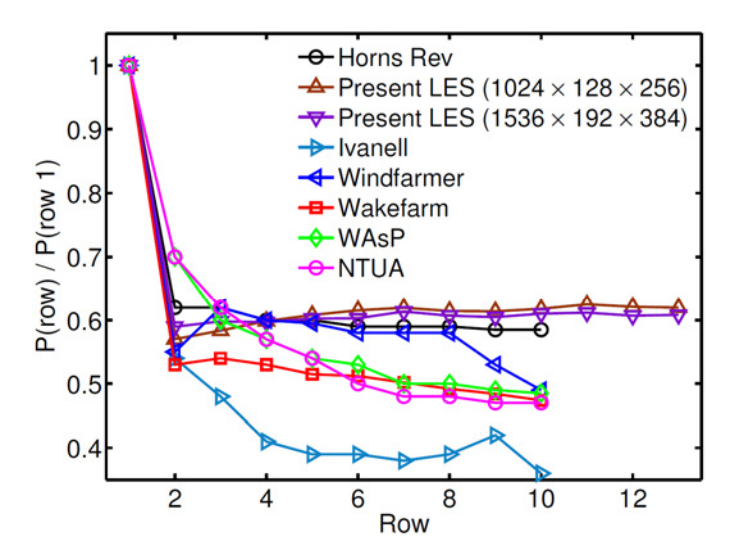


Figure 2.6: Average power output of downstream turbines at the Horns Rev wind farm, obtained with engineering models and LES codes (reproduced from Stevens et al. (2013a)).

Although the improved results were attributed to a more physical description of the ABL, we would like to emphasise that the LES studies differed in other aspects like SGS modelling, numerical schemes and more important, the grid resolution. Grid resolution may alter the accuracy and at a high value may negate the effect of the SGS model, to a certain extent.

In general, it is difficult to confirm which of the three, SGS model, grid resolution or ABL specification, is most conducive to an accurate LES. Only a detailed comparative study of LES codes on wind farms can provide an answer to the above.

2.5.6 Reduced order models and coupling

Using their results, Calaf et al. (2010) modified Frandsen's approach of modelling the turbines as elements of surface roughness in an inflow based on two logarithmic functions (Frandsen, 1992). The new approach includes the effect of wake mixing and accounts for the reduction in the velocity at hub height due to the increased surface roughness (turbines). The modified Frandsen's model was later used by Meyers and Meneveau (2012) to devise a strategy for placing wind turbines within a fully developed wind farm boundary layer (neutral) over a smooth terrain, so as to optimise the power output. However, the effects of yawed inflow and the distinction between spanwise and streamwise spacing were ignored.

Storey et al. (2012) coupled the SnS CFD code (Norris, 2000) with the fatigue, aerodynamics, structures and turbulence (FAST) aero elastic code (Jonk-

man and Guhl, 2005) to study the transient evolution of wakes with changes in blade loading due to atmospheric factors. The Smagorinsky model was implemented with the Mason wall damping function to reduce the value of C_S near the ground due to increased anisotropy. Validations were carried out against data from the *Vindeby offshore wind farm* (Barthelmie et al., 2003, 2006) and the experiments at *Nibe* (Taylor, 1990).

The coupling with FAST permitted the calculation of loads that were dynamically implemented on actuator disks to model the turbines and their wakes using CFD. It was shown that changes in blade loading affect power production and wake development, thus proving the effective coupling. Again, the authors did mention that a more accurate model of the ABL is required for a thorough analysis. More advanced SGS models could have been be employed, but were avoided in this case because the aim was to solely demonstrate if the effective coupling of CFD and aero elastic loading codes is possible or not.

Conclusions from LES studies were also incorporated in a simple and computationally affordable *dynamic wake meandering model* by Keck et al. (2013a,b). The model yields results that are comparable to the LES-AL code used by Churchfield et al. (2012) and serves as an example of how LES can be used to improve simple mathematical models. For another example on the use of LES to validate simple engineering models, please see appendix C.

2.5.7 Numerics

As explained in section 2.5, it is hard to conclude what combination of numerical schemes and models is best for an industrial LES code solely due to the absence of comparative studies. Nonetheless, this section tries to provide a few hints as to what combinations could be worth investigating.

2.5.7.1 Boundary conditions

Figure 2.7 depicts a domain that one would use for the LES of a wind farm. Generally, the upper boundary is assigned a stress free condition (Porté-Agel et al., 2000) or a prescribed shear condition (Jiménez et al., 2007), as long as the height of the domain is greater than that of the boundary layer. At times, a symmetry condition (zero normal velocity and normal gradients) has also been used but this can be erroneous for WTABL simulations that rely on the vertical exchange of momentum and energy (see section 2.5.2).

Through table 2.1, one can surmise that most academic LES codes are based on pseudo-spectral methods for resolving the flow in the horizontal direction, which unfortunately would require periodic boundaries (although spectral formulations for non-periodic boundaries are known). This periodicity permits the simulation of fully developed wind farms or a row of wind turbines deep within the WTABL without requiring a large domain (Calaf et al., 2010). When periodic conditions are used, the flow must be forced artificially through the domain with a constant pressure gradient or driven by

a geostrophic wind (Catalano and Moeng, 2010). However, in certain cases, one may wish to simulate an entire wind farm. In such a situation, using periodic boundaries would require a very large domain, especially downstream of the last row of turbines to prevent their wakes or the WTABL so formed from influencing the inflow through the imposed periodicity. This can be avoided with a precursor-ABL simulation, which also provides a more physically sound rendition of the ABL (see section 2.5.5). In such a simulation, the ABL is generated in a separate periodic domain with the necessary artificial forcing, and is then fed through an inflow boundary into a separate domain with the turbines.

A framework comprising the finite difference method based *Weather Research and Forecasting model* and the coupled OpenFOAM-FAST solver has also been proposed (Churchfield et al., 2013). The intention is to use weather research and forecasting model to provide more appropriate boundary conditions for the LES of wind farms. Such a coupling could permit the simulation of extreme events like gusts or changes in wind speed and direction over a large wind farm, and also help analyse the effect of large wind farms on local weather.

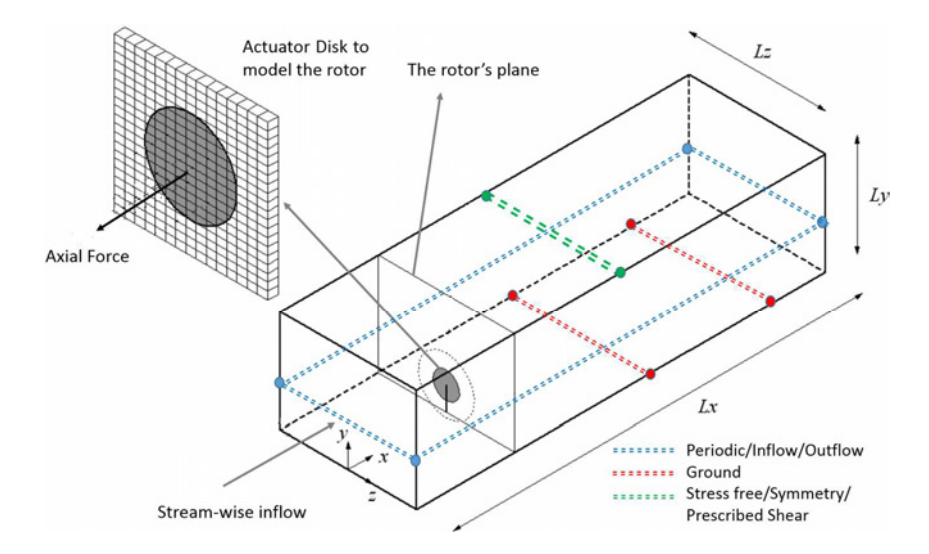


Figure 2.7: An example of a computational domain for simulating wind farms (adapted from Jiménez et al. (2007)).

2.5.7.2 Discretisation schemes

LES is adept at preserving large scale structures over distances between successive turbines due to the more accurate definition of turbulence that it provides. But most wind farm simulations are done on coarse grids, which may lead to immoderate numerical errors with certain discretisation schemes.

RANS based codes are stabilised with upwind schemes that bring along artificial numerical dissipation and on coarse grids, even more so. If left unchecked, numerical dissipation (even through temporal schemes), even in a small amount, can spuriously dampen large scale structures (Sagaut, 2006) (also see chapter 4). As for wind farm simulations, artificial dissipation leads to a quicker recovery of the wake, that is, an under prediction of the velocity deficit at all locations downstream of a turbine (Cabezón et al., 2011).

To come to terms with numerical stability and dissipation, EllipSys3D uses a blend of central and upwind schemes. However, the fractions in which these schemes is influenced by grid resolution and may pose problems. On the other hand, pseudo-spectral methods can combat these effects but require larger computational domains in conjunction with the commonly used periodic boundaries (see section 2.5.7.1). Notwithstanding, pseudo-spectral methods are common in LES codes. EC schemes that are free from numerical dissipation could also be a fine alternative (Verstappen and Veldman, 2003). Initially named as *symmetry-preserving schemes*, they ensure the conservation of KE, which is an invariant property of incompressible flows. Unfortunately, the numerical dissipation is averted through the use of central difference schemes, which as drawback incurs numerical dispersion. Although this may be remedied with higher-order discrete operators, the boundary treatment becomes challenging (Sanderse, 2013).

One must also ensure that the temporal discretisation introduces minimal dissipation if the temporal averaging is used to process data. Although most codes use high-order schemes, none a them are free from numerical dissipation, which consequently demands the restriction of the time step to avoid impacting the large scales, including implicit methods (Bechmann, 2006). With EC methods, the time step could be made relatively larger reducing the computational time. However, the benefits of such a scheme are curbed by the dispersive errors, the presence of boundaries that could lead to an overall reduction in accuracy, the loss of *L-stability* (see Sanderse (2013) and references therein) and most important, the computational time, as we shall demonstrate later.

2.6 CONCLUSIONS

As mentioned earlier, this chapter is adapted from an extensive review of literature to know what combination of numerical schemes, SGS model, boundary conditions etc., would be most effective for an industrial LES code. Based on what we observed, we deem that the following conclusions are most germane to this thesis.

The LES of wind farm has predominantly been done with SGS models based on the concept eddy-viscosity, of which, even the simple Smagorinsky model could be accurate enough for the prediction the velocity field on a wind farm.

- Wind farm simulations rely on accurate wake-ABL interaction, which is possible only with a correct ABL model. This is of great consequence for simulating large wind farms on which the ABL evolves into a WTABL. Generating a synthetic ABL requires lesser computational effort than precursor simulations with LES but may lack the statistical correlations that exist in a physical ABL. However, we are still amenable to believing that for simple industrial applications like power prediction, the effect may not be very significant.
- Using the SDDM with Lagrangian averaging generates an ABL that
 is accurate enough for wind farm simulations but is computationally
 expensive. Nonetheless, it retains its precision even on coarse grids
 making it suitable for advanced LES studies of turbulence properties
 on a wind farm.
- In the LES of wind farms, the *largest scale* that should be resolved is more or less the height of the ABL. For neutral-ABLs, this is generally around a kilometre, as evident in literature.
- As regards to the question, 'how small is large?', i.e. how fine should the grid be or what is the smallest large scale that must be resolved, we notice that most studies use a resolution of $\sim \frac{D}{7}$ or $\frac{D}{10}$. Scales smaller than this certainly belong to the set of large scales but their contribution in terms of power generation, is not as significant as that of their larger counterparts and hence, these 'smaller large scales' needn't be resolved finely.
- Therefore, as per the two preceding conclusions, a range of scales from the height of the ABL to a tenth of the turbine's diameter, is sufficient for the LES of wind farm aerodynamics and makes LES quite affordable.
- From simulations of the Horns Rev wind farm, it is apparent that the
 performance of engineering models is comparable to that of certain
 LES codes, as far as generating averaged statistics. When done with
 accurate ABL modelling and with advanced SGS models, on relatively
 refined grids, LES delivers more accurate averaged statistics.
- For numerical schemes used with explicit LES, it is important to ensure the absence of numerical dissipation for high accuracy. Pseudospectral and EC schemes are useful in this regard, the latter however requires a higher-order formulation to be as accurate as the former. Additionally, time integration should be done carefully as it too can introduce numerical dissipation (for any LES approach).
- A stress-free upper boundary is most appropriate for wind farm simulations. Periodic boundaries required by pseudo-spectral schemes can be avoided with EC schemes, which although not as accurate as the former, would not require a large *empty* region in the domain to avoid spurious effects through periodicity. Thus, one can use more

grid points in regions relevant to wake-ABL interactions, which would perhaps also improve the accuracy with EC schemes.

2.7 MOTIVATION AND OPEN QUESTIONS

Sanderse (2013) demonstrated the theoretical advantages of using an EC spatial discretisation combined with EC time integration to achieve zero numerical dissipation, even on coarse grids and with large time steps. The aim was to develop a numerical framework that could enable the use of LES outside of academic research in a manner that is computationally efficient, accurate and stable.

However, due to constraints on time, the theoretical foundations were not tested in a practical setting involving a high Reynolds number flow and complex turbulent phenomena. This served as the starting point of the research described in this thesis. We noticed three reasons that prompted us evaluate to EC schemes in a practical setting instead of pursuing the former, while using a very simple SGS model for our numerical tests.

• Time integration

- Most LES studies are based on using simple and at times, lower-order, explicit time integration methods (see table 2.2). In spite of their accompanying numerical dissipation, these proved harmless when used with small time steps, which also enabled simulations at a finer temporal resolution. Instability was possibly not consequential, save for the cases in which the so-chosen time step violated the CFL criterion.
- Using an EC implicit time integration could not only help increase the time step but also avert the accompanying numerical dissipation. But would that make a difference in practical applications where one may require good temporal resolution and may have limited computational resources?

Spatial discretisation

- Academic LES codes use pseudo-spectral methods to avert numerical dissipation through spatial discretisation, which required imposing periodicity along the horizontal directions. Whereas, the vertical direction that must be complemented with wall and outflow (symmetry) boundary conditions, is discretised using central difference schemes, both EC and non-EC, and mostly 2nd order accurate, relying merely on the intrinsic *non-dissipative* formulation of central difference schemes (see table 2.1).
- In most cases, the codes afforded acceptable results, especially with comprehensive SGS modelling. Possible numerical dissipation through the central but not necessarily EC discretisation of the vertical, was unreported (perhaps unnoticeable). Additionally,

- certain studies such as the one by Churchfield et al. (2012) for example, demonstrated the possibility of using central difference schemes readily available in open-source codes like OpenFOAM, with agreeable results.
- EC and central difference schemes being similar in construction, implementation and computational requirements, made us curious about their differences, not theoretically as proven earlier but in practical applications. Prompted by existing literature alone, we wanted to know what made either more beneficial than the other, if at all.

• Subgrid scale modelling

- In combination with pseudo-spectral methods, most LES codes use advanced SGS models like the SDDM that require explicit filtering, which as we mentioned earlier, is done rather easily and efficiently in *Fourier space*. These models sought to improve the prediction of small scale behaviour in regions of anisotropy, like near the ground in an ABL, as compared to the simple Smagorinsky model, which is popular in LES.
- Although Porté-Agel et al. (2000) report that the SDDM is highly accurate and more grid-independent for ABL simulations, a similar demonstration for an actual wind farm is missing in literature. Later, Stevens et al. (2013b) while detailing their precursor method for wind farm simulations, obtained relatively improved results with the LES of the Horns Rev wind farm (see section 2.5.5). These were attributed to the precursor based formulation of ABL turbulence rather than a synthetic turbulence based approach used earlier, more than a dissipation free pseudo-spectral method in combination with advanced SGS modelling (as compared to Ivanell (2009)).
- It was also proven that the Smagorinsky model is over dissipative near the ground (a wall boundary), resulting in reduced velocity in the lower part of the ABL and an over prediction in the higher reaches (Porté-Agel et al., 2000). Later, Meyers (2011) tuned the Smagorinsky model implemented in the SP-Wind code with the simple wall damping proposed by Mason (1989), to reduce the dissipation and obtain a reasonably improved and accurate prediction of the velocity profile in a neutral-ABL. We believed that this warrants a series of tests to check whether the ECNS code can also be tuned in a manner similar to that of Meyers (2011).
- Further, a blind test conducted in course of our research, brought to light that a pseudo-spectral method (read *dissipation free*) with a tuned Smagorinsky model, could in fact, be rather accurate for the study of turbulence, even at moderate grid resolutions. This

- strongly cued us to assess the use of a tuned Smagorinsky model with an EC (dissipation free) finite volume method.
- The above was supported by a similar study that compared the JHU-LES code and the *simulator for wind farm applications* (SOWFA) concerning their SGS models. The former uses the SDDM, whereas the latter uses the simple Smagorinsky model. It was noticed that the value of the Smagorinsky constant predicted by the SDDM, must be used with the Smagorinsky model to obtain good results, as the case should be. However, with a different constant, the velocity field was much unaffected till nearly 9D behind the turbine. The turbulence was certainly influenced but mainly in the near wake till 5D, and seemed to be much the same with a correctly tuned Smagorinsky model and the SDDM.

2.8 THE CHALLENGE

In this thesis, we attempt to answer two questions, *a*) whether EC schemes provide a marked advantage over other finite volume methods in the context of LES; and *b*) whether an EC method combined with a tuned Smagorinsky model could be used for the LES of the ABL and wind farms.

A challenge that constantly thwarts us is that of comparing numerical schemes objectively, especially in terms of computational time. The reason lies in the fact that every element of the scheme, from its design to implementation and the involved mathematical operations, influences the result. For example, within a time integration scheme that requires inverting a matrix or linearisation, one could use a range of methods each with their own requirements and accompanying accuracy. Further, even in a simple test case that involves a well-defined initial field, different codes could interpret a fundamental quantity like the field's divergence differently.

The situation is complicated by the numerous errors that are a part of the result that one uses to assess the code's accuracy and to carry out comparisons. Errors like numerical dissipation are not easily quantified; one could derive a mathematical expression comprising the discretisation errors through the *Taylor series* expansion, for instance but it is quite demanding. Nevertheless, the effect of numerical dissipation on the results can be qualitatively assessed and quantitatively evaluated with respect to a reference solution. Even then, it could be hard to attribute the quantitative difference to numerical dissipation stemming from the scheme's design alone.

As a consequence, we restrict ourselves to very simple but turbulent test cases, the simulation of which requires the use of LES. Further, we can only use reference solutions that refer to macroscopic flow properties like the velocity field, KE, TKE, the distribution of energy within the various scales of the flow (energy spectrum) etc.

2.9 CONTENTS

The following are the contents of this thesis:

Chapter 3

- The mathematics behind the ECNS and a summary of the numerical schemes it offers, and how does the implementation of a turbulence model influence the numerics.
- The summary is brief and restricted to what is most relevant for understanding this thesis (for details please see Sanderse (2013)).

• Chapter 4

- We study the influence of EC space and time schemes, independent of each other, while simulating a turbulent flow; the decay of homogeneous isotropic turbulence. Separating the two provides a clearer understanding of their influence on accuracy.
- First, we observe how the time step and time integration scheme affect the evolution of the flow through their numerical dissipation. We also check whether an EC time scheme is most essential to maintain a dissipation-free (with regards to the time scheme) simulation.

Chapter 5

- After examining the EC time integration schemes, we now evaluate whether an EC and a simple central difference scheme (both 2nd order accurate) are any different, both theoretically and more important, practically. The motivation behind this test comes from chapter 2, wherein we noticed that most LES codes used a dissipation-free central difference scheme instead of EC schemes and yet obtain accurate results.
- For simulations with the simple central difference scheme (and a few upwind schemes for discretising the convective term), we recruit the OpenFOAM (Open source Field Operation and Manipulation) toolbox and tune its Smagorinsky model for decaying isotropic homogeneous turbulence. We assess whether the absence of numerical dissipation in EC schemes, helps tune the Smagorinsky model more easily than with a non-EC scheme, for turbulent flows.

Chapter 6

An avant garde comparison of the LES codes mentioned in chapter 2
and that are popular in academia. The contributors were requested to replicate a wind tunnel experiment conducted at the *Delft University of Technology*, during which particle image velocimetry (PIV) was used to quantify the velocity field in the wake of a

- perforated actuator disk that was intended to mimic the actuator disk concept popular with the LES of wind farms.
- The comparison was not very comprehensive in indicating what aspects of the different numerical codes, i.e. their schemes, approach to LES modelling, etc., contributed the most to their results. Nonetheless, it provided a proof that EC schemes could be used for industrial applications, even with a simple Smagorinsky model, once tuned properly for turbulent regimes.

• Chapter 7

- Based on the conclusions from the previous chapters, we repeat
 the process put forth by Meyers (2011) for tuning the SP-Wind
 LES code of the *University of Leuven* (see chapter 6) that uses advanced and highly accurate pseudo-spectral methods with the
 Smagorinsky model; to prepare the ECNS for simulating a developed neutral-ABL.
- We count on the *ad hoc* scheme proposed by Mason (1989) to modify the Smagorinsky constant near the surface of the earth (a simple wall boundary), which was deemed important by Porté-Agel et al. (2000). Although a few academic codes (see chapter 2) use advanced LES models to account for the presence of a wall, the SP-Wind does it effectively with simpler models, which prompted us to do the same with the ECNS. It also served to validate the ECNS-LES combination.
- With the ECNS validated for an actuator disk and a neutral-ABL, we simulate a model wind farm and another small operational wind farm, as a test of the code's operability.

Part II

SCRUTINY

In this part, we shall provide details on the Energy-Conserving Navier-Stokes (ECNS) code and how we intend to use it for the tests that follow. These tests include studying the time integration schemes in terms of their accuracy and computational efficiency, comparing the spatial discretisation scheme with a simpler one already in use for LES and tuning the Smagorinsky model for the ECNS code.

In the presence of periodic or non-penetrative boundaries, the convective and diffusive terms of the incompressible NS equations possess a property called *symmetry* (Verstappen and Veldman, 2003). A discretisation that preserves these *symmetries* and ensures the same with time advancement, is unconditionally stable for any mesh size or time step (Sanderse, 2013). The symmetry is preserved by representing the discrete convective operator by a *skew-symmetric* matrix and the discrete diffusive operator by a *symmetric*, *positive-definite* matrix.

A symmetry-preserving discretisation ensures the conservation of KE, which is an invariant property of inviscid and incompressible flows. The same implies that in the absence of viscosity and provided that the boundaries are periodic or non-penetrative, the KE of the flow remains constant. Owing to this property, a symmetry-preserving discretisation is also known as an energy-conserving discretisation. Mathematically defined for a Newtonian fluid,

$$\frac{\partial K}{\partial t} = -\nu \|\nabla \mathbf{u}\|^2, \tag{3.1}$$

where

K kinetic energy

u velocity vector

 ∇ gradient operator,

i.e. the KE of the flow decreases with time due to viscous dissipation alone or remains unchanged for inviscid flows. The convective operator (due to skew-symmetry) and the pressure gradient do not change the total KE. Please note that vectors are denoted with a bold face.

This chapter begins with a summary of the principles of energy conservation as defined for the incompressible *NS* equations (Sanderse, 2013). Later, these principles will be used to study the transport of KE of the *resolved* (or *large*) scales of a turbulent flow. A scalar for the same will be derived from the filtered *NS* equations, which sets forth a condition that must be satisfied to ensure the conservation of KE in LES.

3.1 CONSERVATION OF KINETIC ENERGY

In vector notation, the NS equations for an incompressible fluid in the absence of body forces read,

$$\nabla \cdot \mathbf{u} = 0 \,, \tag{3.2}$$

$$\frac{\partial \mathbf{u}}{\partial t} + \nabla \cdot (\mathbf{u}\mathbf{u}) = -\nabla p^* + \nu \nabla^2 \mathbf{u} , \qquad (3.3)$$

where

 ∇^2 vector Laplacian.

Upon integrating the above equations over a volume with a defined boundary and using *Gauss's theorem*, one obtains,

$$\int_{\Gamma} \mathbf{u} \cdot \mathbf{n} \ d\Gamma = 0 , \qquad (3.4)$$

$$\int_{\Omega} \frac{\partial \mathbf{u}}{\partial t} \ d\Omega + \int_{\Gamma} (\mathbf{u}\mathbf{u}) \cdot \mathbf{n} \ d\Gamma = -\int_{\Gamma} \mathbf{p}^* \mathbf{n} \ d\Gamma + \int_{\Gamma} \mathbf{v} \nabla \mathbf{u} \cdot \mathbf{n} \ d\Gamma , \qquad (3.5)$$

where

 Ω volume

Γ boundary enclosing the volume

uu *dyad* or the outer product of vectors.

In case the boundaries are periodic, all boundary integrals equate to zero, whereas in the case of non-penetrative boundaries, i.e. $\mathbf{u} \cdot \mathbf{n} = \mathbf{0}$, only the integral of the convective term equates to zero.

The transport of KE is governed by the scalar product of equation 3.5 and **u**. To simplify further analysis, the *convected* and *convecting* quantities of equation 3.5 and the velocity will be distinguished as **u**, **c** and **v**, respectively. Thus, the scalar KE equation reads,

$$\int_{\Omega} \frac{\partial \mathbf{u}}{\partial t} \cdot \mathbf{v} \, d\Omega + \underbrace{\int_{\Omega} \nabla \cdot (\mathbf{c}\mathbf{u}) \cdot \mathbf{v} \, d\Omega}_{e} = -\underbrace{\int_{\Omega} \nabla p^{*} \cdot \mathbf{v} \, d\Omega}_{\mathcal{P}} + \underbrace{\int_{\Omega} \nu \nabla^{2} \mathbf{u} \cdot \mathbf{v} \, d\Omega}_{\mathcal{D}},$$
(3.6)

where

C convective operator

 \mathcal{D} diffusive operator

 \mathcal{P} pressure operator.

In the equations that follow, the integral of the scalar product over the domain Ω will be represented by,

$$(\mathbf{u},\mathbf{v}) = \int_{\Omega} \mathbf{u} \cdot \mathbf{v} \, d\Gamma \,, \tag{3.7}$$

thus, $\|\mathbf{u}\|^2 = \int_{\Omega} |\mathbf{u}|^2 \ d\Omega$. On scrutinising the integral equations, one gains insight into the *symmetries* possessed by the operators \mathfrak{C} , \mathfrak{D} and \mathfrak{P} , in the

presence of periodic or non-penetrative boundaries. For the convective operator, one obtains,

$$((\mathbf{c} \cdot \nabla)\mathbf{u}, \mathbf{v}) = -(\mathbf{u}, (\mathbf{c} \cdot \nabla)\mathbf{v}). \tag{3.8}$$

By denoting $(\mathbf{c} \cdot \nabla)\mathbf{u}$ by $\mathcal{C}(\mathbf{c})\mathbf{u}$, equation 3.8 can be expressed as,

$$\mathcal{C}(\mathbf{c}) = -\mathcal{C}(\mathbf{c})^* \,, \tag{3.9}$$

where

C* Hermitian conjugate of C.

Similarly, the pressure and the diffusive operators obey,

$$(\nabla \mathbf{p}^*, \mathbf{v}) = -(\mathbf{p}^*, \nabla \cdot \mathbf{v}) , \qquad (3.10)$$

$$\mathcal{D} = \mathcal{D}^{\star} \,, \tag{3.11}$$

where

 $\mathcal{D}(\mathbf{u})$ is the vector Laplacian $\nabla^2 \mathbf{u}$.

Owing to these *symmetries*, the pressure and convective operators do not alter the KE of the flow.

By setting $\mathbf{c} = \mathbf{v} = \mathbf{u}$ and by replacing $\nabla^2 \mathbf{u} \cdot \mathbf{u}$ with $\nabla \cdot (\mathbf{u} \cdot (\nabla \mathbf{u})^T) - \nabla \mathbf{u}$: $\nabla \mathbf{u}$, the change in KE with time can be expressed as,

$$\int_{\Omega} \frac{\partial \mathbf{u}}{\partial t} \cdot \mathbf{u} \, d\Omega = \int_{\Gamma} \nu \, \mathbf{u} \cdot \frac{\partial \mathbf{u}}{\partial \mathbf{n}} \, d\Gamma - \int_{\Omega} \nu \, \nabla \mathbf{u} : \mathbf{u} \, d\Omega \,, \tag{3.12}$$

which in the presence of periodic or non-penetrative boundaries simplifies to

$$\frac{\partial k}{\partial t} = -\nu(\nabla \mathbf{u} : \nabla \mathbf{u}) . \tag{3.13}$$

According to Leibniz's rule,

$$\int_{\Omega} \frac{\partial k}{\partial t} d\Omega = \frac{d}{dt} \int_{\Omega} k d\Omega , \qquad (3.14)$$

where1

 $\int_{\Omega} k \, d\Omega = \frac{1}{2}(\mathbf{u}, \mathbf{u}) = K$ integral of KE over the domain.

In case of constant kinematic viscosity, one may alternatively express the change in KE in integral form as,

$$\frac{\partial K}{\partial t} = -\nu (\nabla \mathbf{u}, \nabla \mathbf{u}) , \qquad (3.15)$$

¹ The Frobenius product of two matrices is defined as $X:Y = trace(X^{T}Y)$

where

(*A*,*B*) Frobenius product of tensors *A* and *B*

Equation 3.15 states that the total KE is bounded and reduces with time due to viscous dissipation. For an inviscid fluid however, the KE remains unchanged and is exactly conserved. An EC discretisation ensures that these properties are manifested in a discrete setting.

As long as $\nabla \mathbf{u} : \nabla \mathbf{u} \geqslant 0$ or the local KE is bounded, its integral over the domain, which is a sum in a discrete setting, is also bounded.

3.2 KINETIC ENERGY OF THE LARGE SCALES

The terms *turbulent variable* and *filter*, were defined through equation 2.7, and used definitions to modify the incompressible NS equations in their differential form, to obtain the equations relevant to large eddy simulation. Now, we repeat the same procedure with the integral form of the NS equations, equations 3.2 and 3.3. Unless mentioned otherwise, it will be assumed that the filtering operator obeys the following,

$$\frac{\widetilde{\partial \phi}}{\partial \mathbf{x}} = \frac{\partial \widetilde{\phi}}{\partial \mathbf{x}} \,, \tag{3.16}$$

$$\widetilde{\varphi + \psi} = \widetilde{\varphi} + \widetilde{\psi} \text{ and} \tag{3.17}$$

$$\widetilde{\zeta} = \zeta$$
, (3.18)

where

 ϕ, ψ turbulent variables

Z constant.

Upon filtering, a velocity (or pressure) field is decomposed into its large and dissipative scales, with the former being represented by the filtered field. In vector notation, the *filtered* NS equations for an incompressible fluid in the absence of body forces read,

$$\nabla \cdot \widetilde{\mathbf{u}} = \mathbf{0} \,, \tag{3.19}$$

$$\frac{\partial \widetilde{\textbf{u}}}{\partial t} + \nabla \cdot (\widetilde{\textbf{u}}\widetilde{\textbf{u}}) = -\nabla \widetilde{\textbf{p}^*} + \nu \nabla^2 \widetilde{\textbf{u}} \; . \tag{3.20}$$

Leonard (1974) proposed expressing the term $\widetilde{\mathbf{u}\mathbf{u}}$ in terms of $\widetilde{\mathbf{u}}$ and \mathbf{u}' . The procedure is known as *Leonard's double decomposition*, which is expressed in *Einstein's indicial notation* as,

$$\widetilde{u_{i}u_{j}} = \widetilde{\widetilde{u}_{i}\widetilde{u}_{j}} + \widetilde{\widetilde{u}_{i}u'_{j}} + \widetilde{\widetilde{u}_{j}u'_{i}} + \widetilde{u'_{i}u'_{j}}.$$
 (3.21)

The first term on the right hand side $\widetilde{u_i}\widetilde{u_j}$, requires another application for the filter for direct evaluation (Sagaut, 2006). Leonard corrected this by adding $-\widetilde{u}_i\widetilde{u}_j$ to both sides of equation 3.21,

$$\tau_{ij} = \underbrace{\widetilde{\widetilde{u}_{i}}\widetilde{\widetilde{u}_{j}} - \widetilde{u}_{i}\widetilde{u}_{j}}_{\mathcal{L}_{ij}} + \underbrace{\widetilde{\widetilde{u}_{i}}u'_{j} + \widetilde{\widetilde{u}_{j}}u'_{i}}_{\mathcal{J}_{ij}} + \underbrace{\widetilde{u'_{i}}u'_{j}}_{\mathcal{R}_{ij}}, \qquad (3.22)$$

$$\tau_{ij} = \widetilde{u_i u_j} - \widetilde{u}_i \widetilde{u}_j , \qquad (3.23)$$

where

 τ_{ij} subgrid tensor or SGS tensor

 \mathcal{L}_{ij} Leonard tensor

R_{ii} Reynolds subgrid tensor

 \mathcal{J}_{ij} cross tensor.

 \mathcal{L}_{ij} governs the interaction amongst large scales, \mathcal{R}_{ij} represents the interaction amongst subgrid scales and \mathcal{J}_{ij} reflects the interaction between the filtered and subgrid scales. Thus, *Leonard's triple decomposition* helps gather the terms \mathcal{L}_{ij} , \mathcal{R}_{ij} and \mathcal{J}_{ij} that are not expressible directly in terms of $\widetilde{\mathbf{u}}$ but must be modelled explicitly as τ_{ij} .

The modified filtered momentum equation equation 3.20 now reads,

$$\frac{\partial \widetilde{u}}{\partial t} + \nabla \cdot (\widetilde{u}\widetilde{u}) = -\nabla \widetilde{p^*} + \nu \nabla^2 \widetilde{u} - \nabla \cdot \tau \ . \tag{3.24} \label{eq:3.24}$$

When expressed in their integral form, it is noticed that the filtered equations are similar in all respects to equations 3.2 and 3.3 except that the former govern the dynamics of the *resolved velocity field* and include the subgrid tensor. The filtered NS equations are expressed in their integral form as,

$$\int_{\Gamma} \widetilde{\mathbf{u}} \cdot \mathbf{n} \ d\Gamma = 0 \ , \tag{3.25}$$

$$\int_{\Omega} \frac{\partial \widetilde{\mathbf{u}}}{\partial t} \ d\Omega + \int_{\Gamma} (\widetilde{\mathbf{u}}\widetilde{\mathbf{u}}) \cdot \mathbf{n} \ d\Gamma = -\int_{\Gamma} \widetilde{\mathbf{p}^*} \mathbf{n} \ d\Gamma + \int_{\Gamma} \nu \nabla \widetilde{\mathbf{u}} \cdot \mathbf{n} \ d\Gamma - \int_{\Gamma} \boldsymbol{\tau} \cdot \mathbf{n} d\Gamma.$$
 (3.26)

Subtracting the above equation from equation 3.5, one can obtain the momentum equation for the subgrid scales,

$$\int_{\Omega} \frac{\partial \mathbf{u}'}{\partial t} d\Omega + \int_{\Gamma} (\mathbf{u}\mathbf{u} - \widetilde{\mathbf{u}}\widetilde{\mathbf{u}}) \cdot \mathbf{n} d\Gamma = -\int_{\Gamma} (\mathbf{p}^* - \widetilde{\mathbf{p}^*}) \mathbf{n} d\Gamma + \int_{\Gamma} \mathbf{v} (\nabla \mathbf{u} - \nabla \widetilde{\mathbf{u}}) \cdot \mathbf{n} d\Gamma
+ \int_{\Gamma} \mathbf{\tau} \cdot \mathbf{n} d\Gamma + \int_{\Omega} \frac{\partial \mathbf{u}'}{\partial t} d\Omega
+ \int_{\Gamma} (\mathbf{u}\mathbf{u} - \widetilde{\mathbf{u}}\widetilde{\mathbf{u}}) \cdot \mathbf{n} d\Gamma
= -\int_{\Gamma} (\mathbf{p} - \widetilde{\mathbf{p}}) \mathbf{n} d\Gamma + \int_{\Gamma} \mathbf{v} (\nabla \mathbf{u} - \nabla \widetilde{\mathbf{u}}) \cdot \mathbf{n} d\Gamma
+ \int_{\Gamma} \mathbf{\tau} \cdot \mathbf{n} d\Gamma.$$
(3.27)

Equations 3.26 and 3.27 will now be used to obtain the KE equation for the filtered *NS* equations.

3.3 KINETIC ENERGY EQUATION FOR THE RESOLVED FIELD

Akin to expressing the velocity field as the sum of a filtered (or resolved) and a residual field, the total KE may be expressed as,

$$K = \widetilde{K} + K'. \tag{3.28}$$

Alternatively, K can be further simplified as,

$$\mathsf{K} = \frac{1}{2}(\mathbf{u}, \mathbf{u}) = \frac{1}{2}((\widetilde{\mathbf{u}}, \widetilde{\mathbf{u}}) + 2(\widetilde{\mathbf{u}}, \mathbf{u'}) + (\mathbf{u'}, \mathbf{u'})) = \mathsf{K}_{\widetilde{\mathbf{u}}} + \mathsf{K}_{\widetilde{\mathbf{u}}\mathbf{u'}} + \mathsf{K}_{\mathbf{u'}\widetilde{\mathbf{u}}} + \mathsf{K}_{\mathbf{u'}} \ , \ (3.29)$$

where

 $K_{\widetilde{u}}$ KE of the resolved field

 $K_{\mathbf{u}'}$ subgrid KE

 $K_{\widetilde{\boldsymbol{u}}\boldsymbol{u}'}+K_{\boldsymbol{u}'\widetilde{\boldsymbol{u}}}$ energy of interaction between the resolved and subgrid fields.

In case the filtering operator is a projector², $\widetilde{K}=K_{\widetilde{\mathfrak{u}}}$, otherwise the two are distinct. Finally,

$$K = K_{\widetilde{\mathbf{u}}} + K_{r} , \qquad (3.30)$$

where

K_r residual KE.

The total KE of the flow therefore varies with time as,

$$\frac{\partial K}{\partial t} = \frac{\partial K_{\widetilde{u}}}{\partial t} + \frac{\partial K_r}{\partial t} \ . \tag{3.31}$$

A scalar equation for the first term on the right hand side of equation 3.31 can be obtained from the inner product of equation 3.26 and $\tilde{\mathbf{u}}$, which reads,

$$\int_{\Omega} \frac{\partial \widetilde{\mathbf{u}}}{\partial t} \cdot \widetilde{\mathbf{u}} \, d\Omega + \underbrace{\int_{\Omega} \nabla \cdot (\widetilde{\mathbf{u}}\widetilde{\mathbf{u}}) \cdot \widetilde{\mathbf{u}}}_{\mathbf{c}} \, d\Omega = -\underbrace{\int_{\Omega} \nabla \widetilde{\mathbf{p}}^* \cdot \widetilde{\mathbf{u}} \, d\Omega}_{\mathcal{P}} + \underbrace{\int_{\Omega} (\mathbf{v} \nabla^2 \widetilde{\mathbf{u}}) \cdot \widetilde{\mathbf{u}}}_{\mathcal{D}} \, d\Omega - \underbrace{\int_{\Omega} (\nabla \cdot \mathbf{\tau}) \cdot \widetilde{\mathbf{u}}}_{\mathcal{S}}, \tag{3.32}$$

where

S subgrid or SGS operator.

If the filtering operator commutes with differentiation, one can deduce from the continuity equations 3.2 and 3.3 that,

$$\nabla \cdot \mathbf{u} = \nabla \cdot \widetilde{\mathbf{u}} + \nabla \cdot \mathbf{u'} = 0. \tag{3.33}$$

Thus,

$$\nabla \cdot \mathbf{u}' = 0 , \qquad (3.34)$$

if $\nabla \cdot \tilde{\mathbf{u}} = 0$. Further, in the presence of periodic or non-penetrative boundaries one obtains,

$$\frac{\partial k_{\widetilde{\mathbf{u}}}}{\partial t} = -\nu(\nabla \widetilde{\mathbf{u}} : \nabla \widetilde{\mathbf{u}}) - (\nabla \cdot \mathbf{\tau}) \cdot \widetilde{\mathbf{u}}, \qquad (3.35)$$

$$\int_{\Omega} k_{\widetilde{\mathbf{u}}} d\Omega = K_{\widetilde{\mathbf{u}}} = \frac{1}{2} (\widetilde{\mathbf{u}}, \widetilde{\mathbf{u}}).$$
 (3.36)

Generally in LES, only the filtered momentum and continuity equations are solved. Deconvolution or defiltering can be used to obtain the physical field from the filtered one but the procedure is but an approximation (Sagaut, 2006). Thus, equation 3.27 is redundant in an LES scheme.

An analysis similar to the one described above, can be used to obtain the remaining terms of equation 3.31. At this stage it is important to distinguish between $K_{\widetilde{u}u'}$ and $K_{u'\widetilde{u}}$. The former is obtained as the *dot product* (scalar product) of equation 3.26 and u', whereas the latter is the dot product of equation 3.27 and \widetilde{u} .

A quick calculation reveals that the sum of the transport equations for the components of the total KE is the same as equation 3.15. Thus, for an incompressible fluid in the presence of periodic or non-penetrative boundaries, one concludes,

$$\frac{\partial k}{\partial t} = \frac{\partial k_{\widetilde{\mathbf{u}}}}{\partial t} + \frac{\partial k_r}{\partial t} = -\nu(\nabla \widetilde{\mathbf{u}} : \nabla \widetilde{\mathbf{u}}) - (\nabla \cdot \boldsymbol{\tau}) \cdot \widetilde{\mathbf{u}} + \frac{\partial k_r}{\partial t} = -\nu(\nabla \mathbf{u} : \nabla \mathbf{u}) . \quad (3.37)$$

The integral of equation 3.37 over Ω reads,

$$\begin{split} \frac{\partial K}{\partial t} &= \frac{\partial (K_{\widetilde{\mathbf{u}}} + K_{r})}{\partial t} = -\underbrace{\int_{\Omega} \nu(\nabla \widetilde{\mathbf{u}} : \nabla \widetilde{\mathbf{u}}) \; d\Omega - \int_{\Omega} (\nabla \cdot \boldsymbol{\tau}) \cdot \widetilde{\mathbf{u}} \; d\Omega}_{\chi} + \underbrace{\frac{dK_{r}}{\partial t}}_{y} \\ &= -\int_{\Omega} \nu(\nabla \mathbf{u} : \nabla \mathbf{u}) \; d\Omega \; . \end{split} \tag{3.38}$$

It is known that $\frac{\partial K}{\partial t}$ is bounded. So, the boundedness of \mathcal{X} is sufficient to ensure the boundedness of \mathcal{Y} because the sum or the difference of two bounded functions is also bounded. This is true only when the initial field is free from discontinuities, such as a shock wave or a shear layer discontinuity. The latter can certainly be handled in a discrete setting.

Thus, while modelling the subgrid tensor τ , in terms the filtered velocity field, the following must hold for the boundedness of the KE of the resolved field,

$$-\int_{\Omega} \nu(\nabla \widetilde{\mathbf{u}} : \nabla \widetilde{\mathbf{u}}) \, d\Omega - \int_{\Omega} (\nabla \cdot \mathbf{\tau}) \cdot \widetilde{\mathbf{u}} \, d\Omega \leq 0 \,, \tag{3.39}$$

which is sufficient to ensure that the KE of subgrid scales and that of the interaction between the resolved and subgrid scales is also bounded.

Thus, an energy-conserving discretisation for solving the filtered NS equations must ensure that equation 3.39 is obeyed in a discrete sense.

While simulating a wind farm, the impact of body forces that model wind turbines must also be accounted for. Equation 3.6 reads,

$$\int_{\Omega} \frac{\partial \mathbf{u}}{\partial t} \cdot \mathbf{u} \, d\Omega + \underbrace{\int_{\Omega} \nabla \cdot (\mathbf{u}\mathbf{u}) \cdot \mathbf{u} \, d\Omega}_{\mathcal{C}} = -\underbrace{\int_{\Omega} \nabla p^* \cdot \mathbf{u} \, d\Omega}_{\mathcal{P}} + \underbrace{\int_{\Omega} \mathbf{v} \nabla^2 \mathbf{u} \cdot \mathbf{u} \, d\Omega}_{\mathcal{D}} + \underbrace{\int_{\Omega} \mathbf{f} \cdot \mathbf{u} \, d\Omega}_{\mathcal{F}}.$$
(3.40)

where

f force (represented as acceleration)

 \mathcal{F} force operator.

When the boundaries are periodic or non-penetrative, the KE changes with time as,

$$\frac{\partial k}{\partial t} = -\nu(\nabla \mathbf{u} : \nabla \mathbf{u}) + \mathbf{f} \cdot \mathbf{u} , \qquad (3.41)$$

Similarly, for the KE of the resolved scales change with time as,

$$\frac{\partial k_{\widetilde{\mathbf{u}}}}{\partial t} = -\nu(\nabla \widetilde{\mathbf{u}} : \nabla \widetilde{\mathbf{u}}) - (\nabla \cdot \boldsymbol{\tau}) \cdot \widetilde{\mathbf{u}} + \widetilde{\mathbf{f}} \cdot \widetilde{\mathbf{u}}. \tag{3.42}$$

Thus, the boundedness is retained if the inner product of the body force and velocity is negative or at most such that $\frac{\partial k}{\partial t}$ or $\frac{\partial k_{\bar{\mu}}}{\partial t}$ is zero, unconditionally for any grid size or time step.

3.4 ECNS

In terms of its numerical schemes, the ECNS is designed to comply with the above equations in a discrete sense. This demands that basic operations like interpolating the velocity field to obtain fluxes, finding the gradient of the field etc., must be done in a manner that prevents numerical dissipation. Mathematically this implies the cancellation of the leading order term of the truncation error resulting from *Taylor series* expansion of the operators.

Harlow and Welch (1965) proposed such a scheme that was second order accurate on uniform grids. Central to their approach is the use of a staggered grid, which prevents the discretised pressure gradient from altering the KE (Felten and Lund, 2006). Later, Verstappen and Veldman (2003) used a finite volume approach to extend the existing scheme to a fourth order accurate method on uniform grids. Finally, Sanderse (2013) proposed boundary conditions that are compatible with the fourth order scheme and permit their use with wall bounded flows. Additionally, time integration schemes which ensure that no numerical dissipation is introduced through time advancement, have also been proposed.

For the sake of completeness, we will briefly explain the second order Harlow-Welch scheme and the time integration schemes available with the ECNS.

3.4.1 The Harlow-Welch scheme

For simplicity, the Harlow-Welch discretisation will be described on a uniform and staggered Cartesian grid in two dimensions. equations 3.2 and 3.3 in a semi-discrete formulation (discrete in space and continuous in time) read,

$$\mathfrak{M}\mathbf{u}(\mathsf{t}) = \mathsf{b}_{\mathsf{c}}(\mathsf{t}) \,, \tag{3.43}$$

$$\Omega \dot{\mathbf{u}}(t) = -\mathcal{C}(\mathbf{c}(t), \mathbf{u}(t)) + \nu \mathcal{D}\mathbf{u}(t) - \mathcal{G}\mathbf{p}^*(t) + \mathbf{b}_{\mathbf{m}}(\mathbf{u}(t), t) + \mathbf{f}(t). \tag{3.44}$$

where

 \mathfrak{M} divergence operator.

The vectors $\mathbf{u}(t)$, $\mathbf{c}(t)$ and the scalar $p^*(t)$, are functions of time and are specified as point values at the centres of finite control volumes, the shape and size of which are independent of time, t. $b_c(t)$ and $b_m(\mathbf{u}(t),t)$ represent the boundary conditions for the continuity and momentum equations, respectively.

Figure 3.1 delineates the control volumes $\Omega_{i,j}$ over which the continuity equation is discretised. Because the grid is staggered, the control volumes $\Omega^{u}_{i,j}$ and $\Omega^{v}_{i,j}$ used to discretise the u- and v- momentum equations, are different from $\Omega_{i,j}$, as portrayed in figure 3.2.

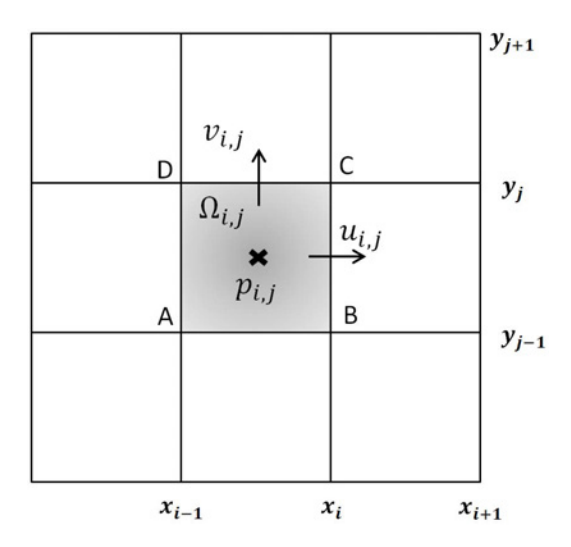


Figure 3.1: The control volume for the discrete continuity equation centred around $p_{i,j}$.

The discrete divergence operator for the control volume $\Omega_{i,j}$ reads,

$$\mathcal{M}^{\Omega}\mathbf{u}_{i,j} = \widehat{\mathbf{u}}_{i,j} - \widehat{\mathbf{u}}_{i-1,j} + \widehat{\mathbf{v}}_{i,j} - \widehat{\mathbf{v}}_{i,j-1} . \tag{3.45}$$

One uses the *midpoint rule* to obtain these quantities³ from the point values of velocity as,

$$\widehat{u}_{i,j} = \delta y_j u_{i,j} \quad \text{ or } \quad \widehat{v}_{i,j} = \delta x_i v_{i,j} \; , \tag{3.46} \label{eq:3.46}$$

$$\delta y_j = y_j - y_{j-1}$$
 and $\delta x_i = x_i - x_{i-1}$. (3.47)

For a uniform grid, $\delta y_j = \Delta y$ and $\delta x_i = \Delta x$. The convective operator must be discretised differently for the u- and v- momentum equations,

$$\mathcal{C}^{\mathbf{u}}\mathbf{u}_{i,j} = \widehat{\mathbf{u}}_{i+1/2,j}\mathbf{u}_{i+1/2,j} - \widehat{\mathbf{u}}_{i-1/2,j}\mathbf{u}_{i-1/2,j}
+ \widehat{\mathbf{v}}_{i+1/2,j}\mathbf{u}_{i,j+1/2} - \widehat{\mathbf{v}}_{i+1/2,j-1}\mathbf{u}_{i,j-1/2},$$
(3.48)

$$\mathcal{C}^{\nu}\mathbf{u}_{i,j} = \widehat{\mathbf{v}}_{i+1/2,j}\mathbf{u}_{i,j+1/2} - \widehat{\mathbf{v}}_{i-1/2,j}\mathbf{u}_{i-1,j+1/2}
+ \widehat{\mathbf{v}}_{i,j+1/2}\mathbf{v}_{i,j+1/2} - \widehat{\mathbf{v}}_{i,j-1/2}\mathbf{v}_{i,j-1/2}.$$
(3.49)

A second order accurate interpolation is required to obtain the values of velocities and face-integrated variables at locations other than the grid points.

³ Variables such as û are face-integrated quantities

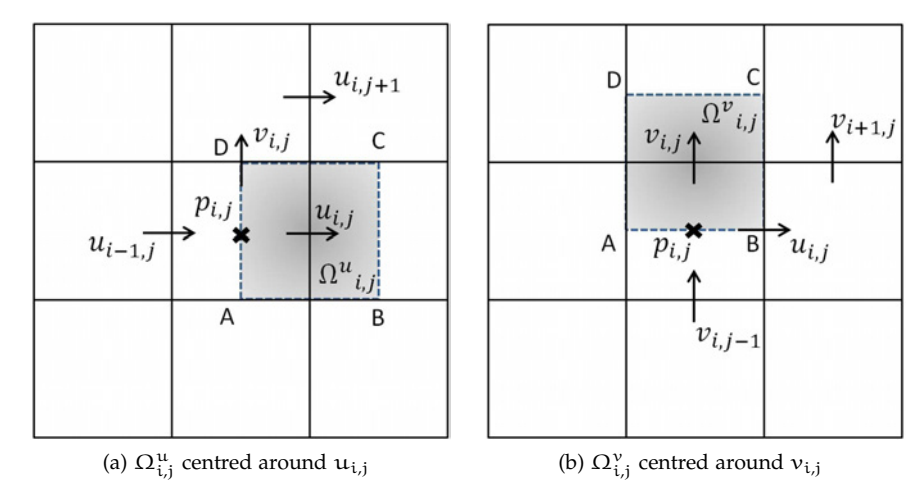


Figure 3.2: The control volumes for the discrete components of velocity.

To retain the *skew-symmetry* of the convective operators in discrete form, this interpolation must be grid-independent. This also ensures that the discrete divergence operator for $\Omega^{\rm u}_{i,j}$ and $\Omega^{\rm v}_{i,j}$ control volumes equates to zero, if it does so for all $\Omega_{i,j}$ (Verstappen and Veldman, 2003).

Thus, the linear interpolation is performed with *constant weights*, for instance,

$$\widehat{u}_{i+1/2,j} = \frac{1}{2} \left(\widehat{u}_{i+1,j} + \widehat{u}_{i,j} \right) .$$
 (3.50)

Whereas, the pressure gradient is discretised as,

$$\mathfrak{G}^{\mathfrak{u}}\mathfrak{p}_{\mathfrak{i},\mathfrak{j}}^{*}=\widehat{\mathfrak{p}^{*}}_{\mathfrak{i}+1,\mathfrak{j}}-\widehat{\mathfrak{p}^{*}}_{\mathfrak{i},\mathfrak{j}} \text{ and } \tag{3.51}$$

$$g^{\nu} p_{i,j} = \widehat{p^*}_{i,j+1} - \widehat{p^*}_{i,j}. \tag{3.52}$$

Finally, the discretised diffusive operator for the *u*- momentum equation is written as,

$$\mathcal{D}^{\mathbf{u}}\mathbf{u}_{i,j} = (\frac{\widehat{\partial \mathbf{u}}}{\partial x})_{i+1/2,j} - (\frac{\widehat{\partial \mathbf{u}}}{\partial x})_{i-1/2,j} + (\frac{\widehat{\partial \mathbf{u}}}{\partial x})_{i,j+1/2} - (\frac{\widehat{\partial \mathbf{u}}}{\partial x})_{i,j-1/2}, \quad (3.53)$$

$$\left(\frac{\widehat{\partial u}}{\partial x}\right)_{i+1/2,j} = \frac{\widehat{u}_{i+1,j} - \widehat{u}_{i,j}}{\Delta x} . \tag{3.54}$$

To obtain the discrete filtered NS equations, one simply replaces the field variables in the above equations with their filtered counterparts.

The subgrid operator is also discretised using the operators described above. For example, with the Smagorinsky model, one uses the discrete diffusive operator to find the fluxes of the gradients, followed by a second order accurate interpolation to help obtain the eddy viscosity at the desired locations. These operators when used for the discretisation of the convective and

the diffusive terms, lead to an energy-conserving discretisation, by design. But using them to discretise the subgrid scale model, does not ensure the absence of numerical dissipation.

Nevertheless, the Smagorinsky model allows tuning through its model constant C_S , which controls the amount of subgrid scale (physical) dissipation that the model brings about. Therefore, this physical dissipation can be clubbed with any numerical dissipation arising from the discretisation, and the Smagorinsky model can be appropriately tuned.

3.4.2 Time integration schemes

Time integration is also capable of introducing numerical dissipation. Sanderse (2013) proposed methods using which, one could reduce or completely remove numerical dissipation through time integration. When such a method is combined with an energy-conserving spatial discretisation, one obtains a complete energy-conserving discretised Navier-Stokes system. Of the various method proposed, the implicit 2^{nd} and 4^{th} order EC Runge-Kutta schemes based on the *Gauss quadrature*, henceforth referred to as the *Im2* and *Im4*, will be used within this thesis. These are advocated because they are not only energy-conserving but also *time-reversible* in the inviscid limit. In addition, we also use a higher order non-EC Runge Kutta method, namely, the classical explicit 4^{th} order scheme or *Ex4*, for a comparative analysis of time integration schemes for LES.

The *Ex4*, as we mentioned, is the classical Runge-Kutta method, which being explicit, is quick but restricted by stability. A very large time step that violates the CFL criterion, leads to certain instability with such an explicit method. Apart of the *Ex4*, various lower order explicit methods have been used for the LES of wind farm aerodynamics with small time steps for accuracy and stability. This was the motivation behind proposing the implicit EC methods, which are not only accurate but also stable at very large time steps.

The Im2 is a single stage method based on the Gauss quadrature, whereas the Im4 is a two stage method. Both are solved using a *linearised system* obtained using Newton's method and data from the previous time levels. This ensures that the method remains EC. However, to make certain that the methods also remain 2^{nd} or 4^{th} order accurate, the error incurred through *linearisation* must be nearly zero (between 10^{-12} and 10^{-9} with the tests described here).

We noticed that unless the error due to linearisation is driven to a very low value, one rarely obtains accurate results with the *Im2* and *Im4*, singularly with small time steps. Further, as the removal of this error is computationally demanding, the methods require proportionately more computational time with small time steps to contain the error. As an alternative, Sanderse (2013) also propose using a simplified Newton method that requires a single Jacobian for that remains constant while solving for a given time step. However,

this reduces the convergence. Other methods such as splitting the velocity and pressure were also evaluated but resulted in the loss of stability and the property of energy conservation, because the splitting rendered intermediate velocity fields with a non-zero divergence, which ultimately contributed to a spurious change in KE.

Thus, within the ECNS, the implicit EC schemes are solved with a full Newton method.

4

TIME INTEGRATION

To assess whether an EC-finite volume method that minimises numerical dissipation is an attractive alternative to pseudo-spectral methods, we study dissipation from time integration and spatial discretisation separately.

Images & content also appear in Mehta (2016)

In this chapter, the consequences of EC time integration schemes on the accuracy of LES are investigated, in combination with an EC spatial discretisation. For simplicity, we restrict ourselves to decaying homogeneous isotropic turbulence in a periodic box. We use the simple Smagorinsky model to observe how changes in the time step and the time integration scheme lead to different results in terms of the decay of KE and the energy spectrum.

To summarise, we observe through this chapter that one needs a relatively small time step with a non-EC integration scheme¹, as opposed to an EC implicit time integration scheme, to obtain numerical dissipation (through time integration) that is negligible in value as compared to the physical dissipation. This is important to ensure the conservation of KE and to prevent any spurious development of the flow. With implicit EC time integration schemes, one can certainly use a larger time step and still obtain minimal numerical dissipation, albeit at the cost of a much higher computational time.

Images & content also appear in Mehta (2016)

4.1 INTRODUCTION

Like every other CFD method, LES has its fair share of errors resulting not only from spatial discretisation and time integration but also from the SGS model representing the scales that LES does not resolve. A comparison of errors from turbulence modelling and spatial discretisation was first addressed in detail by Ghosal (1996), who showed that both are equally consequential.

By decomposing the total error, Meyers et al. (2003); Vreman et al. (1996); Meyers et al. (2007) showed that errors through discretisation and SGS modelling could in fact cancel each other, leading to a desirable solution. Studies by Meyers et al. (2007); Viré and Knaepen (2009) illustrate how different spatial discretisation schemes could lead to different results with the same SGS model. The former also illustrated the dependence of the Smagorinsky constant on the grid resolution. Geurts (2006) presents a review of these interacting errors and also proposes an inverse polynomial interpolation method to predict the Smagorinsky constant for a given resolution.

¹ The tests in this chapter recommend a *Courant* number of roughly 0.15 with a non-EC scheme, and roughly 0.3 with an EC scheme

Most of these studies used a finite volume method for solving the NS equations. These are combinations of $2^{\rm nd}$ and $4^{\rm th}$ order discretisations of the convective and diffusive terms in the NS equations (not necessarily EC, explained shortly hereafter) with a $2^{\rm nd}$ order explicit Runge-Kutta time integration (not EC). Further, they comment mostly on the effect of spatial discretisation and the resulting numerical dissipation, on the overall accuracy of LES.

As an adjunct to these studies, we comment on the use of EC spatiotemporal discretisation schemes for finite volume methods. Although an EC spatial discretisation ensures the absence of numerical diffusion (or dissipation), an EC time integration scheme is necessary to ensure that the conservation of KE remains enforced with time-stepping because numerical dissipation through time integration, can influence how the flow evolves by dissipating more energy than what would physically be dissipated.

Using laminar test cases, it was shown for a certain class of implicit time integration schemes that the resulting EC spatio-temporal discrete system incurs little numerical dissipation and is stable for large time steps, while being highly accurate (Sanderse, 2013). In practical applications with complicated turbulent flows, it is important to decide what time step is large or small and more important, which method is computationally more beneficial while being accurate.

Hence, the question we try to address here is, whether an implicit EC time integration scheme is crucial for averting numerical dissipation or could we use an explicit non-EC scheme and achieve accuracy, while ensuring stability²? In doing so, we also shed light on how the Smagorinsky model must only be tuned in the complete absence of numerical dissipation through time integration, which otherwise can have an influence as strong as that of grid resolution, on the overall dissipation (physical and numerical combined). Our arguments will be based on the simple test case of decaying isotropic homogeneous turbulence, which has many a times been used to assess the accuracy of LES and even study the fundamentals of turbulent flows. Despite the simplicity, we are certain that our conclusions related to the numerical dissipation through time integration, will hold for other test-cases too³.

We are motivated by the fact that most of the LES codes used for wind farm aerodynamics, resort to explicit time integration schemes (Mehta et al., 2014b) and use small time steps for accuracy and stability (at times, a small time step may help collect statistics from simulations at a high temporal resolution). However, if within the same computational time, implicit EC methods can ensure accuracy and stability, they could be an important asset for industrial studies on wind farm aerodynamics, as they would also

² Our discussions concern only *Cartesian* grids on which the theoretical advantages of EC schemes have been established.

³ Valid for accuracy and computational time. Stability is related to the *Courant* number that could change locally on a non-uniform grid. We discuss this in the conclusions.

guarantee computational efficiency for simulations that are otherwise computationally demanding.

4.2 DISSIPATION EXPRESSED MATHEMATICALLY

Within the discrete NS-LES system, the errors that arise can be classified as those from the regular operators of the discrete NS equations for the resolved scales, and the SGS model. The former comprises errors from the discretisation of the convective and diffusive terms, while the later comprises the modelling error due to the nature of the SGS model and the discretisation error through its implementation in the modified NS equations. Further, one must account for the numerical dissipation (if any) introduced by time advancement Sanderse (2013).

One can roughly express the overall dissipation in an LES scheme as,

$$\mathcal{P} = \varepsilon_{C}(\Delta x) + \nu(\mathcal{D} + \varepsilon_{D}(\Delta x)) + \mathcal{S}(\tau) + \varepsilon_{S}(\Delta x) + \varepsilon_{T}(\Delta t) , \qquad (4.1)$$

where

- D diffusive operator (physical dissipation),
- S SGS operator,
- ε_{C} dissipation (numerical) accompanying the convective operator,
- $\varepsilon_{\rm D}$ dissipation (numerical) accompanying the diffusive operator,
- τ SGS model (physical dissipation),
- ε_S dissipation (numerical) accompanying the SGS operator,
- ε_T dissipation (numerical) through time integration.

 ε_D (dissipative) arises from the approximation used to estimate the physical diffusion through molecular viscosity, \mathcal{D} . \mathcal{S} is dissipation through the SGS model τ , which can be tuned (see section 2.2.3.1), whereas, ε_S is the spatial discretisation error in the model's implementation and is a function of the grid resolution, Δx . ε_T is a function of the time step, Δt , and must approach zero with reducing time step.

For simplicity, we ignore the terms in the above equation that are related to the spatial discretisation, and concern ourselves with $\epsilon_T(\Delta t)$. Our aim now, is to determine what time integration schemes can ensure that $\epsilon_T(\Delta t)$ is low enough to avoid numerical dissipation from affecting the flow with minimal computational effort (see section 3.4.2).

4.3 METHODOLOGY

We study the Smagorinsky model using EC schemes implemented in the ECNS. This section provides information on the test case considered in this article and the related numerical tests. For details on the ECNS, please see chapter 3.

4.3.1 *Grid-generated turbulence*

We simulate the recognised experimental campaign by Comte-Bellot and Corrsin (1971) (CBC), who used a grid to generate an isotropic homogeneous turbulent field in a wind tunnel. The experiments provide details on the energy spectrum and the statistical properties of the turbulent flow at three instances of time as it moves through a wind tunnel, at a near constant average velocity, $U_o = 10 \, \text{ms}^{-1}$. We chose this case as it has been widely used for the validation of LES codes and also for the tuning of the Smagorinsky model (Bechmann, 2006).

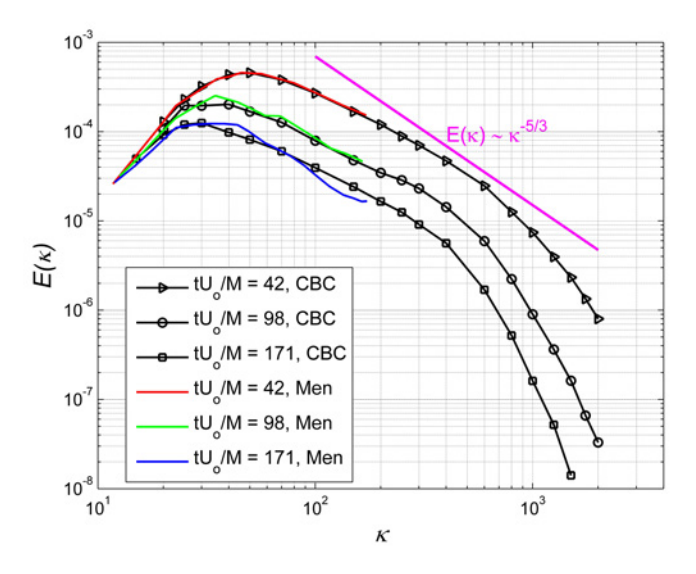


Figure 4.1: A comparison of the energy spectra obtained by Comte-Bellot and Corrsin (1971) and those using a 32^3 grid with the dynamic Smagorinsky model with Lagrangian-averaging by Meneveau et al. (1996) (*Men* in the graph). κ is the wave number related to an eddy's length scale and $E(\kappa)$ is the eddy's energy.

One must bear in mind that the flow's Reynolds number is low, around 34000 based on the average velocity and the size of the grid used to create turbulence ($M_g = 5.08 \, \text{cm}$) and that the flow is not truly isotropic with an isotropy ratio of 0.95 (the ratio of the standard deviations in streamwise velocity to that in transverse velocity). Hence, the TKE is higher in the transverse direction than in the stream wise direction.

Although the slight anisotropy could be overlooked, the low Reynolds number requires attention given that the fundamentals of LES, by definition, consider a high Reynolds number flow with an extended inertial range (Pope, 2000). Further, the experimental energy spectra in the inertial range deviate a little from the -5/3 *Kolmogorov spectrum* that is observed in turbulent flows (Frisch, 1995) (see figure 4.1). These cannot be verified easily, even

through Direct Numerical Simulation (DNS) because of the range of length and time scales in the flow⁴, for which the current computational resources are insufficient.

We shall nevertheless try to assess how closely our simulations can replicate the spectra from the largest to the smallest scales on the grid, which indirectly should also give us the correct decay of TKE with time.

4.3.2 Tests

We notice 3 experimentally obtained spectra in figure 4.1 (CBC). These correspond to three different locations in a wind tunnel, at which the flow was analysed (see figure 4.2). We simulate the flow between Stages I and III, referred to as $U_o t/M_g = 42$ and 171, respectively, in (Comte-Bellot and Corrsin, 1971) with an intermediate stage, $U_o t/M_g = 98$ or Stage II, where t is the time. These numbers refer to distances downstream of the grid that generates the turbulence.

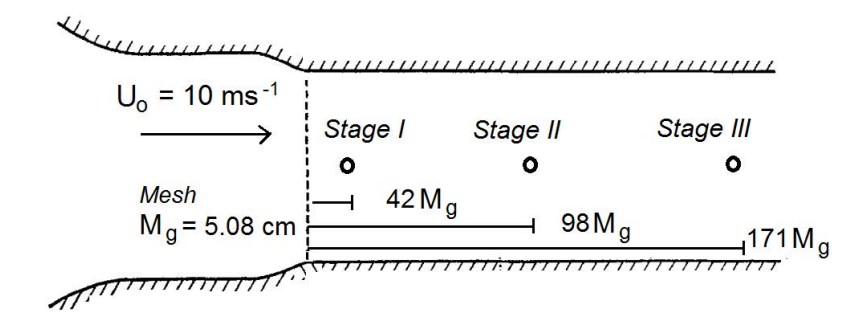


Figure 4.2: A schematic of the experimental set-up used by Comte-Bellot and Corrsin (1971).

To begin with, the energy spectrum at Stage I is used to synthesise a random velocity field that bears the experimentally reported TKE and variances in turbulent fluctuations, within a suitable domain. To ensure that the periodic boundaries used in the simulation do not lead to spurious correlations, the size of the domain in either direction must be large as compared to the longitudinal and transverse length scales of the flow. The domain is chosen to be $L_{\rm box}=10.8{\rm M_g}\sim55{\rm cm}$ in size, based on previous LES studies (Ghosal et al., 1995; Meneveau et al., 1996). The velocity field is generated spectrally using *Rogallo's algorithm* and then converted into discretised physical space through an *inverse-Fourier* transformation (Rogallo, 1981). The algorithm distributes the TKE of the flow across the range of *Fourier modes* in compliance with the energy spectrum provided as input, which in this case comes from the experimental data. During the conversion, it was noticed that the energy of the highest wavenumber modes (the smallest scales of the velocity field)

⁴ A Reynolds number of 30000 is indeed high for DNS.

is reduced in physical space⁵. This is rescaled to the spectrum at Stage I by multiplying the *Fourier modes* individually with the factor that equals the damping they incurred upon conversion to physical space.

Although one generates the velocity field in *Fourier* space, while ensuring that it is divergence free; upon projecting the same on a discrete Cartesian grid and even more so, in *physical* space, one may obtain a field that is not divergence free, at least in terms of how the divergence is defined in the finite volume code. As a result, it is important to adapt the velocity field to an NS solver to adjust its divergence and establish logical space-time correlations within the flow-field (Viré and Knaepen, 2009). To do so, the field is left to decay in accordance with the NS equations and the Smagorinsky model for a while. After its TKE has reduced significantly, the field is scaled up in Fourier space to the energy spectrum at Stage I, similar to what is done to correct the damping of the smallest scales due to inverse Fourier transforms, i.e. by scaling the energy at individual wavenumbers till it matches its counterpart at Stage I.

We simulate the decay on 32^3 , 48^3 and 64^3 uniform 3D grids, with average grid sizes⁶ equalling 1.72 cm, 1.14 cm and 0.86 cm, respectively. These sizes are small compared to the longitudinal length scale of 2.4 cm and larger than the *Taylor micro scale* of 0.48 cm at Stage I, which places the cut-off filter (grid-based) somewhere in the inertial range, as the case should be. Therefore, a 16^3 grid would be quite coarse. In certain cases, we also use 80^3 and 96^3 grids. With regards to time-stepping, we centre our arguments around a time step of $\Delta t = 0.001s$. We use this time step as reference as it was used by Bechmann (2006) to ensure that the *Courant* number was below 0.1 for a second order implicit time integration scheme, while tuning an LES code using this experimental test case for two different grid resolutions.

In addition, we use a range of time steps while investigating the time integration schemes. When a time integration scheme is used with $\Delta t = 0.001s$, it will be quoted by its name alone, i.e. as Ex4 or Im2. For other time steps, we shall add a letter at the end of the scheme's name, for example, Ex4Q. These time steps and their corresponding letters, are summarised in table 4.1 with Ex4 to serve as an example. For most simulations with the Smagorinsky model, the C_S is set to 0.1 (Deardorff, 1970), which will later be determined more accurately for the ECNS. We carry out our analyses without concerning ourselves with the accuracy of the SGS model or grid size.

⁵ Parseval's theorem holds but inaccuracies in the fast-Fourier transform may have led to this dampening

 $^{6 \ \}Delta_g = \sqrt[3]{\prod_{i=1}^3 \Delta_i}$

	NOTATION	TIME STEP
Ex4Q		0.004s
Ex4D		0.002s
Ex4		0.001s
Ex4h		0.0005s
Ex4q		0.00025s
Ex4te		0.0001s

Table 4.1: A summary of the time steps used.

4.4 EFFECT OF TIME STEP AND TIME INTEGRATION SCHEMES

While studying the time integration schemes proposed for the ECNS in (Sanderse, 2013), we monitor the energy spectrum, the rate of decay of TKE and the computational time. Based on how accurately the spectrum and decay of TKE are predicted and with what computational effort, we will try to propose which time integration scheme is most appropriate for the ECNS.

Using the 32³ grid, we simulate the experiment with *Ex4*, *Im2* and *Im4* (the three schemes available within the ECNS), in combination with different time steps, the acronyms for which are defined in section 4.3.2. The reason why we choose to use a 32³ grid, apart from being computationally efficient is that the energy spectra suggest that the inertial range is not that wide (as one would expect) for a high Reynolds number flow. With LES, one can resolve the large energy-containing range and a part of the inertial range but one must avoid the lower inertial range that is comparable with the *Kolmogorov* scales, most of which are represented by the SGS model. Ideally, the cut-off scale should be in the inertial range such that it is comparably smaller (say a factor of 10 to 100) than the large scales but larger by a similar factor with respect to the Kolmogorov scales (see Pope (2000) for a discussion).

Stability

In terms of stability of the Ex4, which is conditionally determined by the CFL criterion for explicit time integration schemes, we observed that at time steps larger than 0.004s, the simulation is unstable with a *Courant* number greater than ~ 2.4 . Reducing the time step to obtain a *Courant* number below 1, for example 0.001s, guarantees stability. On the other hand, owing to its unconditional stability, the Im2 is stable even at a time step of 0.01s that is ten times the original time step as opposed to the Ex4, which is divergent (Sanderse, 2013).

Now to compare the three methods, we must ensure that methods are stable at the time step considered. Therefore, we shall use the *Ex4* only with

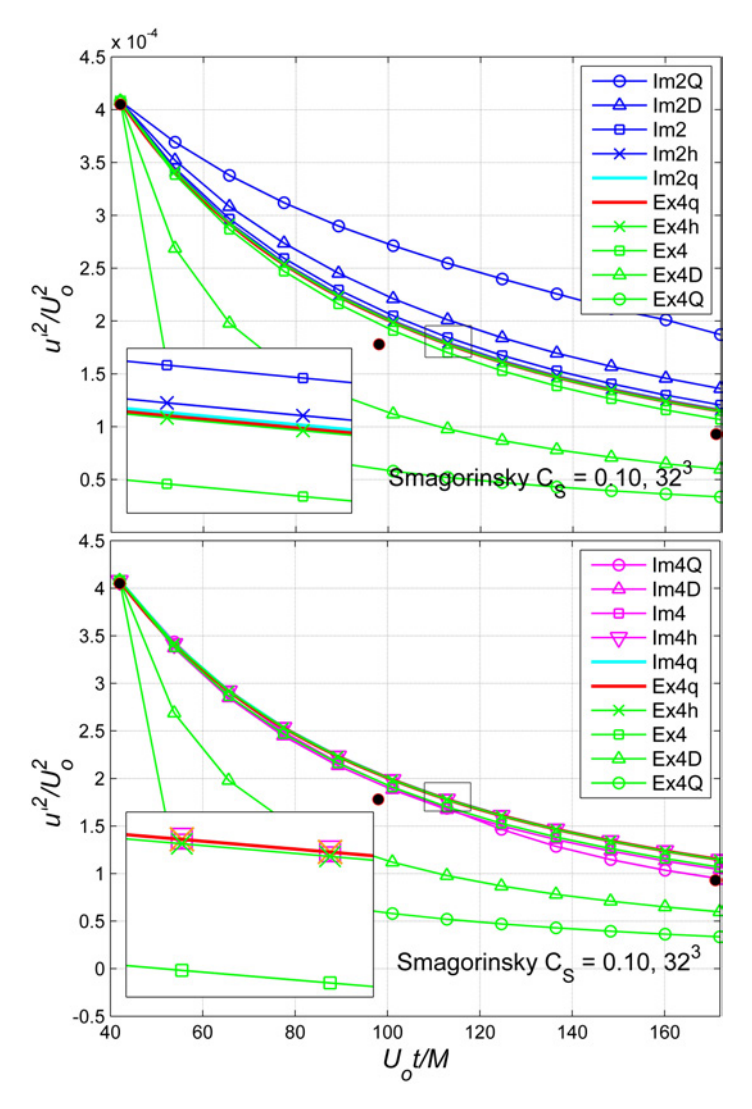


Figure 4.3: A comparison of the decay of TKE as predicted by the Ex4-Im2 (above) and Ex4-Im4 (below) methods with various time steps on a 32^3 grid.

time steps smaller than 0.002s, which ensures stability.

Error analysis

In this section, we evaluate the accuracy of the time integration schemes and present an error analysis. Using Ex4 with a very small time step of 0.00005s, we calculate a reference solution. By comparing the results obtained with time steps comparable with 0.00005s, we noticed that this time step is sufficient to ensure a very low error through time integration, for the three integration schemes considered here. Next, we calculate the root-

mean-square of the difference between the TKE of the field obtained during a simulation and the TKE of the reference solution (interpolated in time for the relevant time step), at every instance of time over the duration of the simulation. One calculates the TKE using:

TKE =
$$\frac{1}{2} \left(\sum_{i=1}^{3} \overline{u'_i u'_i} \right)$$
, (4.2)

where

 $\overline{u_i'u_i'}$ standard deviation in the component of velocity along the ith direction.

This value is the in fact, the average kinetic energy associated with the *fluctuations* in velocity across the range of eddies within the flow (presented as energy per unit mass). Mathematically, it relates to the *root-mean-sqaure* of those fluctuations, as shown in equation 4.2. We choose the TKE instead of the KE because changes in KE are hard to detect due to the high average stream wise velocity of $10 \, \text{ms}^{-1}$ as compared to velocity fluctuations that are only 2.22% of the stream wise value (see Comte-Bellot and Corrsin (1971) for experimental values). The error is calculated using the following definitions of e_2 and e_∞ ,

$$e_2 = \left(\frac{1}{n} \sum_{i=1}^{n} |\varepsilon_i|^2\right)^{\frac{1}{2}},$$
 (4.3)

$$e_{\infty} = \max|\varepsilon_{i}|$$
, (4.4)

where ε is the difference between the *expected* and the obtained TKE at a given instance of time and n is the number of such observations. Figure 4.3 shows the change in TKE with time obtained with various time steps and time integration schemes.

The errors are shown in figure 4.4 with the time required for the simulation. T is the time needed to simulate the test case on a 32^3 grid using Ex4 and $\Delta t = 0.001s$.

Order

Figure 4.4 shows the 2^{nd} order accuracy of the Im2 and the 4^{th} order accuracy of the Ex4 and Im4 (design orders).

For a time step larger than 0.001s, the Ex4 incurs more error as compared to the Im2. This is best explained in terms of the methods' orders of accuracy. The Im2 converges with second order accuracy hence the reduction (or increase) in error with the refinement of time step should be less than what is noticed with the fourth order Ex4. Therefore, Im2 is more accurate at larger time steps with a lower magnitude of error. But as the time step is reduced, it is the non-EC Ex4 method that is more accurate.

Im4 leads to the lowest global error at nearly all time steps. However, at very small time steps, we observe that *Im4* incurs a larger error than *Ex4*,

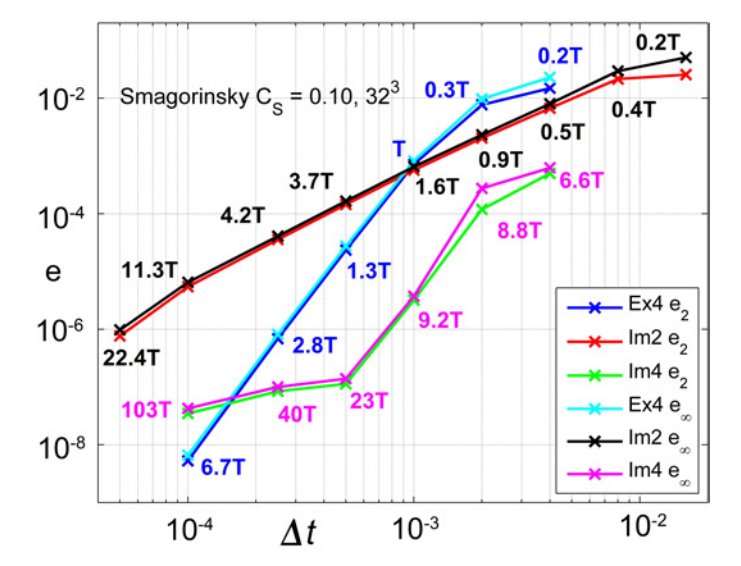


Figure 4.4: An error analysis based on the decay of TKE on a 32^3 grid. The reference solution is obtained with Ex4 and a time step of 0.0002s. T is the time required to obtain a solution with Ex4.

and loses its 4th order accuracy. This is only because the iterative method that is used to solve the *Im4* system, reaches its limit of its accuracy as the tolerance cannot be reduced further due to computational restrictions. Further, at very large time steps (0.004s), the accuracy is compromised because the time step is not sufficient to resolve the turbulent phenomena, that may have a time scale smaller than the time step. We also present figure 4.5 with the similar analysis on 48³ and 64³ grids. One notices slopes corresponding to the accuracy of the relevant method, independent of the grid resolution. Further, the error is larger with refined grids at a given time step, as one must ideally reduce the time step to maintain the same *Courant* number.

Accuracy

To evaluate the accuracy and the combination of the time step and time integration scheme that guarantees accuracy, we must analyse the energy spectra. The TKE is a sum of the energy contained in the various scales of turbulence. However, the spectra clearly show how accurately the energy at various scales is predicted. This will be helpful in chapter 5 where we attempt to tune the Smagorinsky model. If the model is tuned on the basis of the TKE, one will ensure that the sum of the energy is correctly predicted. But tuning with respect to the spectra will not only ensure that the TKE is correct but also its distribution within the various scales of turbulence. Therefore, it is wise to decide what is the level of accuracy required (in

terms of the error), to predict the decay of turbulence without the influence of numerical dissipation.

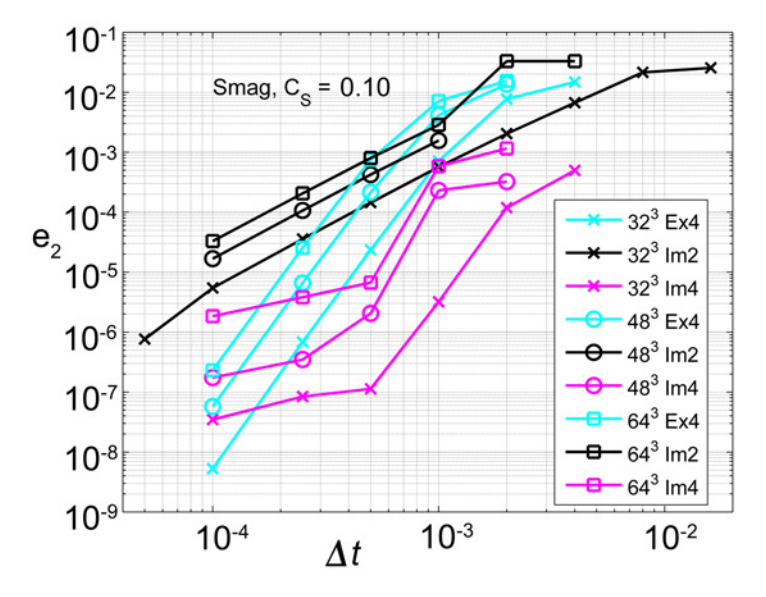


Figure 4.5: An error analysis based on the decay of TKE on different grids.

In figure 4.67, one notices that a time step of 0.002s with the Ex4 results in a large amount of numerical dissipation as compared to 0.001s, causing a marked change in the energy spectra; and the decay of TKE, as shown previously in figure 4.3. We also present the ratio of the energy at a given wavenumber for a certain time step, to the energy at the same wavenumber obtained with the reference solution of Ex4 with a time step of 0.00005s; mentioned as A_{Tw} in the bottom-right plot within figure 4.6. This helps visualise the changes in spectra with time step more easily. One notices that reducing the time step below 0.001s does not lead to marked changes in the spectra (A_{Tw} is nearly 1).

Comparing the error analysis (see figure 4.5) with the change in TKE with time shown in figure 4.3, one can establish that an error below 10^{-4} pertains to a solution obtained without significant influence of numerical dissipation through time integration. With the Ex4, this time step is below 0.005s or a *Courant* number of less than 0.15, indicating that even with a higher order method may need a small time step to avert numerical dissipation.

On the other hand, Im2 requires a time step of 0.0025s due to its lower order of accuracy, to obtain a final error below 10^{-4} . But the Im4 being 4^{th} order accurate and EC by design, is accurate enough in this case at a time step of 0.002s itself⁸, as shown in figure 4.7. As a result, we also notice that the spectra obtained with Im4 do not show much apparent variation in comparison with the energy obtained with the reference solution of Ex4 with

⁷ Compare the energy spectra at Stages II and III

⁸ In fact, even at a time step of 0.002s

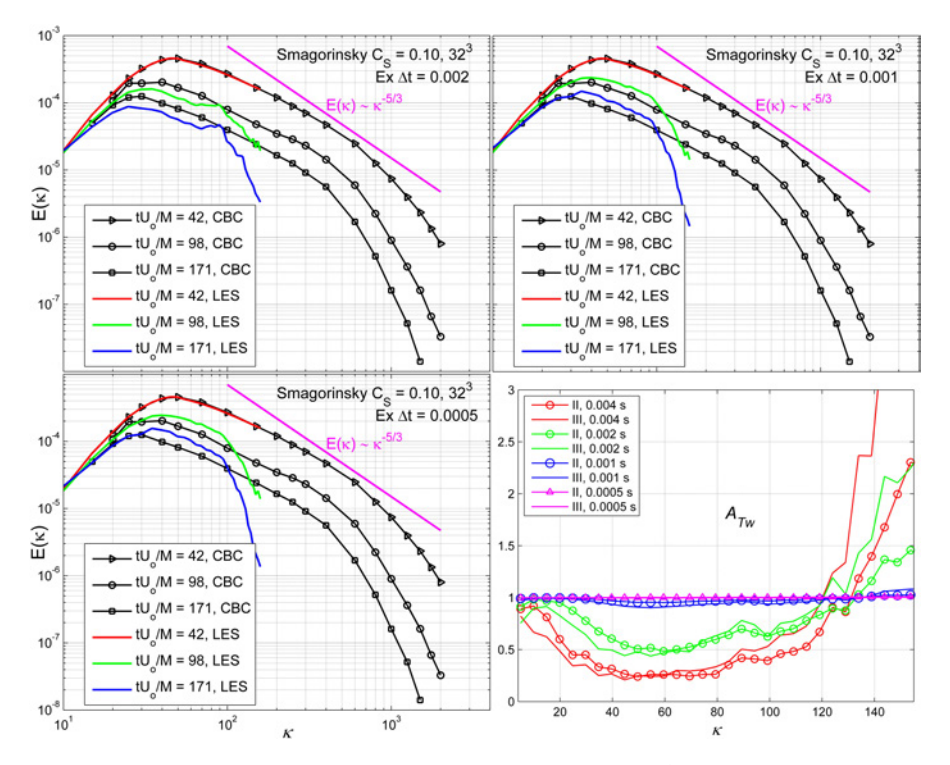


Figure 4.6: Energy spectra obtained using $C_S = 0.1$ on a 32^3 grid with the Ex4 and different time steps.

0.00005s. The A_{Tw} remains nearly 1 at almost all the wavenumbers (see *bottom-right plot* in figure 4.7).

Efficiency

In this section, we assess which method is most suitable in terms of computational efficiency. From the preceding discussion on accuracy, it is clear that Ex4 with a time step of 0.0005s is a good approach to simulate the decay on a 32^3 grid and to obtain a solution independent of time step, with a computational time of 1.3T, where T is the time required by Ex4 (see figure 4.4). This corresponds to an error below 10^{-4} 9.

Upon reducing the time step, the error is driven to below 10^{-8} with Ex4 with a time step of 0.0001s and a computational time of 6.7T, due to the method's high order of accuracy. On the other hand, the Im4 permits using a larger time step of 0.002s but with a very high computational time of 8.8T. This is computationally demanding to the extent that Ex4 with a time step of 0.0001s is as fast as Im4 with a time step of 0.004s.

⁹ The computational times on finer grids show a similar trend with the various schemes and time steps. These are not discussed for succinctness

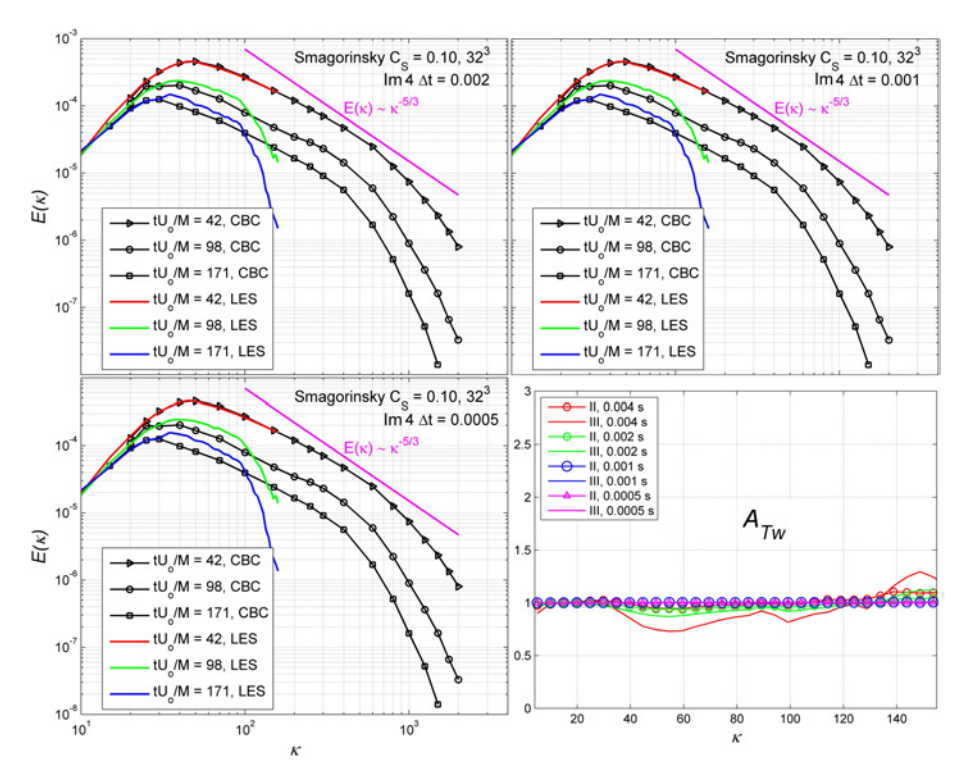


Figure 4.7: Energy spectra obtained using $C_S = 0.1$ on a 32^3 grid with the Im4 and different time steps.

These computational demands are mostly because of the methods used to solve the system of equations within the time integration scheme. One uses the Newton method to linearise the system for solving the implicit EC time integration schemes. The Newton method reaches its limit of accuracy below a time step of 0.00025s as shown in figure 4.5¹⁰. This occurs because the solution obtained is already at machine precision. Further, it is also important to ensure that the error that results from the linearisation of system of equations, is reduced to a value much smaller than the overall discretisation error at every time step. An error from linearisation that is comparable to the overall discretisation error can reduce the accuracy of the implicit methods considered here. Although we do not present the results here, we noted that the accuracy of the Im4 is very strongly related to the tolerance set for the linearisation. For an overall accuracy of 10^{-4} , one must ensure a linearisation error of 10⁻⁸ or lower. If one desires an overall error of 10⁻⁶, the linearisation must be done till a tolerance of 10^{-10} ; and so on smaller time steps. Not doing so can even render the *Im4* less accurate than the *Ex4*.

¹⁰ We notice in figure 4.5 that at higher resolutions, the error levels of at a higher magnitude although the machine precision should remain the same. This is because one may require more number of Newton iterations at a higher resolution to reduce the iterative error in solving the implicit schemes

Hence, the advantage of an implicit method permitting a larger time step, is annulled by the increased computational time required per time step. Although the ECNS is not parallelised, we believe that the ratios of computational times with the implicit methods presented in figure 4.4, would at best remain the same upon parallelisation, as compared to the *Ex4*. An improved computational efficiency with the implicit methods would a more optimal approach to solving the coupled system of equations.

In closing, the EC conserving nature of a time integration method does provide stability with LES at large time steps. In most LES studies reported in literature, the grid size is determined based on a statistical estimate of the *Taylor micro scale*, the *Kolmogorov scale* etc., as done in this study. This is followed by adjusting the time step to satisfy the CFL criterion in case of explicit methods. As an alternative, one can certainly use an EC implicit time integration scheme that is stable with large time steps, while bearing in mind that a very large time step could lead to inadequate resolution of turbulent phenomena with a time scale relatively smaller than the chosen time step. But if one wishes to gather data with a higher temporal resolution of the scales, such that the time step is low enough to ensure accuracy with either method, it would be preferable to use the *Ex4* due to its lower computational requirements, as long as the stability is not compromised.

4.5 CONCLUSION

With regards to an implicit EC time integration scheme, we can conclude that it is capable of averting numerical dissipation at large time steps, while remaining stable and ultimately leading to an accurate solution. But in terms of the test case considered in this article, it appears that a non-EC explicit scheme is computationally efficient even with small time steps, as long as it is of the same order as the implicit EC scheme (4th order in this case). Using a $2^{\rm nd}$ order explicit non-EC scheme may not be favourable as we note that even an implicit EC $2^{\rm nd}$ order scheme requires a reasonably small time step for accuracy.

Further, it is fair to mention that the implicit methods may retain all their advantages in simulations that involve local grid refinement and the presence of walls, the flow near which may have to be resolved with a non-uniform grid to obtain accurate results. In such cases, the stability criteria may be very strict for non-EC explicit methods to resolve the refined regions, possibly rendering them unworkable. However, to harness the accuracy and stability of implicit EC schemes for practical applications, it is imperative to explore methods through which implicit time integration could be executed more efficiently, as computational requirements are their shortcoming. On the other hand, most LES studies on wind farm aerodynamics mentioned in literature, prefer to model the shear stress at the surface instead of refining the flow near it, to reduce computational requirements, thus favouring the non-EC explicit methods.

SPATIAL DISCRETISATION

Images & content also appear in Mehta

In this chapter, we assess whether an EC spatial discretisation for finite volume methods that has theoretically been proven to ensure zero numerical dissipation at every grid size, has significant advantages in practical LES.

Firstly, we compare the *simple central difference scheme on collocated grids* available in OpenFOAM against the *EC scheme on staggered grids* for simulating the convection of an inviscid vortex. Both the schemes, *per se* have no dissipation but only dispersion when used to discretise the convective operator. We assess what possible differences could exist between the two codes and additionally, study the effects of using dissipative (upwind) numerical schemes. In terms of spatial discretisation, these two approaches are mathematically identical on uniform grids, as the *EC* scheme as shown in chapter 3, also has a central difference based formulation.

The only aspect in which these two approaches differ is their formulation for non-uniform grids. The EC scheme remains energy-conserving (or dissipation-free) as it uses the *arithmetic mean* to interpolate and average the velocity field across cell boundaries (Verstappen and Veldman, 2003). Whereas, the central difference scheme in OpenFOAM switches to linear interpolation on non-uniform grids. We wish to evaluate if this difference in approach, makes one scheme more favourable than the other, and under what circumstances.

To avoid confusion, we shall use the term *dissipation-free* instead of *energy-conserving* to indicate the property of *the conservation of energy* obeyed by at least, the *energy-conserving scheme* described in **chapter** 3 and must be obeyed by any dissipation-free scheme in general. Therefore, EC or energy-conserving in this chapter, will strictly refer to the scheme in **chapter** 3 and that is offered within the ECNS, and *not* the property of being dissipation-free.

Secondly, we tune the Smagorinsky model in either code¹ to correctly simulate the decay of isotropic homogeneous turbulence, while ensuring that the time integration does not introduce any dissipation; to prepare both the codes for LES, in terms of predicting the turbulence energy spectrum correctly. Tuning in this manner will ensure that for a given initial turbulent field, both the codes predict the same rate of decay of energy.

¹ ECNS and OpenFOAM with their individual spatial discretisation schemes

SCHEME	ECNS	OPENFOAM
Grid	Staggered	Collocated
Interpolation	Arithmetic mean	Linear
Differencing	Central	Central

Table 5.1: Salient features of the two dissipation-free spatial discretisation methods studied in this chapter.

5.1 INTRODUCTION

Table 5.1 illustrates the two theoretically dissipation free approaches used in this chapter. By studying these approaches, we wish to answer the following questions:

- A central difference scheme on a collocated grid, *per se*, has no dissipative error but a dispersive one. How does this approach compare with the EC scheme on a staggered grid, which itself has a central difference-like formulation?
- Do the dissimilarities between the two approaches listed in table 5.1 significantly affect the outcomes in practical applications like LES?

The interpolation scheme in OpenFOAM is *linear*, which automatically changes to the arithmetic mean on uniform grids.

5.2 SPATIAL DISCRETISATION AND NUMERICAL DISSIPATION

To assess the effects of numerical dissipation through spatial discretisation, we take look at equation 4.1 again that expresses the overall dissipation in an LES scheme as²,

$$\mathcal{P} = \varepsilon_{\mathbf{C}}(\Delta x) + \nu(\mathcal{D} + \varepsilon_{\mathbf{D}}(\Delta x)) + \mathcal{S}(\tau) + \varepsilon_{\mathbf{S}}(\Delta x) + \varepsilon_{\mathbf{T}}(\Delta t) , \qquad (5.1)$$

where

- D diffusive operator (physical dissipation),
- S SGS operator,
- ε_{C} dissipation (numerical) accompanying the convective operator,
- $\varepsilon_{\rm D}$ dissipation (numerical) accompanying the diffusive operator,
- τ SGS model (physical dissipation),
- $\varepsilon_{\rm S}$ dissipation (numerical) accompanying the SGS operator,
- ε_T dissipation (numerical) through time integration.

² The pressure term also leads to numerical dissipation (but not with an EC scheme) but we shall ignore it for now.

 ϵ_D (dissipative) arises from the approximation used to estimate the physical diffusion through molecular viscosity, \mathcal{D} . \mathcal{S} is dissipation through the SGS model τ , which can be tuned (see section 2.2.3.1), whereas, ϵ_S is the spatial discretisation error in the model's implementation and is a function of the grid resolution, Δx . ϵ_T is a function of the time step, Δt , and must approach zero with reducing time step.

Physical dissipation or \mathfrak{P} , pertains to the dissipation that a numerical method must deliver, which would ideally equal what the flow would experience in nature. At higher Reynolds numbers, the *physical* diffusion is very small and so is the error from the discrete diffusive operator, both of which can be neglected. In fact, the diffusive operator is generally set to zero while simulating the ABL³. This leads to (after reducing Δt to a value that gives $\epsilon_T = 0$),

$$\mathcal{P} = \varepsilon_{\mathcal{C}}(\Delta x) + \mathcal{S}(\tau) + \varepsilon_{\mathcal{S}}(\Delta x) . \tag{5.2}$$

In an EC spatial scheme, the error from the convective operator is predominantly dispersive because numerical dissipation has been made zero (see Sanderse (2013)). For high Reynolds number flow, the convective term is large compared to the dissipative term and so is the accompanying numerical dissipation. Therefore, numerical dissipation through $\epsilon_{\rm C}$ can influence the flow to a great extent and should be removed. In consequence, with an LES code based on a dissipation-free scheme (or an EC scheme in our case), one would expect equation 5.2 to read,

$$\mathcal{P}_{FC} = \mathcal{S}(\tau) + \varepsilon_{S}(\Delta x) . \tag{5.3}$$

Whereas, a non-EC scheme remains,

$$\mathcal{P}_{\text{Non-FC}} = \varepsilon_{\text{C}}(\Delta x) + \mathcal{S}(\tau) + \varepsilon_{\text{S}}(\Delta x) . \tag{5.4}$$

Next, we club the dissipative error from the implementation of the SGS model, $\varepsilon_S(\Delta x)$, with the dissipation arising from the model itself, $\delta(\tau)$, and rewrite the above equations as,

$$\mathcal{P}_{EC} \approx \mathcal{S}(\tau, \Delta x) ,$$
(5.5)

$$\mathcal{P}_{\text{Non-EC}} \approx \varepsilon_{C}(\Delta x) + \mathcal{S}(\tau, \Delta x)$$
. (5.6)

It is hard to assess the contribution of Δx within $S(\tau, \Delta x)$ but it is nonetheless apparent that the contribution of Δx , as a whole to \mathcal{P} , reduces with the removal of $\varepsilon_C(\Delta x)$. Therefore, it is fair to hypothesise that with a non-dissipative scheme (EC or pseudo-spectral), the dissipation *unaffected by the grid resolution to a greater extent* that what would be the case with a scheme that has inherent numerical dissipation.

This property may help tune the SGS model more easily as the grid resolution has a relatively minor role to play, when $\varepsilon_{C}(\Delta x)$ is absent or very

³ In this chapter, the viscous term is not neglected. It will be neglected for high Reynolds number flows in chapters 6 and 7

small compared with $S(\tau)$ (if some numerical dissipation is present). In fact, the property of inherent numerical dissipation in terms of $\varepsilon_C(\Delta x)$, is put to good use by Implicit LES methods, wherein, the dissipation introduced by the discretisation replaces the SGS model (see Grindstein et al. (2007)).

Although we cannot completely rule out the dependence of the SGS model on grid resolution (or $\varepsilon_S(\Delta x)$), we have evidence from literature that within a reasonable range of grid resolutions, the dependence is moderate enough for practical applications, which concern us here (confirmed for the Smagorinsky model in Meyers et al. (2010)). It has been observed that at poor grid resolutions, the optimal Smagorinsky constant is quite dependent on the grid resolution. However, once the grid resolution is sufficient to promote adequate resolution of the large scales relevant for high Reynolds number flows, the dependence on increasing grid resolution is relatively weaker.

In the tests that follow, we shall establish qualitatively whether equations 5.5 and 5.6 hold for the spatial discretisation approaches mentioned in table 5.1, and a few approaches that have inherent numerical dissipation, upwind schemes to be precise. We will comment on consequences that result should the equations 5.5 and 5.6 not hold. Finally, we answer whether the differences between a central difference scheme on a collocated grid and an EC scheme on a staggered grid lead to marked differences in their results.

5.3 THE SCHEMES WITHIN OPENFOAM

OpenFOAM⁴ is an open-source simulation package that permits the user to customise an NS solver using a combination of spatial-temporal schemes and a turbulence model. It uses a finite volume approach like the ECNS.

Amongst the host of schemes offered, is the *Gauss Linear* scheme (mentioned earlier in table 5.1, which is a 2^{n.d} order central difference method that inherently has zero numerical dissipation but a non-zero dispersive error (Perić and Ferziger, 2002). To ensure that the comparison with ECNS is fair, we use the *Gauss linear* scheme for all terms to render the OpenFOAM solver as *energy-conserving* as possible because the ECNS uses an EC spatial discretisation method (read dissipation-free), which applies to all operators of the NS equations.

In addition, we also use the Quadratic Upwind Interpolation scheme for Convective Kinematics (3rd order, QUICK)⁵ and the Linear Upwind (2nd order, LU) schemes, which incur numerical dissipation, to assess their effects on the evolution of turbulent flows. For time integration, we use the Crank-Nicolson 2nd order implicit forward time stepping with a rather low time step to avert numerical dissipation through time integration (Perić and Ferziger, 2002). OpenFOAM offers the simple Smagorinsky model that we shall try to tune.

⁴ http://www.openfoam.com/

⁵ As regards to table 5.1, QUICK uses a collocated uniform grid but with upwind differencing and interpolations defined by the QUICK scheme itself.

It is important to mention that the *pressure* can contribute to the change in kinetic energy. This is not the case with the ECNS as it ensures perfect pressure-velocity coupling. On the other hand, we used the Pressure-Implicit with Splitting of Operators (PISO) algorithm with OpenFOAM. PISO does not resolve the pressure-velocity coupling completely but approximates it with predictor-corrector steps. In such a case, we expect the *pressure* to spuriously contribute to the change in kinetic energy (numerical dissipation, see equation 5.1). However, we checked the direct effect of using PISO on our results and ensured that the tolerance and the number of predictor-corrector steps are optimised to guarantee maximum accuracy⁶.

Using the two approaches mentioned in table 5.1, we simulate the convective transport of a vortex in an inviscid flow and two different cases of decaying isotropic homogeneous turbulence, using three dimensional periodic computational domains. For simplicity, we refer to the spatial discretisation approach with the EC schemes on staggered grids directly as ECNS, and the central difference schemes of collocated grids as OpenFOAM.

5.4 CONVECTION OF AN INVISCID VORTEX

For simplicity, we study a simple two dimensional vortex used in numerical experiments with compressible flows (Yee et al., 1999). We use the initial condition that defines the velocity field as a function of the spatial location and initialise a three dimensional field by repeating the two dimensional initial condition along the third dimension. Although we do not present the data here, we have also simulated the same case with different orientations of the vortex, while being convected at different flow velocities, using the ECNS. In either case, we obtained results similar to those presented here, in terms of the conservation of KE with time.

5.4.1 *Set-up: inviscid vortex*

A domain with a length $L_o=10 m$ in either direction, is discretised into 16^3 , 24^3 , 32^3 , 48^3 , 64^3 and 72^3 finite volumes⁷. The centre of the vortex is located at [5,5]m and it is being convected along the x-axis with a flow velocity $u_c=1 m s^{-1}$. The velocity field with the vortex, relative to the flow is defined using,

$$u' = -\frac{\beta}{2\pi} \left(e^{\frac{1-r^2}{2}} \right) (y - y_c) ,$$
 (5.7)

$$v' = \frac{\beta}{2\pi} \left(e^{\frac{1-r^2}{2}} \right) (x - x_c) ,$$
 (5.8)

$$r = \sqrt{(x - x_c)^2 + (y - y_c)^2}$$
, (5.9)

⁶ A tolerance of 10⁻¹⁰ and 2 predictor-corrector steps are sufficient. Further changes did not alter the results noticeably

⁷ One on a staggered grid (ECNS) and one on a collocated grid (OpenFOAM).

where $[x_c, y_c]$ is the centre of the vortex, [x, y] is the location and $\beta = 0.5$.

Throughout the simulations with either code, the time step is adjusted to maintain a *Courant* number of 0.05 that, in this case, is small enough to avert numerical dissipation through time advancement. We observe the KE within the domain as the vortex moves through the periodic boundaries between t=0 and $t=24s^8$. If a code is EC by design, the KE must not be altered in course of this simulation and we shall only observe a straight line when the KE is plotted against time.

5.4.2 Observations

Figure 5.1 depicts the velocity field at t=0s on a coarse (16^3) and a fine grid (72^3); and the velocity fields at t=3s with both the ECNS and OpenFOAM. By definition, any dissipation-free scheme should be able to transport these vortices without reduction in KE that is generally indicative of numerical dissipation. Judging by the structure of the vortices at t=3s, we notice that a low grid resolution such as 16^3 , the vortices show some changes in structure. However, at a more reasonable resolution of 72^3 , both the Open-FOAM and ECNS, show little change in structure. Although not shown here for simplicity, both approaches demonstrate an expected $2^{n \cdot d}$ order rate of convergence through an error analysis. The ECNS, shows a slightly lower global error.

A better insight can be obtained upon plotting the KE against time, we notice a straight line with the ECNS indicating no change in KE or no numerical dissipation, and hence, the KE is perfectly conserved (see *left plot* figure 5.2). This is true even with an 8³ grid, as expected (Sanderse, 2013). On the other hand and despite its non-dissipative formulation, OpenFOAM shows a continuous reduction in KE. This reduction, however, is not very pronounced on finer grids and in fact diminishes constantly with resolution. One could argue that the magnitude does not reduce by a large value, however, for an inviscid vortex within periodic boundaries, the KE should not reduce at all, especially on finer grids (for which we could still observe some reduction).

It could also be surmised from *the right plot* in figure 5.2 that OpenFOAM displays a mildly increasing trend on a 32³ grid. This may be reminiscent of instability but the simulation was let to run for a very long time⁹ and the trend seems to oscillate between increasing and decreasing, around the ideal *zero* line. Further, using the upwind QUICK schemes, we observe distinctive artificial dissipation, despite the higher order of accuracy of the scheme (see *right plot* figure 5.2). Judging by the magnitude of the reduction of KE, it may seem that there is little change with OpenFOAM as compared to the EC scheme than compared to a dissipative upwind scheme.

 $^{8\,}$ Longer durations were also observed to check the behaviour after a very long run time.

⁹ We let the field evolve till t = 120s but the results till t = 24s are sufficient to come to a conclusion.

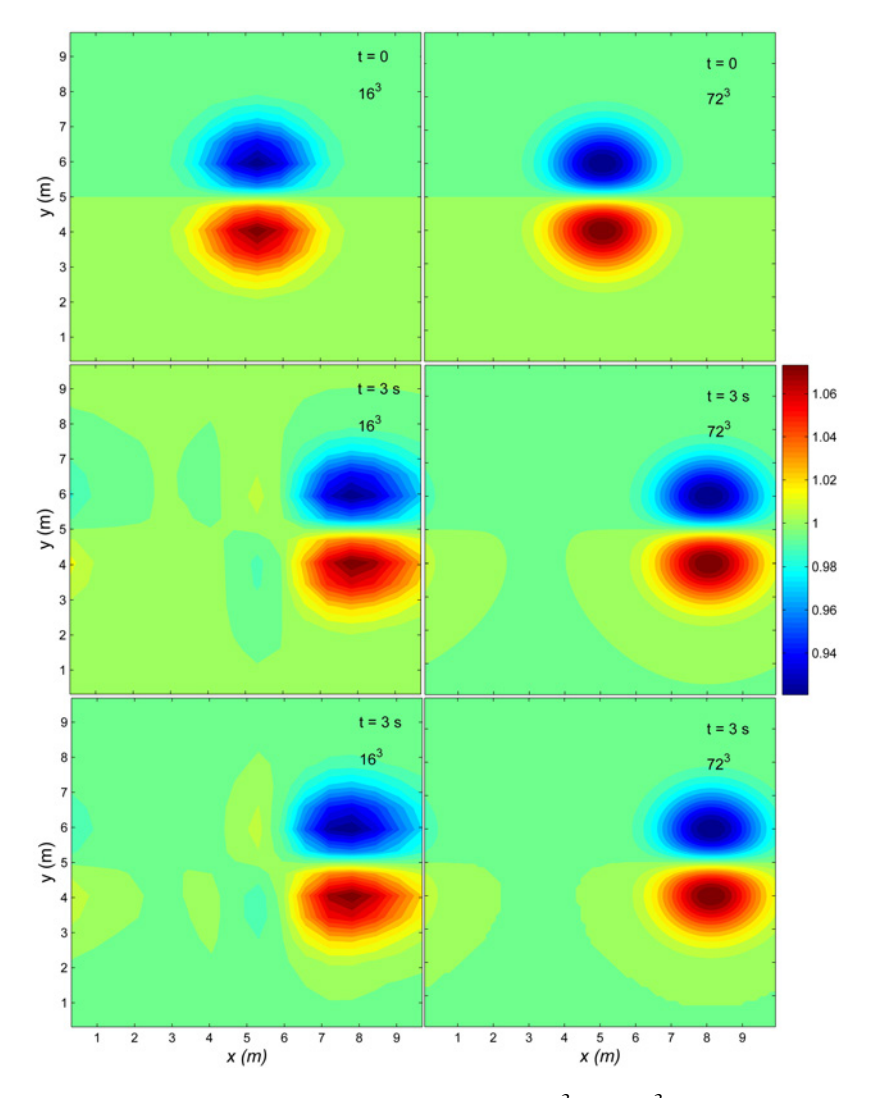


Figure 5.1: Contours of u-velocity at resolutions of 16^3 and 72^3 at t=0s, the initial condition (top). Contours of u-velocity at t=3s with the ECNS (middle) and with OpenFOAM (bottom).

However, with the change in KE, we are also interested in whether the vortex retains its structure or not. Although the non-dissipative schemes maintain the KE, they incur numerical dispersion due to their central formulation, which may show up as *wiggles* in the velocity field. On the other hand, an upwind scheme should dissipate these wiggles easily (they mostly occur at small scales with relatively less energy) and reduce the KE globally. Through the contours of u-velocity in figure 5.3, we note that for OpenFOAM, the vortex remains more or less similar to that rendered by the ECNS, and without

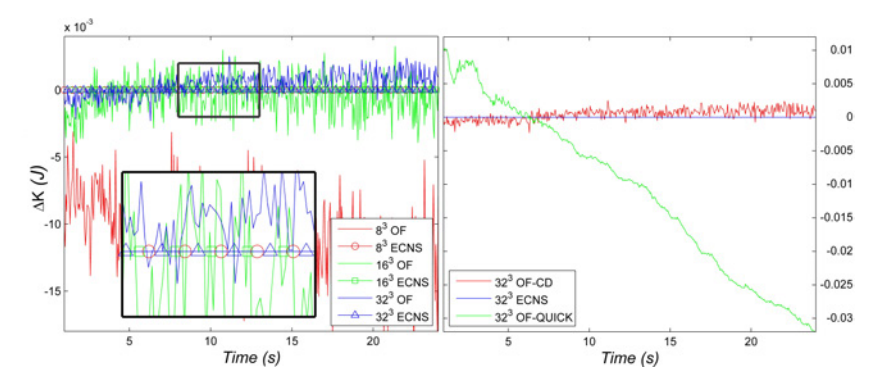


Figure 5.2: Change in KE with time (compared with KE at t=0s) for different grid resolutions with the ECNS and OpenFOAM approaches (left). Change in KE with time on 32^3 grid using a dissipative *upwind* approach (right).

noticeable numerical dispersion. However, an upwind scheme like QUICK, leads to changes in structure and also produces numerical dissipation.

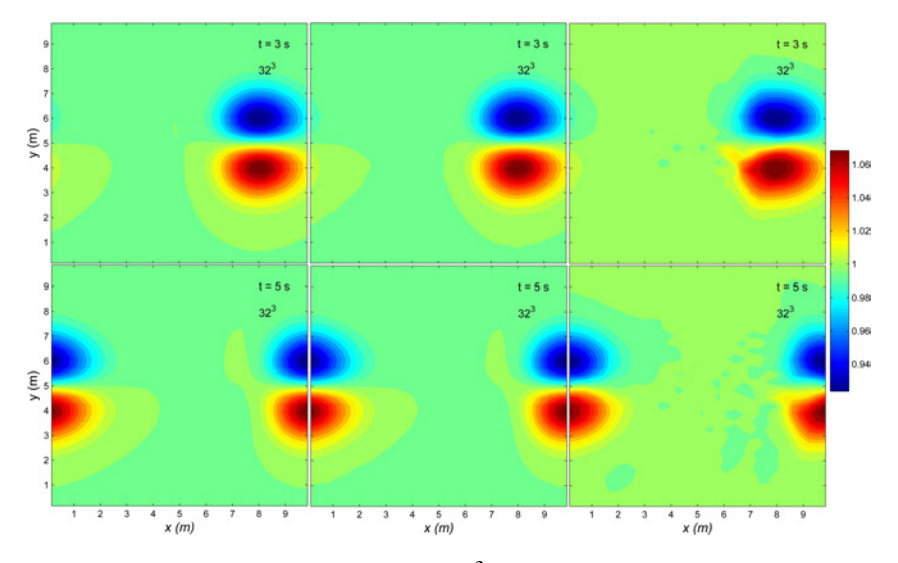


Figure 5.3: Contours of u-velocity on a 32³ grid at two instances of time with the ECNS (left), OpenFOAM(centre) and QUICK (right). One notices a change in structure of the vortex with QUICK, much apparent in the *red-yellow* contours.

Based on the results, it is certain that after a long period ¹⁰, the upwind scheme would lead to a significant decay in the vortex, whereas the Open-FOAM and ECNS approaches would be more or less similar without much decay, at least on uniform grids. In section 5.3, we had mentioned the use of PISO. We suspect the oscillations around 0 with OpenFOAM in figure 5.2

¹⁰ Confirmed by running the simulations till t = 120s.

(on the resolved 32³) may be a remnant of the lack of pressure-velocity coupling. Increasing the tolerance or the predictor-corrector steps with PISO did not improve the result to a straight line through zero (as seen with the ECNS). This may occur once the PISO has reached the limit of its accuracy or the machine precision allows no further improvement of the results. In either case, we don't see an uncontrolled spurious contribution of the pressure term to the decay of kinetic energy.

5.4.3 Non-Uniform Grids

In this section we address the behaviour of the ECNS and OpenFOAM approaches listed in table 5.1 with non-uniform grids.

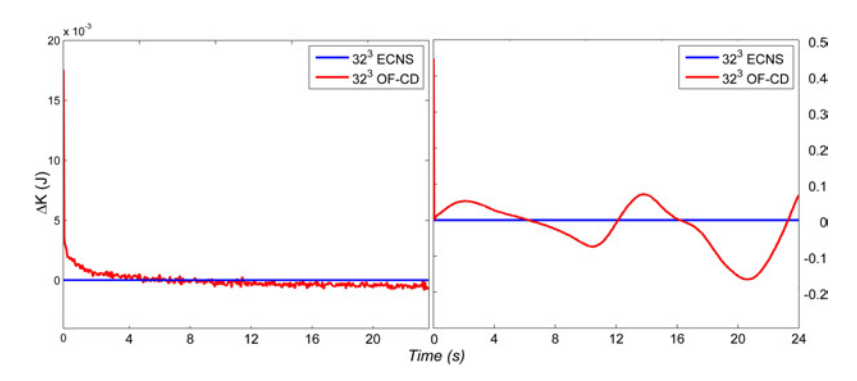


Figure 5.4: Change in KE with time on a uniform grid with a divergence-free initial field superimposed with random fluctuations (*left*). Change in KE with time on a non-uniform grid (*right*).

From the uniform grid used in the previous simulations, we create a non-uniform grid, the cells of which reduce in size towards the centre of the grid, with either dimension along the cardinal axes reducing as a geometric progression. The reduction is designed to ensure that the smallest cell (located near the centre) is a cube with an edge equalling the half the grid size of the original uniform grid. Simultaneously, we reduce the time step by half to avert any numerical dissipation that may arise through local changes in the *Courant* number (see chapter 4). Next, interpolate the velocity field from a highly refined uniform grid (128^3) onto a 32^3 grid and let the flow evolve till $t = 24s^{11}$.

In figure 5.4 (right), we notice that the ECNS shows no change in behaviour and produces a straight line representing zero change in KE. However, the OpenFOAM approach is no longer able to produce the results shown in figure 5.2. We notice that the changes in KE become more prominent and increase by at least an order of magnitude. Additionally, the changes in KE around 0 demonstrate a clearly increasing amplitude. One also notices a

¹¹ We let the field evolve till t=120s but the results till t=24s are sufficient to come to a conclusion.

jump at t=0, a sudden and a large change in KE, which we found out occurs immediately at the first time advancement.

To know more about the latter, we simulated the original vortex superimposed with some minor random fluctuations, with both the codes on a uniform grid. Figure 5.4 (left) shows the change in KE with time.

Although the ECNS retains its EC behaviour, OpenFOAM with the central difference scheme produces the *jump*, after which the change in KE follows a trend similar to that shown in figure 5.2. The random fluctuations imposed on the divergence-free vortex, were done to add a non-zero divergence to the initial field. The ECNS uses a projection method to modify this initial velocity field to a divergence-free field (Chorin, 1968). OpenFOAM, however, does not use such a method but continues with the initial field, which upon the first time advancement is constrained into a divergence-free field leading to the sudden change in KE.

Hence, we may assert that the *jump* in figure 5.4 (right), is due to the divergence-free vortex not remaining divergence-free upon interpolation onto a non-uniform grid. However, the marked changes in KE that follow, are due to the OpenFOAM approach not being able to perform like the ECNS on a non-uniform grid. This pertains to the fact that the ECNS is designed to perform all mathematical operations on the convective operator in a manner that cancels the truncation error leading to numerical dissipation (staggering the grid is also important), even on non-uniform grids (Sanderse, 2013). The approach also requires that velocity fields are interpolated as arithmetic means on both uniform and non-uniform grids (see table 5.1).

We used OpenFOAM with both linear interpolation and the arithmetic mean based approach (see chapter 3), however, noticed no changes in terms of the conservation of KE. Therefore, we attribute the dissipation-free property of the ECNS approach on non-uniform grids, to the use staggered grid or possibly the combination of a staggered grid and the arithmetic mean interpolation (despite the non-uniform grid), as suggested earlier.

Therefore, we conclude that on a non-uniform grid the ECNS approach listed in table 5.1 is more favourable than a simple central difference scheme on a collocated grid. Nonetheless, in the context of wind farm aerodynamics, most LES-based studies use uniform grids, on which, we notice that both the ECNS and OpenFOAM approaches, are more or less, the same. This also explains why most LES codes listed in chapter 2, are able to use the central difference approach to discretise the vertical, in combination with a dissipation-free pseudo-spectral discretisation in the horizontal directions, to ensure a dissipation-free simulation.

5.5 GRID GENERATED TURBULENCE

Now that we are aware of the similarity between the ECNS and OpenFOAM approaches, we turn our attention to equations 5.10 and 5.11.

$$\mathcal{P}_{EC} \approx S(\tau, \Delta x) ,$$
(5.10)

$$\mathcal{P}_{\text{Non-FC}} \approx \varepsilon_{\text{C}}(\Delta x) + S(\tau, \Delta x) . \tag{5.11}$$

According to these equations, the absence of numerical dissipation reduces the dependence of the overall dissipation in an LES schemes, on changes in grid resolution. To study this further, we return to the test case of decaying isotropic homogeneous turbulence, which was introduced in chapter 4. The case is the recognised experimental campaign by Comte-Bellot and Corrsin (1971) mentioned in chapter 4; which shall shall refer to as *CBC* and use in the same manner.

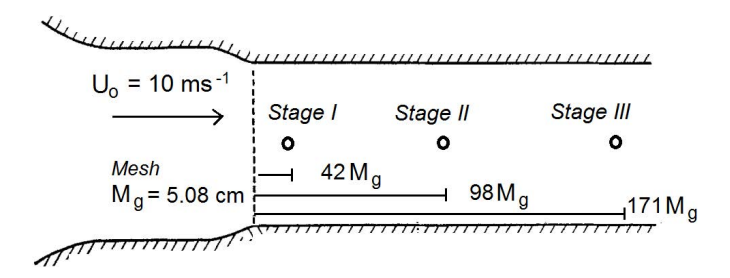


Figure 5.5: A schematic of the experimental set-up used by Comte-Bellot and Corrsin (1971). The nomenclature for the various stages is shown in the figure and shall be used in the discussion.

We simulate the decay on 32³, 48³, 64³ and 96³ three-dimensional uniform grids (listed in table 5.1), as reported in scientific literature related to the simulation of these experiments. Finally, we use a time step of 0.0005s¹² for simulating CBC with OpenFOAM based on conclusions from chapter 4.

5.5.1 *Decaying turbulence: CBC*

The first step to a fair comparison of the ECNS and OpenFOAM with regards to LES, is to tune the Smagorinsky model for the two codes. Per our hypothesis and equations 5.10 and 5.11, the absence of numerical dissipation may reduce the influence of grid resolution on the overall dissipation, which in the case of the Smagorinsky model can be controlled with the Smagorinsky constant or C_S (this represents ε_S and δ in equations 5.10 and 5.11).

¹² Smaller than that for the ECNS because the latter uses the higher order Ex4

Therefore, the absence of numerical dissipation may ensure that C_S is grid-independent to a greater extent that a code with dissipative schemes, especially as the grid resolution is increased.

First, we analyse the effect of grid resolution (for the ECNS) for a given Smagorinsky constant.

5.5.2 Preliminary Analysis

For the time being, we set $C_S = 0.12^{13}$ for the ECNS. Figure 5.6 shows the energy spectra at different grid resolutions. To help understand the effect of grid resolution, the *bottom-right* plot in the figure 5.6 shows the ratio of the simulated and the experimentally determined value of the energy, as a function of the wavenumber; shown in the plot at A_{CBC} .

It is observed that upon increasing the resolution beyond 48^3 , the part of the spectrum close to what was correctly predicted on a 48^3 grid is reproduced appropriately, whereas the dampening continues to occur close to the wavenumber at which it began on the 48^3 grid. However, this dampening is small for the newly introduced wavenumbers and the sharp tail only begins near the cut-off wavenumber for the particular grid. In short, the lower wavenumbers more or less, remain unaffected with increasing grid resolution and the *tail* shifts to higher wavenumbers.

Additionally, the part of the spectrum before the dampening, is continually predicted with improving accuracy with grid resolution. Hence, we may conclude that beyond 96³, the spectra will not be affected much because the contribution of Δx to $\mathbb{S}(\tau,\Delta x)$ in equation 5.10, will be reasonably small. This leads to a more or less constant overall dissipation, governed solely by Smagorinsky model and its constant, $C_S=0.12$, in this case. Therefore, it is reasonable to assume that for refined grids, we could probably resort to a single value of C_S , to correctly predict the spectra up the wavenumber at which the spectra seem to dampen.

We also conducted tests using different SGS models and even without one, to find out what causes the excessive dampening at high wavenumbers near the limit of the grid's resolution. We suspect that it is related to the use of the Smagorinsky model in a finite volume approach, as using the Bardina model (see section 2.2.4) that is not purely dissipative, lead to peak at the higher wavenumbers, representing an accumulation of energy. In short, the functioning of either model was affected at the smaller scales of the resolved flow.

Figure 5.7 shows the results obtained with a pseudo-spectral code with the *Germano* model. We also used the same model but obtained poor results near the higher wavenumbers without any changes in the *tails*. This led us to suspect that the *tails* may arise from the use of a finite volume method. Therefore, we exclude regions that show these *damped tails* from further ana-

¹³ We shall later notice that $C_S = 0.12, 0.125$ is appropriate for the ECNS. We merely use the same value for helping the reader understand the discussion that follows.

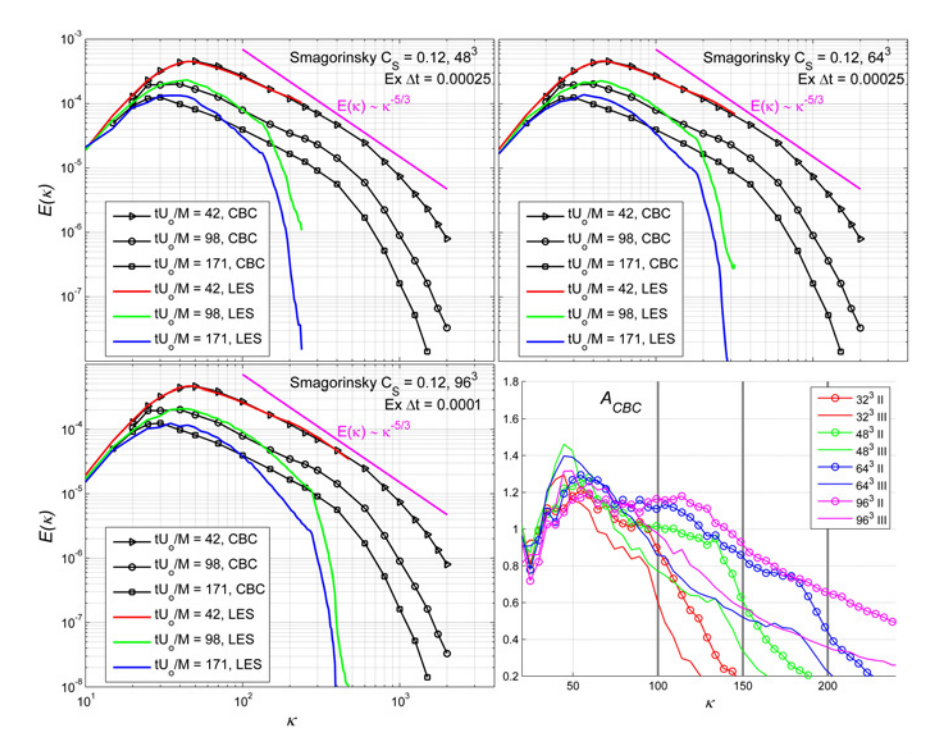


Figure 5.6: Changes in the energy spectra for $C_S = 0.12$ with the ECNS on 48^3 , 64^3 and 96^3 grids. The *bottom-right* plot shows A_{CBC} at different grid resolutions.

lyses on the spectra. The reason behind their occurrence has little relevance to the content of this thesis but could be worth investigating.

Next, we perform an analysis similar to the one followed in Meyers (2011), to tune the Smagorinsky model properly.

5.5.3 An Alternative Analysis

To tune the Smagorinsky model in the ECNS, we first calculate what part of the energy spectra (Stage II and Stage III) can be predicted accurately through the simulations. For example, we check how closely can the solution on a 64^3 , predict the spectra up to a wavenumber equal to the cut-off wavenumber on a 32^3 grid and likewise for different resolutions. We choose to tune the code to predict the energy spectrum instead of the KE correctly, because a correct prediction of the former ensures that of the latter, but not *vice versa*.

We start with $C_S = 0.12$ on a 32^3 grid. The results are compared with LES data from Meneveau et al. (1996) in figure 5.7, which appear to be quite similar, apart from the sudden dampening of energy beyond a wavenumber of $\kappa = 100$. Next, we use the same value of $C_S = 0.12$ (and other values

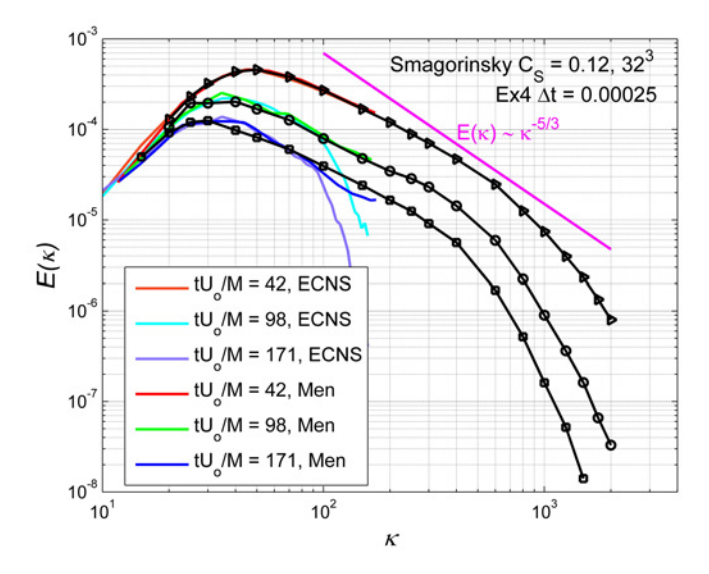


Figure 5.7: A comparison between the ECNS with the Smagorinsky model and $C_S = 0.12$ on a 32^3 grid and a pseudo-spectral code with the *Germano dynamic model* on a 32^3 (*Men* in the plot) from (Meneveau et al., 1996).

close to 0.12, for example, 0.11, 0.115, 0.125 and 0.13) to obtain the energy spectra on grids up to 96^3 . In either case, we ensure that the time integration introduces no numerical dissipation (see chapter 4).

Next, we set three limits \mathcal{A} , \mathcal{B} and \mathcal{C} , where \mathcal{A} is the energy spectrum for a 32^3 grid, \mathcal{B} on a 48^3 grid and \mathcal{C} for 64^3 . Figure 5.8 shows these three limits with grey lines. One notices that these limits are not equal to the cut-off wavenumber of the pertinent grid. This however, ensures that the *damped tail* noticed so far with the spectra obtained using the ECNS, is removed from the analysis, due to the reasons mentioned in section 5.5.2. The same also demands that the grid be finer than the wavenumber up to which we wish to predict the spectra correctly because the tail does span a sensible range of wavenumbers.

To estimate the error incurred while predicting, the part of the spectrum up to the cut-off wavenumber on a 48^3 grid or $\mathfrak B$ but with a 80^3 grid, we first integrate the spectra obtained with a the 80^3 grid till the corresponding grey line in figure 5.8. Then we calculate the difference in energy with respect to the experimental solution integrated till the same wavenumber. This is repeated for all logical combinations 14 and the errors are summarised in percentage within table 5.2 (see figure 5.8 to interpret results).

It is important to note that we calculate the error as the difference between the experimentally determined (from Comte-Bellot and Corrsin (1971)) and the simulated TKE, and not as the root-mean-square error of the differences observed in the spectra at different wavenumbers. This is because the simu-

¹⁴ An illogical combination would be trying to assess the prediction on C with a 48³ grid

			II	(%)				III	(%)		
C_S	N	32	48	64	80	96	32	48	64	80	96
	32	15	19	20	13.4	7.8	10.9	18.8	20.3	15.6	9.4
0.115	48		12.2	14.9	12.6	8.1		7.5	10	7.5	3.9
	64			10.8	10.1	6.5			3	1.1	1.1
	32	11.2	15.5	18.1	12.9	7.8	6.3	14.1	18.8	14	9.3
0.12	48		8.1	12.6	10.1	6.8		2.5	7.5	6.3	3.8
	64			7.1	7.7	4.8			О	О	2.2
	32	6.9	12.9	16.3	12	6.9	О	10.9	15.6	14.1	9.4
0.125	48		4.1	9.5	8.8	6.1		1.3	5	3.8	2.5
	64			3.6	5.4	3			3.3	2.2	3.3
	32	12.1	14.3	17.6	13	7.6	o	14.2	18.4	15.7	9.6
0.13	48		7.7	10.1	9.9	6.3		2.4	7.3	6.2	3.5
	64			6.8	7.9	4.6			3.3	2.6	3.5

Table 5.2: A summary of errors (reported in percentage) using the energy spectra obtained by CBC (Comte-Bellot and Corrsin, 1971).

lated spectra show two regions of marked deviations at smaller wavenumbers (indicated in figure 5.8 as R1 and R2), which as it appears, do not change with grid resolution and could lead to a constant offset in the calculated errors. Further, these region are also noticed in figure 5.7, when simulated with a pseudo-spectral code and the *Germano dynamic model* (indicated in the plot with Men).

In general, the errors are lower for Stage III than Stage II. With $C_S=0.12$ one notices a negligible error in predicting ${\mathfrak C}$ for Stage III, especially with finer grids. But in this case, the corresponding errors for Stage II are higher. On the other hand, $C_S=0.125$ leads to a better result for Stage II than Stage III. Increasing the C_S beyond 0.125 or reducing it to 0.115, leads to a higher error. Therefore, we may conclude that an optimal C_S belongs to the range [0.12, 0.125], with regards to the test case. Also, as hypothesised through equation 5.5, this range of values is quite independent of the grid resolution, possibly due the absence of numerical dissipation guaranteed by the ECNS approach (and the low time step).

Another point worth mentioning is the shape of the experimental spectrum at Stage II (see Ri in figure 5.8). One notices a sharply placed data point at a wavenumber of \sim 25 (indicated with a *cyan* line), as opposed to the smooth spectra at the other stages and the ones obtained through simulations. It is probable that it is the deviation of the simulated spectra from

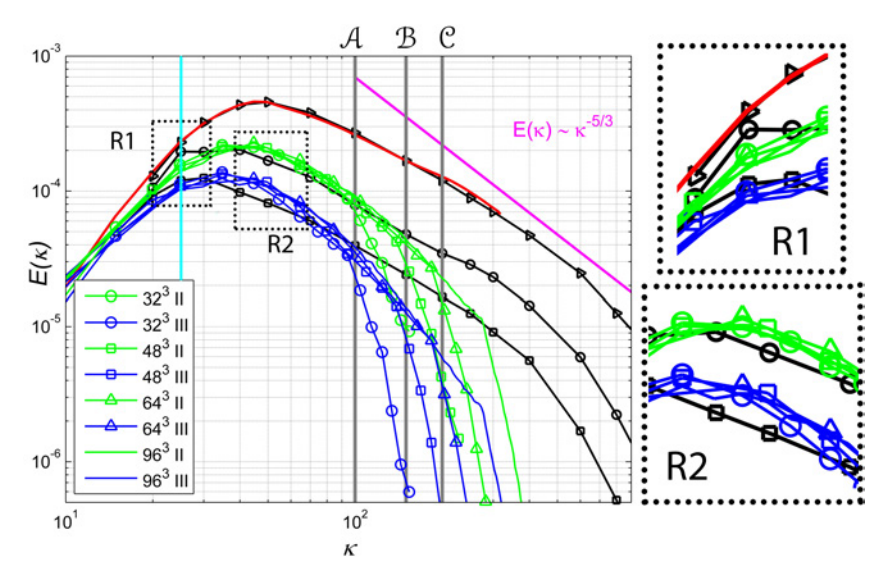


Figure 5.8: Changes in the energy spectra with grid resolution for ECNS and $C_S = 0.12$.

this data point that contributes to the error at Stage II, to a great extent given the energy content at that wavenumber.

In closing, on the one hand, we are able to propose a suitable value of C_S that allows finer grids to predict a fair regime of the large scales correctly with the ECNS. But on the other, we must not forget that the overall error, especially on the coarser grids, is a combination of the contributions from the diffusive and the SGS operators, which can only be studied separately and practically if the Reynolds number is high enough to neglect the diffusive operator; such as within the atmospheric boundary layer.

5.5.3.1 OpenFOAM and the influence of numerical dissipation

We repeat the procedure in section 5.5.3 with the OpenFOAM approach listed in table 5.1, and obtain a value of $C_S = 0.135$ on a 32^3 grid, as shown in figure 5.9. We ensured that time integration does not introduce numerical dissipation by using a very low time step 0.0001s.

Upon increasing the grid resolution, one notices that the OpenFOAM approach of a central difference scheme on a collocated grid behaves similar to the ECNS approach of an EC scheme on a staggered grid. One also obtains the *damped tail* that we noticed with the ECNS, indicating that it is inherent to a finite volume method using the Smagorinsky model. Further, the tail dampens above a certain wavenumber, below which, the scales (the large energy-containing ones) remain nearly unaffected with changes in grid resolution (see figure 5.9). Although on a 96³ grid we see some dampening of the large scales at Stage III, Stage II of the process remains nearly unaffected.

Additionally, we use OpenFOAM with the upwind schemes, QUICK and LU mentioned in section 5.3. As opposed to the OpenFOAM approach detailed in table 5.1, one replaces the central difference scheme with QUICK and LU.

The first observation is the strong effect of numerical dissipation leading to a damping of the spectra, as shown in figure 5.10. As the grid resolution in increased (only shown with QUICK), we observe a reduction in dissipation as the large scales move towards their experimentally established values. However, the spectra as whole does not recover its correct shape indicating incorrect decay rates at multiple wave numbers. Nonetheless, we see that the 3rd order formulation of QUICK introduces relatively lesser dissipation than its 2nd order counterpart, LU (compare *top-left* and *top-right* in figure 5.10).

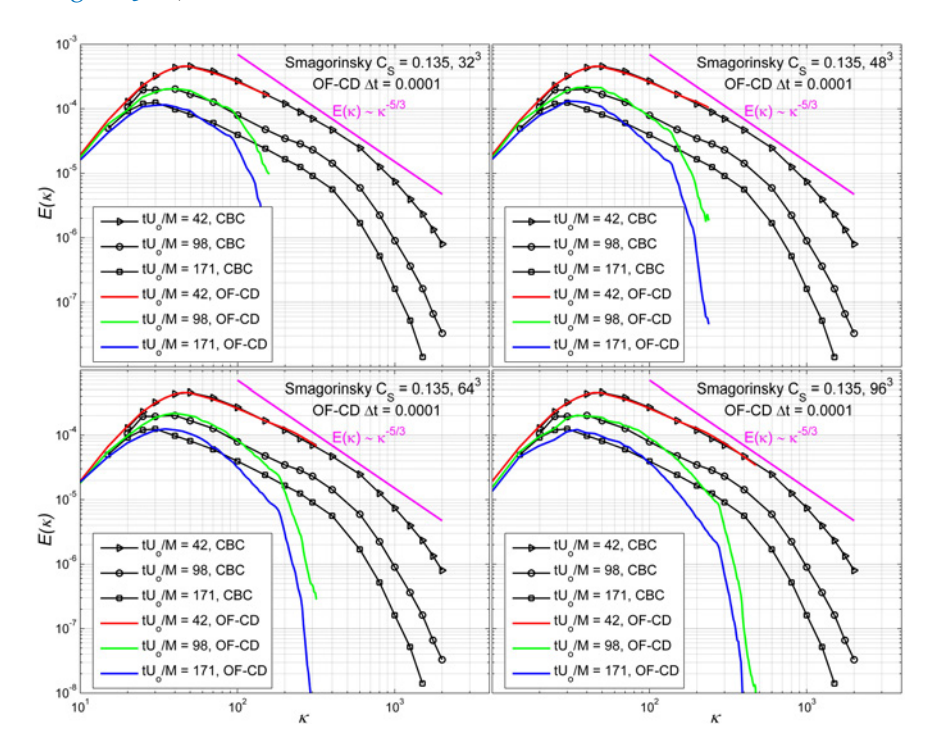


Figure 5.9: Spectra obtained with the OpenFOAM approach and $C_S = 0.135$ on 32^3 , 48^3 , 64^3 and 96^3 grids (*clockwise from top-left*).

In keeping with our hypothesis about an non-dissipative scheme (see equations 5.10 and 5.11) facilitating the tuning (see section 5.2), it seems that both the OpenFOAM and ECNS approaches, equally permit a simpler tuning of the Smagorinsky model. Next, we assess if these approaches predict a similar decay with another velocity field. We are motivated to compare these approaches because of the fact that the simple central difference scheme is used effectively in pseudo-spectral codes, as summarised in table 2.1. Resting on our observations so far, we could presume that EC

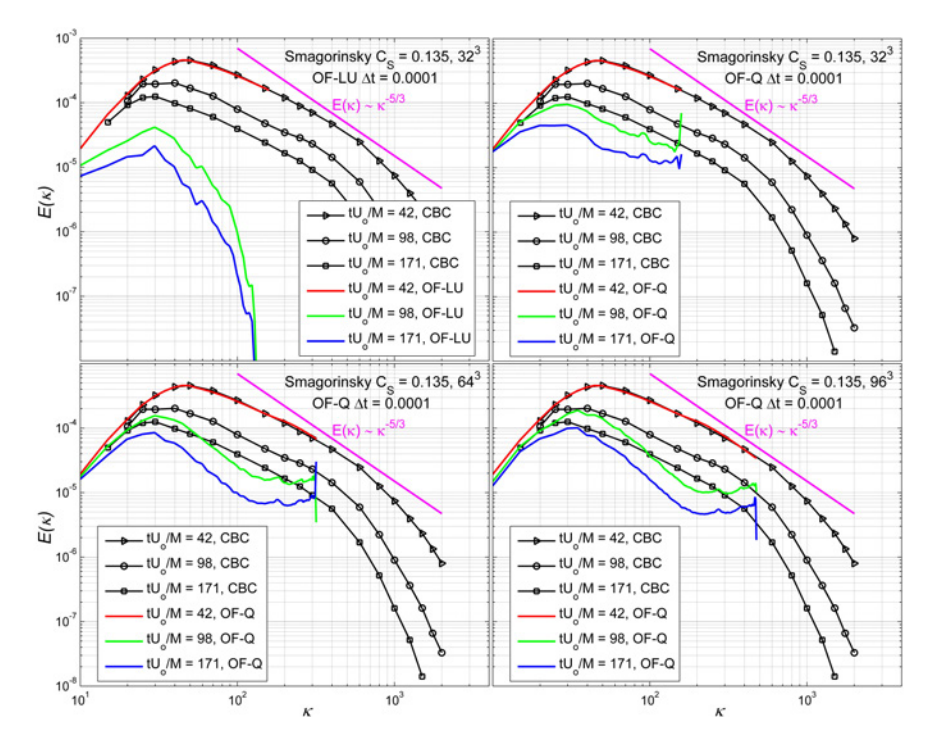


Figure 5.10: Spectra obtained on collocated grids with two different upwind schemes. *Top-Left:* LU on a 32³ grid. *Top-right* and *bottom:* QUICK on 32³, 64³ and 96³ grids.

scheme on staggered uniform grids and the central difference schemes on collocated uniform grids, may not be very different in practical applications (such as ABL and wind farm simulations, which normally rely on uniform grids).

5.6 CONCLUSION

As far as the first question, i.e. is a central difference discretisation of the convective term on a collocated grid, similar to an EC discretisation of the same order on a staggered grid, we can affirm that the two are similar. An EC scheme is formulated just like a central difference scheme but on staggered grids. On the other hand, the changes in KE with a simple central difference are negligible as compared to an upwind scheme, and can practically be ignored as being low enough to guarantee no major changes to the large scale structures of the flow. One may attribute the minor changes in KE to a segregated solver used with OpenFOAM, which could introduce a splitting error through intermediate velocity fields with non-zero divergence, as mentioned in section 3.4.2; or to another numerical artefact.

At the same time, it is important to note that the nearly similar behaviour of the ECNS and OpenFOAM approaches, is restricted to *uniform grids*. On

a non-uniform grid, the ECNS approach retains its dissipation-free behaviour, however, the simple central difference scheme on a collocated grid (OpenFOAM approach) is unable to do the same. Therefore, for applications necessitating local grid refinements, such as next to a wall boundary or for refining a region of interest, we advocate the use of an EC scheme on a staggered grid.

With regards to the second question on the advantage of the ECNS approach in practical applications, we observe that the OpenFOAM approach leads large scale behaviour that is similar to that obtained with the ECNS approach. We could not find any pronounced advantage of latter, which would make it more favourable for wind farm aerodynamics. Further, the *damped tail* in the energy spectra, noticed with either approach, can be attributed with confidence to the use of a finite volume method with the Smagorinsky model. This simple model does not account for changes in dissipation with scale, leading to excessive damping at smaller scales (as confirmed with two different codes).

We conclude that EC scheme on a staggered grid and the central difference scheme on a collocated grid could be similar in the simulation of high Reynolds number flows (on uniform grids), like those in the atmospheric boundary layer, which is the motivation behind developing the ECNS. Central difference schemes are commonly used with pseudo-spectral codes to permit the implementation of wall and outflow boundaries in the LES of wind farms; a practice that has hitherto delivered results (Mehta et al., 2014b).

As a suggestion, we still recommend a more comprehensive test case at a higher Reynolds number, which may bring to light a major difference between ECNS and OpenFOAM approaches. Further, we believe that an ECNS-finite volume approach could find its way into practical applications, as an alternative to pseudo-spectral methods. We will also assess the tuned Smagorinsky model in the ECNS, can also be used to simulate a boundary layer correctly, as done previously with a pseudo-spectral method by Meyers (2011).

Part III

THE TEST

This part comprises an *avant garde* study that compared various large eddy simulation codes and provided insight into the nature of the ECNS and its capabilities as a finite volume method for wind farm aerodynamics. Next, we simulate a neutral atmospheric boundary layer and assess if the large scale properties of a such a flow are correctly rendered by the code. For completeness, we simulate two simple wind farms, following a validation of the ECNS for an actuator disk and a neutral-ABL.

A COMPARATIVE STUDY OF LES CODES

This chapter stems from a collaborative effort between the Delft University of Technology, the Johns Hopkins University (JHU), the University of Leuven (LEU), the Technical University of Denmark (DTU) and the Energy research Centre of the Netherlands (ECN). It concerns Stereoscopic Particle Image Velocimetry (SPIV) measurements conducted in the wake of a model wind turbine and a perforated actuator disk in an open jet wind tunnel, at the Delft University of Technology (Lignarolo et al., 2014a). Later, this experiment was simulated with four different LES codes to perform a comparison (Lignarolo et al., 2015).

One may recall from chapter 2 that most LES studies of wind farms rely on modelling the wind turbines as actuator disks (AD) with or without flow rotation, as a trade-off between accuracy and computational effort. In their experiments, Lignarolo et al. (2014a) calibrated a perforated actuator disk to generate the same *axial thrust* as a model wind turbine that they choose for their regular experiment. SPIV provided insight into the near and the far wake of the actuator disk, with details on velocity, turbulence intensity and other higher order statistics. Should an LES code use an AD that is uniformly loaded with the force measured during the experiments, it must be able to replicate the wake of the model actuator disk.

Adapted from Lignarolo et al. (2015)

In this chapter, we adapt a part of the publication, Lignarolo et al. (2015). We compare the codes in terms of their numerical schemes, especially when relevant or similar to the ECNS 1 . Apart from the comparison, the aim of this chapter is to validate the ECNS using the value of C_S (0.125) obtained in chapter 5. For completeness, we had initially studied the effects of changing the Smagorinsky constant on wake velocity and turbulence; the results can be found in Appendix D. The value of 0.125 although obtained for a relatively low Reynolds number flow (decaying turbulence), it seemed to be appropriate for the case considered in this chapter.

6.1 THE EXPERIMENTAL SET-UP

Figure 6.1 shows the experimental set-up (the turbine is replaced with a perforated actuator) and the field of measurement, while table 6.1 summarises the test conditions. Each coloured patch in the figure indicates a field of view, which is the extent of the laser sheet used to perform the measurements. After the necessary measurements in every field of view, a carefully selected stitching algorithm is used to combine the data into one. Within

¹ Please note that ECNS is the code that belongs to ECN. To avoid confusion, the ECNS will be referred to as ECN in this chapter.

each field of view, 200 random samples are averaged to obtain the three components of velocity and its variance along the three directions.

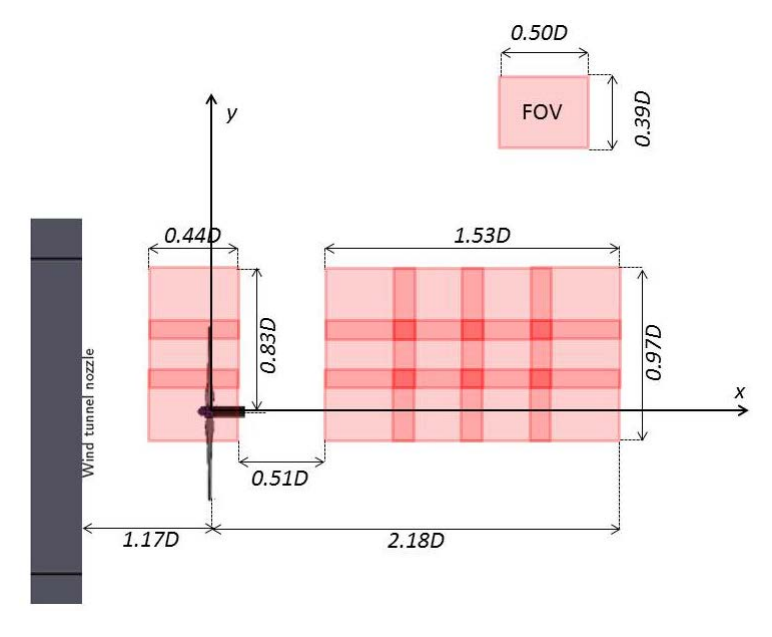


Figure 6.1: The experimental set-up (reproduced from Lignarolo et al. (2015)).

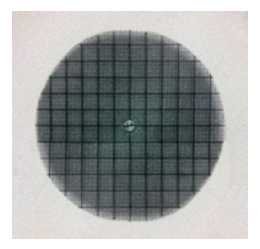


Figure 6.2: The perforated actuator disk used for the experiment (reproduced from Lignarolo et al. (2014b)).

The actuator model was created using three fine sheets of metal resulting in a porosity of 32% and an overall drag coefficient of $C_D = 0.93$ (see figure 6.2). This drag coefficient equals the thrust coefficient of the model wind turbine or C_T , that was operated at a tip speed ratio of 6.97.

6.2 ANALOGY

The parallel is that the LES codes must be able to replicate the experiment if they use the correct thrust coefficient for the actuator disk, simulate the

PARAMETER	SYMBOL	MAGNITUDE
Velocity	\mathfrak{u}_{∞}	4.7 ms ⁻¹
Turbulence intensity	σ_{∞}	0.5%
Density	ρ	$1.225~{ m kgm}^{-3}$
Molecular viscosity	μ	18.4 µPas
Disk diameter	D	0.6 m
Reynolds number	$Re_D = \frac{\rho u_\infty D}{\mu}$	188000

Table 6.1: Experimental conditions (Lignarolo et al., 2015).

inflow conditions as they were in the wind tunnel and use the experimental sampling rate to gather data from the simulations.

The codes involved in this comparative study are the JHU-LES, SP-Wind, EllipSys3D and ECNS. A comparison of their numerical schemes was previously discussed in chapter 2 but is provided again with their differences elaborated on. Table 6.2 summarises the grids used by the various codes. The normalised grid size is calculated using,

$$\Delta_{g} = \frac{\sqrt[3]{\prod_{i=1}^{3} \Delta_{i}}}{D} , \qquad (6.1)$$

where

- Δ_i grid size along the ith direction
- D diameter of the actuator disk model.

We list out the observations with the following codes and grids,

- The ECNS code of ECN 0.0659D,
- JHU-LES code of JHU 0.0259D,
- SP-Wind code of LEU 0.0405D and
- EllipSys3D code of DTU 0.0147D.

For simplicity, we will refer to a code by the acronym of the name of the organisation it belongs to. To begin with, we take a look at the salient features of the codes, which are listed in table 6.3. This information is important because most of the observations, can to a good extent, be explained in terms of the codes' numerical schemes and SGS models. All the codes use explicit non-EC time integration, however, report that their time step was conservatively low. Therefore, we shall not consider numerical dissipation through time integration while interpreting our observations. In addition to basic numerics, the codes also differ in how they generate *turbulent* inflow.

CODE	DOMAIN	POINTS	SIZE
	14D × 10D × 10D	98 × 70 × 70	0.1470
ECNS	$14D \times 5D \times 5D$		0.0926
	$14D \times 3D \times 3D$		0.0659
	24D \times 6D \times 6D	192 × 48 × 796	0.0992
		384 × 96 × 192	0.0496
		$512 \times 128 \times 256$	0.0372
JHU-LES		512 × 128 × 512	0.0295
		$768 \times 192 \times 384$	0.0248
		$768 \times 192 \times 768$	0.0197
		1024 × 256 × 1024	0.0148
SP-Wind	25D × 10D × 10D	72 × 64 × 128	0.1618
		144 \times 128 \times 256	0.0809
		$288 \times 256 \times 512$	0.0405
EllipSys3D	22D × 4.43D × 4.43D	384 × 192 × 192	0.0147

Table 6.2: Grids used (the column *Size*, represents the average grid size in *metres*).(Lignarolo et al., 2015).

JHU's code follows the precursor simulation approach they proposed in Stevens et al. (2013b) for wind farm simulations. ECN's code uses a similar approach by scaling the spectrum of isotropic-homogeneous turbulence reported by Kang et al. (2003) and using Rogallo's algorithm (Rogallo, 1981) to generate a divergence-free field, which is left to develop in a periodic domain while being transported at the mean flow velocity of 4.7 ms⁻¹. Once the initial field is sensitised to the solver, slices of the field are stored and later used as inflow for the *turbulent* test case. DTU's code generates the turbulence synthetically using the Mann model and imposes the fluctuations on the mean flow (Mann, 1994, 1998). LEU's code use a similar approach to synthesise a field with an integral length scale of disk's diameter and a turbulent intensity of 0.5.

In terms of numerical schemes, the pseudo-spectral codes have higher accuracy and typically negligible or zero numerical dissipation compared to finite volume methods (Canuto et al., 1988). LEU's code uses an EC scheme for the vertical discretisation that ensures negligible numerical dissipation in addition to the pseudo-spectral method. While, JHU's code uses a simple central difference schemes, the numerical dissipation through vertical discretisation can be assumed to be negligible given the high grid resolution it uses (see chapter 5).

CODE	SUBGRID SCALE MODEL	SPATIAL DISCRETISATION		
JHU	Scale Dependent	Horizontal: pseudo-spectral		
JIIO	Dynamic Smagorinsky	Vertical: 2 nd order		
		finite difference		
ECN	Smagorinsky	Finite volume		
ECIV	$C_S = 0.125$	2 nd order		
		energy-conserving		
	Smagorinsky	Horizontal: pseudo-spectral		
LEU	$C_{S} = 0.14$	Vertical: 4 th order		
		energy-conserving		
		finite difference		
DTU	Eddy-viscosity	Convective: Blended 3 rd order		
	model with	QUICK and 4 th order		
	vorticity as	central difference		
	field variable,	Others: 2 nd order		
	see Tenaud et al. (2005)	central difference		

Table 6.3: The codes at a glance (Lignarolo et al., 2015).

On the other hand, the two finite volume codes owned by ECN and DTU, differ in most aspects. Although DTU's code uses central schemes that are more dispersive than dissipative, the use of the quadratic upwind scheme for convective kinematics (QUICK) for stability through artificial or numerical dissipation, could lead to a premature decay of turbulence (Sanderse, 2013). Thus, as done in this case, the EllipSys3D is best used with very fine grids. In contrast, the ECN code uses EC schemes and does not incur numerical dissipation. Therefore, one can assume that the three codes from JHU, LEU and ECN, act with very little or no numerical dissipation (even through time integration as the time step is very low in either case) and their differences could be governed by the LES model². Amongst the codes from JHU and LEU, the former uses a more advanced LES model, the Scale Dependent Dynamic model that accounts for the variation of the Smagorinsky constant with scale and anisotropy. Therefore, given the similarity in their numerical schemes and accuracies, any difference between the codes from JHU and LEU could be attributed primarily to the different SGS models they use.

Table 6.3 shows that the length of the domain used with ECN's code is rather small as compared to that used by the others. To increase the grid resolution, the domain is reduced in size along the spanwise directions, while

² Errors through dispersion are not considered because we analyse mean velocity and turbulence statistics, instead of instantaneous flow structures

maintaining the same number of grid points. This is a favourable feature of a finite volume methods that permit an easy implementation of outflow boundaries within a domain. The effect of these boundaries in terms of the proximity to the disk in both the spanwise and streamwise directions was assessed to be negligible (the results are not shown here), allowing us to reduce the computational time significantly even with a higher grid resolution.

6.3 TESTS

In addition to $C_S = 0.125$, we also tested the ECN code with values of C_S equalling 0.10, 0.11, 0.12, 0.15 and 0.17. Values 0.10 and 0.15 were chosen from literature, whereas the remaining values were observed to help predict the decay of isotropic homogeneous turbulence with good accuracy (from chapter 4). For simplicity, we only present the results obtained with $C_S = 0.125$ in this thesis. Appendix D explains why this value was chosen based on an analysis of the effects of changing the C_S on the wake velocity and turbulence.

A grid convergence analysis was carried out for both $C_S = 0.125$ and $C_S = 0.17$ (in the original article Lignarolo et al. (2015)) using the domains listed in table 6.2. The domain spanning $14D \times 5D \times 5D$ with $98 \times 70 \times 70$ control volumes, has an average grid size of 0.0926m^3 . This places roughly 14 discrete volumes along the disc's diameter measuring 0.6m. The finest domain has nearly volumes 23 along the disc, whereas the coarsest one has only 7.

The tests were carried out with inflows that were both laminar and turbulent. We hypothesise that the ECN code with a tuned Smagorinsky model and the careful minimisation of numerical dissipation, should deliver a performance similar to that of LEU's code with accurate pseudo-spectral schemes with a Smagorinsky model tuned as defined in Meyers (2011).

We present the streamwise velocity after normalising it by the inflow velocity, u_{∞} , whereas we calculate the turbulence intensity using:

$$\sigma = \frac{1}{u_{\infty}} \sqrt{\frac{1}{3} \sum_{i=1}^{3} \overline{u'_{i} u'_{i}}}, \qquad (6.2)$$

where

 $\underline{\mathfrak{u}_{\infty}}$ inflow velocity,

 $\overline{u_i'u_i'}$ standard deviation in the component of velocity along the ith direction.

$$_{3}\ \overline{\Delta_{g}=\sqrt[3]{\prod\limits_{i=1}^{3}\Delta_{i}}}$$

The standard deviation is obtained using,

$$\frac{\overline{u_i'u_i'} = \sum_{n=1}^{N} [u_i(t_n) - \overline{u_i}]^2}{N} ,$$
(6.3)

where

N number of samples

 $\overline{\mathfrak{u}_{\mathfrak{i}}}$ average velocity in the \mathfrak{i}^{th} direction

t_n time at which the sample is collected.

The results are presented as radial profiles of flow variables; mean velocity and turbulence intensity in this case. In figure 6.3 for example, the *x-axis* represents the magnitude of the field variable and the *y-axis* represents the radial distance from the centreline of the actuator disk. The disk extends from $\frac{y}{D} = 0$ (centreline) to $\frac{y}{D} = 0.5$ (edge), where D is the diameter of the actuator disk. The shear layer spans $\frac{y}{D} = 0.4$ to $\frac{y}{D} = 0.7$, the region beyond which, will be called the outboard shear layer.

6.4 GRID CONVERGENCE

The comparative study also includes a convergence study. It appears from table 6.2 that only the codes from JHU, LEU and ECN could be analysed for their sensitivities to grid resolution, since they are the only ones that use a range of grids for their simulations. We noticed that there is no particular trend in the accuracy of predictions and downstream distance (as we shall see later in section 6.5). Therefore, we would use the data at 2.2D for comparison, which we believe is unbiased given that the three codes deliver accurate results after 1.8D (see figures 6.7 and 6.8, which will be discussed later).

Nearly (except one) all results provided by JHU use a continuous laminar inflow. While, the data from the codes used by ECN and LEU was obtained with a turbulent inflow.

With regards to velocity, the results obtained with the codes from ECN and LEU improve consistently with increasing grid resolution. The latter leads to an excellent result at maximum resolution (see figure 6.3). One must note that the meshes used with the ECN code are the coarsest amongst the three codes. In fact, the finest mesh used with the ECN code is nearly as coarse as the coarsest mesh used with the code from JHU; and comparable to the medium mesh used with LEU's code. Nevertheless, as regards to section 2.5.3, the grids used by the ECN code, are sufficiently resolved to predict the properties of the wake accurately.

Further, the codes from LEU and ECN demonstrate a steady rate of convergence to the experimental data. In contrast, the best prediction with

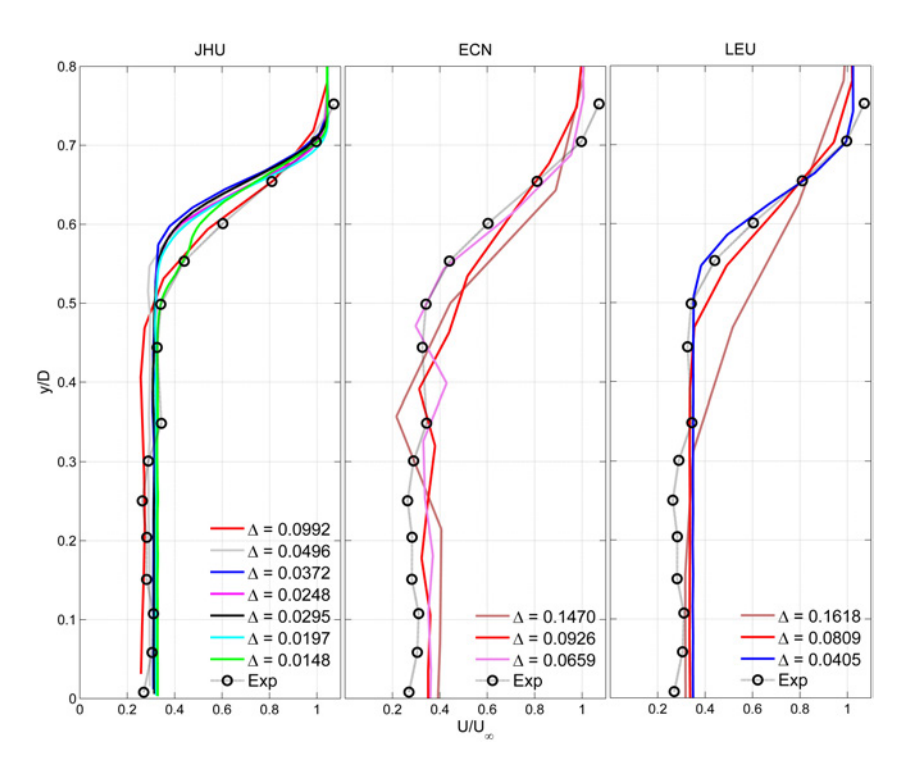


Figure 6.3: Profiles of mean velocity in the wake at different grid resolutions obtained with the codes from JHU, ECN and LEU. (adapted from Lignarolo et al. (2015)).

JHU's, is afforded by the coarsest mesh (0.0992m, see table 6.2))⁴, which is comparable to the medium meshes used by the other two codes. All the other meshes provide nearly similar results and as shown in figure 6.3, overestimate the velocity.

We would also like to draw attention to the velocity profile outside the shear layer where the incoming flow is undisturbed. In figure 6.3, one notices that around $\frac{y}{D}=0.8$, the velocity equals the freestream velocity. Readers are requested to note that the actual domain spans much beyond $\frac{y}{D}=0.8$ and the velocity profile in that region shows a speed-up to account for the reduced mass flow in the wake of the disk. We do not show this region for succinctness.

In terms of turbulence intensity, ECN's code does not show any growth in turbulence with grid resolution (see figure 6.4). This alludes to the purely dissipative nature of the Smagorinsky model that easily smothers any weak turbulence (recall that the inflow had a turbulence intensity of only 0.5%). Although LEU's code used the same model, it nevertheless shows a small

⁴ We are unable to offer an explanation for this.

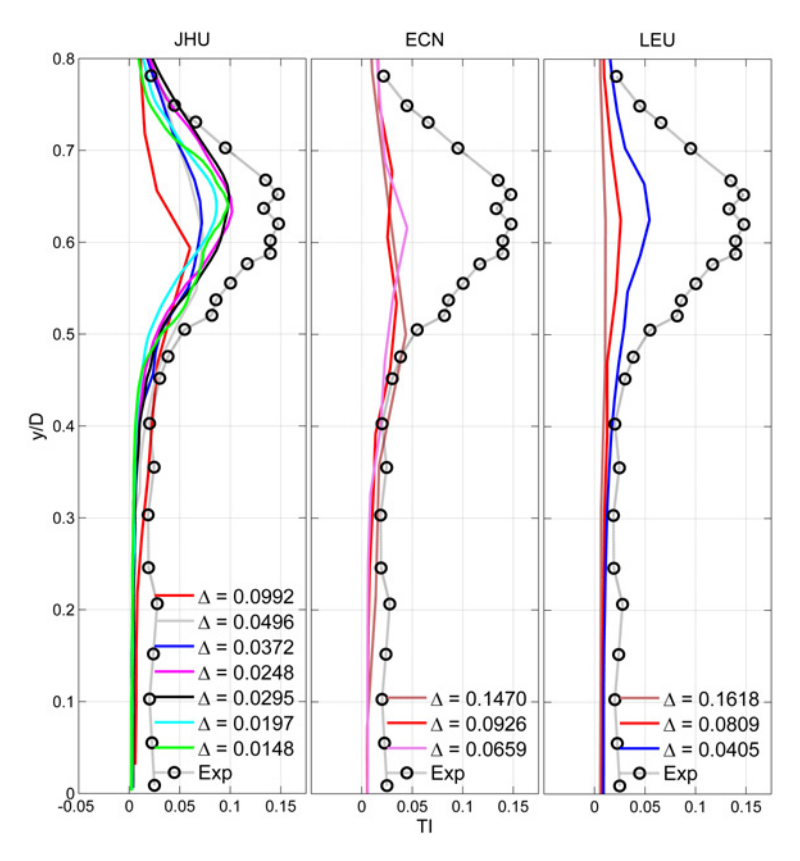


Figure 6.4: Profiles of turbulence intensity in the wake at different grid resolutions (adapted from Lignarolo et al. (2015)).

growth of turbulence on finer grids, possibly due to the pseudo-spectral method that is comparable to a very high-order finite volume method.

Akin to what was observed with the velocity field, JHU's code leads to a different observation with regards to turbulence intensity. On the coarsest mesh that lead to excellent predictions of the velocity field, one notices little growth of turbulence, although more in magnitude than predicted with the other two codes (see figure 6.4). As the grid resolution increases, the turbulence grows further and approaches quite close to the experimental value but only to an extent ($\Delta=0.0295$). Further increase in grid resolution leads to a reduction in peak value and a less accurate prediction (with $\Delta=0.0197$ and 0.0148). We are unable to offer an explanation regarding this irregular trend in the prediction of wake profiles with changes in grid resolution with JHU's code.

6.5 OBSERVATIONS

Next, compare the profiles of velocity and turbulence intensity behind the actuator model obtained with the LES codes against that from SPIV. For either code, we use the results obtained on the finest meshes. DTU's results were obtained on a single highly refined mesh, whereas those JHU did not display a regular trend with increasing grid resolution. Therefore, we choose the most accurate result from the latter for the comparison.

The results in this section are presented as radial profiles of velocity and turbulence intensity, at different locations downstream of the actuator disk (see figure 6.5 for example). For every downstream location, *x-axis* represents the magnitude of the field variable (velocity or turbulence intensity) and the *y-axis* represents the radial distance from the centreline of the actuator disk.

The disk extends from $\frac{y}{D} = 0$ (centreline) to $\frac{y}{D} = 0.5$ (edge), where D is the diameter of the actuator disk. The shear layer spans $\frac{y}{D} = 0.4$ to $\frac{y}{D} = 0.7$, the region beyond which, will be called the outboard shear layer.

6.5.1 With a laminar inflow

In terms of the velocity profiles, all codes predict the velocity correctly near the centreline and towards the outboard shear layer, as one sees in figure 6.5. However, ECN's code predicts a reduced velocity deficit inside the shear layer. This is observed clearly beyond a downstream distance of 0.7D. On the other hand, the codes from JHU and LEU underestimate the deficit in the shear layer with increasing downstream distance (deficit being the expected profile with velocities lower than the inflow).

In terms of turbulence intensity, it is noticed that using a laminar inflow leads to a delay in the build-up of turbulence (see figure 6.6). DTU's code generates a reasonable amount of turbulence that develops quickly with downstream distance, albeit with its peak value shifted towards the centreline with respect to the experimentally determined location of the peak. On the other hand, the codes from LEU and ECN do not show any growth of turbulence even as far as 2.2D. The turbulence profile in fact, does not evolve with downstream distance. While, JHU's code allows the turbulence to develop from a laminar inflow but does achieve the correct peak value in the shear layer; but the peak's location is correctly predicted (compare the locations of the peak turbulence intensity in figure 6.6 for the codes from JHU and DTU).

6.5.2 With a turbulent inflow

With a turbulent inflow, ECN's code delivers an improved velocity profile and wake width, especially after 1.8D (see figure 6.7). Additionally, the codes owned by DTU and LEU also show an improvement, with the lat-

ter being quite accurate after 1.8D. The observations with JHU's code remain unchanged, with agreeable predictions near the centreline and over predicted deficits in the shear layer.

With regards to turbulence intensity, the codes from ECN and LEU are yet unable to display a reasonable growth in turbulence, although the turbulence intensity increases slightly with a turbulent inflow (see figure 6.8). JHU's code is able to reach the correct predictions around 1.8D, whereas DTU's code shows a steady and steep growth in turbulence, leading to an eventual over-prediction. This over-prediction is also noticed in the region between $\frac{y}{D}=0$ and $\frac{y}{D}=0.5$, where the negligible turbulence intensity if overestimated.

6.6 CONCLUSIONS

Table 6.3 shows that the codes from JHU and LEU use pseudo-spectral schemes albeit with different SGS models, which is the major difference between the two. With pseudo-spectral schemes, one can expect the code to be free from numerical dissipation. Further, with either code, the time step was chosen rather conservatively to prevent dissipation through time integration. Therefore, at finer resolutions, we can expect the codes' behaviours to be dominated by SGS modelling. A direct proof is the grid convergence shown by LEU's code (see figures 6.3 and 6.4). However, due to the Smagorinsky model, LEU's code permits little growth of turbulence at coarse resolutions; this turbulence influences the recovery of the wake and hence, the velocity profile. The advanced Scale Dependent Dynamic model used with JHU's code serves as a fine example of the same. With increasing resolution, the predictions of turbulence intensity improve, whereas the velocity predictions do not show a constantly improving trend.

As mentioned earlier, the codes from ECN and LEU use non-dissipative schemes with the Smagorinsky model, with the only difference being their finite volume and pseudo-spectral formulations, respectively. The grid convergence studies and wake profiles, clearly hint at a comparable performance of the two codes. We surmise that ECN's code with a tuned Smagorinsky model, may serve as a finite volume based alternative to pseudo-spectral code used by LEU, with a tuned Smagorinsky model. At the same time, we are convinced that correctly predicting the velocity field and the turbulence intensity, could be a challenge with the simple Smagorinsky model, as our observations suggest. Both the codes predict the velocity field correctly but do not permit the growth of turbulence as a consequence of the Smagorinsky model. Nonetheless, we must acknowledge that the flow has little turbulence to begin with, 0.5%, and that the Smagorinsky model, being purely dissipative, is not able to predict laminar to turbulent transitions (see chapter 2).

Therefore, a single validation of the ECNS against the test-case described in this chapter will not amount to a comprehensive validation, as regards to wind farm aerodynamics. This is because the Reynolds number of the flow in this test-case does not represent the regime of high Reynolds number turbulent flows for which the fundamentals of LES are theoretically valid. Thus, in chapter 7, we check whether the ECNS with $C_S=0.125$ (and relevant modifications) is able to simulate a neutral-ABL correctly in terms of both the velocity and turbulence statistics, to comply with the requirements of a higher Reynolds number and to ensure more relevance to our aim of simulating wind farms.

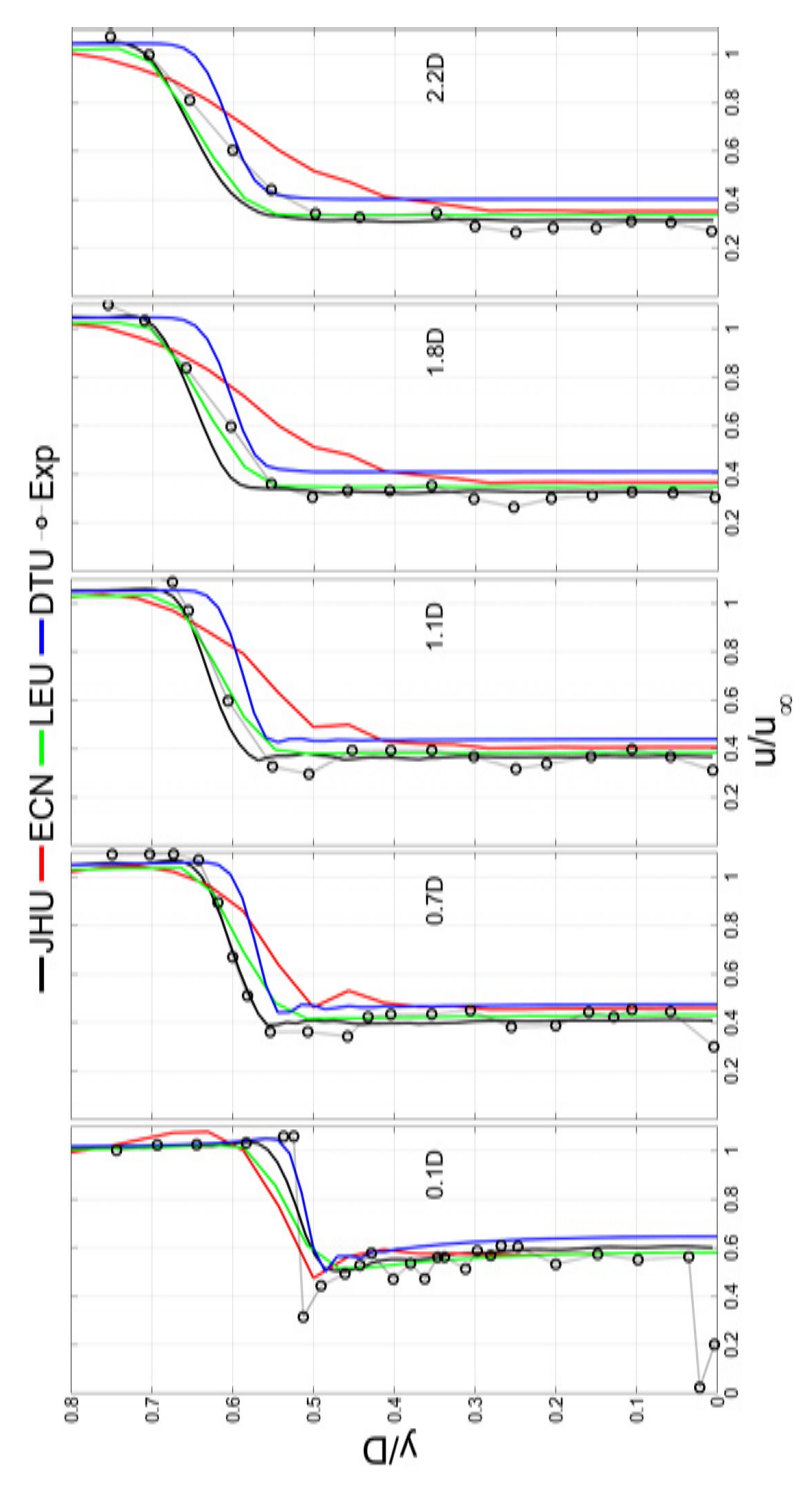


Figure 6.5: Profiles of velocity in the wake with an initially laminar inflow at five different locations downstream of the actuator disk (adapted from Lignarolo et al. (2015)). These locations are presented in terms of the actuator disk's diameter, D.

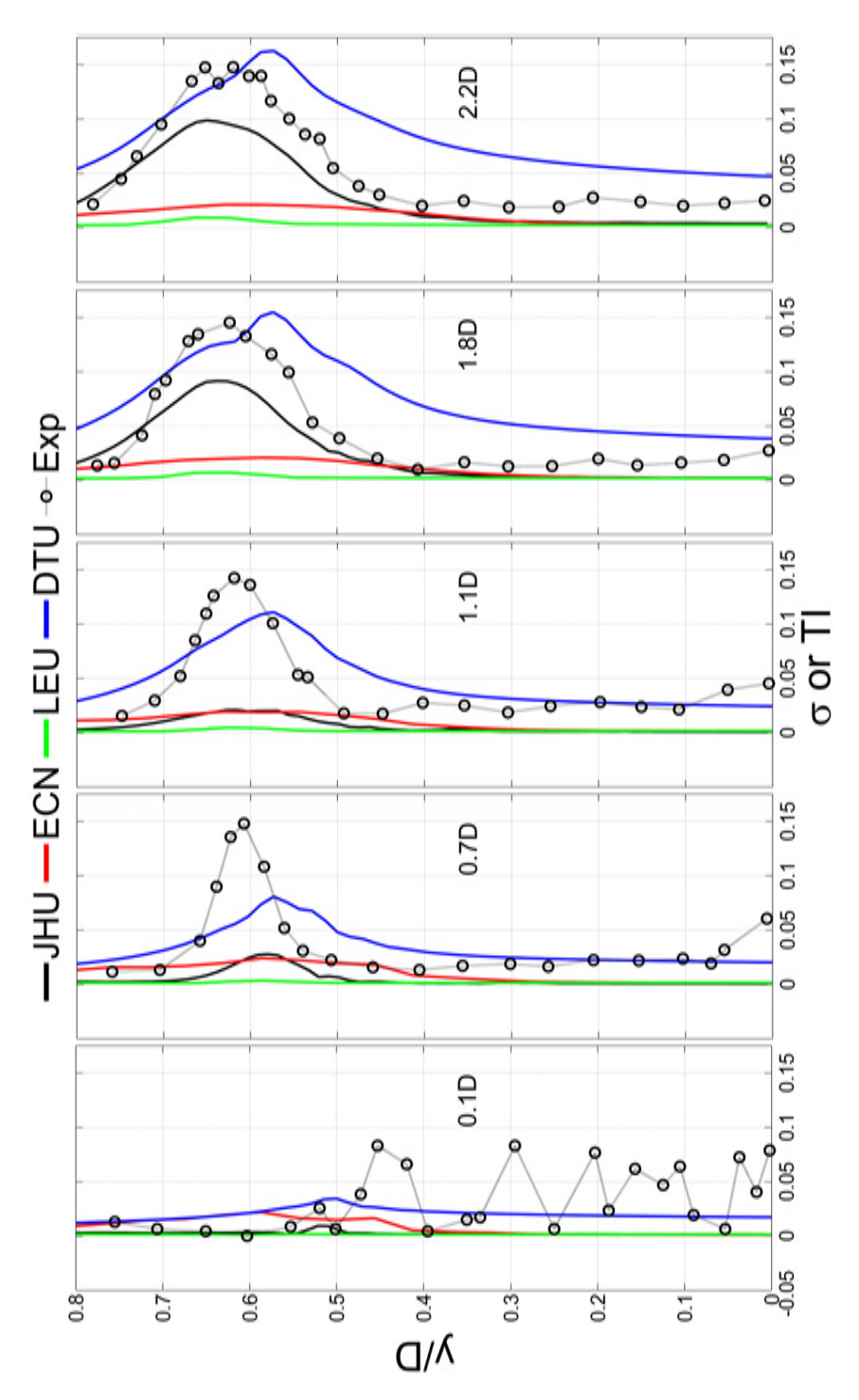


Figure 6.6: Profiles of turbulence intensity in the wake with an initially laminar inflow (adapted from Lignarolo et al. (2015)).

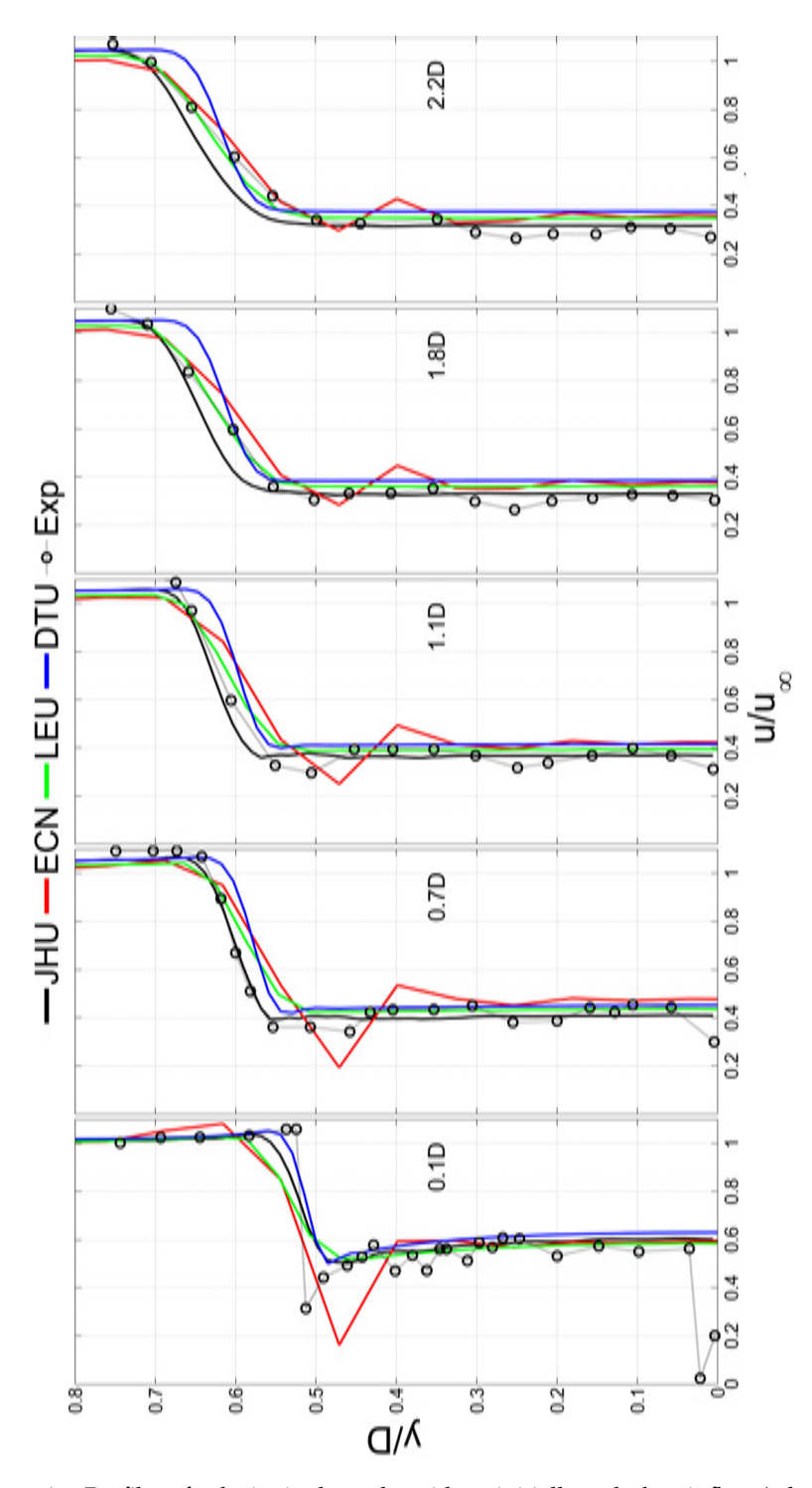


Figure 6.7: Profiles of velocity in the wake with an initially turbulent inflow (adapted from Lignarolo et al. (2015)).

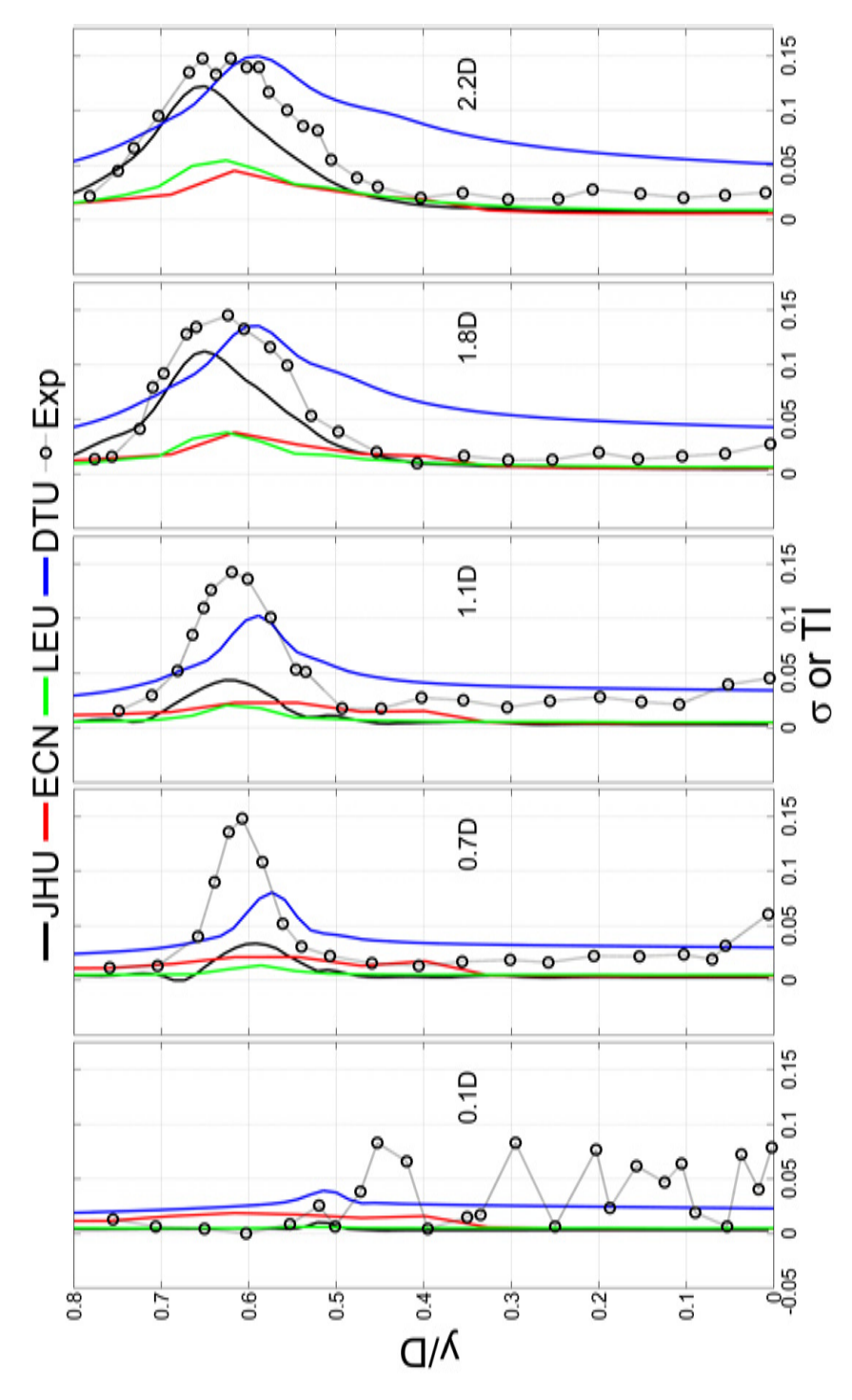


Figure 6.8: Profiles of turbulence intensity in the wake with an initially turbulent inflow (adapted from Lignarolo et al. (2015)).

7

WIND FARM AERODYNAMICS

Here we present an evaluation of the code's ability to simulate an ABL and its interaction with a wind farm, based on the conclusions we have made in the previous chapters. First, we modify the ECNS to simulate an ABL. Next, we simulate a small model wind farm for a qualitative insight, followed by a simulation of the turbines positioned at the ECN Wind Turbine Test Site Wieringermeer (EWTW).

Based on the tests described so far, we have an indication that the value of C_S for the ECNS lies between [0.1, 0.13]. Now, for tuning the ECNS to simulate an ABL correctly, we would have to account for the reduction of C_S near the ground in compliance with increased anisotropy. This has been explored in detail (see Porté-Agel et al. (2000)) and is known to be consequential to the proper prediction of velocity in the surface layer. If the value of C_S that is pertinent to unbounded atmospheric flow is not reduced, it may result in an increased streamwise velocity near the ground. To correct this, we will rely on the ad hoc wall damping function, proposed by (Mason, 1989). The value of C_S that we reported in chapter 5 is based on the decay of isotropic homogeneous turbulence. The same value may not hold for a more complex case like an ABL. A good reason is that the scales change their nature from being homogeneous and isotropic to ones that lose these properties with proximity to the ground. The scales close to the ground would be smaller in size as compared to the larger scales, and we know from our tests in chapter 5 that a finite volume method with the Smagorinsky model led to some dampening of these scales. Finally, the tests shown in appendix D, and done as an extension of chapter 6, demonstrated that changing the value of C_S affects both the velocity and turbulence profiles.

Images & content also appear in Mehta (2016)

Through our previous investigations we know that:

- Numerical dissipation through time integration can be reduced using the *Ex4* for time advancement and maintaining a *Courant* number such that the resulting numerical dissipation is significantly lower than the dissipation through molecular viscosity and the SGS model.
- A finite volume scheme that is dissipation-free ensures that the Smagorinsky model-Mason requires minimal or no tuning at all with changes in grid resolution.

This chapter is similar to the study conducted by Meyers (2011) to tune the SP-Wind code for ABL simulations. We only expect to see a difference between using a pseudo-spectral scheme and a finite volume EC scheme, possibly in the form of increased grid resolutions to achieve similar accuracy. The motivation lies in the results with SP-Wind reported in chapter 6

confirming its ability to predict average velocity fields with good accuracy even with the simple Smagorinsky model.

7.1 START-UP

We will begin by describing how we intend to simulate a neutral-ABl with the ECNS. Such a simulation comprises three parts as described below.

- An initial velocity profile with turbulent fluctuations to permit the growth of turbulence. This is important with models like the Smagorinsky model that generally do not permit the transition of an initially laminar flow into a turbulent one, due to the purely dissipative nature of the model.
- A function to imitate the presence of the ground. In LES, one is unable
 to use a no-slip condition when the first grid point does not lie within
 the viscous sub layer (Hultmark et al., 2013). One must instead rely on
 a function that imposes the relevant shear stress on the flow at the first
 grid point.
- A modification to the SGS model to modulate its behaviour near the ground. In the case of the Smagorinsky model, this could be an *ad hoc* function to reduce the Smagorinsky constant in the regions close to the ground.

The reason behind our choice of developing a neutral-ABL from a simple velocity profile with synthetic isotropic homogeneous fluctuations is to sensitise the turbulent field to the ECNS and to develop spatio-temporal correlations based on a statistically-converged neutral-ABL, which could be missing in a purely synthetic turbulent ABL. One can read the details in section 2.5.5.

Finally, the readers must note that in the tests described hereafter, the x and z-axes will always represent the streamwise and spanwise directions, respectively and the y-axis, the vertical (as shown in figure 2.7).

7.1.1 Velocity profile

A mathematical representation of the velocity in the planetary boundary layer that is commonplace, is the log wind profile (Panofsky and Dutton, 1984) or,

$$u(y) = \frac{u_{\star}}{\kappa} ln\left(\frac{y}{y_o}\right) + \psi_M , \qquad (7.1)$$

where

u component of velocity along the streamwise direction

y height above the ground

 \mathfrak{u}_{\star} friction velocity

к von Kármán constant

yo aerodynamic roughness length

 ψ_{M} stability correction.

For neutral-ABLs that concern us here, the stability correction is zero. The constant κ , is set to 0.4, as used in many similar studies (Lu and Porté-Agel, 2010; Meyers, 2011). The roughness length on the other hand, must be changed as per the terrain. It is the height at which the wind speed is theoretically zero and varies between 0.0001 m for open seas to 1 m or more for forests and cityscapes.

In a regular simulation, we use equation 7.1 and the velocity that we desire at the hub-height of the turbine to obtain the friction velocity. This will be used to calculate the relevant shear stress to be imposed as the boundary condition.

7.1.2 Wall stress

Using Monin-Obukhov's similarity theory (see Businger et al. (1971)), one relates the instantaneous wall shear stress to the average horizontal velocity at the first grid point as,

$$\tau_{iy} = -u_{\star}^{2} \frac{\widetilde{u_{i}}}{u_{\Delta_{1}}} , \qquad (7.2)$$

$$\tau_{iy} = -\left(\frac{\kappa}{\ln(\frac{y_{\Delta_1}}{y_0})}\right)^2 u_{\Delta_1} \widetilde{u_i} , \qquad (7.3)$$

where1

i direction x or z

 \mathfrak{u}_{Δ_1} average horizontal velocity at the first grid point

 $\widetilde{u_i}$ —instantaneous velocity in the i^{th} direction

 Δ_1 height of the first grid point.

Although the above formulation was introduced for averaged quantities, one uses it to calculate the instantaneous shear stress as well. This is simply because an equivalent theory for instantaneous flows does not exist. Further, the average horizontal velocity is defined by,

$$\mathfrak{u}_{\Delta_1} = \langle \sqrt{\widetilde{\mathfrak{u}^2} + \widetilde{\mathfrak{w}^2}} \rangle |_{\Delta_1} , \qquad (7.4)$$

¹ Recall the tilde represents the resolved velocity field in LES

where

u streamwise velocity

w spanwise velocity.

Bou-Zeid et al. (2005) addressed the consequences of using the instantaneous velocity field in using the above formulation based on the average velocity field. As opposed to equation 7.3, the *log-law* was validated to be used simply as,

$$\tau_{iy}^{log} = -\left(\frac{\kappa}{\ln(\frac{y_{\Delta_1}}{y_0})}\right)^2 \langle \widetilde{u} \rangle^2 . \tag{7.5}$$

The quantity $\langle \widetilde{u} \rangle^2$ is less than $\langle \widetilde{u}^2 \rangle$ because \widetilde{u} fluctuates between being negative and positive. As a result, one may often obtain the stress through equation 7.4 to be greater than its value dictated by equation 7.5. Simply put, a higher value of τ_{iy} would lead to a reduced value of velocity near the ground.

Resorting to averaging can help remove fluctuations that lead to an over predicted shear stress. This however, is not an option with non-homogeneous surfaces, for which, Bou-Zeid et al. (2005) suggested explicit filtering as a scale greater twice as big as the grid resolution (2Δ). Although the filtering proves quite effective, we will rely on averaging as we use a homogeneous surface. Further, explicit filtering with a finite volume method by transforming the velocity fields into *Fourier* modes requires a computational effort and mandatory accuracy, without which the conversion from physical to *Fourier* space and back, may lead to dampening of the small-scale fluctuations, as mentioned in section 4.3.2.

Therefore, despite the drawbacks pointed out by Bou-Zeid et al. (2005), we shall use equation 7.3 to model the wall stress.

7.1.3 Modulation of the Smagorinsky constant

Mason (1989) proposed the following *ad hoc* function to reduce the value of the Smagorinsky constant near walls in keeping with increased anisotropy and loss of scale invariance (Porté-Agel et al., 2000).

$$C_{S_{y}} = \left[C_{S_{o}}^{-n} + \left\{\kappa + \left(\frac{y}{\Delta} + \frac{y_{o}}{\Delta}\right)\right\}^{-n}\right]^{-\frac{1}{n}}, \tag{7.6}$$

where

PARAMETER	SYMBOL	MAGNITUDE
Height	L _y	1000 m
Length/Breadth	L_x, L_z	2π L _y m
Density	ρ	$1.225~{ m kgm}^{-3}$
Molecular viscosity	μ	18.1 µPas
Roughness length	yo	0.01 m
Friction velocity	\mathfrak{u}_{\star}	0.3561 ms ⁻¹
Grid points	$N_x \times N_y \times N_z$	$64 \times 64 \times 64$
		96 × 96 × 96
Grid resolution	Δ_{64}	53.2 m
	Δ_{96}	35.5 m

Table 7.1: The size and configurations of the domain used for ABL simulations.

y height above the ground

 C_{S_u} Smagorinsky constant at height y

C_{So} Smagorinsky constant for homogeneous isotropic turbulence

 Δ grid resolution

n an integer of choice.

Despite the facilitation the formulation offers in simulating wall-bounded flows with the Smagorinsky model, the above function led to excess dissipation near the ground (Porté-Agel et al., 2000). The only alternative to this is using the SDDM or the modulated gradient model (Lu and Porté-Agel, 2010), which have not yet been used in finite volume methods.

We understand that a faulty prediction near the ground, especially in the region between 10 to 40 metres, could influence predictions of power generation while simulating wind farms. Nevertheless, we choose a damping function because of its simple and tunable formulation but certainly recommend an alternative approach with the SDDM being used to obtain the values of the Smagorinsky constant near the ground, which could then be combined with the simple Smagorinsky model. Further, a comparative study of LES codes as done in chapter 6 but for an actuator disk within an ABL, could provide more insight into the above.

7.2 ATMOSPHERIC SIMULATIONS

To standardise our simulations, we use the domain often used by Porté-Agel et al. (2000) in the study of neutral-ABLs, the dimensions of which are listed in table 7.1. For all our simulations we use a time step, $\Delta t = 0.125s^2$. We

operate the ECNS till the flow statistics reach a quasi-steady state, i.e. they do not change as averages over a fixed period of time (10 minute averaged data in our case). This generally required simulating a few hours of real time, following which, flow quantities averaged over 10 minutes showed little change with time. To tune the ECNS, we use the values of C_S we found to be suitable through the tests in chapter 5, while using a value of 1 or 2 for n. We compare our results in terms of the average streamwise velocity profile and the energy spectra as a function of height. To complement our tests, we also used $C_S = 0.1$, n = 1 and $C_S = 0.15$, n = 1, which turned out to under and over dissipative near the walls, leading to a peaks or a sharp tail in the energy spectra. However, the average streamwise velocity was not strongly affected.

For clarity, we only discuss the most relevant results and use a *semi-logarithmic* plot for the velocity profiles. These results pertain to the combinations $C_S=0.125, n=1$ and $C_S=0.12, n=2$ that rendered the most accurate velocity profiles. Other combinations were tested but the results are not reported here for succinctness.

A 64^3 grid seems appropriate for tuning the Smagorinsky model-Mason system as Meyers (2011) used a $64 \times 48 \times 64$ uniform Cartesian grid. Nonetheless, we must also take in account our observations from chapter 4 regarding the dampening of higher wavenumbers, possibly due to a finite volume method with the Smagorinsky model. Therefore, we also use a 96^3 grid to corroborate the values of C_S and n that we obtain.

Figure 7.1 depicts how the velocity prediction improves with resolution, especially in the lower part of the boundary layer close to the ground, regardless of the tuning parameters. Outside of this region, above $y/L_y=0.1$, the tuning parameters do not affect the profile. On a 96^3 grid, the combination $C_S=0.125$, n=1, approximates the *log-law* closely till around 20m above the ground, followed by a under estimated velocity regime. On the other hand, the combination $C_S=0.120$, n=2, under estimates the velocity below $y/L_y=0.1$. Although increasing the grid resolution improves the prediction with both $C_S=0.120$, n=2 and $C_S=0.125$, n=1, the latter renders a more accurate average velocity profile.

A slight dependence on the grid resolution can be expected at this stage as the pseudo-spectral code used by Meyers (2011) is more accurate than the ECNS for a given grid resolution, in terms of the discretisation errors. Therefore, one can expect a weaker dependence of the Smagorinsky model-Mason system on grid resolution with the SP-Wind than with the ECNS.

Next, we take a look at the spectra at various heights in the ABLs. One expects the spectra to segregate into two regimes. The first with a slope of nearly -1 in the region near the ground and the second with a slope of -5/3, located away from the ground, as noticed by various studies (see

² To ensure the absence of numerical dissipation we consider a maximum *Courant* number of 0.01, which is conservative as per our observations in chapter 4

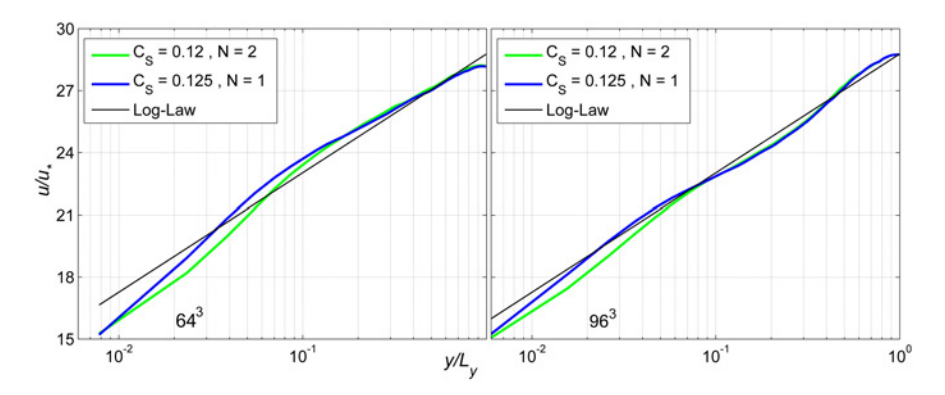


Figure 7.1: The average streamwise velocity with height for different grids and combinations of the Smagorinsky-Mason model. The *y-axis* is the ratio of the streamwise velocity to the friction velocity, u_* and *x-axis* is the ratio of the height and the height of the domain, L_u .

Porté-Agel et al. (2000) and references therein). Figure 7.2 shows that around 400m above the ground, the spectra collapse onto the standard -5/3 slope for isotropic homogeneous turbulence, more or less, independently of the tuning parameters.

But it is the region below 400m that we are interested in. Here, we anticipate the inertial range to exhibit a slope of -1. Notwithstanding, we also notice the sharp dampening of the spectra at higher wavenumbers that we noticed earlier in chapter 4, which we attributed to the finite volume approach used in the ECNS. Therefore, in this case too, we will only observe how the spectra up to this *sharp tail* responds to changes in C_S and n.

One notices in figure 7.2, that the spectra near the ground do not depend much on the combination of the C_S and $\mathfrak n.$ In fact, they collapse well onto the -1 slope, apart from the sharp dampening at higher wavenumbers, which we also noticed in chapter 4. Thus, with nearly similar spectra for either combination, $C_S = 0.12$, $\mathfrak n = 2$ and $C_S = 0.125$, $\mathfrak n = 1$, we choose the latter as it renders a more accurate velocity profile.

It is important to mention that Meyers (2011), did not observe the *damped tails* while finding an appropriate tuning combination with the KUL code, SP-Wind. This is probably due to the relatively accurate pseudo-spectral method they use (as compared to the ECNS). Further, they did not observe any strong under prediction in the velocity profile near the ground, as reported by (Porté-Agel et al., 2000), which Meyers (2011) attributed to a possibly high value of $C_S = 0.17$, n = 1 used by Porté-Agel et al. (2000). Instead, the optimal combination of $C_S = 0.14$ and n = 1 chosen by Meyers (2011), resulted in an agreeable velocity profile.

Therefore, we expect that the ECNS tuned with correct values of C_S and n can indeed be used for wind farm simulations. We are unable to explain whether the under prediction in the velocity near the ground is a

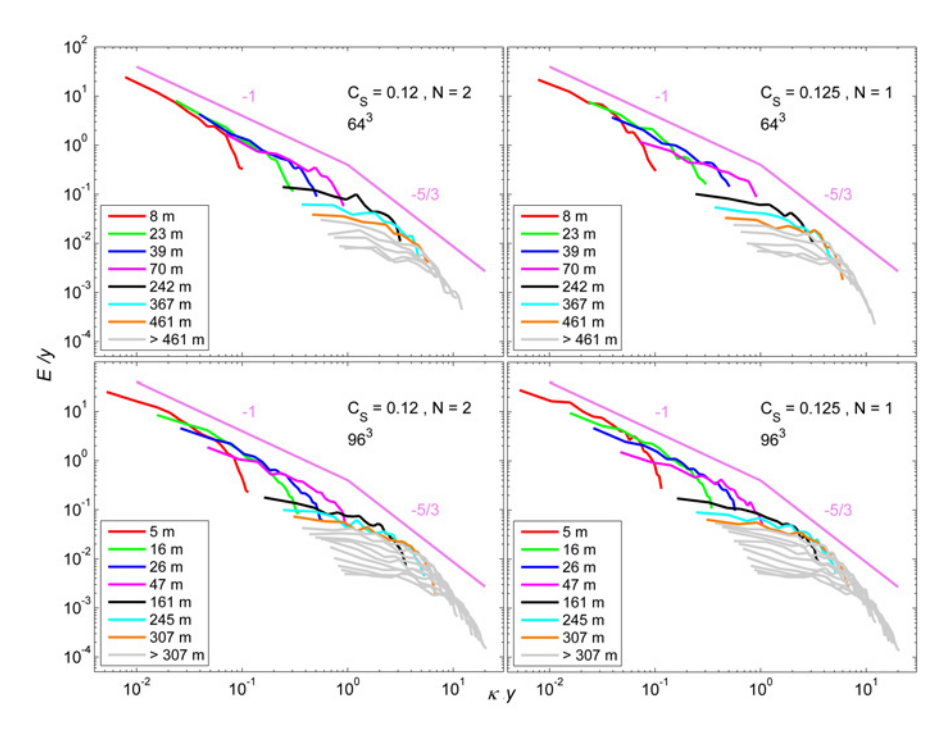


Figure 7.2: The energy spectra with height on 64^3 (top) and 96^3 (bottom), for $C_S = 0.12$, N = 2 (left) and $C_S = 0.125$, N = 1 (right).

consequence of the loss in energy due to the *damped tails* resulting from a finite volume approach with the Smagorinsky model, the use of the Monin-Obukhov theory in an instantaneous sense and without explicit filtering (proposed by Bou-Zeid et al. (2005) to reduce this under prediction) or a combination of the two.

7.3 SIMULATION OF A SIMPLE WIND FARM

The ECNS includes an immersed interface method to implement a simple actuator disk within a *Cartesian* grid (Sanderse, 2013). We use the approach detailed in Meyers and Meneveau (2010) to impart a tangential force to the flow in addition to the axial force through an actuator disk or an actuator disk with rotation. LES studies have shown that the latter could be a reasonable alternative to the actuator line approach for wind farm simulations (Wu and Porté-Agel, 2011).

The parameters that govern the turbines' operations, namely, the thrust coefficient, tip speed ratio, axial induction etc., are borrowed from Meyers and Meneveau (2010). Unlike the formulation for a stand alone turbine, one must now use the local velocity field averaged at the actuator disk to obtain the force it imparts to the flow. Further, the thrust and power coefficients

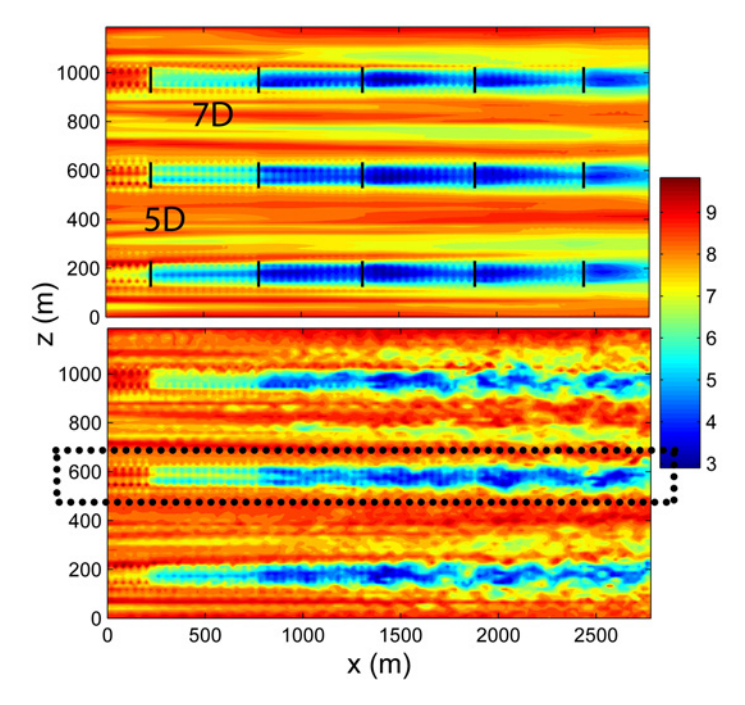


Figure 7.3: Contours of time-averaged (above) and instantaneous (below) streamwise velocity in a plane through the centres of the turbines' rotors and parallel to the ground, at y = 80 m. x is the streamwise direction (separation 7D) and z is the spanwise direction (separation 5D).

pertinent to a single turbine (C_T and C_P) must be modified using the local velocity field ($C_{T'}$ and $C_{P'}$, for turbines on a wind farm. Table 7.2 summaries these parameters.

We simulate a farm within a domain spanning $2800m \times 1000m \times 1200m$ and discretised into $140 \times 96 \times 90$ finite volumes along the, streamwise direction, the vertical and the span wise direction, respectively. Fifteen turbines are introduced into the domain, each with a rotor spanning 80m (D) and mounted 80m above the ground. The turbines are separated by 7D in the streamwise direction and 5D in the span wise direction, and are placed as shown in figure 7.3.

An ABL inflow is generated using the approach mentioned in section 7.2, with the parameters shown in table 7.1. This should lead to a *log-law* profile with a velocity of around 8ms⁻¹ at a height of 80m (using equation 7.1). The simulations are run for long enough to establish a quasi-steady state, following which time-averaged statistics on the velocity and turbulence are collected³. We present the profiles of streamwise velocity and turbulence

³ For most cases in this chapter, the spin-up time is about 8 hours (simulated time) after which the relevant time-averaged statistics (10 minutes) are collected. We obtained statistical convergence.

PARAMETER	SYMBOL	MAGNITUDE
Thrust coefficient	C_{T}	0.75
Modified C _T	$C_{T'}$	$\frac{4}{3}$
Power coefficient	C_{P}	0.34
Modified C _P	$C_{P'}$	0.8
Axial induction	α	0.25

Table 7.2: The turbine parameters used for the simulation of a simple wind farm (borrowed from Meyers and Meneveau (2010)).

intensity at 2D, 4D and 6D behind every turbine⁴. The profiles at 1D before the first turbine (T1 in the plots) serve as a reference (*log-law* inflow).

One notices how the first two turbines introduce a large velocity deficit in their wakes (see figure 7.4). However, this deficit reduces slightly beyond the third turbine. Concomitant to this phenomenon, is the increase in turbulence behind the first two turbines, reaching a near constant trend in the profiles behind the remaining turbines, as shown in figure 7.5. This turbulence causes the wakes of T4 and T5 to recover faster than that of T3 through increased mixing that draws energy from the faster freestream into the wake; as confirmed through various LES studies (see chapter 2). The recovery is clearly seen through the time-averaged contours in figure 7.3. Figure 7.7 shows isosurfaces of *Q-criterion* coloured by streamwise velocity, in the wake of the turbines.

7.4 SIMULATION OF THE EWTW

The test site at Wieringermeer comprises five turbines with 80m rotors mounted at 80m above the ground and separated from each other by 305m or 3.8125D (Bot, 2015). Each turbine has a rated capacity of 2.5MW. We shall follow the approach in section 7.3 to simulate the farm in an aligned condition (shown in figure 7.6, exposed to an ABL with a wind velocity of 8ms⁻¹ at hub height. For the same, we will use $u_{\star} = 0.4787 \text{ms}^{-1}$ and $y_o = 0.1 \text{m}$ to obtain the relevant *log-law* profile (using equation 7.1). At the given velocity at hub height, the thrust coefficient, C_T of the turbine is 0.789.

The computational domain with the turbine spans $2440m \times 750m \times 1650m$, discretised into $106 \times 150 \times 105$ finite volumes. As opposed to the previous case, the grid resolution along the vertical is much higher and so are the number of points on the turbines. After generating the inflow and feeding it concomitantly into this domain, we gather statistics on velocity that are also compared with the predictions made by *FarmFlow*, ECN's engineering

⁴ Except for the last turbine, for which we only have the profiles up to 4D due to the size of the domain

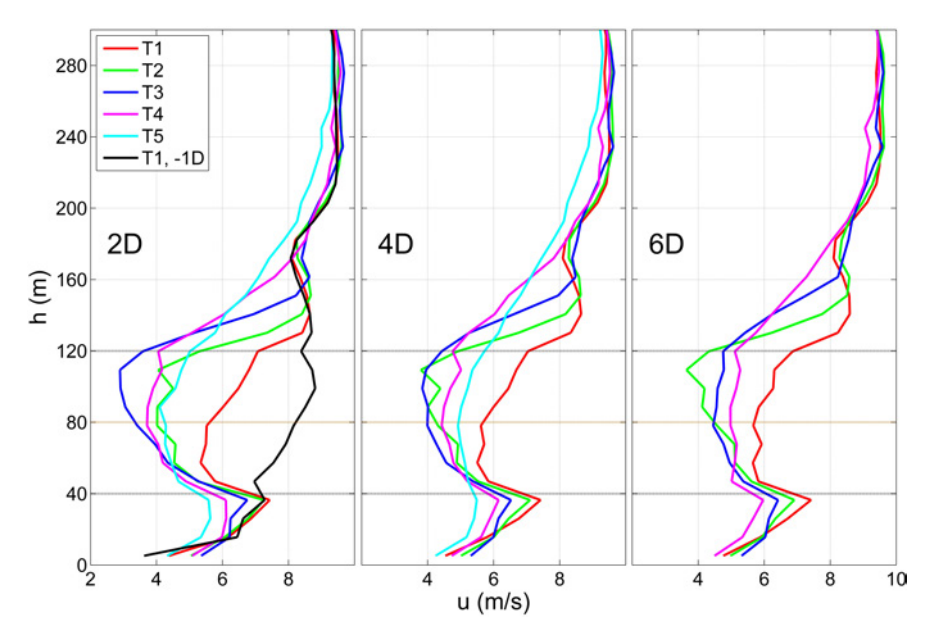


Figure 7.4: Streamwise velocity u, at three downstream locations, 2D, 4D and 6D, where D=80m; for the five turbines (see highlighted row in figure 7.3), as a function of height, h. To serve as reference, the inflow profile at 1D before the first turbine, T1 (or -1D) is also shown.

model (Bot, 2015). For completeness, we also present data on turbulence intensity.

Figure 7.8 shows the variation in streamwise velocity with height, in the wake of the five turbines at EWTW, obtained by both the ECNS and Farm-Flow (dashed lines). The profiles of velocity have been plotted at five locations between one turbine and the next. Similar to what was noticed in section 7.3, the velocity deficit recovers faster for downstream turbines, concomitant with the increase in turbulence intensity, which brings about mixing between the slower wake and the faster free stream flow in the ABL, as predicted by the ECNS (the turbulence intensity is shown in figure 7.9).

On the other hand, FarmFlow predicts a much quicker recovery of the wake. For all the turbines (except for T5 for which FarmFlow data is not available), the wakes recover to velocity profile that is the same for the three turbines downstream of the first one (T1), within a small distance of 3D. As mentioned earlier in chapter 2, parabolic models such as the one used in FarmFlow, tend to predict the velocity deficit correctly in the near wake. However, we do not have any relevant experimental data on the velocity profiles to confirm this. All experimental aerodynamic data at the EWTW is collected at a single point at hub-height, with a mast that is not aligned with the turbines and hence, is exposed only to the uninterrupted ABL flow.

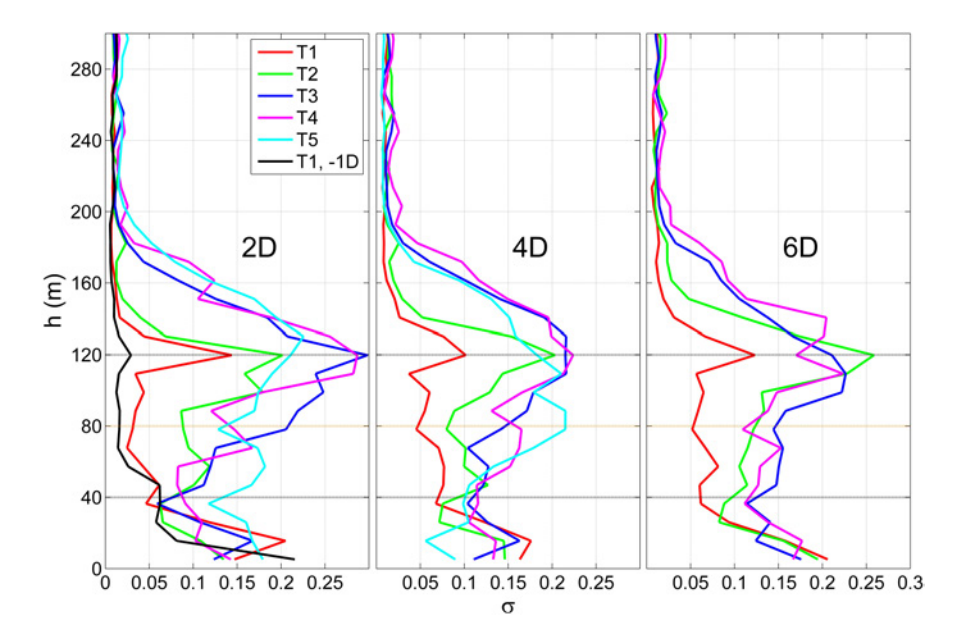


Figure 7.5: Streamwise turbulence intensity σ , at three downstream locations, 2D, 4D and 6D, where D = 80m; for the five turbines (see highlighted row in figure 7.3), as a function of height, h. To serve as reference, the inflow profile at 1D before the first turbine, T1 (or -1D) is also shown.

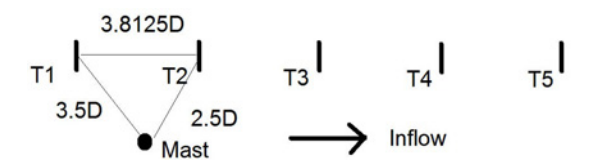


Figure 7.6: The locations of the five turbines at the EWTW (T1 to T5) and of the meteorological mast.

7.5 CONCLUSION

We observe that upon using the *ad hoc* Mason function to modulate the Smagorinsky constant near a wall boundary, we are able to use the simple Smagorinsky model to simulate the flow within an ABL. Based on the velocity profile and the turbulence spectra at various heights in the ABL, we propose two possible combinations for the ECNS, $C_S = 0.125$, N = 1 and $C_S = 0.12$, N = 2, of which, the former seems to be more appropriate. Nonetheless, we are unable to explain why either combination leads to a marked under prediction in the velocity near the ground. This could be a consequence of the loss in energy due to the *damped tails* resulting from the combination of a finite volume approach and the Smagorinsky model (as

noticed in previous chapters), the use of the Monin-Obukhov theory in an instantaneous sense and without explicit filtering (proposed by Bou-Zeid et al. (2005) to reduce this under prediction) or a combination of either of these sources.

An analysis of a model wind farm reveals that the ECNS-Smagorinsky approach is capable of resolving the basic trends in wake velocity and turbulence observed at wind farms. The turbulence is shown to develop and reach a nearly steady value, after two wake-turbine interactions. This also causes a quicker and similar recovery of the wakes of downstream turbines, through turbulence. Due to lack of computational resources, we are unable to validate this for a real wind farm, or a larger model wind farm with more turbines.

We also perform a comparison between an engineering model and the ECNS-Smagorinsky approach for a set of turbines separated by a small distance (4D). ECNS predicts a trend similar to what was observed for the model wind farm but the engineering model predicts a quicker recovery of the wake. Although it has been established that parabolic engineering models (such as the one used here) are accurate in the near wake, we are unable to compare the ECNS and the engineering model comprehensively, due to limitations on experimental data.

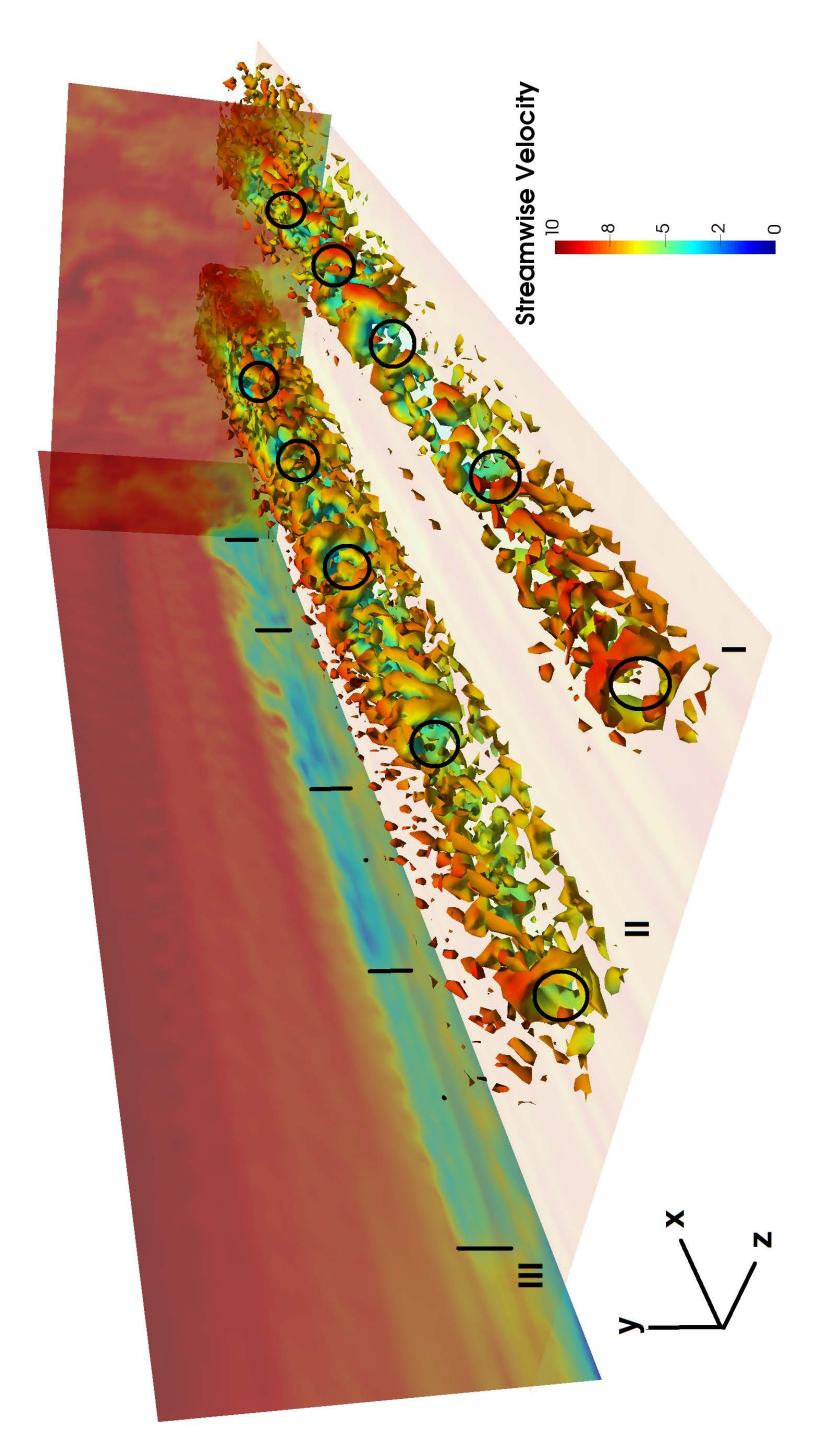


Figure 7.7: Isosurfaces of *Q-criterion* coloured by streamwise velocity in the wake of turbines shown in figure 7.3. For one of the rows (III), the contours of streamwise velocity have been shown in a place passing through the centre of the turbines and normal to *z-axis*.

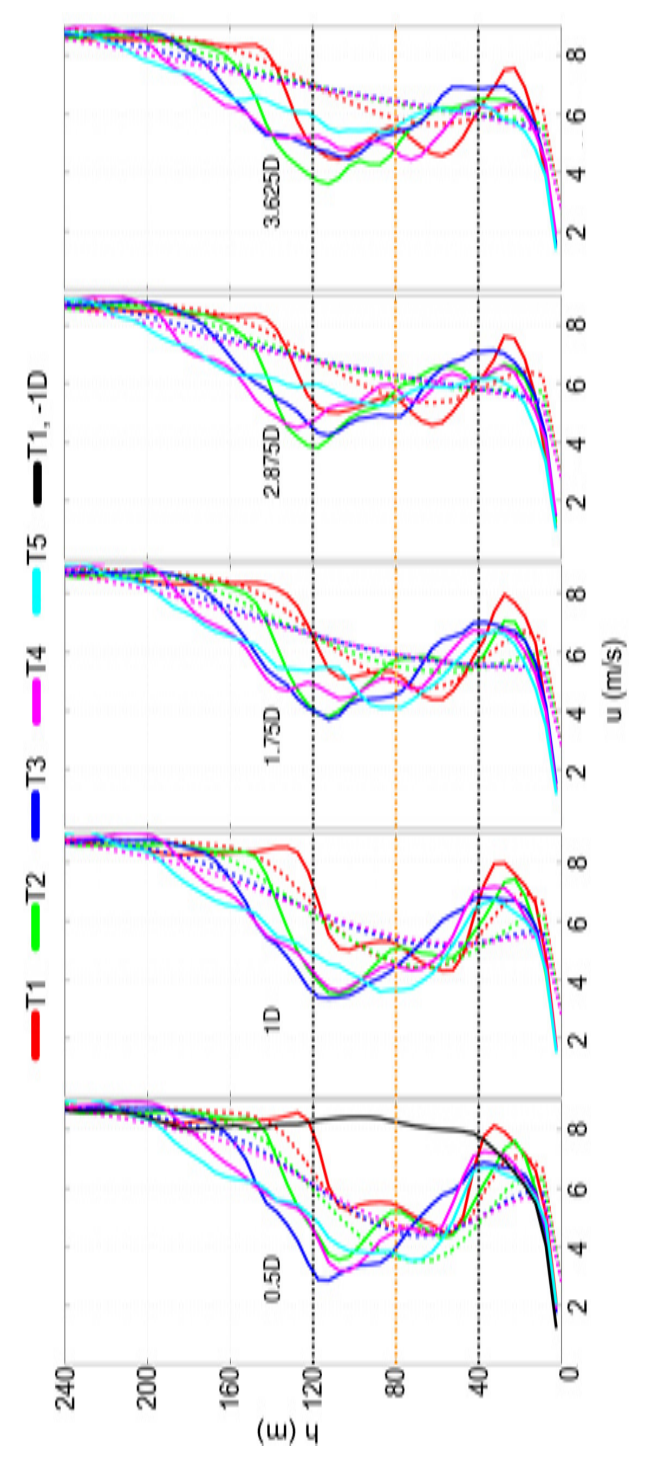


Figure 7.8: Streamwise velocity u, at five downstream locations as a function of height, in the wake of the turbines at EWTW. The dashed lines represent the results obtained with FarmFlow (expect T5).

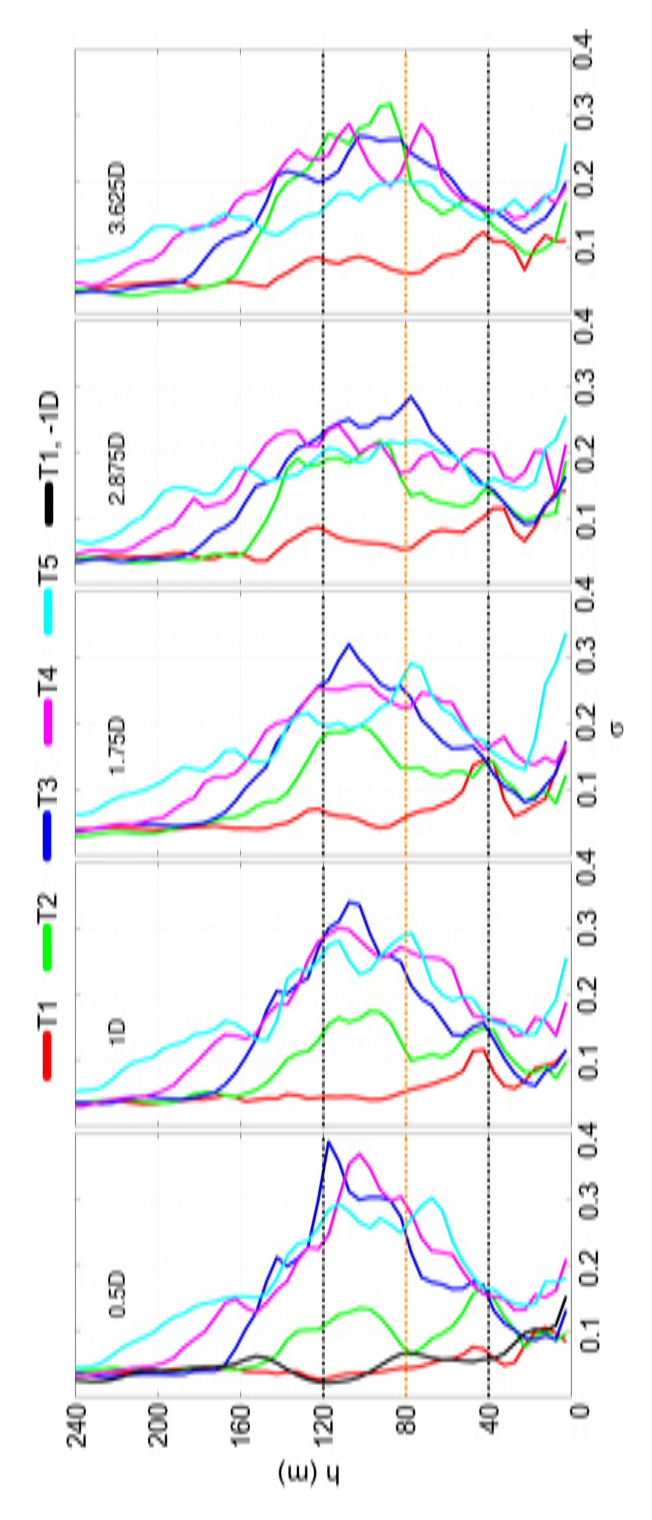


Figure 7.9: Streamwise turbulence intensity σ , at five downstream locations as a function of height, in the wake of the turbines at EWTW.

Those who cannot renounce attachment to the fruits of their labour, are far from the path to enlightenment

Bhagavad Gita, 6-2

As regards to the large eddy simulation with energy-conserving schemes, we obtain the following conclusions, which hold only in the case of incompressible flows and strictly, in the study of wind farm aerodynamics. We present these conclusions as answers to the questions mentioned in section 2.7, which we shall also quote here.

- The first question concerns the advantages and practicality of *energy-conserving implicit time integration* schemes.
 - In general, a non energy-conserving explicit time integration scheme, when used in combination with a small *Courant* number¹, is sufficient to minimise numerical dissipation to a magnitude significantly lower than the subgrid scale dissipation. Although this is true for an explicit method of any order, a higher-order method is more suitable due to its higher efficiency.
 - An energy conserving implicit time integration scheme removes the restrictions on *Courant* number and increases the accuracy as compared to a non energy-conserving explicit method of the same order, for a given time step. This however, comes at the cost of computational time, which increases due to complexity of the system of equations used for time advancement. Further, the gain in accuracy is disproportionate to the extra computational effort, making explicit time integration the favourable option.
 - With regards to industrial LES, apart from accuracy, the computational time is also of consequence (and the practical consideration of using existing codes or developing new ones). Therefore, we advise an explicit method with a suitable time step.
- The second questions concerns the similarities and differences between central difference and energy-conserving spatial discretisation schemes, which mathematically have a non-dissipative formulation.
 - As long as the grids are uniform, a central difference on a collocated grid and an energy-conserving scheme on a staggered

¹ Chapter 4 recommends a Courant number below 0.15 with Ex4.

- grid, are essentially the same, in formulation and function. On non-uniform grids however, only an energy-conserving scheme on a staggered grid can guarantee the absence of numerical dissipation, due to a difference in interpolation of the velocities and fluxes based on arithmetic means instead of linear interpolation.
- Notwithstanding, uniform grids remain the norm for wind farm simulations dealing with large scale phenomena on wind farms and hence, central difference schemes could be used.
- The third question concerns the tuning of the Smagorinsky model and how the tuning is made less sensitive to changes in grid resolution by the absence of numerical dissipation.
 - Tuning while ensuring the absence of numerical dissipation, enables the simple Smagorinsky model to accurately render the most energetic scales of a flow, over a range of grid sizes capable of resolving those scales.
 - An energy-conserving scheme² with a finite volume method enables the above, similar to a pseudo-spectral scheme.
 - When the Smagorinsky model is used with a general finite volume approach, scales comparable to the grid size suffer from excessive dissipation, despite predictions of the most energetic scales being similar to those rendered by pseudo-spectral schemes.
- Finally, the question regarding the performance of a tuned Smagorinsky model with a dissipation-free numerical scheme, in practical applications.
 - For an actuator disk: A tuned Smagorinsky model produces acceptable profiles of mean velocity. Turbulence intensity on the other hand, is generally under predicted, possibly due to the simplicity of the Smagorinsky model in not accounting for scale-dependent behaviour of turbulence. This however, is a conclusion from studies only in the near wake of the actuator disc and for an inflow with little (0.5%) turbulence, wherein the range of turbulent scales is not wide enough and scale-dependent behaviour is more significant. Therefore, this conclusion should be verified against a test case relevant to wind farms (a higher ambient turbulence, a sheared inflow and a detailed analysis of both, the near and the far wake), with a higher Reynolds number and a wider range of scales. It is likely that when the ambient turbulence is high and that the large scales are distinctly resolvable, the Smagorinsky model may deliver a better performance in terms of turbulence statistics.

² Also a central difference scheme but on a uniform grid

- For a neutral atmospheric boundary layer: As noticed earlier, an accurate velocity profile can be obtained by controlling the dissipation through the Smagorinsky model. However, the turbulence spectra show dampening near the higher wavenumbers.
- For a wind farm: Qualitative trends in the evolution of wake velocity and turbulence were shown by the ECNS code³. A comparison with data from an engineering model revealed that the ECNS predicts a higher deficit in the near wake. However, due to the lack of experimental data, we are unable to state which method is more accurate.

³ Staggered Cartesian grid with an energy-conserving spatial discretisation

As per the conclusions, we recommend the following:

- Energy-conserving implicit time integration schemes are accurate but computationally demanding. The procedure involved in solving the system of equations is iterative and demands a very low tolerance. However, the computational time can be reduced by increasing the tolerance and not iterating till the system is perfectly solved. Although this will lead to a *non-EC* implicit scheme, the incurred error could be as low as that incurred by the non-EC *explicit* schemes that we recommend. We chose to solve the system perfectly as we intended to study EC schemes in detail, for which we needed a perfect solution. As a recommendation, one could study the effects of using a perfectly EC implicit scheme but with a small error in its iterative process, which will not reduce it accuracy by a big margin or hamper its stability, but save a lot of computational effort.
- Should the above be possible, the schemes can be used for applications other than wind farm aerodynamics that involve local grid refinement (near wall boundaries, for instance), unstructured grids etc.
- For wind farm aerodynamics, future studies could rely on central difference schemes on collocated grids for averting numerical dissipation (as long as the common uniform grids are used). Such schemes are readily available in open-source codes like OpenFOAM and can be a fine alternative to the development of newer schemes and codes.

Additionally, we advocate research involving the following for the development of large eddy simulation for industrial wind farm aerodynamics.

- As an alternative to the Mason ad hoc damping function, one could use
 the values of the Smagorinsky constant reported by the comprehensive
 scale dependent dynamic model near a wall boundary, to modulate the
 constant used with the simple Smagorinsky model.
- A comparative study of subgrid models and numerical schemes with clearly defined grid, time and turbulence parameters can help ascertain the effects of numerical schemes and turbulence models on the overall accuracy of a computational approach.

To conserve, or not to conserve . . .

This thesis concerns the use of large eddy simulation for wind farm aerodynamics. The aim is to suggest an approach that the industry could use to predict quickly and accurately the interaction between wind turbines and the atmospheric boundary layer and, by extension, the power generated by the wind farms. Further, this approach should be able to generate accurate aerodynamic data that could be used to tune engineering models more appropriately.

Central to this thesis are energy-conserving schemes, which guarantee the absence of numerical dissipation and ensure stability at any grid resolution and time step. Our primary objective is to use these schemes to simulate turbulent flows using large eddy simulation and in doing so, evaluate how numerical dissipation could affect the overall accuracy.

Our research questions concern the accuracy and efficiency of EC time integration schemes; the similarity and differences between an EC and central difference spatial discretisation; and the tuning of the Smagorinsky model in the absence of numerical dissipation.

EC schemes should guarantee the absence of numerical dissipation that spuriously contributes to the withdrawal of energy, which in large eddy simulation is ideally the task of molecular viscosity and the subgrid scale model. A review of existing literature suggests that the Smagorinsky model could be a fine choice to start with because of its simple formulation and ease of implementation. On the contrary, literature specific to the large of eddy simulation of wind farm aerodynamics, suggests the use of more comprehensive models for higher accuracy. The pertinent conclusions raise concerns over the purely dissipative nature of the Smagorinsky model and its inability to function correctly in regions of anisotropy, such as in the wake of a turbine (actuator disk) or near wall boundaries. Further, literature on wind farm aerodynamics alludes to a preference for pseudo-spectral spatial discretisation over finite volume methods for accuracy and the absence of numerical dissipation. However, in either case, the time integration is generally done with non energy-conserving explicit time integration schemes. These explicit time schemes were challenged in terms of accuracy and stability, which led to the proposal of energy-conserving implicit time integration schemes.

Despite all the concerns over the accuracy and appropriateness of the Smagorinsky model, some studies report acceptable results with necessary modifications to the Smagorinsky model, non-dissipative finite volume schemes (central difference schemes) and with explicit methods for time integration,

as regards to simulating the atmospheric boundary layer. To know more about which schemes are most relevant to industrial wind farm aerodynamics, we carry out a series of tests on both ideal and practical turbulent flows. The former are used to assess how minimising numerical dissipation using an EC scheme makes the tuning of the Smagorinsky model less sensitive to changes in grid resolution. Whereas, tests concerning practical applications help validate the combination of energy-conserving schemes and the tuned Smagorinsky model for large eddy simulation.

We conducted controlled tests with isotropic homogeneous turbulence, which reveal that numerical dissipation through both time integration and spatial discretisation can spuriously contribute to the decay of energy. An energy-conserving implicit time integration scheme guarantees stability, even at large time steps but requires more computational effort than a non energyconserving explicit scheme of the same order. This increase in computational time is such that a non energy-conserving scheme with a smaller time step, is sufficient to minimise numerical dissipation and becomes practically more workable. Further, reducing the time step with an energy conserving implicit time integration scheme does not alter the computational time proportionately. For instance, reducing the time step by half increases the computational time by a factor of two (nearly) with a non energy-conserving explicit time scheme. But the same with an energy-conserving implicit scheme leads to a computational time much higher than twice because the system of equations being solved iteratively, must be solved more accurately with smaller time steps.

In terms of spatial discretisation, the absence of numerical dissipation is important for accuracy. On uniform grids, which are commonplace in the large eddy simulation of wind farms, a simple central difference scheme is as accurate as an energy-conserving spatial scheme. Both schemes enable the tuning of the Smagorinsky model independent of the grid resolution, as long as the grids accommodate the relevant energetic scales. This tuning, when attempted with a scheme that introduces numerical dissipation (through time integration or spatial discretisation, or both), is hard to realise.

These simple tests help conclude that an energy-conserving spatial scheme (could be replaced with a central difference scheme on a uniform grid), combined with a non energy-conserving time integration and an appropriately tuned Smagorinsky model, may be used for practical applications. A comparison against other large eddy simulation codes, with comparable or superior numerical schemes, in terms of simulating a model actuator disk, reveals that our approach is accurate. The combination of the absence of numerical dissipation and a tuned Smagorinsky model, delivers accurate velocity profiles in the wake, however, the turbulence statistics are not up to the mark. Notwithstanding, it is important to note that these conclusions were obtained from analyses in the near wake for an inflow with very little turbulence. A more germane validation would involve far wake analyses with a reasonably turbulent inflow.

Next, the tuned Smagorinsky model is combined with a simple *ad hoc* damping model, to modulate its dissipation near wall boundaries. For the high *Reynolds* number flow with an atmospheric boundary layer, we obtain a good velocity profile, contrary to the known dissipative nature of the Smagorinsky model and in keeping with the tuned model-dissipation free approach used previously with a pseudo-spectral code. A simulation of a cluster of actuator disks within the boundary layer, produces agreeable results. We notice basic qualitative trends in wake velocity and turbulence being correctly rendered with our approach.

Te behouden, of niet te behouden . . .

Dit proefschrift betreft het gebruik van large eddy simulation¹ voor windmolenpark aerodynamica. Het doel is een werkwijze voor te stellen, die gebruikt kan worden door de industrie om de interactie tussen windturbines en de atmosferische grenslaag snel en nauwkeurig te voorspellen en daaruit volgend de energie die wordt opgewekt door het windpark te voorspellen. Daarnaast zou deze aanpak ook geschikt moeten zijn om nauwkeurige aerodynamische gegevens genereren waarmee *engineering modellen* af te stemmen.

Centraal in dit proefschift staat een groep van numerieke methodes, de zogenaamde energiebehoudende schema's. Deze schema's garanderen de afwezigheid van numerieke dissipatie² en verzekeren stabiliteit ongeacht de resolutie van het rekenrooster en tijdstap. Het primaire doel is het gebruik van deze schema's voor de simulatie van turbulente stromingen met behulp van een large eddy simulatie en daarbij te evalueren hoe numerieke dissipatie de algehele nauwkeurigheid beïnvloedt.

De onderzoeksvragen betreffen de nauwkeurigheid en efficië ntie van energiebehoudende tijdsintegratie; de overeenkomsten tussen een energiebehoudende en een centrale ruimtelijke discretisatie; en de kalibratie van het Smagorinsky model in de afwezigheid van numerieke dissipatie.

Een energiebehoudend schema zou de afwezigheid van numerieke dissipatie moeten garanderen, die een foutieve onttrekking van de energie veroorzaakt. In het kader van large eddy simulation is deze onttrekking bij uitstek de taak van het subgrid scale model en moleculaire viscositeit. Een overzicht van de literatuur suggereert dat het Smagorinsky model een prima eerste keuze is vanwege zijn eenvoudige formulering en gemak van implementatie. Daarentegen adviseert de academische literatuur die specifiek gaat over large eddy simulatie van windparken het gebruik van uitgebreidere modellen voor hogere nauwkeurigheid. Met name het zuiver energie-onttrekkende gedrag van het Smagorinsky model en het onvermogen om anisotropie in de turbulentie mee te nemen, zoals dat optreedt in het zog van een windturbine (actuator disk) of in de buurt van wanden³, zijn aanleiding tot zorg. Bovendien suggereert de literatuur over windmolenpark aerodynamica dat er een voorkeur is voor pseudo-spectrale methoden boven eindige volume methoden gezien hun nauwkeurigheid en afwezigheid van

¹ De simulatie van de grote wervelingen in een turbulent stroming.

² De reductie van energie door numerieke fouten.

³ Noodzakelijk voor het simuleren van de grond.

numerieke dissipatie. Hoewel, de eindige volume methode met een energiebehoudende ruimtelijke discretisatie al eerder werd voorgesteld als alternatief, is deze methode slechts geverifieerd voor laminaire stromingen. Niettemin, zijn beide methodes alleen gebruikt in combinatie met een nietenergiebehoudende, expliciete tijdsintegratie. Hiervan werden de nauwkeurigheid en stabiliteit in twijfel getrokken wat leidde tot het voorstel om gebruik te maken van de energiebehoudende impliciete tijdsintegratie schema's.

Ondanks de vragen omtrent de nauwkeurigheid en toepasbaarheid van het Smagorinsky model, zijn er studies die acceptabele resultaten rapporteren voor de simulatie van een atmosferische grenslaag, gebruik makend van een aangepast Smagorinsky model, dissipatieloze eindige volume discretisatie (centraal-differentie schema) en expliciete tijdsintegratie. On te achterhalen welke schema's het relevantst zijn voor industriële windpark aërodynamica, worden numerieke experimenten gedaan op academische en praktische turbulente stromingen. De academische problemen worden gebruikt om in te schatten in hoeverre vermindering van numerieke dissipatie met een energiebehoudend schema ervoor zorgt dat de kalibratie van het Smagorinsky model in een large eddy simulatie minder afhankelijk wordt van rooster fijnheid. De praktische problemen dienen vooral ter validatie van een large eddy simulatie met de combinatie van een energie behoudend schema en het Smagorinsky model.

Gecontroleerde testen aan een stroming met isentrope, homegene turbulentie laten zien dat numerieke dissipatie door zowel tijdsintegratie als ruimtelijke discretisatie de afname van energie op een foutieve manier kan beïnvloeden. Een impliciete, energiebehoudende tijdsintegratie garandeert stabiliteit, zelfs voor grote tijdstappen, maar is ook reken intensiever dan een expliciete tijdsintegratie van dezelfde orde die geen energiebehoud heeft. De grotere rekentijd die dit met zich mee brengt is dusdanig dat de nietenergiebehoudende methode praktischer toepasbaar is, zelfs met een kleinere tijdstap die de numerieke dissipatie voldoende verminderd. Daarbij komt ook nog dat de rekentijd van de energiegehoudende, impliciete tijdsintegratie niet proportioneel toeneemt als de tijdstap wordt verkleind. Bijvoorbeeld, als de tijdstap wordt gehalveerd, leidt dit tot een (bij benadering) verdubbeling van rekentijd bij een expliciet, niet-energiebehoudend schema, maar tot een veel meer dan verdubbeling van rekentijd bij een energiebehoudend, impliciet schema. Dit komt met name doordat het stelsel vergelijkingen, dat het impliciete schema iteratief oplost, ook tot een hogere nauwkeurigheid opgelost moet worden.

Voor de nauwkeurigheid van de oplossing is het van belang een ruimtelijke discretisatie te hebben zonder numerieke dissipatie. Voor uniforme rekenroosters, die gemeengoed zijn in de simulatie van windparken, is een standaard centrale differentie even nauwkeurig als een energiebehoudende discretisatie. Beide methodes staan een calibratie van het Smagorinsky model toe, die onafhankelijk is van de rooster fijnheid, zolang wordt voldaan aan de voorwaarde dat de meest relevante energetische schalen kunnen worden

gerepresenteerd op het rooster. Kalibratie voor een methode die numerieke dissipatie toevoegd, is moeilijk te realiseren.

De resultaten van de academische problemen ondersteunen de conclusie dat een energiebehoudende, ruimtelijke discretisatie (wat ook verkregen kan worden met een centrale differentie op een uniform rekenrooster), gecombineerd met een niet-energiebehoudende tijdsintegratie en met een naar behoren gekalibreerd Smagorinsky model, gebruikt kan worden voor praktische toepassingen. Een vergelijking met andere large eddy simulatie programma's, die vergelijkbare of betere numerieke methodes gebruiken, laat zien dat de voorgestelde methode nauwkeurig is bij toepassing op een trekkende schijf. De afwezigheid van numerieke dissipatie en een gekalibreerd Smagorinsky model resulteert in nauwkeurige snelheidsprofielen in het zog, hoewel de turbulente intensiteit niet goed voorspeld wordt. Een kanttekening die hierbij geplaatst kan worden is dat deze conclusies zijn gebaseerd op de analyse van het nabije zog en voor een instroming met een lage turbulente intensiteit. Een analyse van het zog verder stroomafwaarts voor een instroming met een aanzienlijke turbulente intensiteit zou toepasselijker zijn.

Vervolgens is het gekalibreerde Smagorinsky model gecombineerd met een *ad hoc* demping model om de dissipatie van het Smagorinsky model dicht bij de grond aan te passen. Voor een atmosferische grenslaagstroming bij een hoog *Reynolds* getal worden goede gemiddelde snelheidsprofielen gevonden, dit in tegenstelling tot de dissipatieve eigenschap van het Smagorinsky model en in overeenstemming met een gekalibreerd model dat vrij is van dissipatie en al eerder toegepast is met een pseudo-spectraal methode. Een simulatie van een groep trekkende schijven binnen een atmosferische grenslaag produceert goede resultaten. De te verwachten trends in de snelheid en turbulentie in het zog worden kwalitatief goed weergegeven met de in dit proefschrift voorgestelde methode.

To conserve, or not to conserve . . .

In closing, we would like to provide an answer to the question, *to conserve*, *or not to conserve* but only within the scope of our research and the domain of wind farm aerodynamics. The question relates to the mathematical representation of the physics of a flow. Physically, the energy of a flow remains *conserved*¹. A correct mathematical representation of a flow in a *continuous sense*, in essence, also *conserves* the energy of a flow.

However, this is not always the case when a flow is represented mathematically in a *discrete sense*. It is known that both spatial discretisation and time integration introduce numerical dissipation that can spuriously alter the energy of a flow leading to non-compliance with *energy-conservation*. To ensure compliance in a discrete setting, the numerical (or artificial) dissipation can either be forced mathematically to remain zero or be reduced to tolerably low value. The latter is relevant when factors like computational time, the expected (or practically required) accuracy of the method, the ease of implementation etc., outweigh the requirement of a numerical scheme that guarantees zero numerical dissipation.

A much pertinent case is the simulation of wind farm aerodynamics for which one may a non-energy conserving explicit time integration (that introduces numerical dissipation) with a small time step to reduce the numerical dissipation, instead of using an energy-conserving implicit time integration that is computationally very demanding. Nonetheless, at the same time, the dissipation through spatial discretisation should be avoided with an energy-conserving discretisation on a staggered grid or a central difference discretisation on a collocated uniform grid². One may also use a non-energy conserving upwind discretisation with a very refined grid, which will only lead to an increased computational time.

Thus, as regards to the energy-conserving schemes used in this thesis, we conclude that they are not an absolute requirement for the large eddy simulation of wind farm aerodynamics.

¹ Or changes as per the equations defined in chapter 3

² As mentioned earlier, uniform grids are the norm in wind farm simulations.

Part IV APPENDICES



SIMPLE NUMERICAL TESTS WITH THE ECNS

The early stages in developing the ECNS to ECNS-LES witnessed a lot of simple numerical tests that were used to assess the behaviour of various LES models to choose the most appropriate one and more important, verify if the implementations are correct. This appendix describes a couple of such tests that helped us choose the Smagorinsky model and understand the requirement for tuning it.

EC schemes are mainly designed to avert numerical dissipation while the NS equations are solved over a discrete computational domain. However, one the flow is turbulent and an SGS model is introduced to make up for the scales that are not being represented on the computational grid, the accuracy is governed by a more dominant factor, the SGS dissipation.

Adapted from (Mehta et al., 2014a)

With simple tests we noticed how two fundamentally different SGS models, the *Smagorinsky* and the *Bardina* model, affect the growth of turbulence and the dissipation of TKE, which in turn influence how the flow evolves. The theoretical aspects and relevant algebra has been outlined in chapter 3. For these tests, we use a very small time step in combination with the Ex4, the reasons for which have been outlined in chapter 4. We will analyse the results in terms of the following equation,

$$\frac{\mathrm{d}}{\mathrm{d}t} \int_{\Omega} k_{\widetilde{\mathbf{u}}} \, \mathrm{d}\Omega = \underbrace{-\nu \int_{\Omega} \|\nabla \widetilde{\boldsymbol{u}}\|^2 \, \mathrm{d}\Omega}_{\boldsymbol{\psi}_{\nu}} - \underbrace{\int_{\Omega} (\nabla \cdot \boldsymbol{\tau}) \cdot \widetilde{\boldsymbol{u}} \, \mathrm{d}\Omega}_{\boldsymbol{\psi}_{s}} , \qquad (A.1)$$

where

 ψ rate of change of KE.

 $\psi_{\nu} + \psi_{s} = \psi$, are obtained through post-processing and characterise the contribution of molecular viscosity and the SGS tensor, and their total contribution to the change in KE, respectively (equation A.1 is not solved).

SGS models have been compared in terms of how they predict; the roll-up of shear layer in 2-D and the decay of a *Taylor-Green* vortex in 3-D. The Smagorinsky model is used with two values of C_S ; 0.17 corresponding to homogeneous isotropic turbulence as suggested by Lilly (1967) and 0.1 that is apt for anisotropic flows and leads to lower dissipation (Porté-Agel et al., 2000). The *Bardina scale-similarity model* relates the stresses at the scale of the grid's cell and the same scale filtered spatially at another test scale; the ratio of the two scales or β governs the model's dynamics (Bardina et al., 1983; Meneveau and Katz, 2000). The test scale should not be large in comparison to the grid resolution for the hypothesis of scale-similarity to hold. We use

two values of β ; one equal in size to the grid resolution ($\beta = 1$) and the other, twice its value ($\beta = 2$).

We must impress upon the fact that this is not a rigorous validation exercise but merely a qualitative analysis of the code's ability.

A.1 SHEAR LAYER IN 2-D

LES is employed to repeat the detailed simulations done by Brown and Minion (1995) on a perturbed doubly-periodic shear layer and the ensuing vorticity, at a Reynolds number of 10000. Although turbulence is intrinsically 3-D, a 2-D verification of the ECNS will provide insight into numerical inconsistencies that could be adverse in 3-D.

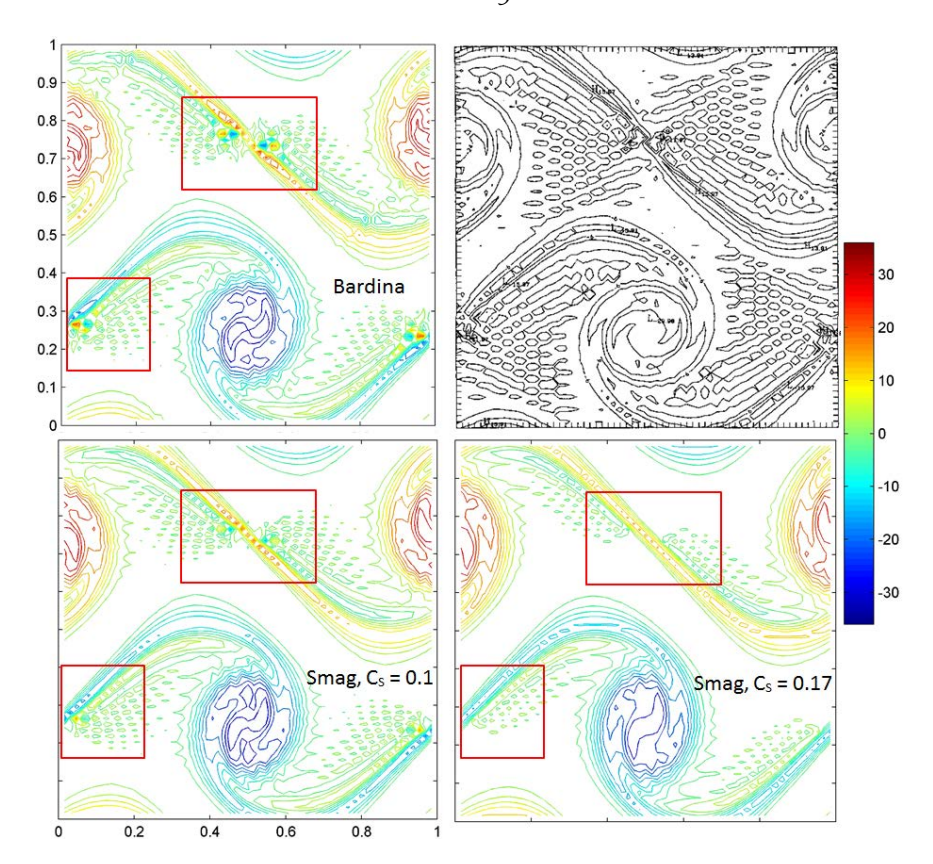


Figure A.1: Contours of vorticity with different SGS models. The spurious wiggles disappear with higher SGS dissipation (top-right: solution from Brown and Minion (1995)).

All simulations used a $[0,1]^2$ domain discretised into 32^2 , 64^2 , 128^2 and 256^2 points. We however, only present the results for the 64^2 . Due to the unavailability of DNS, a reference solution was obtained with the ECNS on a 320^2 grid with a time step of 10^{-4} s. In terms of spatial resolution, 256^2

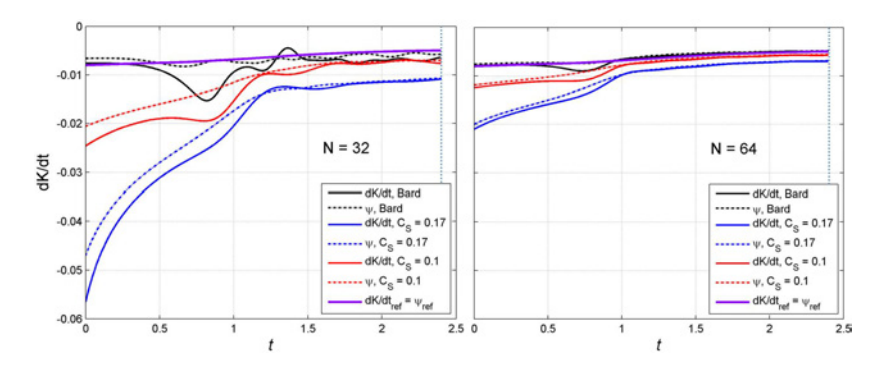


Figure A.2: The evolution of KE with different SGS models. $\psi=\frac{dK}{dt}$ is clearly enforced on finer grids.

and 320^2 grids produced identical results. Following a thorough investigation, the time step was set to 0.005s to avert a significant influence of time integration on the solution. A solution obtained by Brown and Minion (1995) with a centred fourth-order finite difference method on a 64^2 grid is used for a qualitative comparison.

At a macroscopic level, the ECNS does render the large scale structures correctly at a resolution of 64^2 , as shown by the contours of vorticity in figure A.1. An error analysis revealed that the spatial accuracy is indeed second order (juxtaposed with the 320^2 solution, not shown here). One easily observes the dispersion stemming from the central EC discretisation schemes that is most apparent with the Bardina model ($\beta = 1$), which by construction is not purely dissipative, unlike the Smagorinsky model (Bardina et al., 1983). The Smagorinsky model helps dampen the wiggles by smoothing the solution for a better representation on a coarse grid. But in doing so, the large scale structures are rendered incorrectly in terms of an elliptical rather than circular structure of the large vortex (an error analysis showed that the Bardina model is more accurate, despite the wiggles).

The ECNS is constructed to enforce KE conservation in a discrete setting for an inviscid flow. An analysis of KE dissipation as $\frac{dK}{dt}$, reveals that equation A.1 is satisfied by all SGS models in the limit of fine grid resolution, assessed using the reference solution obtained on a 320^2 grid. However, on coarse grids, the decay is predicted more correctly with the Bardina model or with Smagorinsky model using a smaller C_S , which makes the latter less dissipative. In fact, the Bardina model is quite accurate even on a 64^2 grid. Further, Smagorinsky model shows a large deviation near t=0s, which reduces only when the simulation becomes less dynamic near t=2s, as shown in figure A.2.

Mathematically, the SGS tensor alters the velocity field through the momentum equation, which in turn determines the KE, albeit with some error. Whereas, ψ is obtained through post-processing but also depends on the SGS tensor. Smagorinsky model regularises the velocity field to be easily

rendered on a coarse grid, in turn ensuring accurate post-processing, which is noticeable by the closeness of ψ and $\frac{dK}{dt}$ for $C_S=0.17$. But this leads to a large inaccuracy in predicting either of them correctly.

Compliance with equation A.1 is purely an aspect of post-processing. An EC-LES merely prevents numerical dissipation from altering the velocity field and hence its KE, which must ideally be dissipated through the SGS tensor.

A.2 TAYLOR-GREEN VORTEX IN 3-D

2-D tests revealed that an EC spatial discretisation will lead to a dispersive solution that will however, be more accurate than a solution obtained with a dissipative model, which will be free from spurious wiggles. But the true nature of turbulence can only be interpreted with a 3-D test case.

This experiment records the decay of an initially isotropic Taylor-Green vortex in a $[-\pi,\pi]^3$ domain, at a Reynolds number of 1600. This case is particularly interesting as the flow is initially laminar and transitions into turbulence with time (Aubard et al., 2013). Data on the rate of decay of turbulence KE, ε or $-\frac{dK}{dt}$, from earlier DNS studies serves as a reference. LES was done on 16^3 , 32^3 , 48^3 and 64^3 uniform grids.

Visualising the vorticity is made easy with the *Q-criterion*, a positive value of which indicates a dominance of vorticity over shear (Jeong and Hussain, 1995). Figure A.3 depicts how the flow transitions from being laminar with vortex tubes into small-scale turbulence. A comparison between the Bardina model, $\beta=1$ and Smagorinsky model, $C_S=0.17$, reveals the effects of SGS dissipation on the velocity (indirectly vorticity) field in figure A.4. Although the Smagorinsky model renders a smoother field due to increased dissipation, the field's KE as suggested by the colour bars is relatively lower.

But which model is more accurate can only be deduced by observing the evolution of KE with time. Although Smagorinsky model renders a smoother field, the Bardina model with $\beta=1$ is more accurate than Smagorinsky model at estimating ϵ , and more so a 64^2 grid. Also, a more accurate *peak dissipation* is obtained with the Bardina model. The deviation with Smagorinsky model near t=0 as noticed in 2-D tests, is also also apparent in 3-D, although diminishing with grid resolution. Further, the Bardina model with $\beta=2$ is as accurate as the Bardina model with $\beta=1$ on a finer grid. This happens because using $\beta=2$ on a coarse grid, sets the test-scale to a relatively larger value at which the hypothesis of scale-similarity may not hold true, as opposed to a finer grid on which scale-similarity would be plausible with $\beta=2$ (see figure A.5).

To summarise, it is evident that the ability of an EC-LES to correctly predict the velocity field and hence its KE is, to a great extent, determined by the SGS model. A more dissipative model, such as Smagorinsky model, may render a smooth solution of a coarse grid, which may not be accurate.

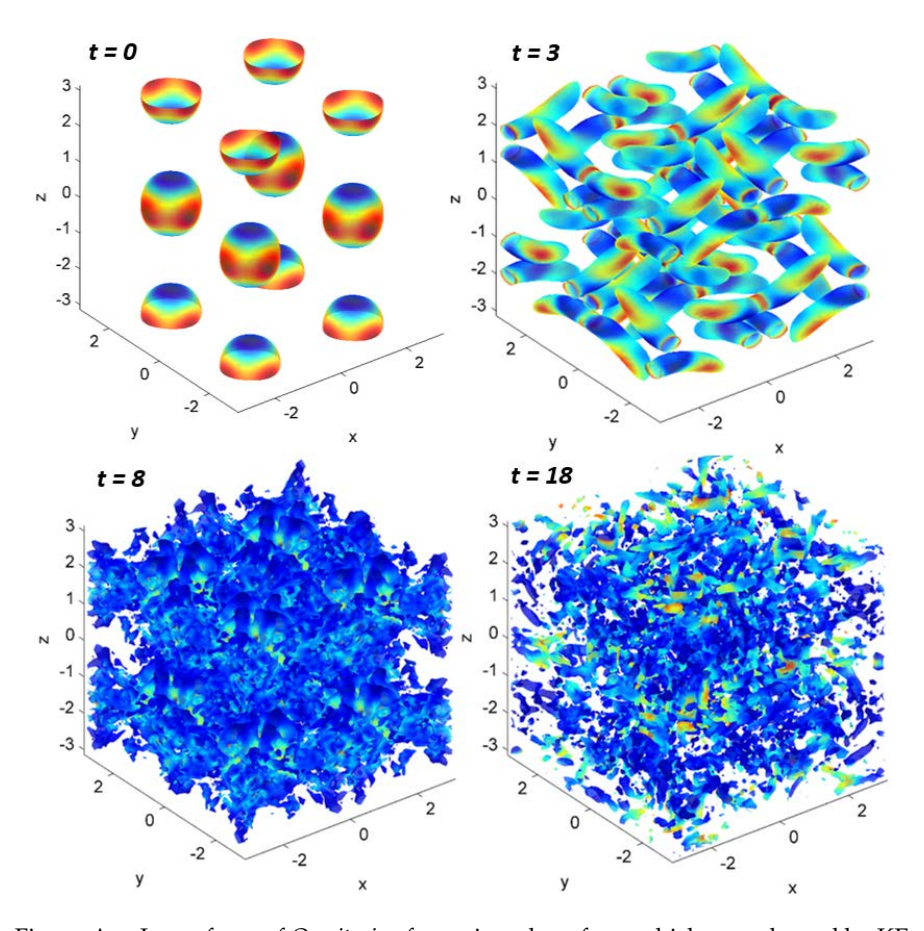


Figure A.3: Isosurfaces of *Q-criterion* for an isovalue of 0.5, which are coloured by KE at various instances using the Bardina model with $\beta=1$. t=0s: initial, t=3s: laminar, t=8s: in transition and t=18s: small-scale turbulence.

Having said that, it is important to mention that the basic assumptions of Smagorinsky model lack experimental support, as opposed to those of the Bardina mdoel (Zang et al., 1993). However, its ease of implementation and ability to generate agreeable mean flow statistics have made Smagorinsky model and its higher-order extensions dominant in wind farm LES codes.

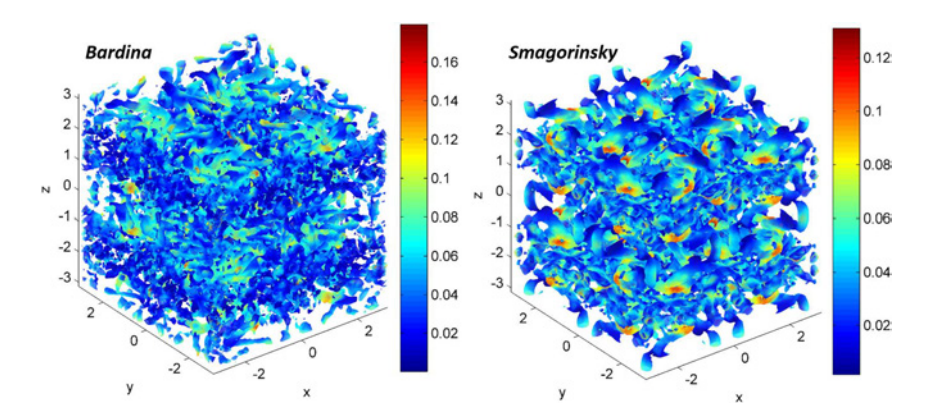


Figure A.4: Isosurfaces of *Q-criterion* for an isovalue of 0.5, which are coloured by KE at t=14s, using the Bardina model with $\beta=1$ and Smagorinsky model with $C_S=0.17$.

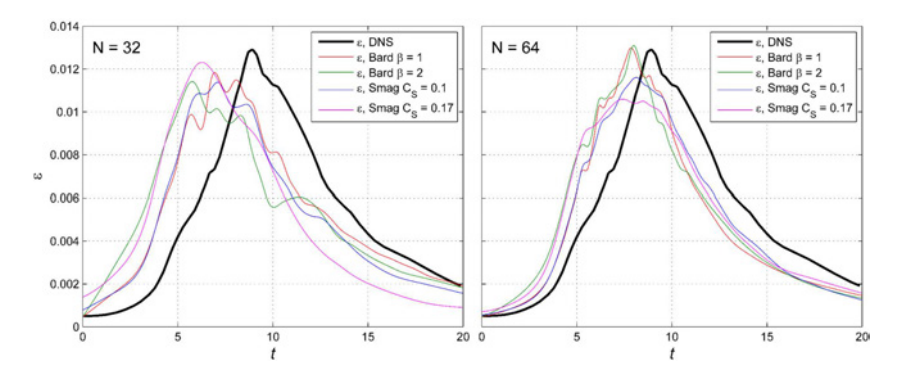


Figure A.5: The evolution of ε with time on 32^2 & 64^2 grids obtained with two variants of the Bardina and Smagorinsky models.

HIGHER ORDER REQUIREMENT

Here we will be describing the 4th order formulation in brief, followed a test of its accuracy. The readers are referred to Sanderse (2013) for details. We first investigate the effect of using a 4th order convective operator, without the SGS model. The numerical test is exactly the same as described in section 5.4; the advection of an isentropic vortex in the absence of viscosity and body forces, and in the presence of periodic boundaries.

Next, we shall repeat the tests in chapter 4 and also the final analyses on the dependence of the Smagorinsky constant on grid resolution, if the dominant convective term is discretised as a 4th order accurate operator.

B.1 THE FOURTH ORDER FORMULATION

In this section, we shall refer many a times to the equations in section 3.4 that pertain to a 2nd order EC spatial scheme. With the symbols retaining their previously-mentioned meaning, equations 3.43 and 3.44, are rewritten as,

$$\mathcal{M}_{\mathsf{II}}\mathbf{u}(\mathsf{t}) = \mathsf{0} \;, \tag{B.1}$$

$$\Omega_{\mathrm{I}}\dot{\mathbf{u}}(t) = -\mathcal{C}_{\mathrm{II}}(\mathbf{c}(t), \mathbf{u}(t)) + \nu \mathcal{D}_{\mathrm{II}}\mathbf{u}(t) - \mathcal{G}_{\mathrm{O2}}\mathbf{p}^{*}(t). \tag{B.2}$$

where

 $M_{\rm II}$ 2nd order accurate divergence operator

 $\Omega_{\rm I}$ the control volume

As Figures 3.1 and 3.2 depict, the discrete volume is Ω , which will be mentioned as Ω_1 (or Ω_{II} hereafter. For simplicity, we have neglected the effect of body forces and non-periodic boundary conditions, the formulation of which must change with the intended order of accuracy.

To obtain a 4th accurate formulation, Verstappen and Veldman (2003) discretised the above equations on control volumes that are three times as coarse as Ω_1 , Ω_3 , and combined the two different equations in a manner that cancels the leading order error, resulting in a 4th order accurate method. For example, equation B.2 for simple convection would read,

$$\Omega_1 \dot{\mathbf{u}}(t) + \mathcal{C}_1(\mathbf{c}(t), \mathbf{u}(t)) = 0. \tag{B.3}$$

where

 \mathcal{C}_1 convective operator discretised over a volume Ω^1

Whereas, on a control volume that is three times Ω_1 ,

$$\Omega_3 \dot{\mathbf{u}}(t) + \mathcal{C}_3(\mathbf{c}(t), \mathbf{u}(t)) = 0. \tag{B.4}$$

where

 \mathcal{C}_3 convective operator discretised over a volume Ω_3

 Ω_3 equals $3^3\Omega_1$ or $27\Omega_1$. Next, using the reasoning described in Verstappen and Veldman (2003), the equations B.3 and B.4 are combined into,

$$\Omega_{\text{IV}}\dot{\mathbf{u}}(t) + \mathcal{C}_{\text{IV}}(\mathbf{c}(t), \mathbf{u}(t)) = 0. \tag{B.5}$$

where

 $\mathcal{C}_{\mathrm{IV}}$ the 4th order accurate convective operator

 Ω_{IV} effective control volume for the 4th order formulation

 \mathcal{C}_{IV} and Ω_{IV} can be expressed as,

$$\Omega_{IV} = 3^{2+d}\Omega_1 - \Omega_3 \text{ and} \tag{B.6}$$

$$\mathcal{C}_{\text{IV}} = 3^{2+d}\mathcal{C}_1 - \mathcal{C}_3 \,, \tag{B.7}$$

where

d number of dimensions, 3 is this case

Using the above formulation, we simulate the convection of a vortex in the absence of viscosity.

B.2 CONVECTION OF AN INVISCID VORTEX

The vortex is simulated on 8^3 , 16^3 , 24^3 , 32^3 , 48^3 , 64^3 and 72^3 uniform grids, while the reference solution is calculated separately on a 96^3 grid. On each grid, the convective operator is obtained with both, the $2^{\rm nd}$ and $4^{\rm th}$ order formulations. A simple error analysis in terms of the u and v components of velocity reveals the order of accuracy of either formulation (see figures B.1 and B.2).

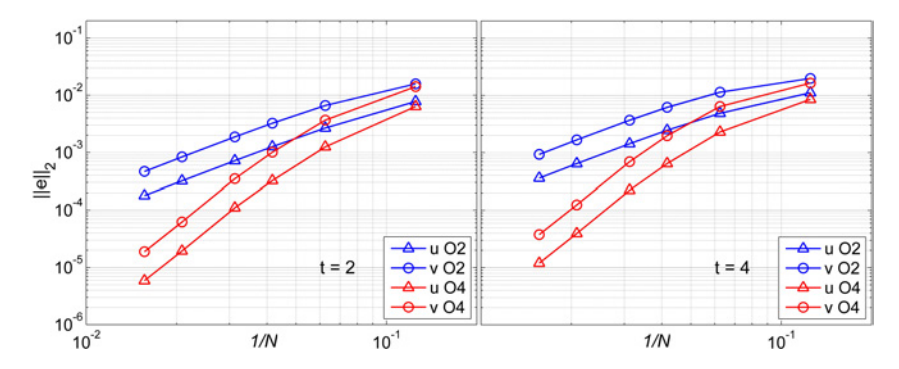


Figure B.1: Convergence of $||e||_2$ at two instances of time.

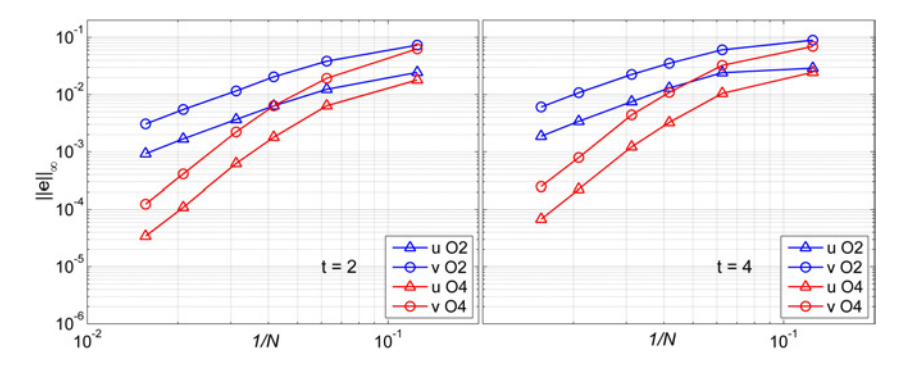


Figure B.2: Convergence of $\|e\|_{\infty}$ at two instances of time.

VALIDATION OF A FAR WAKE ENGINEERING MODEL

This section describes how the ECNS-LES was employed to successfully validate a simple physical model designed to improve the far wake deficit models common in the wind industry. We add this appendix to emphasise one of the conclusions in Mehta et al. (2014b), regarding the use of advanced tools like LES to study and improve simpler engineering models for industrial use through careful benchmarking.

Central to method was an improved prediction of the wake deficit in the near wake as opposed to simply prescribing an empirically determined value (see section 2.1.2 for traditional far wake methods). A accurate near wake deficit was prescribed using a simple vortex ring model for which the turbine is represented by a uniformly loaded actuator disk that is free to shed discrete vortex rings, which are later processed to obtain the velocity field (Baldacchino and van Bussel, 2014). Next, the field calculated with the vortex ring model, is fed to the far wake models proposed by Jensen (1983) and (Larsen et al., 2008). The former is relatively simple and widely popular, whereas the latter that is based on an an eddy-viscosity formulation, is more compatible with the vortex ring model. The aim is to use the vortex ring model instead of the original stream-tube approach of the Larsen model in the near wake, to improve the prediction of the overall velocity field in the wake.

Adapted from (van Heemst et al., 2015)

To validate the new model, the ECNS along with its Smagorinsky model, is used to simulate an actuator disk, with parameters similar to those mentioned in table 6.1. For succinctness, we will not be detailing the vortex ring model or the other models mentioned above, for which the readers are referred to van Heemst et al. (2015).

We simulate a single actuator disk with a diameter of 0.6m with an initially laminar inflow velocity of 4.7ms^{-1} and a thrust coefficient of 0.93. The computational domain measures $12D \times 8D \times 8D$, where D is the actuator disk's diameter; and is discretised into $120 \times 80 \times 80$ control volumes. The disk itself, is placed at 4D from the inflow boundary.

However, we used the ECNS without its Smagorinsky model being tuned, as this test was done before we considered the effect of the model constant, C_S , on the flow. The results mentioned here were generated with $C_S = 0.15$, which as per appendix D is different from the more accurate value of $C_S = 0.125$ for the ECNS. However, the differences resulting from various values of C_S are more apparent through the profiles of turbulence intensity than through the profiles of velocity deficit, which are quite similar for both $C_S = 0.125$ and $C_S = 0.15$ (see appendix D).

Figure C.1 suggests that the coupled vortex ring-Jensen model results in a more gradual wake recovery as compared with the reference Jensen model.

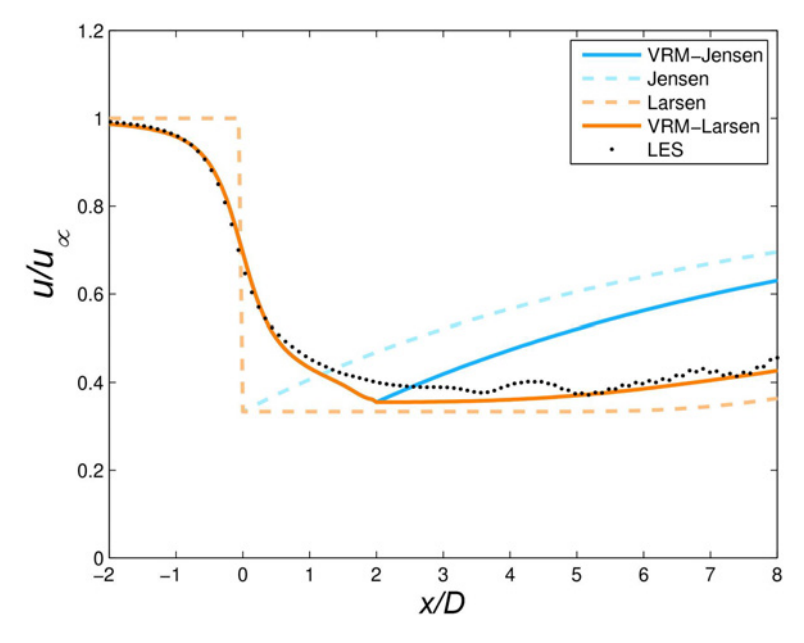


Figure C.1: The streamwise velocity normalised by the inflow velocity and plotted along the wake's centreline

On the other hand, the vortex ring-Larsen model shows a reasonable resemblance with LES in the near and the far wake, as can be seen in figure C.2. The stream tube near wake model used by Larsen et al. (2008) appears to over predict the wake losses in the near wake, resulting in a lower centreline velocity in the far wake.

With regards to the LES itself, one notices some untoward behaviour along the edge of the rotor, where the velocity in the near wake experiences a sudden drop that is much apparent at the first three locations depicted in figure C.2. This is probably due to the Immersed Interface Approach used to implement the circular actuator disc on a Cartesian grid of limited resolution. One could circumvent this by smearing the relevant body force smoothly across the domain with a *Gaussian* distribution, as done in many other LES codes (see Porté-Agel et al. (2011) for example). We also repeated the simulation using a higher grid resolution, albeit on a smaller domain due to limited computational power, only to notice a reduction in the effect of the abrupt implementation of the body force.

As compared to the engineering models, the LES results displayed a contraction of the wake at 8D. Also noticed was that the wake recovery promoted by the turbine-generated turbulence in the far wake, begins beyond the previously assumed distance of 2D. Ideally, the vortex ring near wake model should be extended to a position between 2D-4D, however, a strong vortex ring interaction after 2D prohibited a converging velocity field in this region.

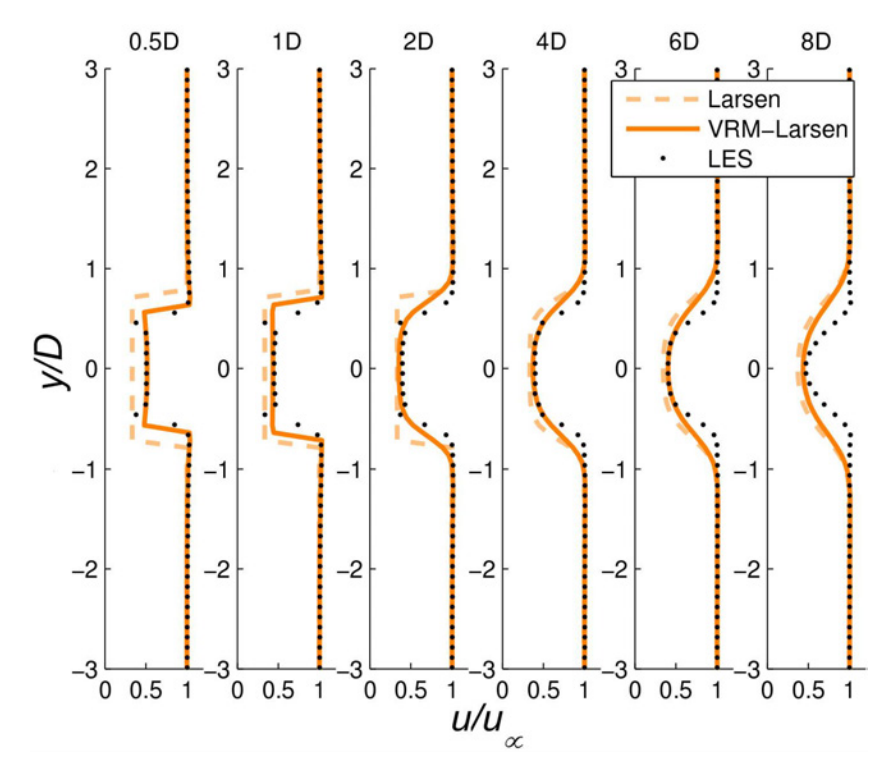


Figure C.2: Radial profiles of streamwise velocity normalised by the inflow velocity at different downstream locations.

We observed that the excellent agreement afforded by the vortex ring-Larsen model, was achieved in nearly a hundredth of the computational effort put into the LES. This prompted further research into wake interaction and multiple turbine simulations.



EFFECT OF THE SMAGORINSKY CONSTANT ON ACTUATOR DISK PREDICTIONS

In Lignarolo et al. (2015), the ECNS was used with $C_S = 0.17$. Later we studied the effect of the following values on the wake velocity and turbulence; 0.10, 0.11, 0.12, 0.125 and 0.15. Values 0.10 and 0.15 were chosen from literature, whereas the remaining values were observed to help predict the decay of isotropic homogeneous turbulence with good accuracy (see chapter 4). The tests were carried out for a turbulent inflow using the grids mentioned in table 6.2, referred to as *coarse*, *medium* and *fine*.

D.1 SENSITIVITY TO THE SMAGORINSKY CONSTANT

As evident from existing literature, average flow properties change with the amount of dissipation the Smagorinsky model brings. Upon reducing the Smagorinsky constant from 0.17 and simulating the flow on a *medium* grid, we notice the following changes.

- A minor reduction in C_S does not lead to the growth of turbulence. But with a value of \sim 0.12, the turbulence intensity increases consistently with downstream distance. Although the peak value of turbulence achieved is rather low, the spurious growth of turbulence outside of the shear layer and in proximity to the disc (see figure 6.8, x/D = 0.7 & 1.1), is no longer seen.
- Further reduction in C_S, causes a large growth in turbulence. Although
 the peak value is yet unachievable, the turbulence grows in the region
 behind the disc to relatively large values as compared to the experimental predictions (see figure D.1).
- These changes in turbulence can be related to the changes observed in the average velocity field in the wake, shown in figure D.2. Excessive turbulence promotes a lot of turbulence mixing, which in turn leads to a quicker recovery of the wake deficit, as is the case with $C_S = 0.10$. The recovery itself, is more apparent as one moves further from the disc.
- In general, a value of C_S less than 0.17, demonstrate a relatively lower deficit or a higher velocity in the shear layer. But unlike $C_S = 0.10$, the controlled growth of turbulence does not lead to a spuriously quick recovery of wake deficit.

D.2 SENSITIVITY TO GRID RESOLUTION

Figure D.3 depicts how the velocity field improves consistently with down-stream distance while using the *fine* grid and setting C_S to 0.125, a value that we chose from the previous section. The improvement is mostly noticeable around the shear layer, which is well predicted at x = 2.2D.

On the other hand, the changes in turbulence intensity do not show a conclusive trend. The turbulence grows relatively easily on the *fine* grid, and more so, with downstream distance (see figure D.4). Although the growth in turbulence is much less as compared to that observed when using $C_S = 0.17$ on a fine grid, the latter results in an incorrectly high value of turbulence in the near wake, especially behind the actuator disk (between y/D = 0 & 0.5). This however, vanishes around x/D = 1.8 with more turbulence in the shear layer than predicted with $C_S = 0.125$, on a positive note.

D.3 INFERENCE

A preliminary inference while using a *turbulent* inflow includes the following.

- An appropriate value of C_S leads to an improvement in the prediction
 of the velocity field, especially with improvement in grid resolution.
 This is closely related to how correctly the Smagorinsky model dissipates the KE (or TKE).
- Using the appropriate value of C_S as suggested by predictions of the velocity field, does not lead to improved turbulence statistics. Although the growth of turbulence is promoted by a lower value of C_S and improved grid resolution, it may not be consistent with downstream distance and could be excessive.

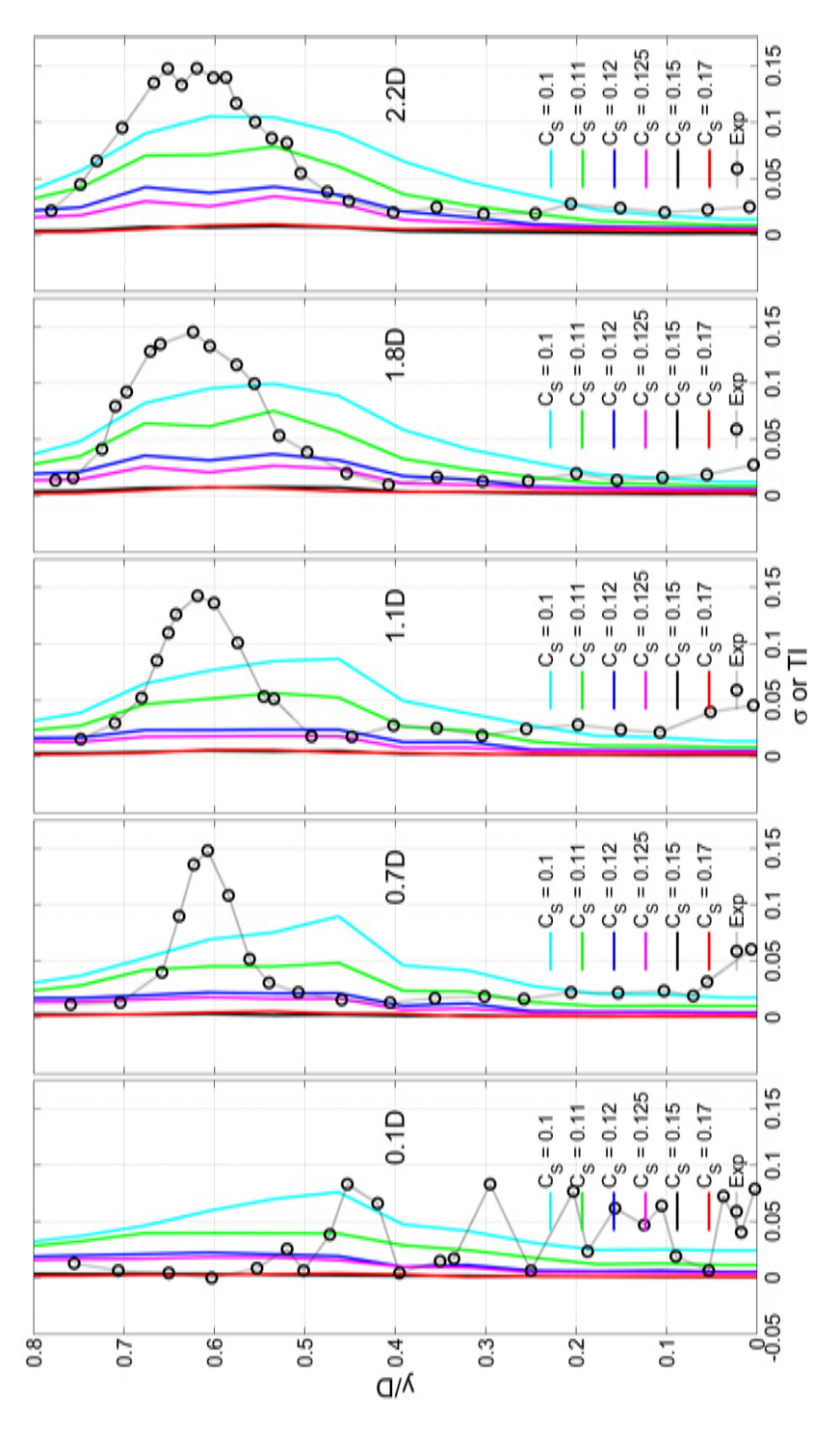


Figure D.1: Profiles of turbulence intensity with different values of C_S .

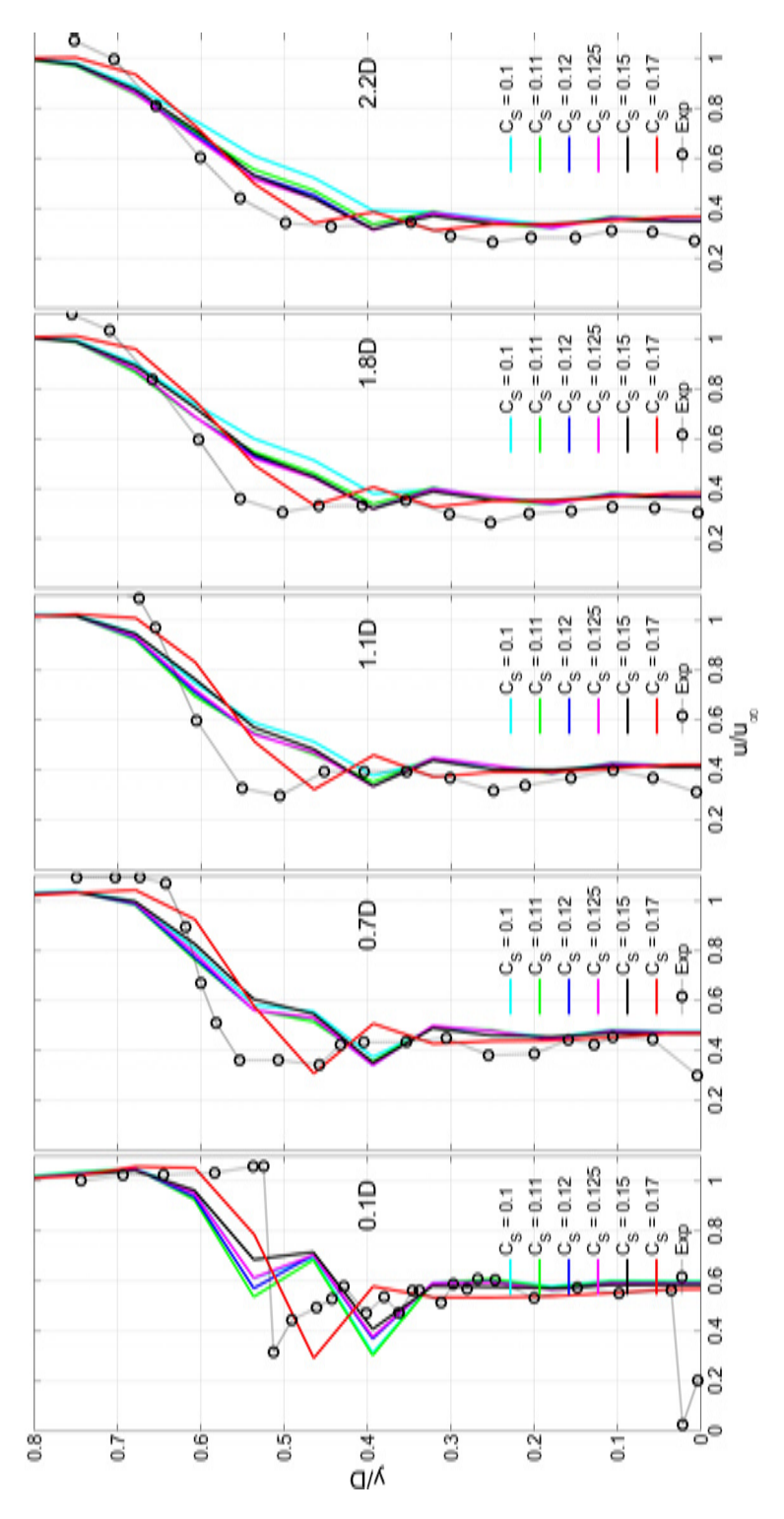


Figure D.2: Profiles of streamwise velocity with different values of C_S .

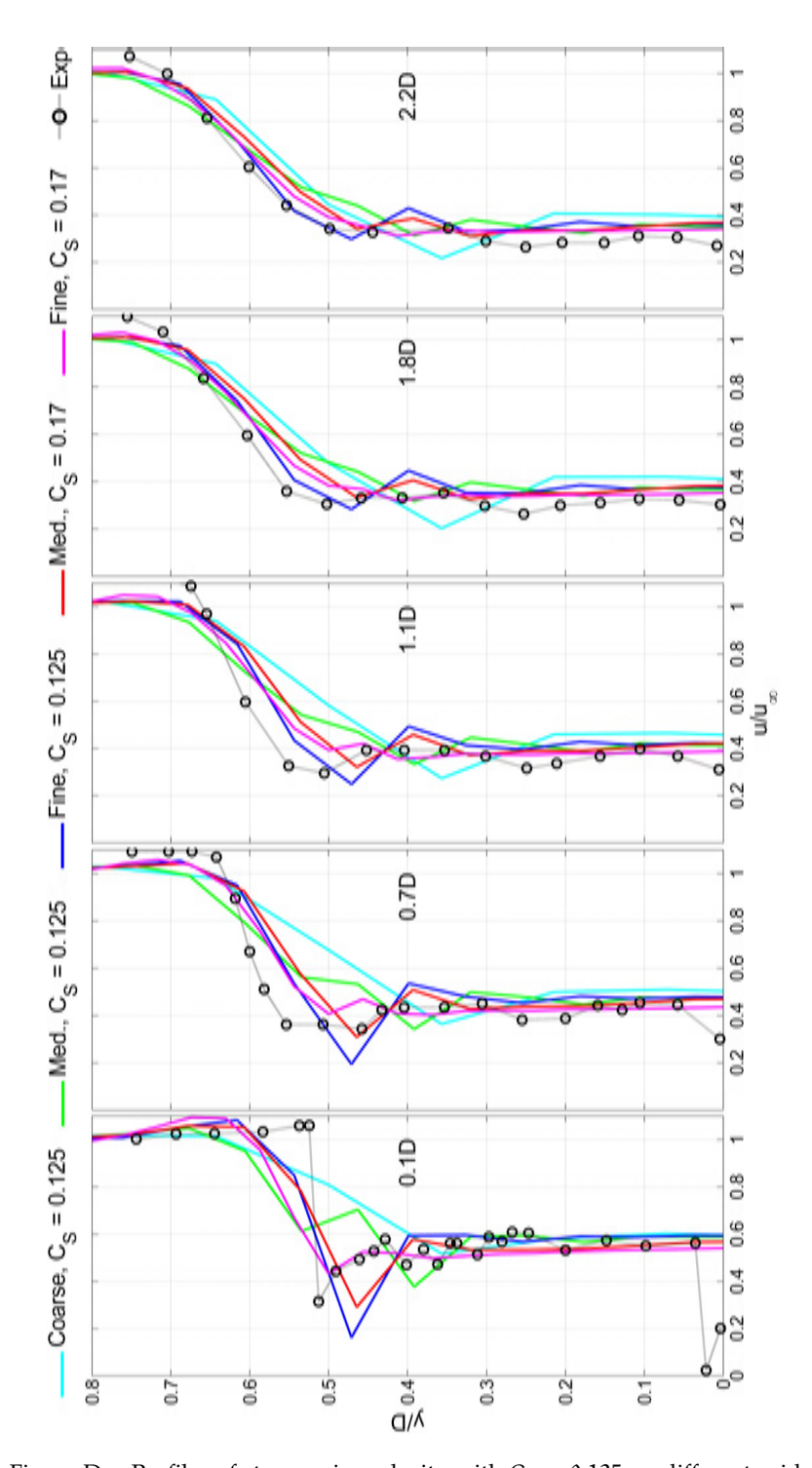


Figure D.3: Profiles of streamwise velocity with $C_S=0.125$ on different grids.

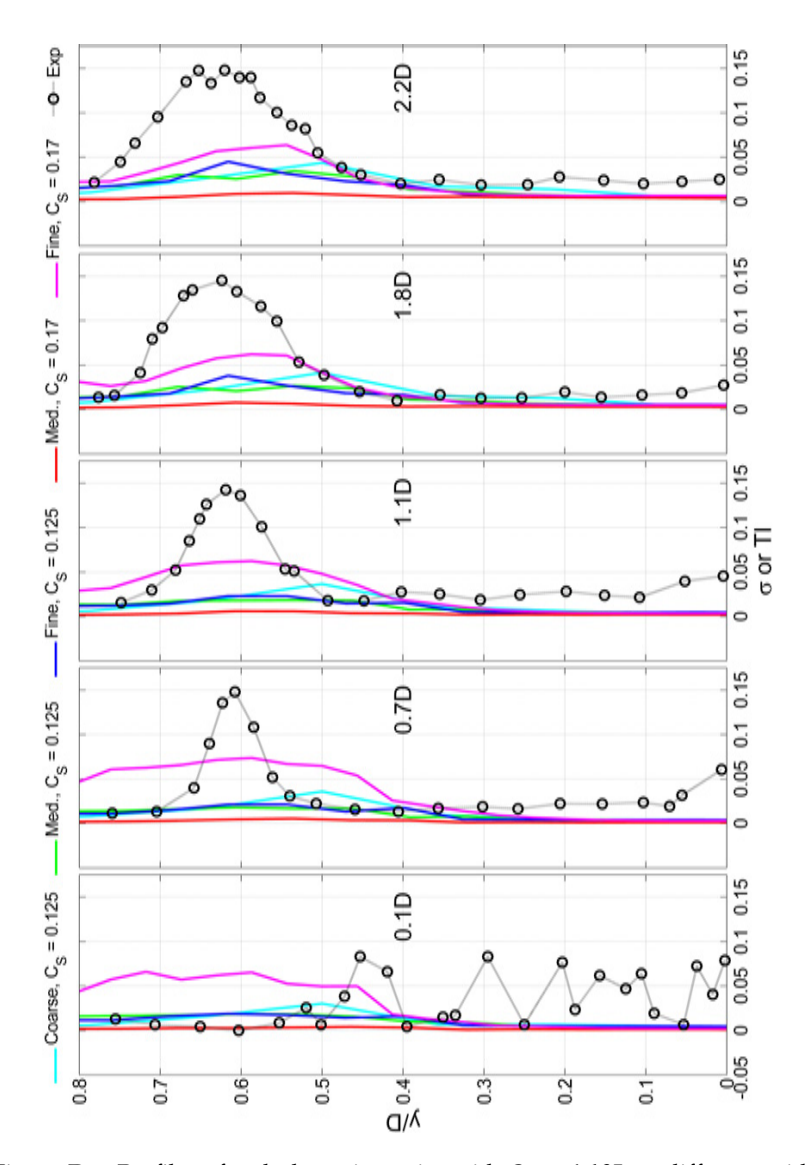


Figure D.4: Profiles of turbulence intensity with $C_{\text{S}}=0.125$ on different grids.

- Abramovich, G. N. *The Theory of Turbulent Jets*. MIT Press, Cambridge, MA, 1 edition, 1963. (see page 8)
- Ainslie, J. F. Development of an eddy viscosity model for wind turbine wakes. In *Proceedings of the* 7th *BWEA Wind Energy Conference*, pages 61–66, Oxford, 1985. (see page 8)
- Aubard, G., Stefanin Volpiani, P., Gloerfelt, X., and Robinet, J. Comparison of subgrid-scale viscosity models and selective filtering strategy for large-eddy simulations. *Flow, Turbulence and Combustion*, 91:497–518, 2013. (see page 138)
- Baldacchino, D. and van Bussel, G. J. W. Wind turbine wake stability investigations using a vortex ring modelling approach. *Journal of Physics: Conference Series*, 555:012111, 2014. (see page 144)
- Bardina, J., Ferziger, J. H., and Reynolds, W. C. *Improved turbulence models based on large eddy simulation of homogeneous, incompressible, turbulent flows*. PhD thesis, Department of Mechanical Engineering, Stanford University, 1983. (see pages 15, 19, 23, 135, and 137)
- Barthelmie, R. J., Frandsen, S. T., Réthoré, P. E., and Jensen, L. Analysis of the atmospheric impacts on the development of wind turbine wakes at the Nysted wind farm. In *European Offshore Wind Conference*, Berlin, 2007. (see page 2)
- Barthelmie, R. J., Frandsen, S. T., Hansen, K., Schepers, J. G., Rados, K., Schelz, W., Neubert, A., Jensen, L. E., and Neckelmann, S. Modelling the impact of wakes on power output at Nysted and Horns Rev. In *European Wind Energy Conference*, Marseille, 2009. (see pages 3, 8, and 32)
- Barthelmie, R., Folkerts, L., Ormel, F., Sanderhoff, P., Eecen, P., Stobbe, O., and Nielsen, N. Offshore wind turbine wakes measured by sodar. *Journal of Atmospheric and Oceanic Technology*, 20:466–477, 2003. (see page 34)
- Barthelmie, R., Folkerts, L., Larsen, G., Rados, K., Pryor, S., Frandsen, S., Lange, B., and Schepers, G. Comparison of wake model simulations with offshore wind turbine wake profiles measured by sodar. *Journal of Atmospheric and Oceanic Technology*, 23:888–901, 2006. (see page 34)
- Basu, S. and Porté-Agel, F. Large-eddy simulation of stably stratified atmospheric boundary layer turbulence: A scale-dependent dynamic modeling approach. *Journal of the Atmospheric Sciences*, 63:2074–2091, 2006. (see pages 21 and 31)

- Beare, R. J., Macvean, K. M., Holtslag, A. A. M., Cuxart, J., Esau, I., Golaz, J. C., Jimenez, M. A., Khairoutdinov, M., Kosovic, B., Lewellen, D., Lund, T. S., Lundquist, J. K., Mccabe, A., Moene, A. F., Noh, Y., Raasch, S., and Sullivan, P. An intercomparison of large-eddy simulations of the stable boundary layer. *Boundary-Layer Meteorology*, 118:247–272, 2006. (see page 31)
- Bechmann, A. Large-Eddy Simulation of Atmospheric Flow over Complex Terrain. PhD thesis, Department of Wind Energy, Risø National Laboratory Technical University of Denmark,, 2006. (see pages 19, 36, 60, and 62)
- Bot, E. T. G. FarmFlow validation against full scale wind farms. Technical Report ECN-E-15-045, Energy Research Centre of the Netherlands, 2015. (see pages 116 and 117)
- Bou-Zeid, E., Meneveau, C., and Parlange, M. A scale-dependent Lagrangian dynamic model for large eddy simulation of complex turbulent flows. *Physics of Fluids*, 17:025105, 2005. (see pages 19, 21, 110, 114, and 119)
- Boussinesq, J. V. Essai sur la théorie des eaux courantes (in French). *Mémoires présentés par divers savants à l'Académie des Sciences, Paris*, 23:1–680, 1877. (see page 11)
- Brown, D. and Minion, M. Performance of under-resolved two-dimensional incompressible flow simulations. *Journal of Computational Physics*, 122:165–183, 1995. (see pages 136 and 137)
- Burton, T., Sharpe, D., Jenkins, N., and Bosanyi, E. *Wind Energy Handbook*. John Wiley & Sons: Chichester, 2001. (see page 24)
- Businger, J. A., Wyngaard, J. C., Izumi, Y., and Bradley, E. F. Flux-profile relationships in the atmospheric surface layer. *Journal of the Atmospheric Sciences*, 28:181–189, 1971. (see pages 31 and 109)
- Cabezón, D., Migoya, E., and Crespo, A. Comparison of turbulence models for the computational fluid dynamics simulation of wind turbine wakes in the atmospheric boundary layer. *Wind Energy*, 14:909–921, 2011. (see pages 8, 9, 10, and 36)
- Calaf, M., Meneveau, C., and Meyers, J. Large eddy simulation study of fully developed wind-turbine array boundary layers. *Physics of Fluids*, 22: 015110, 2010. (see pages 26, 28, 33, and 34)
- Calaf, M., Parlange, M. B., and Meneveau, C. Large eddy simulation study of scalar transport in fully developed wind-turbine array boundary layers. *Physics of Fluids*, 23:126603, 2011. (see page 29)
- Canuto, C., Hussaini, M., Quarteroni, A., and Zang, T. *Spectral Methods in Fluid Dynamics*. Springer-Verlag Berlin, 1 ed. edition, 1988. (see page 94)

- Canuto, V. M. and Cheng, Y. Determination of the smagorinsky-lilly constant c_s. *Physics of Fluids* (1994-present), 9:1368–1378, 1997. (see page 19)
- Catalano, F. and Moeng, C. Large-eddy simulation of the daytime boundary layer in an idealized valley using the weather research and forecasting numerical model. *Boundary-Layer Meteorology*, 137:49–75, 2010. (see page 35)
- Chamorro, L. P. and Porté-Agel, F. A wind tunnel investigation of wind turbine wakes: Boundary layer turbulence effects. *Boundary-Layer Meteorology*, 132:129–149, 2009. (see page 29)
- Chamorro, L. P. and Porté-Agel, F. Effects of thermal stability and incoming boundary-layer flow characteristics on wind-turbine wakes: A wind-tunnel study. *Boundary-Layer Meteorology*, 136:515–533, 2010. (see pages 29 and 32)
- Chamorro, L. P. and Porté-Agel, F. Turbulent flow inside and above a wind farm: A wind tunnel study. *Energies*, 4:1916–1936, 2011. (see pages 2 and 29)
- Chorin, A. J. Numerical solution of the navier-stokes equations. *Mathematics of Computation*, 22:745–762, 1968. (see page 80)
- Churchfield, M. J., Michalakes, J., Vanderwende, B., Lee, S., Sprague, M. A., Lundquist, J. K., and Moriarty, P. J. Using mesoscale weather model output as boundary conditions for atmospheric large-eddy simulations and wind-plant aerodynamic simulations. Technical Report PR-5000-61122, National Renewable Energy Laboratory, Colorado, USA, 2013. (see page 35)
- Churchfield, M., Lee, S., Moriarty, P., Martínez, L., Leonardi, S., Vijayakumar, G., and Brasseur, J. A large-eddy simulation of wind-plant aerodynamics. In 50th AIAA Aerospace Sciences Meeting Including the New Horizons Forum and Aerospace Exposition, Nashville, Tennessee, 2012. (see pages 34 and 39)
- Comte-Bellot, G. and Corrsin, S. Simple Eulerian time correlation of fulland narrow-band velocity signals in grid-generated, 'isotropic' turbulence. *Journal of Fluid Mechanics*, 48:273–337, 1971. (see pages 60, 61, 65, 81, 84, and 85)
- Crespo, A., Manuel, F., Moreno, D., Fraga, G., and Hernández, J. Numerical analysis of wind turbine wakes. In *Proceedings of the Delphi Workshop on Wind Energy Applications*, pages 15–25, Delphi, Greece, 1985. (see page 8)
- Crespo, A., Frandsen, S., Gómez-Elvira, R., and Larsen, S. E. Modelization of a large wind farm, considering the modification of the atmospheric boundary layer. In *Proceedings of the 1999 European Union Wind Energy Conference*, Nice, France, 1999a. (see page 9)

- Crespo, A., Hernández, J., and Frandsen, S. Survey of modelling methods for wind turbine wakes and wind farms. *Wind Energy*, 2:1–24, 1999b. (see pages 6, 7, and 8)
- Davidson, P. A. *Turbulence An Introduction for Scientists and Engineers*. Oxford University Press: Oxford, 2004. (see page 12)
- Deardorff, J. W. A numerical study of three-dimensional turbulent channel flow at large Reynolds numbers. *Journal of Fluid Mechanics*, 41:453–480, 1970. (see page 62)
- Elliot, D. L. Status of wake and array loss research. In *Windpower Conference*, Palm Springs, California, 1991. (see page 8)
- Felten, F. N. and Lund, T. S. Kinetic energy conservation issues associated with the collocated mesh scheme for incompressible flow. *Journal of Computational Physics*, 215:465–484, 2006. (see page 52)
- Frandsen, S. On the wind speed reduction in the center of large clusters of wind turbines. *Journal of Wind Engineering and Industrial Aerodynamics*, 39: 251 265, 1992. (see pages 9 and 33)
- Frandsen, S., Barthelmie, R., Pryor, S., Rathmann, O., Larsen, S., Højstrup, J., and Thøgersen, M. Analytical modelling of wind speed deficit in large offshore wind farms. *Wind Energy*, 9:39–53, 2006. (see page 9)
- Frisch, U. *Turbulence, the legacy of A.N. Kolmogorov*. Cambridge University Press: Cambridge, 1995. (see pages 14 and 60)
- Germano, M. A proposal for a redefinition of the turbulent stresses in the filtered Navier-Stokes equations. *Physics of Fluids*, 29:2323–2324, 1986. (see page 21)
- Germano, M. Turbulence: the filtering approach. *Journal of Fluid Mechanics*, 238:325–336, 1992. (see pages 19 and 20)
- Germano, M., Piomelli, U., Moin, P., and Cabot, W. H. A dynamic subgrid-scale eddy viscosity model. *Physics of Fluids A: Fluid Dynamics*, 3:1760–1765, 1991. (see page 20)
- Geurts, B. Interacting errors in large-eddy simulation: A review of recent developments. *Journal of Turbulence*, 7:1–16, 2006. (see page 57)
- Ghosal, S. An analysis of numerical errors in large-eddy simulations of turbulence. *Journal of Computational Physics*, 125:187–206, 1996. (see pages 19 and 57)
- Ghosal, S. Mathematical and physical constraints on large-eddy simulation of turbulence. *AIAA Journal*, 37:425–433, 1999. (see page 21)

- Ghosal, S., Lund, T. S., Moin, P., and Akselvoll, K. A dynamic localization model for large-eddy simulation of turbulent flows. *Journal of Fluid Mechanics*, 286:229–255, 1995. (see page 61)
- Gómez-Elvira, R., Crespo, A., Migoya, E., Manuel, F., and Hernández, J. Anisotropy of turbulence in wind turbine wakes. *Journal of Wind Engineering and Industrial Aerodynamics*, 93:797–814, 2005. (see page 8)
- Grindstein, F. F., Margolin, L. G., and Rider, W. J. *Implicit Large Eddy Simulation: Computing Turbulent Fluid Dynamics*. Cambridge University Press: Cambridge, 1 edition, 2007. (see pages 15 and 74)
- Hamilton, N., Kang, H., Meneveau, C., and Cal, R. Statistical analysis of kinetic energy entrainment in a model wind turbine array boundary layer. *Journal of Renewable and Sustainable Energy*, 4, 2012. (see pages 28 and 29)
- Hansen, M. O. L. *Aerodynamics of Wind Turbines*. Earthscan: London, 2 edition, 2008. (see page 24)
- Harlow, F. H. and Welch, J. E. Numerical calculation of time-dependent viscous incompressible flow of fluid with free surface. *Physics of Fluids*, 8: 2182–2189, 1965. (see page 52)
- Horiuti, K. A proper velocity scale for modeling subgrid-scale eddy viscosities in large eddy simulation. *Physics of Fluids A: Fluid Dynamics*, 5:146–157, 1993. (see page 19)
- Hultmark, M., Calaf, M., and Parlange, M. A new wall shear stress model for atmospheric boundary layer simulations. *Journal of the Atmospheric Sciences*, 70:3460–3470, 2013. (see page 108)
- Ivanell, S. Numerical Computations of Wind Turbine Wakes. PhD thesis, Department of Mechanics, Royal Institute of Technology, Stockholm, Sweden,, 2009. (see pages 32 and 39)
- Ivanell, S., Mikkelsen, R., Sørensen, J. N., and Henningson, D. Validation of methods using EllipSys3D. Technical Report TRIRA-MEK 2008:12, Royal Institute of Technology, Sweden, 2008. (see page 26)
- Jensen, N. O. A note on wind generator interaction. Technical Report Risø-M-2411, Risø National Laboratory, Roskilde, Denmark, 1983. (see page 144)
- Jeong, J. and Hussain, F. On the identification of a vortex. *Journal of Fluid Mechanics*, 285:69–94, 1995. (see page 138)
- Jha, P., Churchfield, M., Moriarty, P., and Schmitz, S. Guidelines for volume force distributions within actuator line modeling of wind turbines on large-eddy simulation-type grids. *Journal of Solar Energy Engineering, Transactions of the ASME*, 136, 2014. (see page 24)

- Jiménez, Á., Crespo, A., Migoya, E., and Garcia, J. Advances in large-eddy simulation of a wind turbine wake. *Journal of Physics: Conference Series*, 75: 012041, July 2007. (see pages 34 and 35)
- Jonkman, J. M. and Guhl, M. L. FAST users' guide. Technical Report EL-500-38230, NREL, 2005. (see page 33)
- Kang, H., Chester, S., and Meneveau, C. Decaying turbulence in an active-grid-generated flow and comparisons with large-eddy simulation. *Journal of Fluid Mechanics*, 480:129–160, 2003. (see pages 14 and 94)
- Keck, R.-E., de Maré, M., Churchfield, M. J., Lee, S., Larsen, G., and Madsen, H. A. On atmospheric stability in the dynamic wake meandering model. *Wind Energy*, 2013a. (see page 34)
- Keck, R.-E., de Maré, M. J., M.and Churchfield, Lee, S., Larsen, G., and Madsen, H. A. Two improvements to the dynamic wake meandering model: including the effects of atmospheric shear on wake turbulence and incorporating turbulence build-up in a row of wind turbines. *Wind Energy*, 2013b. (see page 34)
- Keck, R.-E., Mikkelsen, R., Troldborg, N., de Maré, M., and Hansen, K. S. Synthetic atmospheric turbulence and wind shear in large eddy simulations of wind turbine wakes. *Wind Energy*, 2013c. (see page 30)
- Larsen, G. C., Madsen, H. A., Torben, J., and Troldborg, N. Wake modeling and simulation. Technical Report Risø-R-1653(EN), Technical University of Denmark, Denmark, 2008. (see pages 144 and 145)
- Leonard, A. Energy cascade in large-eddy simulations of turbulent fluid flows. *Advances in Geophysics*, 18:237–248, 1974. (see pages 13, 16, and 47)
- Lesieur, M. and Metais, O. New trends in large-eddy simulations of turbulence. *Annual Review of Fluid Mechanics*, 28:45–82, 1996. (see page 14)
- Lignarolo, L., Ragni, D., Krishnaswami, C., Chen, Q., Simão-Ferreira, C., and van Bussel, G. Experimental analysis of the wake of a horizontal-axis wind-turbine model. *Renewable Energy*, 70:31 46, 2014a. (see page 91)
- Lignarolo, L., Ragni, D., Simão-Ferreira, C., and van Bussel, G. Kinetic energy entrainment in wind turbine and actuator disc wakes: an experimental analysis. *Journal of Physics: Conference Series*, 524(1), 2014b. (see page 92)
- Lignarolo, L., Mehta, D., Stevens, R., Yilmaz, A., Meyers, J., Andersen, S., van Kuik, G., Meneveau, C., Holierhoek, J., Simão-Ferreira, C., Ragni, D., and van Bussel, G. Validation of four les and a vortex model against piv measurements of the near wake of an actuator disk and a wind turbine. *Renewable Energy*, 111:111–111, 2015. (see pages 32, 91, 92, 93, 94, 95, 96, 98, 99, 103, 104, 105, 106, and 147)

- Lilly, D. K. The representation of small-scale turbulence in numerical simulation experiments. In *Proceedings of the IBM Scientific Computing Symposium on Environmental Sciences*, New York, 1967. (see pages 19 and 135)
- Lilly, D. K. A proposed modification of the Germano subgrid-scale closure method. *Physics of Fluids A: Fluid Dynamics*, 4:633–635, 1992. (see page 21)
- Lissaman, P. Energy effectiveness of arbitrary arrays of wind turbines. *Journal of energy*, 3:323–328, 1979. (see page 8)
- Liu, S., Meneveau, C., and Katz, J. On the properties of similarity subgridscale models as deduced from measurements in a turbulent jet. *Journal of Fluid Mechanics*, 275:83–119, 1994. (see pages 13, 19, and 23)
- Lu, H. and Porté-Agel, F. A modulated gradient model for large-eddy simulation: Application to a neutral atmospheric boundary layer. *Physics of Fluids*, 22:1–12, 2010. (see pages 23, 109, and 111)
- Lu, H. and Porté-Agel, F. Large-eddy simulation of a very large wind farm in a stable atmospheric boundary layer. *Physics of Fluids*, 23:065101, 2011. (see page 31)
- Lu, H. and Porté-Agel, F. A modulated gradient model for scalar transport in large-eddy simulation of the atmospheric boundary layer. *Physics of Fluids*, 25, 2013. (see page 23)
- Lund, T. S. On dynamic models for large eddy simulation. Technical Report 177, Annual Research Briefs, Centre for Turbulence Research, Standford University NASA Ames, 1991. (see page 19)
- Mann, J. The spatial structure of neutral atmospheric surface-layer turbulence. *Journal of Fluid Mechanics*, 273:141–168, 1994. (see pages 26, 30, and 94)
- Mann, J. Wind field simulation. *Probabilistic Engineering Mechanics*, 13:269 282, 1998. (see pages 30 and 94)
- Markfort, C. D., Zhang, W., and Porté-Agel, F. Turbulent flow and scalar transport through and over aligned and staggered wind farms. *Journal of Turbulence*, 13:1–36, 2012. (see page 27)
- Mason, P. J. Large-eddy simulation of the convective atmospheric boundary layer. *Journal of the Atmospheric Sciences*, 46:1492–1516, 1989. (see pages 19, 39, 42, 107, and 110)
- Mehta, D., van Zuijlen, A., and Bijl, H. Energy-conserving schemes for wind farm aerodynamics. *Journal of Physics: Conference Series*, 524(1), 2014a. (see page 135)

- Mehta, D., van Zuijlen, A., Koren, B., Holierhoek, J., and Bijl, H. Large eddy simulation of wind farm aerodynamics: A review. *Journal of Wind Engineering and Industrial Aerodynamics*, 133:1 17, 2014b. (see pages 6, 24, 58, 89, and 144)
- Mehta, D. Large eddy simulation of wind farm aerodynamics with energy-conserving schemes. In Ostachowicz, W., McGugan, M., Schröder-Hinrichs, J. U., and Luczak, M., editors, *MARE-WINT: New Materials and Reliability in Offshore Wind Turbine Technology*, chapter 20, pages 347–358. Springer International Publishing, Switzerland, 2016. (see pages 57, 71, and 107)
- Meneveau, C. and Katz, J. Scale-invariance and turbulence models for large-eddy simulation. *Annual Review of Fluid Mechanics*, 32:1–32, 2000. (see pages 13, 14, 23, and 135)
- Meneveau, C., Lund, T. S., and Cabot, W. H. A Lagrangian dynamic subgrid-scale model of turbulence. *Journal of Fluid Mechanics*, 319:353–385, 1996. (see pages 60, 61, 83, and 84)
- Meyers, J. and Meneveau, C. Large eddy simulations of large wind-turbine arrays in the atmospheric boundary layer. In 48th AIAA Aerospace Sciences Meeting Including the New Horizons Forum and Aerospace Exposition, Orlando, Florida, 2010. (see pages 26, 27, 114, and 116)
- Meyers, J. and Meneveau, C. Optimal turbine spacing in fully developed wind farm boundary layers. *Wind Energy*, 15:305–317, 2012. (see page 33)
- Meyers, J. and Meneveau, C. Flow visualization using momentum and energy transport tubes and applications to turbulent flow in wind farms. *Journal of Fluid Mechanics*, 715:335–358, 2013. (see page 28)
- Meyers, J., Geurts, B. J., and Sagaut, P. A computational error-assessment of central finite-volume discretizations in large-eddy simulation using a Smagorinsky model. *Journal of Computational Physics*, 227:156 173, 2007. (see page 57)
- Meyers, J. Error-landscape assessment of large-eddy simulations: A review of the methodology. *Journal of Scientific Computing*, 49:65–77, 2011. (see pages 24, 39, 42, 83, 89, 96, 107, 109, 112, and 113)
- Meyers, J. and Sagaut, P. On the model coefficients for the standard and the variational multi-scale smagorinsky model. *Journal of Fluid Mechanics*, 569: 287–319, 2006. (see page 19)
- Meyers, J., Geurts, B. J., and Baelmans, M. Database analysis of errors in large-eddy simulation. *Physics of Fluids* (1994-present), 15, 2003. (see page 57)

- Meyers, J., Meneveau, C., and Geurts, B. J. Error-landscape-based multiobjective calibration of the smagorinsky eddy-viscosity using high-reynolds-number decaying turbulence data. *Physics of Fluids*, 22:125106, 2010. (see page 74)
- Michelsen, J. A. Basis3d a platform for development of multiblock pde solvers. Technical Report AFM 92-06, Department of Fluid Mechanics, Technical University of Denmark,, 1992. (see page 19)
- Michelsen, J. A. Block structured multigrid solution of 2D and 3D elliptic pde's. Technical Report AFM 94-06, Department of Fluid Mechanics, Technical University of Denmark,, 1994. (see page 26)
- Moeng, C. H. A large eddy simulation model for the study of planetary boundary-layer turbulence. *Journal of the Atmospheric Sciences*, 41(13):2052–2062, 1984. (see pages 8 and 31)
- Munters, W., Meneveau, C., and Meyers, J. Turbulent inflow precursor method with time-varying direction for large eddy simulations and applications to wind farms. *Boundary-Layer Meteorology*, 159:305–328, 2016. (see page 31)
- Norris, S. *A Parallel Navier-Stokes solver for Natural Convection and Free Sur-face Flow*. PhD thesis, School of Aerospace, Mechanical and Mechatronic Engineering, University of Sydney, Australia, 2000. (see pages 19 and 33)
- Norris, S., Storey, R., Stol, K., and Cater, J. Modeling gusts moving through wind farms. In *50th AIAA Aerospace Sciences Meeting Including the New Horizons Forum and Aerospace Exposition*, Nashville, Tennessee, 2012. (see page 19)
- Panofsky, H. and Dutton, J. *Atmospheric Turbulence: Models and Methods for Engineering Applications*. John Wiley & Sons: New York, 1984. (see pages 12 and 108)
- Perić, M. and Ferziger, J. *Computational Methods for Fluid Dynamics*. Spring-Verlag: Berlin, 3 edition, 2002. (see pages 12 and 74)
- Pope, S. B. *Turbulent Flows*. Cambridge University Press: Cambridge, 2000. (see pages 13, 14, 60, and 63)
- Porté-Agel, F. A scale-dependent dynamic model for scalar transport in large-eddy simulations of the atmospheric boundary layer. *Boundary-Layer Meteorology*, 112:81–105, 2004. (see pages 17 and 31)
- Porté-Agel, F., Meneveau, C., and Parlange, M. B. A scale-dependent dynamic model for large-eddy simulation: application to a neutral atmospheric boundary layer. *Journal of Fluid Mechanics*, 415:261–284, 2000. (see pages 16, 19, 21, 22, 26, 31, 34, 39, 42, 107, 110, 111, 113, and 135)

- Porté-Agel, F., Lu, H., and Wu, Y. T. A large-eddy simulation framework for wind energy applications. In *Fifth International Symposium on Computational Wind Engineering*, Chapel Hill, North Carolina, 2010. (see pages 11 and 29)
- Porté-Agel, F., Wu, Y. T., Lu, H., and Conzemius, R. J. Large-eddy simulation of atmospheric boundary layer flow through wind turbines and wind farms. *Journal of Wind Engineering and Industrial Aerodynamics*, 99:154 168, 2011. (see pages 7, 17, 22, 24, 29, 30, and 145)
- Porté-Agel, F., Lu, H., and Wu, Y.-T. Interaction between large wind farms and the atmospheric boundary layer. *Procedia IUTAM*, 10:307 318, 2014. (see pages 17 and 31)
- Rogallo, R. S. Numerical experiments in homogeneous turbulence. Technical Report NASA-TM-81315, National Aeronautics and Space Administraion, USA, 1981. (see pages 61 and 94)
- Sagaut, P. *Large Eddy Simulation for Incompressible Flows.* Springer-Verlag: Berlin, 3 edition, 2006. (see pages 5, 15, 16, 19, 20, 36, 48, and 50)
- Sanderse, B. *Energy-conserving discretization methods for the incompressible Navier-Stokes equations*. PhD thesis, Department of Mathematics and Computer Science, Eindhoven University of Technology, Eindhoven, 2013. (see pages 4, 25, 26, 36, 38, 41, 44, 52, 55, 58, 59, 63, 73, 76, 80, 95, 114, and 141)
- Sanderse, B., van der Pijl, S., and Koren, B. Review of computational fluid dynamics for wind turbine wake aerodynamics. *Wind Energy*, 14:799–819, 2011. (see pages 7, 9, and 24)
- Schelz, W., Umana, A., Barthelmie, R., Larsen, G., Rados, K., Lange, B., Schepers, G., and Hegberg, T. ENDOW: Improvement of wake models within offshore wind farms. *Wind Engineering*, 25:281–287, 2001. (see page 8)
- Schepers, J. G. Engineering models in wind energy aerodynamics: Development, implementation and analysis using dedicated aerodynamic measurements. PhD thesis, Faculty of Aerospace Engineering, Delft University of Technology, Delft, 2012. (see page 32)
- Sforza, P., Sheerin, P., and Smorto, M. Three-dimensional wakes of simulated wind turbines. *AIAA journal*, 19:1101–1107, 1981. (see page 8)
- Shen, W. Z., Mikkelsen, R., Sørensen, J. N., and Bak, C. Tip loss corrections for wind turbine computations. *Wind Energy*, 8:457–475, 2005. (see page 24)
- Smagorinsky, J. General circulation experiments with the primitive equations, Part 1: The basic experiment. *Monthly Weather Review of the American Meteorological Society*, 91:99–164, 1963. (see pages 5 and 18)

- Snel, H. Review of the present status of rotor aerodynamics. *Wind Energy*, 1:46–69, 1998. (see page 7)
- Snel, H. Review of aerodynamics for wind turbines. *Wind Energy*, 6:203–211, 2003. (see page 7)
- Sørensen, J. N. Instability of helical tip vortices in rotor wakes. *Journal of Fluid Mechanics*, 682:1–4, 2011. (see page 6)
- Sørensen, J. N. and Shen, W. Z. Numerical modelling of wind turbine wakes. *Journal of Fluids Engineering*, 124:393–399, 2002. (see page 24)
- Sørensen, N. N. General purpose flow solver applied to flow over hills. PhD thesis, Risø National Laboratory, Roskilde, Denmark,, 1995. (see page 19)
- Stevens, R. J. A. M., Gayme, D. F., and Meneveau, C. Effect of turbine alignment on the average power output of wind-farms. In *International Conference on Aerodynamics of Offshore Wind Energy Systems and Wakes*, Lyngby, Denmark, 2013a. (see pages 3, 27, 28, and 33)
- Stevens, R. J. A. M., Graham, J., and Meneveau, C. A concurrent precursor inflow method for Large Eddy Simulations and applications to finite length wind farms. In *Submitted to Renewable Energy*, Personal Communication, 2013b. (see pages 39 and 94)
- Stevens, R. J. A. M., Graham, J., and Meneveau, C. A concurrent precursor inflow method for large eddy simulations and applications to finite length wind farms. *Renewable Energy*, 68:46 50, 2014. (see page 32)
- Stoll, R. and Porté-Agel, F. Dynamic subgrid-scale models for momentum and scalar fluxes in large-eddy simulations of neutrally stratified atmospheric boundary layers over heterogeneous terrain. *Water Resources Research*, 42:Wo1409, 2006. (see page 21)
- Stoll, R. and Porté-Agel, F. Large-eddy simulation of the stable atmospheric boundary layer using dynamic models with different averaging schemes. *Boundary-Layer Meteorology*, 126:1–28, 2008. (see pages 22 and 31)
- Storey, R. C., Norris, S. E., Stol, K. A., and Cater, J. E. Large eddy simulation of dynamically controlled wind turbines in an offshore environment. *Wind Energy*, 2012. (see page 33)
- Taylor, G. J. Wake measurements on the Nibe wind turbines in Denmark. Technical Report CEC contract EN3W0039UK, UK National Power,, 1990. (see pages 2 and 34)
- Tenaud, C., Pellerin, S., Dulieu, A., and Ta Phuoc, L. Large Eddy Simulations of a spatially developing incompressible 3D mixing layer using the v- ω formulation. *Computers & Fluids*, 34:67–96, 2005. (see pages 25 and 95)

- Tennekes, H. and Lumley, J. L. *A First Course in Turbulence*. MIT Press: Cambridge, MA, 1972. (see page 12)
- Thomsen, K. and Sørensen, P. Fatigue loads for wind turbines operating in wakes. *Journal of Wind Engineering and Industrial Aerodynamics*, 80:121–136, 1999. (see page 2)
- Troldborg, N. *Actuator Line Modeling of Wind Turbine Wakes*. PhD thesis, Department of Mechanical Engineering, Technical University of Denmark, Lyngby, Denmark,, 2009. (see page 27)
- Troldborg, N., Sørensen, J. N., Mikkelsen, R., and SÞrensen, N. N. A simple atmospheric boundary layer model applied to large eddy simulations of wind turbine wakes. *Wind Energy*, 2013. (see page 30)
- van der Pijl, S. P. Numerical modelling of wind farm aerodynamics. Technical Report ECN Internal, Energy Research Centre of the Netherlands,, 2007. (see page 11)
- van Heemst, J. W., Baldacchino, D., Mehta, D., and van Bussel, G. J. W. Coupling of a free wake vortex ring near-wake model with the Jensen and Larsen far-wake deficit models. *Journal of Physics: Conference Series*, 625: 012041, 2015. (see page 144)
- Vermeer, L. J., Sørensen, J. N., and Crespo, A. Wind turbine wake aerodynamics. *Progress in Aerospace Sciences*, 39:467–510, 2003. (see pages 7, 8, and 10)
- Verstappen, R. W. C. P. and Veldman, A. E. P. Symmetry-preserving discretization of turbulent flow. *Journal of Computational Physics*, 187:343 368, 2003. (see pages 4, 36, 44, 52, 54, 71, 141, and 142)
- Viré, A. and Knaepen, B. On discretization errors and subgrid scale model implementations in large eddy simulations. *Journal of Computational Physics*, 228:8203–8213, 2009. (see pages 19, 57, and 62)
- Vreman, B., Geurts, B., and Kuerten, H. Comparison of numerical schemes in large-eddy simulation of the temporal mixing layer. *International Journal for Numerical Methods in Fluids*, 22:297–311, 1996. (see page 57)
- Wan, F. and Porté-Agel, F. Large-eddy simulation of stably-stratified flow over a steep hill. *Boundary-Layer Meteorology*, 138:367–384, 2011. (see page 31)
- Wu, Y. T. and Porté-Agel, F. Large-eddy simulation of wind-turbine wakes: Evaluation of turbine parametrisations. *Boundary-Layer Meteorology*, 138: 345–366, 2011. (see pages 29, 31, and 114)
- Wu, Y. T. and Porté-Agel, F. Simulation of turbulent flow inside and above wind farms: Model validation and layout effects. *Boundary-Layer Meteorology*, 146:181–205, 2013. (see page 22)

- Yee, H., Sandham, N., and Djomehri, M. Low-dissipative high-order shock-capturing methods using characteristic-based filters. *Journal of Computational Physics*, 150:199–238, 1999. (see page 75)
- Zang, Y., Street, R. L., and Koseff, J. R. A dynamic mixed subgrid-scale model and its application to turbulent recirculating flows. *Physics of Fluids A: Fluid Dynamics*, 5:3186–3196, 1993. (see pages 19, 21, 23, and 139)
- Zhang, W., Markfort, C. D., and Porté-Agel, F. Wind-turbine wakes in a convective boundary layer: A wind-tunnel study. *Boundary-Layer Meteorology*, 146:161–179, 2013. (see pages 29 and 32)

Well Tim Maloney raised his head When a bottle of whiskey flew at him He ducked, and landing on the bed The whiskey scattered over Tim Bedad he revives, see how he rises Tim Finnegan rising in the bed Saying "Whittle your whiskey around like blazes, T'underin' Jaysus, do ye think I'm dead?"

Whack fol the dah will ya dance to yer partner Around the flure yer trotters shake Wasn't it the truth I told you? Lots of fun at Finnegan's Wake

Finnegan's Wake, an Irish street ballad, performed by The Dubliners.

'Who in the world am I?' Ah, that's the greatest puzzle.

Alice in Wonderland Lewis Carroll

Dhruv Mehta was born in Pune in the state of Maharashtra in India, on June 10, 1990. Owing to the transferable nature of his father's employment, he moved to various places in India, changing schools as he went along.

In 2007, he completed his schooling in Science from Navy Children School Mumbai, in Bombay (he prefers the original name) and joined the Indian Institute of Technology Kanpur, to pursue a bachelor's degree in Biological Sciences and Bioengineering. In course of his studies, he was an ardent swimmer and played water-polo, skipping most of his lectures, during which he gained interest in aerodynamics.

In 2011 after completing his undergraduate education, Dhruv joined Cranfield University in the UK to read Aerodynamics for the degree of Master of Science and submitted a thesis titled 'CFD Study of a Scramjet's Intake Aerodynamics'. After graduating in 2012, he joined the Energy research Centre of the Netherlands as a PhD researcher, in 2013 and pursued his doctoral studies at the Delft University of Technology till the end of 2015.

He currently lives in Delft and spends most of his free time exercising.

